CHEMICAL REVIEWS

pubs.acs.org/CR

Review

Borates: A Rich Source for Optical Materials

Miriding Mutailipu, Kenneth R. Poeppelmeier,* and Shilie Pan*

Cite This: *Chem. Rev.* 2021, 121, 1130−1202

Read Online

ABSTRACT: The primary goal of this review is to present a clear chemical perspective of borates in order to stimulate and facilitate the discovery of new borate-based optical materials. These materials, which exhibit structures as varied as they are complex, are needed to meet the urgent technological milestones. In the current period of rapid socio-technological breakthroughs, the need for the rational design and discovery of novel borates with superior performance is greater than ever before. Through the sustained efforts of chemists and material scientists, more than 3900 boron-containing compounds, including borate minerals and synthetic borates, have been documented in the scientific literature. This review provides a survey of all the reported anhydrous borates and an analysis of their complex structural chemistry. State-of-the-art progress related to technological advances in borate-based nonlinear optical, birefringent, and self-frequency-doubling materials is surveyed, with special emphasis on the relationships between structural architectures and optical properties. More importantly, this review serves both as a scientific introduction for graduates and post-doctoral researchers to the chemical richness of solid-state borates and as a comprehensive reference for researchers interested in borate-based optical materials.

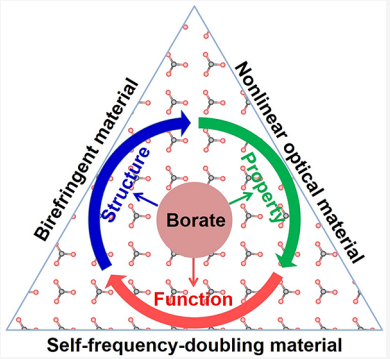

CONTENTS

Received: July 30, 2020
Published: December 14, 2020

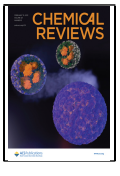

https://dx.doi.org/10.1021/acs.chemrev.0c00796
Chem. Rev. 2021, 121, 1130−1202

1. INTRODUCTION

Borates consisting of boron oxyanions are a rapidly growing part of solid-state chemistry with important and well-established functionality.[1−3] During the past several decades, newly discovered borates have been in the research spotlight due to the large number of complex molecular, one-, two-, and three-dimensional (0D, 1D, 2D, and 3D) structures found in no other mixed metal oxides.[4,5] Because metal- and mixed-metal borates exhibit both unique structures and modes of boron−oxygen (B−O) bonding, many borates are key components in the field of laser science and in modern optoelectronic devices.[6−9] The progress in borate investigations is so great that every year an increasing number of new borate structures are discovered and reported (Figure 1).[10−12]

It follows then that borates with unique structures can be applied as advanced functional materials, such as optical materials,[2,6−9,13] flame retardants,[14] and detergents,[15] *etc.* Thousands of borates are characterized by the great variety in their crystal structures, which is caused by the varied linkage in boron−oxygen/fluorine (B−O/F) fundamental building blocks (FBBs). From the performance perspective, one of the most exciting aspects of borates is their potential to be applied as novel optical materials, and [redacted] Borates exhibit ever-greater possibility to form noncentrosymmetric structures, have wide optical

https://dx.doi.org/10.1021/acs.chemrev.0c00796
Chem. Rev. 2021, 121, 1130−1202

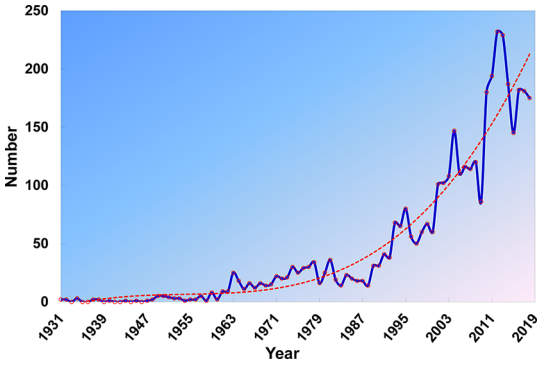

Figure 1. Number of all the available borate structures included in ICSD versus per year through 2019. Composition search criteria: B and O. ICSD with the version of 4.3.0, the latest release of ICSD-2019/02.

transparency windows, maintain excellent chemical stability, and also demonstrate large polarizabilities to achieve the coexistence of suitable second-order NLO coefficients and birefringence, making borate a unique and special class of the candidates for optical applications.[2,6−9,18−20] Several borate crystals including $KB_5O_8{\cdot}4H_2O$, β-BaB_2O_4, LiB_3O_5, CsB_3O_5, $CsLiB_6O_{10}$, α-BiB_3O_6, $Sr_2Be_2B_2O_7$, and $KBe_2BO_3F_2$ have been developed as novel NLO materials to generate UV and deep-UV coherent light.[3,21−27] In addition, metal borates, such as α-BaB_2O_4, $Ca_3(BO_3)_2$, $Ba_3Y(B_3O_6)_2$, $Ba_2M(B_3O_6)_2$ (M = Mg and Ca), and $Ca(BO_2)_2$, with large birefringence are promising birefringent materials for light polarization in deep-UV spectral region.[28−33] The active ions doped rare-earth borates $YAl_3(BO_3)_4$, $RECa_4O(BO_3)_3$ (RE = Y, Gd), and $La_2CaB_{10}O_{19}$ can be employed as practical SFD laser crystals to create the high power, high efficiency lasers with certain characteristic wavelengths.[34−36]

In the meantime, natural and even synthetic borate crystals have reached the limits of their structural diversity and the creation of new borates with optical active structures is mainly restrained by theoretical, methodological, and also technical problems. Thus, at the present time, scientific research is highly concerned with understanding the chemical basis of structure−property−function relationships occurring in the borate systems. Several reviews have appeared in recent years that summarize the synthesis and applications of borates,[1,2,4,6,8,9,12,20,37−45] but these reviews, while very useful, focus either on a specific structural group of borates, or on specific properties. It is thus the right time to write a comprehensive and up-to-date review that summarizes the structural chemistry of borates and their varied structure−property−function relationships for optical applications based on all the available anhydrous borates from the year 1931 to 2019. In this review, the syntheses, crystal structure features, symmetries, and different types of B−O/F FBBs of many borate-based NLO, birefringent, and SFD laser materials are summarized and analyzed. In the following six sections, Structure−property relationship studies focusing on the influence of B−O/F building blocks on the optical properties will be a key feature of these sections. This paper aims to be a comprehensive, authoritative, critical, and accessible review of general interest to both chemistry and materials science communities.

The review is organized as follows. In section 1, we start from a brief description of the research status of borate, with emphasis its importance on related solid-state chemistry and optical materials. In section 2, about a thousand anhydrous borates were chosen to discuss the structural chemistry of borate system. In this section, structural diversity of borates is highlighted and unconventional borates with interesting structure characteristics are discussed. We also provide a comprehensive summary of many borate-based optical crystals as high performance NLO (section 3), SFD laser (section 4), and birefringent (section 5) materials. The recent efforts and active advances in searching of borate-based optical crystals and in understanding of their structure−property relationships are the key of these sections. Finally, this review ends with the giving of conclusions as well as discussing of perspectives and challenges related to the borate chemistry and borate-based optical materials (section 6).

2. STRUCTURAL CHEMISTRY OF ANHYDROUS BORATES

Since the first single crystal structure of a borate formulated with $Be_2BO_3(OH)$ was determined by Zachariasen[46] at the University of Chicago in 1931, more than 3900 boron-containing crystal structures (Figures 1 and 2), including

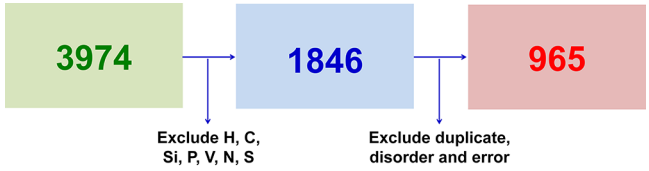

Figure 2. Search and simplification process of target anhydrous borates. ICSD with the version of 4.2.0, the latest release of ICSD-2019/01.

borate minerals and synthetic borates, have been synthesized, and their structures have been determined to build a huge database for the chemistry and materials science communities. The flexibility of anhydrous borate structures provides a strong impetus for the extensive exploration of their crystal chemistry shedding light upon the relationships among structure, property, and function. Thus, anhydrous borates with their extremely rich structural chemistry form the basis of this review. The available anhydrous borates (composition search criteria: B, O, −H, −C, −Si, −P, −V, −N, −S; "−" means exclude the related elements) were checked by screening the web-assisted Inorganic Crystal Structure Database[47] (ICSD with the version of 4.2.0, the latest release of ICSD-2019/01). Note that where multiple refinements were available for the same phases and structures, the most reliable and correct result was selected. Those structures with disorder and obvious errors were not considered in the statistical data. Finally, 965 anhydrous borates (Figure 2 and Tables S1−S4 in the SI) that satisfied the above criteria were chosen to discuss the structural chemistry and applications as optical materials. ***One point should be noted that there are still some borates not included in ICSD but showing interesting structural features or excellent optical properties. Thus, in this review, some of them are also within the scope of the discussion but not in the statistical data.***

https://dx.doi.org/10.1021/acs.chemrev.0c00796
Chem. Rev. 2021, 121, 1130−1202

2.1. Space Group Statistics and Chemical Constituents of Borates

2.1.1. Space Group Statistics. Examination of the selected structures of anhydrous borates reveals rich diversity in the chemical constituents and adopted space groups. The collected statistics demonstrate that the borates cover all the available seven crystal systems: triclinic, monoclinic, orthorhombic, tetragonal, trigonal, hexagonal, and cubic systems. The related proportions are found to be 7.2, 37.2, 26.7, 3.5, 16.9, 5.9, and 2.6% for these seven branches, respectively. Out of a total of 230 space groups in three dimensions, 97 types are observed in the borate system, occupying approximately 42.2% of available types. Among them, the most common space group is monoclinic $P2_1/c$ (no. 14), and about 19.0% of all entries are reported to crystallize in this space group, which makes it retain its position as the highest-ranking space group type. This trend is consistent with the space group frequency ordering summarized by Cambridge Structural Database (CSD) based on all of the available 986 061 CSD structures on January 1, 2019.[48] In addition, $C2/c$, $P\bar{1}$, *Pnma*, and *R*32 make up the rest of the top five space group types. In contrast to these common space groups, there are still many other space groups that are not assigned to any borates. For the rarest types, there are 26 space groups, including *Pm*, $Pmc2_1$, *Amm*2, *Aba*2, *Fdd*2, *Cmca*, *Cmma*, *Fddd*, *Ibca*, $P4_1$, $I4/m$, $P4_122$, $I4cm$, $I4_1cd$, $P\bar{4}2_1c$, $I\bar{4}c2$, $I\bar{4}2m$, $P4_2/nmc$, $I4_2/acd$, *P*3, *R*3, $P3_221$, $P\bar{3}m1$, $R\bar{3}m$, $Ia\bar{3}$, and $P\bar{4}3m$, that are assigned to one sole borate structure.

With respect to borate structures in the 32 crystallographic point groups, no example is found in crystallographic point group 432. Also, $Tl(BO_2)$,[49] $Cu_2(Al_6B_4O_{17})$,[50] and BaB_8O_{13}[51] are the sole cases that are assigned to the crystallographic point groups of 4, $4/m$, and 422, respectively. The occurrence frequency of structures that crystallize in the branches of $6/mmm$, $m\bar{3}$, $m\bar{3}m$, $\bar{6}$, and 622 is very low, and less than five borates belong to the corresponding crystallographic point groups, respectively. In contrast to these examples, $2/m$ and *mmm* are the two most common point groups, and 312 (about 32.3%) and 150 (15.5%) cases of borates are assigned to these two branches and they are all centrosymmetric. For the noncentrosymmetric branch, *mm*2 (8.3%) and 32 (6.6%) are the two classes with high proportion. The classical NLO crystals LiB_3O_5,[23] CsB_3O_5,[24] $CsLiB_6O_{10}$,[25] and $KBe_2BO_3F_2$[27] belong to the above two point groups. It is noteworthy that the corresponding proportions of borates are in total 34.9% and 65.1% for the branches of noncentrosymmetric and centrosymmetric borate structures (Figures 3a,b), whereas for all the inorganic crystal structures, the structures belonging to the noncentrosymmetric structures is only approximately 15%,[2] which is considerably lower than that of borates systems. Therefore, the probability that a new borate structure lacks a center of symmetry is more than double that for non-borate structures. Thus, borates can be regarded as a rich source of functional materials that require a noncentrosymmetric structure, such as second-order NLO, piezoelectric, ferroelectric, photorefractive materials, as well as electro-optic crystals with both Pockets (linear optics) and Kerr (nonlinear optics) effects, *etc.*[2,6−9,12,17,20,37,38,41,43−45]

2.1.2. Chemical Constituents. The frequency of occurrence of the related elements as chemical constituents in borate system is shown in Figures 4 and 5. Apart from B and O elements, the most common constituents that are beyond 10% in proportion are the element Ba (129), Na (114), Li (109), and F (97), corresponding to the species of barium borates, sodium borates, lithium borates, and borate fluorides (or fluorooxoborates). These examples are a reflection of the functionality of related species with certain chemical constituents. For optical and electronic devices, such as optical parametric oscillators (OPO),[52] laser frequency multipliers, and pyroelectric devices, they exploit the microcosmic nature of core materials, in which the core materials are borate fluorides, fluorooxoborates, and barium borates for nonlinear optics as well as sodium/lithium borates for temperature-responsive anion conductors. It is noteworthy that fluorine containing borates are ranked top-five in terms of the frequency of occurrence of fluorine. This is reasonable when considering the positive roles of fluorine on broadening the structural chemistry and regulating the optical properties of borates in the following crucial aspects:[8,45,53,54]

(a) The fluorine with the largest electronegativity (3.98) can reduce the negative effective charges of terminal oxygen in borate system and shift the absorption edges to the shorter wavelength region, resulting in widened transparency area. This will make the target borate-based crystals require higher energy for electronic excitation when irradiated by the laser source (see section 3.9).

(b) The fluorine often forms fluorine-centered distorted polyhedra, which can serve as the secondary building units to adjust the local environments to improve the second harmonic generation (SHG) efficiencies in related NLO materials.

(c) The fluorine can substitute for oxygen to form oxyfluoride $[BO_{4-x}F_x]$ units, which exhibit stronger polarizability anisotropy and hyper-polarizability compared to $[BO_4]$ units, thus $[BO_{4-x}F_x]$ units can be considered as new chromophores to balance the

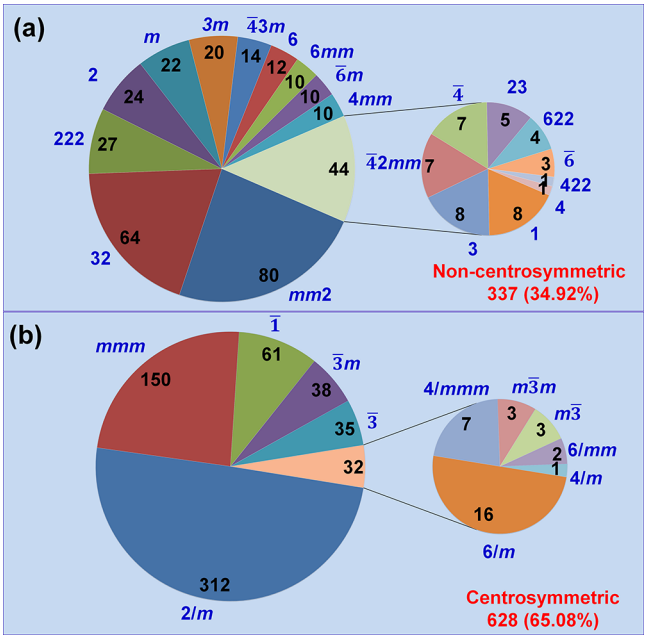

Figure 3. Analysis of the noncentrosymmetric (a) and centrosymmetric (b) crystal database based on all the available borates. The corresponding proportions of borates are in total 34.9% and 65.1% for the branches of noncentrosymmetric and centrosymmetric borate structures. Inset: number in black gives the occurrence frequency of specific point groups (in blue).

https://dx.doi.org/10.1021/acs.chemrev.0c00796
Chem. Rev. 2021, 121, 1130−1202

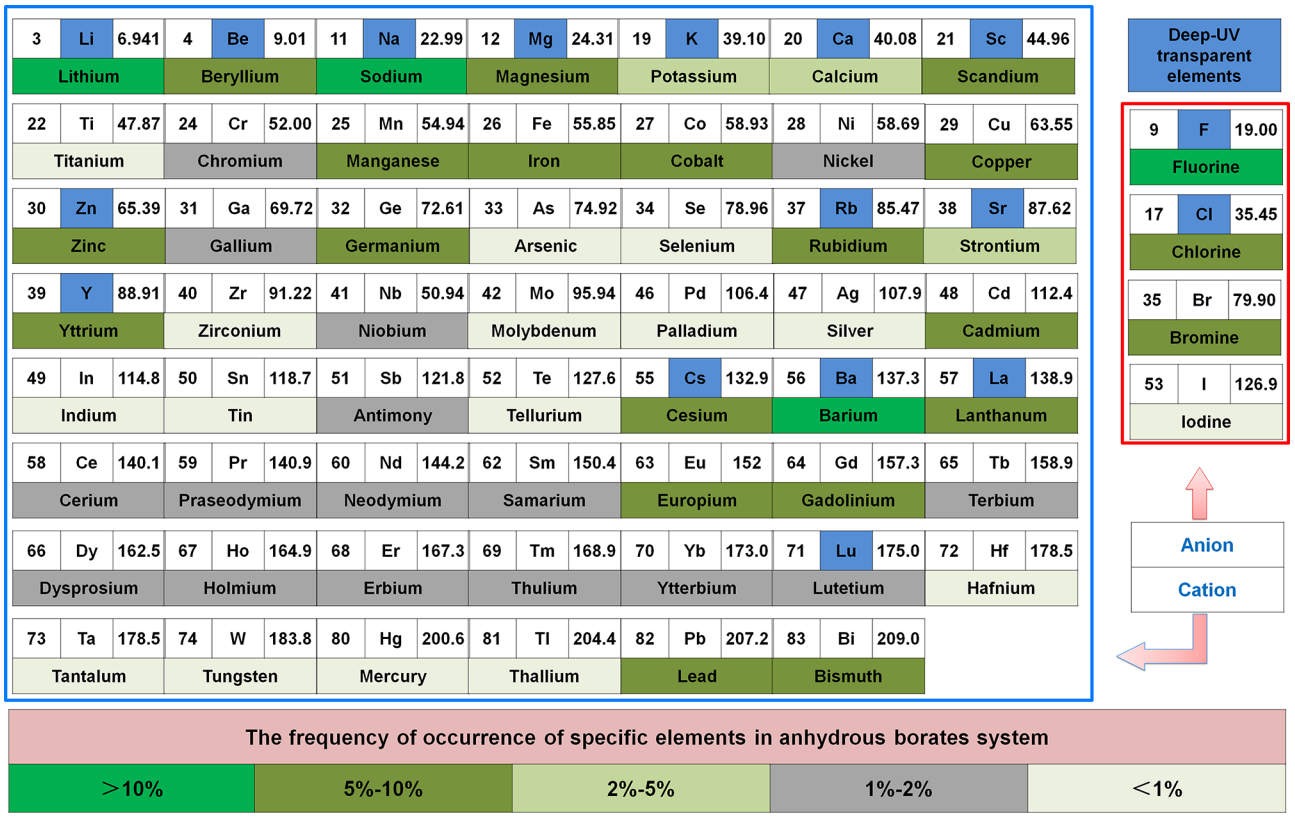

Figure 4. Frequency of occurrence chemical constituents in borate system, and the specific elements are color-coded according to the occurrence frequency (last line). The deep-UV transparent elements are marked as blue.

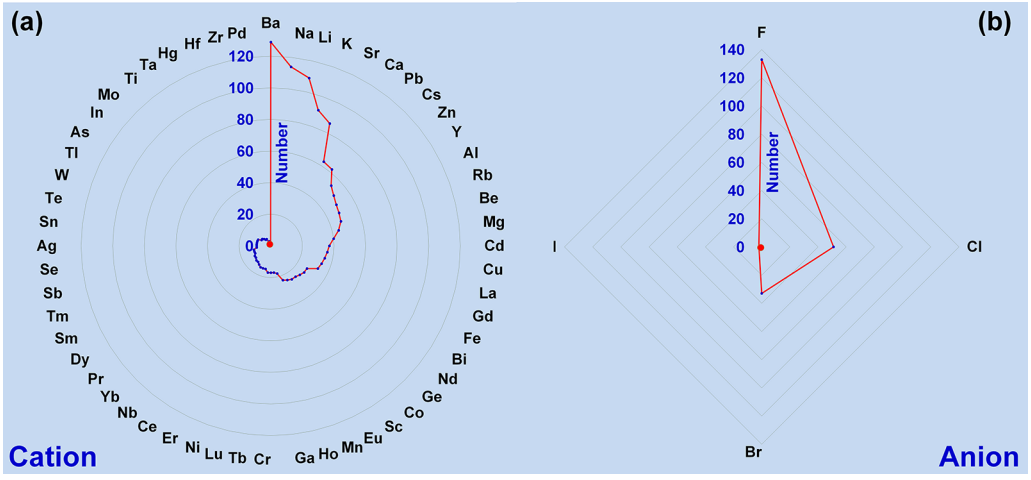

Figure 5. Frequency of occurrence cation (a) and anion (b) in borate system.

multiple criteria among the critical parameters for NLO and birefringent materials (see section 2.2.4).

(d) Structurally, when compared with the borate family, the incorporation of fluorine into borates to construct borate fluorides and fluorooxoborates reduces the symmetry and improves the probability of achieving a noncentrosymmetric structure. This can be further verified by the increased proportions of noncentrosymmetric structures from borates (35%) to borate fluorides (38%) and especially to fluorooxoborates (65%).

The element K (91), Sr (86), Ca (63), Pb (62), Cs (54), Zn (51), Cl (51), Y (49), and Al (48) are also important in the dataset as a whole, and the related proportions are all above 5% (see Figures 4 and 5). Alkali and alkaline-earth metals are the most abundant elements in borates and they are all free of *d*−*d* or *f*−*f* electronic transitions, which is beneficial for good transparency in the UV spectral region with deep-UV absorption edges below 200 nm. Thus, they become the best alternative elements with respect to the design and synthesis of deep-UV transparent materials with large bandgaps (see sections 3.2 and 3.3). Other metallic elements, like Pb, Al, and Zn, also have the positive roles on enhancing the polarizability anisotropy and hyper-polarizability of borates, which can result in enlarged birefringence and NLO effects (see sections 3.5, 3.6, 3.7 and 3.8). The anomalously large number of rare earth elements (RE = Y, Sc, La, Ho, *etc.*) is due

https://dx.doi.org/10.1021/acs.chemrev.0c00796
Chem. Rev. 2021, 121, 1130−1202

to the formation of RE-based deformed polyhedra to enhance the NLO coefficients in rare earth borates, which can increase the output power and efficiency when used as host materials in SFD laser crystals (see sections 3.4 and 4.2).

For anhydrous borates, high-temperature syntheses are used more often than aqueous solution methods. These reaction temperatures, however, are too high to synthesize many rare earth borates. That is why the number of rare earth element containing borates is less than that of alkali and alkaline-earth metal borates. For the rarest chemical constituents, there are less than 10 borates that contain Se, Ag, Sn, Te, W, Tl, As, In, I, Mo, Ti, Ta, Hg, Zr, Hf, and Pd, with the corresponding proportions less than 1% (Figures 4 and 5, Tables S1−S4 in the SI). For example, among them, PdB_2O_4 is the sole case that contains Pd element in borates.[55] Unlike other halogens, iodine is rare in borates owing to the difficulty in synthesis of such borate iodides. For high-temperature synthesis process, iodine sublimes at high temperatures[56] and can display phase transitions, which makes borate iodides difficult to synthesize. For low-temperature solution methods, iodates[57] and borates have totally different favorable acid−base environments, which makes it difficult to find suitable potential of hydrogen (pH) to synthesize the borate iodides.

2.2. Structural Diversity of B−O/F Basic Units

Compared to carbonates, nitrates, silicates, phosphates, sulfates, and vanadates, the crystal chemistry of borates is unique and shows many structural and functional features.[1,2,4,5,41,43−45] Unlike the fixed coordination environment of central cations (coordinated with O/F atoms) in carbonates ($[CO_3]$), nitrates ($[NO_3]$), silicates ($[SiO_4]$ and $[SiO_{6-x}F_x]$), vanadates ($[VO_4]$ and $[VO_{6-x}F_x]$), phosphates ($[PO_{4-x}F_x]$), and sulfates ($[SO_{4-x}F_x]$), the overlap of atomic B 2*s* and 2*p* orbitals can result in *sp*, sp^2, and sp^3-hybridized orbitals, which can further bond with O/F atoms to construct the linear $[BO_2]$, triangular $[BO_3]$, and tetrahedral $[BO_{4-x}F_x]$ units, respectively. Thus, seven B−O/F basic units, including $[BO_2]$, $[BO_3]$, $[BO_4]$, $[BO_3F]$, $[BO_2F_2]$, $[BOF_3]$, and $[BF_4]$ units, have been identified to date (Figure 6). The variety of existing

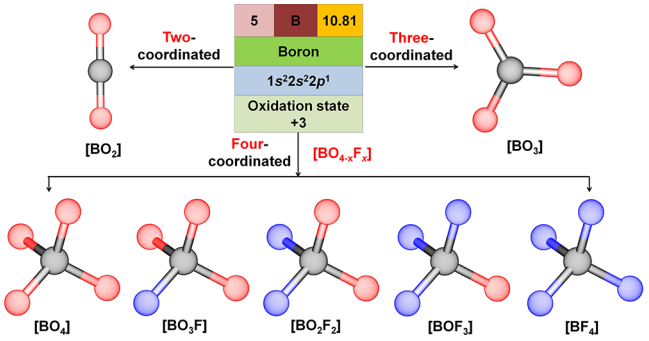

Figure 6. Geometric configuration of the available seven B−O/F basic units in borates. The atoms in black, red, and blue are B, O, and F atoms, respectively.

and possible structural connection modes of these basic building blocks contributes to the diverse structural chemistry of borates and to the many borates constantly being reported with new unique structures.

2.2.1. Linear $[BO_2]$ Units. Among the three series of B−O/F basic units with different coordination environments, the two-coordinated $[BO_2]$ with linear configuration is the rarest motif and fewer than three or four-coordinated B−O/F units. Geometrically, the central B atoms (Figure 6) are bonded with two O atoms to construct linear $[BO_2]$ units with the B−O bond lengths and O−B−O angles close to their statically averaged values of 1.221 Å and 180°, but there are still no disorder-free borates with $[BO_2]$ units available to date. To the best of our knowledge, the sole case with linear $[BO_2]$ units in a borate is $Gd_4(BO_2)O_5F$[58] obtained under the closed experimental environment, in which the F(1) and O(4) atoms are assigned to occupy the same position with equal proportion. Even in the other phases, the linear $[BO_2]$ units are also extremely rare and are only observed in a few *apatite*-type structures,[59] for example, $Sr_{9.402}Na_{0.209}(PO_4)_6(B_{0.996}O_2)$,[60] $Sr_7La_3[(PO_4)_{2.5}(SiO_4)_3(BO_4)_{0.5}](BO_2)$,[61] and $Sr_{10}(PO_4)_{5.5}(BO_4)_{0.5}(BO_2)$.[62] The common structural characteristic of these $[BO_2]$ units in the aforementioned structures is their special coordination positions. The linear $[BO_2]$ units in these related *apatite-type* structures locate within the channels formed by metal-based polyhedra and running along the three-fold inversion axis. Whereas for the $[BO_2]$ units in $Gd_4(BO_2)O_5F$, they locate between the layers built up by the Ga−O/F polyhedra and hold the layers together to form the overall 3D architecture. Owing to this special feature, the $[BO_2]$ units in *apatite-type* structures can be replaced by X ($X = F^-$, Cl^-, Br^-, I^-, OH^-, O^{2-}) units.[63] Thus, the dimeric $[BO_2]$ units with only one electron short to electronic shell closing and high electron affinity can be regarded as the super-halogen in the cluster chemistry.[63] The $[BO_2]$ units also belong to the family of molecular moieties with the "magic" number of 16 electrons, just like fulminate $[CNO]^-$, carbide-borate $[CBC]^{5-}$, and nitride-borate $[BN_2]^{3-}$.

2.2.2. Triangular $[BO_3]$ Units. Statistics show that 838 and 527 cases of anhydrous borates contain and are only composed of the $[BO_3]$ units, respectively. The proportions in the two categories are as high as 86.8 and 54.6%, respectively, which makes the $[BO_3]$ motifs the most common B−O basic unit. Among these many phases, although their elemental compositions are extremely different, however, the geometric characteristics of the $[BO_3]$ units are consistent and share many common features. The central B atoms (Figure 6) are bonded to three O atoms to construct planar $[BO_3]$ triangles with the average B−O bond lengths and O−B−O angles close to their statically averaged values (1.371 Å and 120°). The triangular $[BO_3]$ units feature π-conjugated structure with the $p_\pi-p_\pi$ configurations of π_4^3, which can delocalize the π electrons across all the adjacent aligned *p* orbitals. Owing to this configuration, the $[BO_3]$ units will exhibit a large optical anisotropy between the two directions, which is parallel and perpendicular to the plane.[43] When the $[BO_3]$ units polymerize into the highly polymerized B−O groups by sharing the terminal O atoms along the same plane, the improved optical anisotropic polarizabilities are expected in them when compared with isolated $[BO_3]$ units. Thus, borates with B−O units polymerized by $[BO_3]$ units are the preferred system to search the optical materials that require large anisotropic polarizabilities. On the basis of this, $Sr_2Be_2B_2O_7$ with $[BO_3]$ units,[3] $KBe_2BO_3F_2$ with $[BO_3]$ units,[27] and β-BaB_2O_4 with $[B_3O_6]$ units[22] as novel NLO materials as well as α-BaB_2O_4 with $[B_3O_6]$ units,[28] $Ba_2M(B_3O_6)_2$ (M = Mg and Ca) with $[B_3O_6]$ units,[31,32] and $Ca(BO_2)_2$[33] with $^1[BO_2]_\infty$ infinite chains as birefringent materials were developed and investigated in great detail. Among the borates only containing $[BO_3]$ units, only four polymerized B−O groups can be

https://dx.doi.org/10.1021/acs.chemrev.0c00796
Chem. Rev. 2021, 121, 1130−1202

formed; to date, there are the dimeric $[B_2O_5]$, ring-like $[B_3O_6]$, trimeric $[B_3O_7]$, tetramerized $[B_4O_8]$ groups as well as 1D $^1[BO_2]_\infty$ infinite chains.

2.2.3. Tetrahedral $[BO_{4-x}F_x]$ (x = 0−4) Units. There are 438 cases of anhydrous borates containing the four-coordinated $[BO_{4-x}F_x]$ units. The tetrahedral units can be $[BO_4]$, $[BO_3F]$, $[BO_2F_2]$, $[BOF_3]$, and $[BF_4]$ units (Figure 6). Among them, the $[BO_4]$ units are the most frequent tetrahedral B−O/F units and about 422 and 118 anhydrous borates contain and are only composed of $[BO_4]$ units, respectively. The most noticeable features of borates that consist exclusively of tetrahedral $[BO_4]$ units are their synthesis conditions, and more than half were obtained under high pressure-driven conditions. As expected, the high-pressure borates exhibit four-fold-coordinated B with O, which is in accordance with the pressure coordination rules.[64,65] The triangular $[BO_3]$ groups can also be transformed into tetrahedral $[BO_4]$ units with the drive of high pressure, which is associated with the anomalous pressure dependence of viscosity and topological disorder. Both trends demonstrate that high pressure-driven conditions are favorable for the syntheses of borates that consist exclusively of tetrahedral $[BO_4]$ units. Structurally, the oxyfluorinated tetrahedral $[BO_{4-x}F_x]$ units can be evolved by substituting the terminal O positions of $[BO_4]$ templates with F atoms. Compounds with oxyfluorinated units offer a new materials platform from which superior functionality may arise.[66,67] In these tetrahedral units, the $[BOF_3]$ and $[BF_4]$ derivatives are uncommon species and are only observed in $BaBOF_3$ ($Pnma$)[68] and $(ClO_2)(BF_4)$,[69] respectively, in which the two types of B−O/F units are in isolated configurations. However, borates with tetrahedral units of $[BO_3F]$ and $[BO_2F_2]$ are more prevalent because of the rapidly growing number of studies of fluorooxoborates with unique B−F bonds in recent years. The *aurivillius-like* $BaBOF_3$ ($P2_1/c$)[70] and $MB_2O_3F_2$ (M = Ba, Pb, Sn)[71−73] are the two series that only contain $[BO_2F_2]$ and $[BO_3F]$ units, respectively. These basic B−O/F units further condense into 1D infinite chains for $BaBOF_3$ ($P2_1/c$) and 2D single-layers for $MB_2O_3F_2$ (M = Ba, Pb, Sn). It is worth noting that, in only $[BO_{4-x}F_x]$ units containing borates, different types of isolated and polymerized B−O/F units can be formed, such as, 0D $[B_2O_7]$, 0D $[B_3O_9]$, and 0D $[B_3O_3F_6]$ units as well as 1D $^1[BO_3]_\infty$, 1D $^1[BOF_2]_\infty$, and 1D $^1[B_2O_6F]_\infty$ infinite chains.

2.2.4. Microstructure and Electronic Properties of B−O/F Basic Units. To further investigate the microstructure of these B−O/F basic units at the molecular level, their frontier molecular orbitals were visualized by using the density functional theory implemented by the Gaussian09 package (Figure 7).[74] To ensure the reliability of the results, all seven B−O/F basic units, including $[BO_2]$, $[BO_3]$, $[BO_4]$, $[BO_3F]$, $[BO_2F_2]$, $[BOF_3]$, and $[BF_4]$ units, are all based on the experimentally obtained single crystal structures rather than build related ideal linear, triangular, and tetrahedral B−O/F models. The origin of these seven B−O/F basic units is $Gd_4(BO_2)O_5F$[58] for $[BO_2]$, $KBe_2BO_3F_2$[27] for $[BO_3]$, $AsBO_4$ ($I\bar{4}$)[75] for $[BO_4]$, $SrB_5O_7F_3$[76] for $[BO_3F]$, $BaBOF_3$ ($P2_1/c$)[70] for $[BO_2F_2]$, $BaBOF_3$ ($Pnma$)[68] for $[BOF_3]$, and $(ClO_2)(BF_4)$[69] for $[BF_4]$ units, respectively. Figure 7 shows the calculated frontier molecular orbitals of seven available B−O/F basic units, including the highest occupied molecular orbitals (HOMO) and lowest unoccupied molecular orbitals (LUMO). It is evident that the HOMO is mainly occupied by the nonbonding orbitals of O 2p in $[BO_2]$, $[BO_3]$, $[BO_4]$, $[BO_3F]$, $[BO_2F_2]$, and $[BOF_3]$ units with some involving of F 2p orbitals in $[BO_2F_2]$ and $[BOF_3]$ units. The F 2p orbitals are not significantly involved in the HOMO because of its large electronegativity (see Figure 7). The HOMO of the $[BF_4]$ units is occupied by F 2p orbitals, showing different molecular orbital features. The LUMO of all seven anionic groups consist of the anti-σ B−O/F bonds (Figure 7). It is noteworthy that the introduction of F in $[BO_4]$ to form $[BO_{4-x}F_x]$ units can result in the enhanced anisotropy in both HOMO and LUMO due to their B−O/F-based tetrahedral distortions, which can further lead to large optical anisotropy.

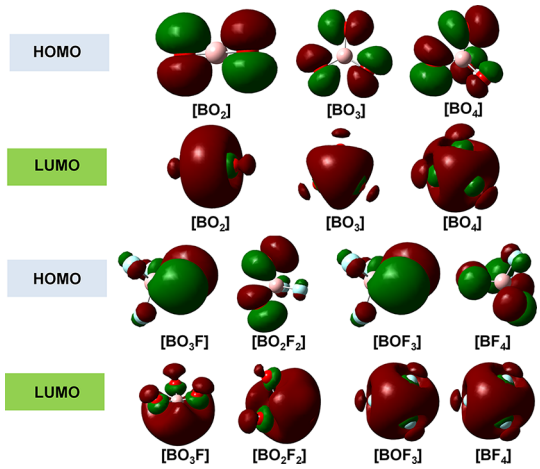

Figure 7. Frontier molecular orbitals of seven B−O/F basic units in borates, including HOMO and LUMO. The pink, red, and blue balls represent the B, O, and F atoms, respectively. The corresponding geometric models of $[BO_2]$, $[BO_3]$, $[BO_4]$, $[BO_3F]$, $[BO_2F_2]$, $[BOF_3]$, and $[BF_4]$ units are established by using the experimentally obtained single structures of $Gd_4(BO_2)O_5F$,[58] $KBe_2BO_3F_2$,[27] $AsBO_4$ ($I\bar{4}$),[75] $SrB_5O_7F_3$,[76] $BaBOF_3$ ($P2_1/c$),[70] $BaBOF_3$ ($Pnma$),[68] and $(ClO_2)(BF_4)$,[69] respectively.

In addition, we theoretically analyzed the polarizability anisotropy of seven B−O/F anionic groups and the polarizability anisotropies of $[BO_{4-x}F_x]$ units are larger than those of $[BO_4]$ and $[BF_4]$ units but still smaller than those of linear $[BO_2]$ and triangular $[BO_3]$ units (Table 1). The polarizability anisotropy of $[BO_2]$ units ranks first among the seven B−O/F anionic groups, and thus a large birefringence determined by polarizability anisotropy in $[BO_2]$ containing borates can be expected. Besides, all the seven typical B−O/F units are deep-UV transparent with large bandgaps changing from 8.48 eV in $[BO_3]$ to 15.51 eV in $[BF_4]$ units. That means, when the dangling bonds of terminal O atoms in the related borates are effectively eliminated, the bandgaps can be blue-shifted to get close to their theoretical values. Taking the classical $KBe_2BO_3F_2$ crystal without O dangling bonds as an example, the bandgap of $KBe_2BO_3F_2$ is as large as 8.44 eV (corresponding to a short absorption edge of 147 nm),[27] which is quite close to the HOMO−LUMO bandgap of $[BO_3]$ units (8.48 eV), indicating the feasibility of evaluation of macroscopic optical properties of borates based on the microscopic properties of their B−O basic units, especially for alkali and alkaline-earth metals, in which the metal cations contribute less to their optical properties.[20] Besides, the largest hyper-polarizability tensor of $[BO_3F]$, $[BO_2F_2]$, and $[BOF_3]$ units is much larger than those of $[BO_3]$ (~3−5 times), $[BO_4]$ (~10−16 times), and $[BF_4]$ (~7−11 times) units, indicating

https://dx.doi.org/10.1021/acs.chemrev.0c00796
Chem. Rev. 2021, 121, 1130−1202

Table 1. Basic Electronic Properties of $[BO_2]$, $[BO_3]$, $[BO_4]$, $[BO_3F]$, $[BO_2F_2]$, $[BOF_3]$, and $[BF_4]$ Anionic Units, Including HOMO−LUMO Bandgap (E_g), Eigenvalues of Polarizability Tensor (ε), Polarizability Anisotropy (δ), Hyperpolarizability Tensor (β_{xyz}), and Largest Hyperpolarizability Tensor (β_{max})[a]

property	direction	$[BO_2]$	$[BO_3]$	$[BO_4]$	$[BO_3F]$	$[BO_2F_2]$	$[BOF_3]$	$[BF_4]$
HOMO		22.82	15.95	28.80	22.82	15.93	8.77	−3.45
LUMO		32.64	24.42	39.56	32.64	26.10	18.31	12.06
Eg (eV)		**9.82**	**8.48**	**10.76**	**9.82**	**10.17**	**9.54**	**15.51**
ε	1	9.10	21.04	20.84	17.45	18.31	12.97	10.97
	2	9.10	21.04	20.84	20.68	16.71	13.50	10.86
	3	22.34	14.03	19.28	18.35	14.28	15.92	10.77
δ		**13.23**	**7.01**	**1.56**	**3.23**	**4.03**	**2.95**	**0.20**
β_{xyz}	*xxx*	0.00	0.00	0.00	−38.04	−0.65	−7.99	−0.59
	xxy	0.00	−10.79	0.00	−1.69	−6.14	16.98	−1.00
	xyy	0.00	0.00	0.00	−25.49	−3.70	−2.23	0.63
	yyy	0.00	10.80	0.00	6.53	−48.15	32.01	−1.22
	xxz	0.00		3.61	0.00	−3.62	0.00	1.30
	xyz	0.00	0.00	0.00	0.00	1.57	0.00	−4.27
	yyz	0.00		−3.61	0.00	−16.75	0.00	−1.64
	xzz	0.00	0.00	0.00	−25.74	1.63	−17.96	−1.08
	yzz	0.00	−0.01	0.00	−7.79	−9.69	12.51	−0.22
	zzz	0.00		0.00	0.00	−13.61	0.00	−0.36
β_{max}		**0.00**	**10.80**	**3.61**	**-38.04**	**-48.15**	**32.01**	**-4.27**

[a]These values were calculated by building the corresponding geometric models of $[BO_2]$, $[BO_3]$, $[BO_4]$, $[BO_3F]$, $[BO_2F_2]$, $[BOF_3]$, and $[BF_4]$ units from $Gd_4(BO_2)O_5F$,[58] $KBe_2BO_3F_2$,[27] $AsBO_4$ (*I*4),[75] $SrB_5O_7F_3$,[76] $BaBOF_3$ ($P2_1/c$),[70] $BaBOF_3$ (*Pnma*),[68] and $(ClO_2)(BF_4)$,[69] respectively.

that larger second-order nonlinearities can be expected in fluorooxoborates than those in related borates.[8,45,54]

2.3. Structural Chemistry of FBBs

Structurally, B−O/F building units can further connect in different ways (corner-sharing or/and edge-sharing) to condense and form the typical B−O/F polynuclear anions, which can be regarded as the FBBs of borates chemistry. Along with the rapid development in potential applications of borates as optical materials, the classification and description of new FBBs urgently demand further investigation that covers the newest aspects of borates in structural chemistry and structure−property relationships. In borates, polynuclear anions are formed by $[BO_3]$ and $[BO_4]$ units, sharing corners and edges so that a compact insular group generally results, in which these groups are called FBBs.[77−82] The FBB, should be the simplest units that can reflect the basic structural information on an assigned crystallographic frame, which is different from the repeat unit of a borate structure.[77] Generally, the repeat unit of a borate structure should contain at least one FBB. These FBBs can polymerize into complex borate polyanions, such as those with infinite chains, layers, and network anions. The great diversity in the crystal structure of borates makes it necessary to introduce the algebraic descriptors for B−O units, which are the basis for structural classification schemes for borate systems. Thus, structural classification and topological description of FBBs was first introduced by C. L. Christ and J. P. Clark in 1977,[78] where they introduced the notation (n: $i\mathbf{\Delta} + j\mathbf{T}$) for each FBB which includes the total number of B atoms (n), $[BO_3]$ triangles (i), and $[BO_4]$ tetrahedra (j) as well as the symbols for a $[BO_3]$ triangle ($\mathbf{\Delta}$) and a $[BO_4]$ tetrahedron ($\mathbf{T}$). By using the above convenient shorthand notation, they can distinguish the cases of borates with the n value changing from 1 to 9. For example, the FBB of α-CsB_5O_8[79] can be written as 5:4$\mathbf{\Delta}$ +1$\mathbf{T}$ and it has five B atoms, in which four and one B atoms adopt $[BO_3]$ triangles and $[BO_4]$ tetrahedra, respectively. Researchers have widely used this approach to analyze and classify the structure of borates for several decades.

In 1995, Burns *et al.*[80] further developed the modern descriptors for borate clusters in every FBB with more emphasis on the connectivity between $[BO_3]$ and $[BO_4]$ units as well as the linkage within and between the rings formed by $[BO_3]$ and $[BO_4]$ units. In this descriptor, the $[BO_3]$ triangles and $[BO_4]$ tetrahedra are represented as $\mathbf{\Delta}$ and □, respectively. The delimiter (⟨ ⟩) indicates that borate polyhedra form a single cyclic ring, and the symbols "−" or "=" indicate the number of shared polyhedra between two rings, "−" for one and "=" for two polyhedra, respectively.[80] Thus, the borates consisting of isolated $[BO_3]$ triangles and $[BO_4]$ tetrahedra can be denoted as 1B:1$\mathbf{\Delta}$:$\mathbf{\Delta}$ and 1B:1□:□, respectively. With this descriptor, the FBB of penta-borate α-CsB_5O_8[79] can be written as 5B:4$\mathbf{\Delta}$:1□:⟨2$\mathbf{\Delta}$□⟩−⟨2$\mathbf{\Delta}$□⟩, which can better describe the connectivity between two three-membered B−O rings in $[B_5O_{10}]$ FBB. A few years later, Strunz[81] developed a classification system for mineral borates based on the recognition of FBBs according to Christ and Clark. The B−O clusters that underlie the grouping of borates as *mono-*, *di-*, *tri-*, *tetra-*, *penta-*, and *hexa*-borates were referred to as FBBs in related borates.[81] Within each category, the B−O anionic groups of borates are further classified to *soro-* (isolated groups), *ino-* (chain), *phyllo-* (layered), and *tecto-* (framework) units according to the polymerized dimensions. Later on, Touboul *et al.*[82] updated the notation of B−O FBBs of borates, and the shorthand notation is symbolized as

$$n: \infty^{r}a[(m: b\mathbf{\Delta} + c\mathbf{T}) + (m': b'\mathbf{\Delta} + c'\mathbf{T}) + \cdots]$$

https://dx.doi.org/10.1021/acs.chemrev.0c00796
Chem. Rev. 2021, 121, 1130−1202

Table 2. Basic Structural Information of Several Representative FBBs Categories with the Number of B Atoms Ranging from 1 to 63 in a Borate System[a]

no.	chemical formula	N_B	FBBs	shorthand notation
1	$KBe_2BO_3F_2$[27]	1	$[BO_3]$	1:[(1**Δ**)]
2	$AsBO_4$ ($I\bar{4}$)[75]	1	$[BO_4]$	1:[(1**T**)]
3	CaB_2O_4[83]	1	$[BO_3]$	$1{:}\infty^1[(1{:}\mathbf{\Delta})]$
4	γ-$LiBO_2$[84]	1	$[BO_4]$	$1{:}\infty^3[(1{:}\mathbf{T})]$
5	$Al_4B_6O_{15}$[85]	2	$[B_2O_5]$	2:[(2**Δ**)]
6	$Se_2B_2O_7$[86]	2	$[B_2O_7]$	2:[(2**T**)]
7	$TlBO_2$[49]	2	$[B_2O_6]$	$2{:}\infty^1[(2{:}\mathbf{\Delta}+\mathbf{T})]$
8	β-BaB_2O_4[22]	3	$[B_3O_6]$	3:[(3**Δ**)]
9	α-$KBe_2B_3O_7$[87]	3	$[B_3O_7]$	3:[(3**Δ**)]
10	$K_2B_3SbO_8$[88]	3	$[B_3O_8]$	$3{:}[(3{:}\mathbf{\Delta}+2\mathbf{T})]$
11	$GdBO_3$ ($R32$)[89]	3	$[B_3O_9]$	3:[(3**T**)]
12	$NaBeB_3O_6$[87]	3	$[B_3O_7]$	$3{:}\infty^1[(3\mathbf{\Delta})]$
13	$KSeB_3O_7$[90]	3	$[B_3O_7]$	$3{:}\infty^1[(3{:}2\mathbf{\Delta}+\mathbf{T})]$
14	LiB_3O_5[23]	3	$[B_3O_7]$	$3{:}\infty^3[(3{:}2\mathbf{\Delta}+\mathbf{T})]$
15	$Li_6B_4O_9$[91]	4	$[B_4O_8]$	4:[(4**Δ**)]
16	$Rb_2GeB_4O_9$[92]	4	$[B_4O_9]$	$4{:}[(4{:}2\mathbf{\Delta}+2\mathbf{T})]$
17	$Gd_4B_4O_{11}F_2$[93]	4	$[B_4O_{11}]$	$4{:}[(2{:}\mathbf{\Delta})+(2{:}\mathbf{T})]$
18	$AgBO_2$[94]	4	$[B_4O_9]$	$4{:}\infty^1[(4{:}2\mathbf{\Delta}+2\mathbf{T})]$
19	$Na_3Zn(B_5O_{10})$[95]	5	$[B_5O_{10}]$	$5{:}[(5{:}4\mathbf{\Delta}+\mathbf{T})]$
21	$YBe_2B_5O_{11}$[96]	5	$[B_5O_{11}]$	$5{:}[(5{:}3\mathbf{\Delta}+2\mathbf{T})]$
22	α-CsB_5O_8[79]	5	$[B_5O_{10}]$	$5{:}\infty^2[(5{:}4\mathbf{\Delta}+\mathbf{T})]$
23	α-KB_5O_8[97]	5	$[B_5O_{10}]$	$5{:}\infty^3[(5{:}4\mathbf{\Delta}+\mathbf{T})]$
24	$KZnB_3O_6$[99,100]	6	$[B_6O_{12}]$	$6{:}[(6{:}4\mathbf{\Delta}+2\mathbf{T})]$
25	$Ba_3Ge_2B_6O_{16}$[101]	6	$[B_6O_{16}]$	$6{:}[(6{:}2\mathbf{\Delta}+4\mathbf{T})]$
26	$CsLiB_6O_{10}$[25]	6	$[B_6O_{13}]$	$6{:}\infty^3 2[(3{:}2\mathbf{\Delta}+\mathbf{T})]$
27	$Li_4Cs_3B_7O_{14}$[102]	7	$[B_7O_{14}]$	$7{:}[2(3{:}2\mathbf{\Delta}+\mathbf{T})+(1{:}\mathbf{\Delta})]$
28	$Na_3B_7O_{12}$[103]	7	$[B_7O_{16}]$	$7{:}\infty^3[(3{:}2\mathbf{\Delta}+\mathbf{T})+(3{:}\mathbf{\Delta}+2\mathbf{T})+(1{:}\mathbf{\Delta})]$
29	$MgB_7O_{13}Cl$ ($F\bar{4}3c$)[104]	7	$[B_7O_{18}]$	$7{:}\infty^3[(5{:}5\mathbf{T})+(1{:}\mathbf{\Delta})+(1{:}\mathbf{T})]$
30	$K_2BaB_{16}O_{26}$[105]	8	$[B_8O_{16}]$	$8{:}\infty^3[(5{:}4\mathbf{\Delta}+\mathbf{T})+(3{:}2\mathbf{\Delta}+\mathbf{T})]$
31	$Na_2B_4O_7$[106]	8	$[B_8O_{17}]$	$8{:}\infty^3[(5{:}3\mathbf{\Delta}+2\mathbf{T})+(3{:}2\mathbf{\Delta}+\mathbf{T})]$
32	$K_2B_4O_7$[107]	8	$[B_8O_{17}]$	$8{:}\infty^3[(4{:}5\mathbf{\Delta}+2\mathbf{T})+(3{:}\mathbf{\Delta}+2\mathbf{T})+(1{:}\mathbf{\Delta})]$
33	$LiRbB_4O_7$[109]	8	$[B_8O_{17}]$	$8{:}\infty^3[(5{:}4\mathbf{\Delta}+\mathbf{T})+(3{:}\mathbf{\Delta}+2\mathbf{T})]$
34	$Pb_8(B_9O_{21})F$[110]	9	$[B_9O_{21}]$	$9{:}[(3{:}3\mathbf{T})+6(1{:}\mathbf{\Delta})]$
35	β-$Na_2B_6O_{10}$[111]	9	$[B_9O_{19}]$	$9{:}\infty^2[(5{:}4\mathbf{\Delta}+\mathbf{T})+(3{:}2\mathbf{\Delta}+\mathbf{T})+(1{:}\mathbf{T})]$
36	$Na_2Cs_2BaB_{18}O_{30}$[105]	9	$[B_9O_{19}]$	$9{:}\infty^3 3[(3{:}2\mathbf{\Delta}+\mathbf{T})]$
37	α-$Na_2B_6O_{10}$[113]	9	$[B_9O_{19}]$	$9{:}\infty^3[(5{:}4\mathbf{\Delta}+\mathbf{T})+(4{:}2\mathbf{\Delta}+2\mathbf{T})]$
38	$Pb_6(B_{10}O_{21})$[114]	10	$[B_{10}O_{21}]$	$10{:}2[(4{:}2\mathbf{\Delta}+2\mathbf{T})+(1{:}\mathbf{\Delta})]$
39	$Pb_4Zn_2B_{10}O_{21}$[115]	10	$[B_{10}O_{24}]$	$10{:}\infty^2[(3{:}\mathbf{\Delta}+2\mathbf{T})+(1{:}\mathbf{\Delta})+(1{:}\mathbf{T})]$
40	$Cs_2K_2B_{10}O_{17}$[116]	10	$[B_{10}O_{21}]$	$10{:}\infty^2[(5{:}3\mathbf{\Delta}+2\mathbf{T})]$
41	δ-CsB_5O_8[117]	10	$[B_{10}O_{17}]$	$10{:}\infty^3 2[(5{:}4\mathbf{\Delta}+\mathbf{T})]$
42	$Li_6Rb_5(B_{11}O_{22})$[118]	11	$[B_{11}O_{22}]$	$11{:}[2(5{:}3\mathbf{\Delta}+2\mathbf{T})+(1{:}\mathbf{\Delta})]$
43	$Li_3NaBaB_6O_{12}$[119]	12	$[B_{12}O_{24}]$	$12{:}[6(1{:}\mathbf{\Delta})+6(1{:}\mathbf{T})]$
44	β-$Tl_2B_4O_7$[122]	12	$[B_{12}O_{26}]$	$12{:}\infty^3[(7{:}4\mathbf{\Delta}+3\mathbf{T})+(5{:}2\mathbf{\Delta}+3\mathbf{T})]$
45	$Rb_3B_7O_{12}$[123]	14	$[B_{14}O_{30}]$	$14{:}\infty^2[2(5{:}3\mathbf{\Delta}+2\mathbf{T})+(3{:}2\mathbf{\Delta}+\mathbf{T})+(1{:}\mathbf{T})]$
46	$Sr_2B_{16}O_{26}$[124]	16	$[B_{16}O_{32}]$	$16{:}\infty^3[3(3{:}2\mathbf{\Delta}+\mathbf{T})+(5{:}4\mathbf{\Delta}+\mathbf{T})+2\mathbf{\Delta}]$
47	$Sr_8MgB_{18}O_{36}$[121]	18	$[B_{18}O_{36}]$	$18{:}[6(3{:}3\mathbf{\Delta}+\mathbf{T})]$
48	$K_5B_{19}O_{31}$[125]	19	$[B_{19}O_{35}]$	$19{:}\infty^3 2[(5{:}4\mathbf{\Delta}+\mathbf{T})+(3{:}2\mathbf{\Delta}+\mathbf{T})+(1{:}\mathbf{\Delta})+0.5(1{:}\mathbf{T})]$
49	$Na_8CsB_{21}O_{36}$[126]	21	$[B_{21}O_{36}]$	$21{:}\infty^3[4(5{:}3\mathbf{\Delta}+2\mathbf{T})+(1{:}\mathbf{T})]$
50	$Cs_3B_{13}O_{21}$[127]	26	$[B_{26}O_{48}]$	$26{:}\infty^2[2(5{:}4\mathbf{\Delta}+\mathbf{T})+4(3{:}2\mathbf{\Delta}+\mathbf{T})+4(1{:}\mathbf{\Delta})]$
51	$Cs_3B_7O_{12}$[128]	63	$[B_{63}O_{133}]$	$63{:}\infty^2[(7{:}3\mathbf{\Delta}+4\mathbf{T})+10(5{:}3\mathbf{\Delta}+2\mathbf{T})+(5{:}2\mathbf{\Delta}+3\mathbf{T})+(1{:}\mathbf{T})]$

[a] N_B refers the total number of B atoms in corresponding FBBs.

in which n is the number of B atoms in each FBB. r is the dimension of B−O anionic structure and can take the value of 1 for 1D chains, 2 for 2D layers, and 3 for 3D networks. When the B−O anionic structure is isolated and the part of "∞^r" will be removed for clarity. $b(b')$ and $c(c')$ represent the number of $[BO_3]$ triangles and $[BO_4]$ tetrahedra in each FBB, respectively, while m (m') represents the total number of B atoms, that is, $m = b + c$, $m' = b' + c'$, $a = n/(m + m')$, when $a = 1$, a will be removed for clarity. According to above notation, the FBB of penta-borate α-CsB_5O_8[79] can be simplified to 5:[(5:4**Δ** + **T**)]. By using this shorthand notation, several representative FBBs categories can be symbolized with the number of B atoms ranging from 1 to 63 in borates (see Table 2):

https://dx.doi.org/10.1021/acs.chemrev.0c00796
Chem. Rev. 2021, 121, 1130−1202

(a) The FBBs with one B atom, such as, 0D $[BO_3]$ 1:[(1**Δ**)] in $KBe_2BO_3F_2$[27] and its isomorphic phases, 0D $[BO_4]$ 1:[(1**T**)] in $AsBO_4$ ($I\bar{4}$),[75] the 1D infinite chain of $^1[BO_2]_\infty$ 1:∞^1[(1:**Δ**)] constructed by $[BO_3]$ FBBs in CaB_2O_4,[83] and the 3D framework of $^3[BO_2]_\infty$ 1:∞^3[(1:**T**)] constructed by $[BO_4]$ FBBs in γ-$LiBO_2$.[84]

(b) The FBBs with two B atoms, such as, 0D $[B_2O_5]$ 2:[(2**Δ**)] in $Al_4B_6O_{15}$,[85] 0D $[B_2O_7]$ 2:[(2**T**)] in $Se_2B_2O_7$,[86] and the 1D infinite chain of $^1[B_2O_5]_\infty$ built up by $[B_2O_6]$ FBBs 2:∞^1[(2:**Δ** + **T**)] in $TlBO_2$.[49]

(c) The FBBs with three B atoms, such as, 0D $[B_3O_6]$ 3:[(3**Δ**)] in α- and β-BaB_2O_4,[22,28] 0D $[B_3O_7]$ 3:[(3**Δ**)] in α-$KBe_2B_3O_7$,[87] 0D $[B_3O_8]$ 3:[(3:**Δ** + 2**T**)] in $K_2B_3SbO_8$,[88] 0D $[B_3O_9]$ 3:[(3**T**)] in $GdBO_3$ ($R32$),[89] the 1D infinite chain of $^1[B_3O_6]_\infty$ 3:∞^1[(3**Δ**)] built up by $[B_3O_7]$ FBBs in $NaBeB_3O_6$,[87] the 1D infinite chain of $^1[B_3O_6]_\infty$ 3:∞^1[(3:2**Δ** + **T**)] constructed by $[B_3O_7]$ FBBs in $KSeB_3O_7$,[90] as well as the 3D network of $^3[B_3O_5]_\infty$ 3:∞^3[(3:2**Δ** + **T**)] built up by $[B_3O_7]$ FBBs in LiB_3O_5.[23]

(d) The FBBs with four B atoms, such as, 0D $[B_4O_8]$ 4:[(4**Δ**)] in $Li_6B_4O_9$,[91] 0D $[B_4O_9]$ 4:[(4:2**Δ** + 2**T**)] in $Rb_2GeB_4O_9$,[92] 0D $[B_4O_{11}]$ 4:[(2:**Δ**) + (2:**T**)] in $Gd_4B_4O_{11}F_2$,[93] and the 1D infinite chain of $^1[B_4O_8]_\infty$ 4:∞^1[(4:2**Δ** + 2**T**)] constructed by $[B_4O_9]$ FBBs in $AgBO_2$.[94]

(e) The FBBs with five B atoms, such as, 0D $[B_5O_{10}]$ 5:[(5:4**Δ** + **T**)] in $Na_3Zn(B_5O_{10})$,[95] 0D $[B_5O_{11}]$ 5:[(5:3**Δ** + 2**T**)] in $YBe_2B_5O_{11}$,[96] the 2D infinite layer of $^2[B_5O_8]_\infty$ 5:∞^2[(5:4**Δ** + **T**)] constructed by $[B_5O_{10}]$ FBBs in α-CsB_5O_8,[79] and the 3D network of $^3[B_3O_5]_\infty$ 5:∞^3[(5:4**Δ** + **T**)] built up by $[B_5O_{10}]$ FBBs in α- and β-KB_5O_8.[97,98]

(f) The FBBs with six B atoms, such as, 0D $[B_6O_{12}]$ 6:[(6:4**Δ** + 2**T**)] in $KZnB_3O_6$,[99,100] 0D $[B_6O_{16}]$ 6:[(6:2**Δ** + 4**T**)] in $Ba_3Ge_2B_6O_{16}$,[101] and the 3D framework of $^3[B_6O_{10}]_\infty$ 6:$\infty^3$2[(3:2**Δ** + **T**)] constructed by $[B_6O_{13}]$ FBBs in $CsLiB_6O_{10}$.[25]

(g) The FBBs with seven B atoms, such as, 0D $[B_7O_{14}]$ 7:2[(3:2**Δ** + **T**) + **Δ**] in $Li_4Cs_3B_7O_{14}$,[102] the 3D network of $^3[B_7O_{12}]_\infty$ 7:∞^3[(3:2**Δ** + **T**) + (3:**Δ** + 2**T**) + (1:**Δ**)] constructed by $[B_7O_{16}]$ FBBs in $Na_3B_7O_{12}$,[103] and the 3D framework of $^3[B_7O_{13}]_\infty$ 7:∞^3[(5:5**T**) + (1:**Δ**) + (1:**T**)] built up by $[B_7O_{18}]$ FBBs in $MgB_7O_{13}Cl$ ($F\bar{4}3c$).[104]

(h) The FBBs with eight B atoms, such as, the 3D network of $^3[B_8O_{13}]_\infty$ 8:∞^3[(5:4**Δ** + **T**) + (3:2**Δ** + **T**)] built up by $[B_8O_{16}]$ FBBs in $K_2BaB_{16}O_{26}$,[105] the 3D framework of $^3[B_8O_{14}]_\infty$ 8:∞^3[(5:3**Δ** + 2**T**) + (3:2**Δ** + **T**)] constructed by $[B_8O_{17}]$ FBBs in $Na_2B_4O_7$,[106] the 3D network of $^3[B_8O_{14}]_\infty$ 8:∞^3[(4:5**Δ** + 2**T**) + (3:**Δ** + 2**T**) + (1:**Δ**)] constructed by $[B_8O_{17}]$ FBBs in $K_2B_4O_7$[107] and $Rb_2B_4O_7$,[108] as well as the 3D network of $^3[B_8O_{14}]_\infty$ 8:∞^3[(5:4**Δ** + **T**)+(3:**Δ** + 2**T**)] constructed by $[B_8O_{17}]$ FBBs in $LiKB_4O_7$[106] and $LiRbB_4O_7$.[109]

(i) The FBBs with nine B atoms, such as, 0D $[B_9O_{21}]$ 9:[(3:3**T**) + 6(1:**Δ**)] in $Pb_8(B_9O_{21})F$,[110] the 2D infinite layer of $^2[B_9O_{15}]_\infty$ 9:∞^2[(5:4**Δ** + **T**) + (3:2**Δ** + **T**) + (1:**T**)] constructed by $[B_9O_{19}]$ FBBs in β-$Na_2B_6O_{10}$,[111] the 3D framework of $^3[B_9O_{15}]_\infty$ 9:$\infty^3$3[(3:2**Δ** + **T**)] built up by $[B_9O_{19}]$ FBBs in $Na_2Cs_2BaB_{18}O_{30}$[105] and $NaBaB_9O_{15}$,[112] as well as the 3D framework of $^3[B_9O_{15}]_\infty$ 9:∞^3[(5:4**Δ** + **T**) + (4:2**Δ** + 2**T**)] built up by $[B_9O_{19}]$ FBBs in α-$Na_2B_6O_{10}$.[113]

(j) The FBBs with ten B atoms, such as, 0D $[B_{10}O_{21}]$ 10:2[(4:2**Δ** + 2**T**) + (1:**Δ**)] in $Pb_6(B_{10}O_{21})$,[114] the 2D infinite layer of $^2[B_{10}O_{21}]_\infty$ 10:$\infty^2$2[(3:**Δ** + 2**T**) + (1:**Δ**) + (1:**T**)] constructed by $[B_{10}O_{24}]$ FBBs in $Pb_4Zn_2B_{10}O_{21}$,[115] the 2D infinite layer of $^2[B_{10}O_{17}]_\infty$ 10:$\infty^2$2[(5:3**Δ** + 2**T**)] constructed by $[B_{10}O_{21}]$ FBBs in $Cs_2K_2B_{10}O_{17}$,[116] as well as the 3D network of $^3[B_{10}O_{16}]_\infty$ 10:$\infty^3$2[(5:4**Δ** + **T**)] built up by $[B_{10}O_{17}]$ FBBs in δ-CsB_5O_8.[117]

(k) The FBBs with more than ten B atoms, such as, 0D $[B_{11}O_{22}]$ 11:[2(5:3**Δ** + 2**T**) + (1:**Δ**)] in $Li_6Rb_5(B_{11}O_{22})$,[118] 0D $[B_{12}O_{24}]$ 12:[6(1:**Δ**) + 6(1:**T**)] in $Li_3NaBaB_6O_{12}$,[119] 0D $[B_{18}O_{36}]$ 18:[6(3:3**Δ** + **T**)] in $NaSr_7Al(B_{18}O_{36})$[120] and $Sr_8MgB_{18}O_{36}$,[121] the 3D framework of $^3[B_{12}O_{21}]_\infty$ 12:∞^3[(7:4**Δ** + 3**T**) + (5:2**Δ** + 3**T**)] constructed by $[B_{12}O_{26}]$ FBBs in β-$Tl_2B_4O_7$,[122] the 2D infinite layerof $^2[B_{14}O_{24}]_\infty$ 14:∞^2[2(5:3**Δ** + 2**T**) + (3:2**Δ** + **T**) + (1:**T**)] built up by $[B_{14}O_{30}]$ FBBs in $Rb_3B_7O_{12}$,[123] the 3D framework of $^3[B_{16}O_{26}]_\infty$ 16:∞^3[3(3:2**Δ** + **T**) + (5:4**Δ** + **T**) + 2**Δ**] built up by $[B_{16}O_{32}]$ FBBs in $Sr_2B_{16}O_{26}$,[124] the 3D frameworkof $^3[B_{19}O_{31}]_\infty$ 19:$\infty^3$2[(5:4**Δ** + **T**) + (3:2**Δ** + **T**) + (1:**Δ**) + 0.5(1:**T**)] constructed by $[B_{19}O_{35}]$ FBBs in $K_5B_{19}O_{31}$,[125] the 3D frameworkof $^3[B_{21}O_{28}]_\infty$ 21:∞^3[4(5:3**Δ** + 2**T**) + (1:**T**)] built up by $[B_{21}O_{36}]$ FBBs in $Na_8CsB_{21}O_{36}$,[126] the 2D infinite layer of $^2[B_{26}O_{42}]_\infty$ 26:∞^2[2(5:4**Δ** + **T**) + 4(3:2**Δ** + **T**) + 4(1:**Δ**)] constructed by high polymerized $[B_{26}O_{48}]$ FBBs in $Cs_3B_{13}O_{21}$,[127] as well as the 2D infinite layer of $^2[B_{63}O_{108}]_\infty$ 63:∞^2[(7:3**Δ** + 4**T**) + 10(5:3**Δ** + 2**T**) + (5:2**Δ** + 3**T**) + (1:**T**)] built up by the largest $[B_{63}O_{133}]$ FBBs in $Cs_3B_7O_{12}$.[128]

This approach proposed by Touboul *et al.*[82] allows us to characterize and classify most borates with different B−O FBBs, but the structure of borates is regularly complicated, particularly the connection characteristics in these FBBs, which makes the classification and description of their structural characteristics difficult to be correctly identified to date. In some cases, the borates with the identical notation of FBBs have different FBBs and even structural characteristics, such as the shorthand notation of α-$KBe_2B_3O_7$[87] and β-BaB_2O_4[22] are identical and can be expressed as 3:[(3**Δ**)], even though they are both composed of three $[BO_3]$ units, their FBBs and structural characteristics are completely different. The $[B_3O_7]$ FBBs of α-$KBe_2B_3O_7$ are in chain-like configuration, while the $[B_3O_6]$ FBBs of β-BaB_2O_4 are in ring-like configuration. Facing with this, Xue *et al.* proposed a new classification and algebraic description of the borates by including the polymerization of each FBB,[77] which can reflect more structural information on FBBs than previous approaches. They classified all the available FBBs of borates into seven categories, namely, single ($[B\varphi_3]$ and $[B\varphi_4]$), branched, normal-ring, bridge-ring, "8"-shaped-ring as well as combined-ring FBBs, in which φ can be O^{2-} and OH^-. Then they introduced a new algebraic description based on their topological classification and previous description schemes. The updated notation can be written as

$$n{:}\ \infty^r[\langle b\mathbf{\Delta}c\mathbf{T}\rangle + m'\langle b'\mathbf{\Delta}c'\mathbf{T}\rangle^b + m''\langle b''\mathbf{\Delta}c''\mathbf{T}\rangle^8 + \cdots]$$

https://dx.doi.org/10.1021/acs.chemrev.0c00796
Chem. Rev. 2021, 121, 1130−1202

Similar to previous description schemes, *n* is the number of B atoms in FBBs, and *r* reflects the dimension of B−O anionic structure, whereas the characteristic strings in bracket contain the information on connectivity of polyhedral groups (and rings) in and within the FBBs. In addition, several new symbols, including &, | |, and **TT**, are also included to distinguish some complex linkages, namely, & to separate two unconnected B−O parts, | | for B−O units which are connected by more than two other polyhedra or clusters, and **TT** for edge-sharing [BO_4] tetrahedra. By using this approach, several borates with rare linkage type or complicated FBBs can be expressed as follows: $Na_3GaB_4O_9$ (4:[⟨2Δ2T⟩^{b}]),[129] α-CsB_5O_8 (5:∞^{2}[⟨4ΔT⟩^{8}]),[79] $Pb_2B_5O_9I$ (5:∞^{3}[⟨2Δ3T⟩^{8}]),[130] BaB_8O_{13} (8:∞^{3}[⟨4ΔT⟩^{8} + ⟨Δ2T⟩]),[51] $Na_3Zn(B_5O_{10})$ (5:[⟨4ΔT⟩^{8}]),[95] $Dy_4B_6O_{15}$ (6:∞^{1}[2T + **TT** + 2T]),[131] $Na_2B_4O_7$ (8:∞^{3}[⟨3Δ2T⟩^{8} + ⟨2ΔT⟩]),[106] CaB_4O_7 ($P2_1/c$) (8:∞^{3}[⟨2Δ2T⟩^{b} + T + ⟨2ΔT⟩]),[132] BaB_4O_7 (8:∞^{3}[⟨3Δ2T⟨^{8} + ⟨Δ2T⟩]),[133] β-NaB_3O_5 (9:∞^{3}[⟨4ΔT⟩^{8} + ⟨2ΔT⟩ + T]),[134] $Rb_3B_7O_{12}$ (14:∞^{2}[⟨3Δ2T⟩^{8} + T + ⟨Δ2T⟩ + ⟨Δ2T⟩^{8}]),[123] $K_5B_{19}O_{31}$ (19:∞^{3}[2(⟨4ΔT⟩^{8} + Δ + ⟨2ΔT⟩) + T]),[125] and $Cs_3B_7O_{12}$ (63:∞^{2}[(⟨4Δ3T⟩$^{2\text{-}8}$ + 10⟨3Δ2T⟩^{8} + ⟨2Δ3T⟩^{8} + T)]).[128] Obviously, when compared to those previous description schemes, the above notation can reflect more detail about the connection characteristics within these B−O FBBs. On the basis of these approaches, modified descriptors for the description of FBBs in borates were also worked out by many other researchers, which makes it possible to re-assign those new borates with updated descriptors and also reveal structural features among them to open new thoughts on the structure−property−function relationships. Lacking still are some descriptors for linear [BO_2] and fluorinated [$BO_{4-x}F_x$] units, which need to be investigated and expanded in the further studies.

2.4. Dimensionality of B−O/F Anionic Groups

In this section, the distribution of the dimensionality of B−O/F anionic frameworks in anhydrous borates is examined (Tables S1−S4 in the SI). Classification of the available 965 anhydrous borate structures stored in the ICSD according to their specific dimensionality is shown in Figure 8. It is shown that the frequencies of occurrence for B−O/F anionic framework in these borates are as follows: 0D isolated clusters (65.5%, see Table S1 in the SI), 1D infinite chains (6.1%, see Table S2 in the SI), 2D infinite layers (10.3%, see Table S3 in the SI), and 3D frameworks (18.1%, see Table S4 in the SI). This distribution of frequency is highly consistent with the dimensionality frequency orderings of B−O anionic frameworks summarized by Becker in 2001 and Xue *et al.* in 2007 based on the selected anhydrous and hydrous/anhydrous borates, respectively.[77,135]

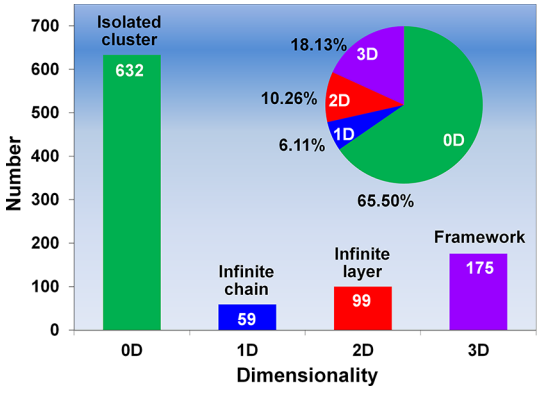

Figure 8. Distribution of borates with specific dimensionality of B−O/F anionic framework. Inset: corresponding proportion in %.

2.4.1. Borates with 0D B−O/F Isolated Clusters. The most common dimensionality is 0D, and more than half borates (65.5%) contain only isolated B−O clusters (Figure 8 and Table S1 in the SI). It should be noted that most borates with isolated B−O clusters are composed of metal cations with strong covalence, including Zn, Be, Al, Mg, and Cd atoms, *etc.*, that is mainly because cations with a higher valence state (like transition-metal cations) have stronger coordination ability to form rigid coordinated bonds and break the B−O anionic groups into 0D configuration to achieve the coordination distinction. With respect to the borates with 0D B−O/F isolated clusters, about 65.5% of all these available borates belong to this sort with 66.3% represented by borates with isolated [BO_3] (419) units. Other categories occurring often include isolated [B_2O_5] (50), [B_5O_{10}] (34), [B_3O_6] (25), and [BO_4] (22) units (see Figure 9). Likewise, the formation of isolated B−O/F groups with low polymerization degree of B atoms is more preferred, particularly, for *mono-*, *di-*, *tri-*, *tetra-*, and *penta*-borates. And about 97.0% of anhydrous borates contain isolated B−O/F clusters with the total number of B atoms less than six in their FBBs (Table S1 in the SI). This trend is similar to that found by Becker *et al.*[135] and Hawthorne *et al.*,[136] respectively, the corresponding proportions from two groups are all about 90% from their independent analysis of 460 anhydrous borates and 80 borate mineral structures. Structurally, further condensation of above isolated B−O/F units can lead to a larger cluster *via* shared [BO_3] and [BO_4] units. Several highly polymerized B−O/F clusters are formed by the condensation of *mono-*, *di-*, *tri-*, *tetra-*, and *penta*-groups consisting of different numbers of B−O/F polyhedra, but the high polymerized B−O/F clusters are seldom observed experimentally and less than 3.0% borates are found to possess such units. Several B−O clusters, however, have been found in isolated form with the high polymerization degree ($n > 6$), such as, [B_6O_{12}], [B_6O_{16}], [B_7O_{14}], [B_9O_{21}], [$B_{10}O_{21}$], [$B_{11}O_{22}$], [$B_{12}O_{24}$], and [$B_{18}O_{36}$] units (Figure 9 and Table S1 in the SI).[99−101,110,114,118−121]

A unique hexa-group is found to be [B_6O_{12}] in $KZnB_3O_6$,[99,100] which is formed by condensing two three-membered [B_3O_7] rings in a particular fashion way: two groups are linked *via* two edge-sharing [BO_4] tetrahedra. The longest B−O σ bonds in [B_6O_{12}] clusters that connect the edge-sharing [BO_4] tetrahedra provide a stable solid framework for $KZnB_3O_6$. The detailed discussion about the formation of edge-sharing [BO_4] tetrahedra in $KZnB_3O_6$ will be given in section 2.5, whereas the cyclic [B_6O_{16}] units in $M_3Ge_2B_6O_{16}$ (M = Sr and Ba)[101,137] are formed by two [BO_3] triangles and four [BO_4] tetrahedra and they can also be conceptually constructed from two [B_3O_9] units. To date, the isolated [B_7O_{14}] unit constructed by three continuous linked rings is rare in borates and only found in $ABa_7Mg_2B_{14}O_{28}F_5$ (A = Na, K)[138,139] with atomic disorder and disorder-free $Li_4Cs_3B_7O_{14}$.[102] The three compounds, $Pb_8(B_9O_{21})F$,[110] $Pb_6B_{10}O_{21}$,[114] and $Li_6Rb_5(B_{11}O_{22})$,[118] are the sole examples of the [B_9O_{21}], [$B_{10}O_{21}$], and [$B_{11}O_{22}$] clusters, respectively. The [B_9O_{21}] cluster is composed of a central [B_3O_9] unit and six [BO_3] triangles interlined by sharing terminal O atoms. The [$B_{10}O_{21}$] cluster is composed of a central [B_2O_5] and two [B_4O_9] units that are interconnected by two of its four terminal

https://dx.doi.org/10.1021/acs.chemrev.0c00796
Chem. Rev. 2021, 121, 1130−1202

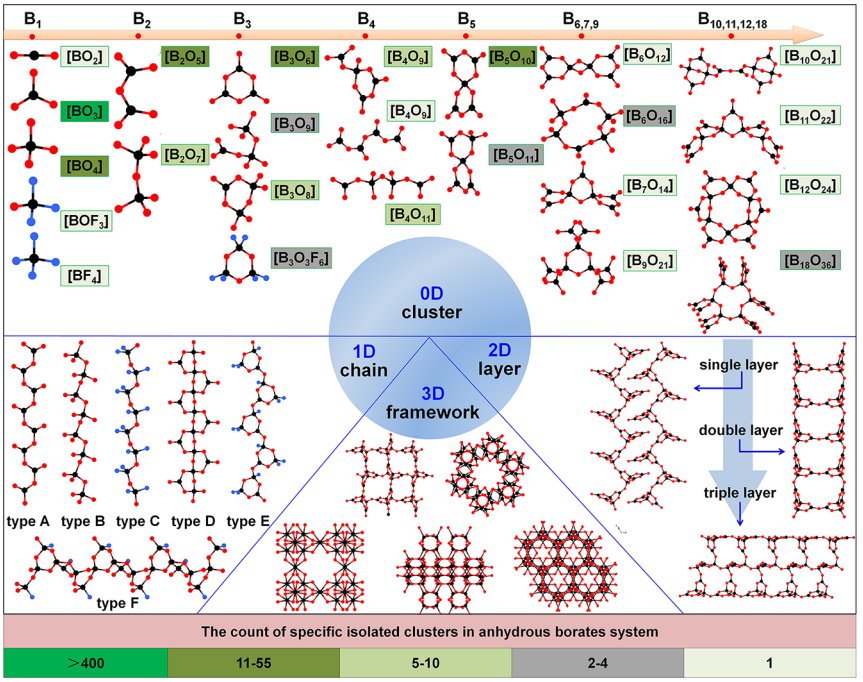

Figure 9. Structural chemistry of borates with different dimensionality of B−O/F anionic frameworks. The count of specific isolated clusters in anhydrous borate system is given in the last row with different marked colors. All of the structure diagrams were drawn by using the crystallographic information file of each structure that stored in the ICSD.

Table 3. Basic Information of Borates with Two Kinds of Isolated B−O Clusters[a]

no.	chemical formula	space group	anionic cluster	N_B	ICSD code
1	$Ni_7U(BO_3)_2(BO_4)_2O_2$	*Pnnm*	$[BO_3]+[BO_4]$	2	65676
2	$Ho_{31}O_{27}(BO_3)_3(BO_4)_6$	$R\bar{3}$	$[BO_3]+[BO_4]$	2	421761
3	$Na_2Be_4(BO_3)_2(B_2O_5)$	*P*1	$[BO_3]+[B_2O_5]$	3	237764
4	$Cu_{15}(BO_3)_6(B_2O_5)_2O_2$	$P\bar{1}$	$[BO_3]+[B_2O_5]$	3	35201
5	$Cu_9Ti_2(BO_3)_2(B_2O_5)_2O_6$	$P\bar{1}$	$[BO_3]+[B_2O_5]$	3	400772
6	$K_4Sr_4(UO_2)_{13}(BO_3)_2(B_2O_5)_2O_{12}$	$P\bar{1}$	$[BO_3]+[B_2O_5]$	3	254478
7	$Sr_2Sc_2(BO_3)_2(B_2O_5)$	$P\bar{1}$	$[BO_3]+[B_2O_5]$	3	86435
8	$Sr_2LiBe(BO_3)(B_2O_5)$	$P2_1/c$	$[BO_3]+[B_2O_5]$	3	262730
9	$Ba_2Sc_2(BO_3)_2(B_2O_5)$	$C2/c$	$[BO_3]+[B_2O_5]$	3	86436
10	$Ba_5(BO_3)_2(B_2O_5)$	$P2_12_12_1$	$[BO_3]+[B_2O_5]$	3	172399
11	$Pb_4B_2O_7/Pb_8(BO_3)_2(B_2O_5)O_3$	*Ama*2	$[BO_3]+[B_2O_5]$	3	183637
12	$Ca_{10}Ge_{16}(BO_4)_2(B_2O_7)_2O_{29}$	*Pba*2	$[BO_4]+[B_2O_7]$	3	261970
13	$K_3Be_6(BO_3)_3(B_3O_6)_2$	$P2_1$	$[BO_3]+[B_3O_6]$	4	248204
14	$CsZn_2B_3O_7/Cs_3Zn_6(BO_3)_3(B_3O_6)_2$	$Cmc2_1$	$[BO_3]+[B_3O_6]$	4	238088
15	$Cs_3Zn_6(BO_3)_3(B_3O_6)_2$	$Cmc2_1$	$[BO_3]+[B_3O_6]$	4	194211
16	$La_4(BO_3)(B_3O_8)F_2$	$P2_1/c$	$[BO_3]+[B_3O_8]$	4	420439
17	$Ca_3Be_6(BO_3)_2(B_3O_{10})F$	$P6_3/m$	$[BO_3]+[B_3O_{10}]$	4	192456
18	α-$Pb_2Ba_4Zn_4(B_2O_5)(B_6O_{13})_2$	*P*1	$[B_2O_5]+[B_6O_{13}]$	8	238677
19	β-$Pb_2Ba_4Zn_4(B_2O_5)(B_6O_{13})_2$	*Cc*	$[B_2O_5]+[B_6O_{13}]$	8	238676
20	γ-$Pb_2Ba_4Zn_4(B_2O_5)(B_6O_{13})_2$	$P3_2$	$[B_2O_5]+[B_6O_{13}]$	8	238678
21	$Cs_{18}Mg_6(B_5O_{10})_3(B_7O_{14})_2F$	$C2/c$	$[B_5O_{10}]+[B_7O_{14}]$	12	428172
22	$Rb_{18}Mg_6(B_5O_{10})_3(B_7O_{14})_2F$	$C2/c$	$[B_5O_{10}]+[B_7O_{14}]$	12	428171
23	$Ca_3Na_4LiBe_4B_{10}O_{24}F/Ca_6Na_8Li_2Be_8(BO_3)_8(B_{12}O_{24})F_2$	$R\bar{3}$	$[BO_3]+[B_{12}O_{24}]$	13	238295
24	$Cd_3Na_4LiBe_4B_{10}O_{24}F/Cd_6Na_8Li_2Be_8(BO_3)_8(B_{12}O_{24})F_2$	$R\bar{3}$	$[BO_3]+[B_{12}O_{24}]$	13	429574
25	$Sr_3LiNa_4Be_4B_{10}O_{24}F/Sr_6Na_8Li_2Be_8(BO_3)_8(B_{12}O_{24})F_2$	$R\bar{3}$	$[BO_3]+[B_{12}O_{24}]$	13	429575
26	$Ba_6Al_4B_{14}O_{33}/Ba_6Al_4(BO_3)_2(B_6O_{13})(B_6O_{14})$	$P\bar{1}$	$[BO_3]+[B_6O_{13}]+[B_6O_{14}]$	13	242282

[a] N_B refers the total number of B atoms in two corresponding clusters. The compounds on either side of the "/" sign are the same one in the chemical formula column.

O atoms. Quite different for the previous two examples, the $[B_{11}O_{22}]$ cluster is constructed by five continuously linked three-membered rings. Further polymerization of single rings to form larger B−O groups is realized in $Li_3NaBaB_6O_{12}$[119] and its isomorphic phases. The $[B_{12}O_{24}]$ units in them are formed by the condensation of three-membered $[B_3O_8]$ single-rings consisting of one $[BO_3]$ triangle and two $[BO_4]$ tetrahedra. The most complex isolated B−O cluster to date is cyclic

https://dx.doi.org/10.1021/acs.chemrev.0c00796
Chem. Rev. 2021, 121, 1130−1202

$[B_{18}O_{36}]$ unit in $NaSr_7Al(B_{18}O_{36})$[120] and $Sr_8M(B_{18}O_{36})$ (M = Mg, Zn, Cd).[121,140] The exceptional complexity of this family is caused by the further condensation of six $[B_3O_7]$ units to form highly polymerized $[B_{18}O_{36}]$ clusters *via* corner-sharing. The orientations of these $[B_3O_7]$ subgroups in $[B_{18}O_{36}]$ clusters fall into three pairs, where every two $[B_3O_7]$ rings are arranged in parallel, and the dihedral angles between these pairs are nearly 120°, which is consistent with their centrosymmetric point group $R\bar{3}m$.

More importantly, the surprising discovery of two (or more) isolated B−O clusters in one compound significantly expands the structural diversity of borates with 0D configurations. In contrast to borates with only one isolated unit, the number of borates with two types (or more) of isolated clusters is much smaller and only 26 cases belong to this species (Table 3). Most of them (25/26) contain $[TO_n]$ (T = Be, Al, Zn, Cu, Ti, Ni, La, Sc, Y, Mg, *etc.*; n = 4, 6) tetrahedra with comparatively strong T−O covalence bonds, in which the $[TO_n]$ units may play a "bond terminator" role to reduce the B−O anionic framework and introduce low dimensionality and separate the isolated B−O units in the meantime. Among them, the simplest one is the combination of isolated $[BO_3]$ and $[BO_4]$ units in high-pressure synthesized $Ho_{31}O_{27}(BO_3)_3(BO_4)_6$[141] and high-temperature synthesized $Ni_7B_4UO_{16}$.[142] It is noteworthy that all of the $[BO_3]$ and $[BO_4]$ units in them are isolated without any linkage to each other, which is the first and sole borate that contains such B−O configurations. The most frequently occurring types are $[BO_3]$ + $[B_2O_5]$, which are found in the structures of $M_2Sc_2B_4O_{11}$ (M = Sr, Ba),[143] $Na_2Be_4B_4O_{11}$,[144] and $Li_3Ba_4Sc_3(BO_3)_4(B_2O_5)_2$.[145] It should be noted that the $[B_2O_5]$ units in $Sr_2Sc_2B_4O_{11}$ adopt an unusual geometry and exhibit a planar orientation with a B−O−B angle of 180° and the central O atom occupying a site with inversion symmetry. It is interesting to note that all the $[BO_3]$ and $[B_2O_5]$ units in $Sr_2Sc_2B_4O_{11}$ are in coplanar configurations, which is totally different from other borates with isolated $[BO_3]$ and $[B_2O_5]$ units.[143] Many other polyborates, including $M_3Na_4LiBe_4B_{10}O_{24}F$ (M = Ca, Sr, Cd),[146,147] $Ba_4Na_2Zn_4(B_3O_6)_2(B_{12}O_{24})$,[148] and $A_{18}Mg_6(B_5O_{10})(B_7O_{14})_2F$ (A = Rb, Cs),[149] were found to exhibit two types of isolated polyborate groups. After analyzing the topological arrangement of polyborate anionic units in $A_{18}Mg_6(B_5O_{10})(B_7O_{14})_2F$ (A = Rb, Cs) and related compounds, one can observe that their topological structures are a result of substituting $[BO_3]$ and $[B_2O_5]$ clusters in $Na_2Be_4B_4O_{11}$ with high polymerized $[B_5O_{10}]$ and $[B_7O_{14}]$ units, respectively, with different layer connectors. Additionally, the coexisting B−O clusters in any one borate tend to have similar structures to decrease the conflict with Pauling's fifth rule.[149] It should be noted that $Ba_6Al_4B_{14}O_{33}$ exhibits three different isolated clusters,[150] namely, $[BO_3]$, $[B_6O_{13}]$, and $[B_6O_{14}]$ units, which is the first and sole case of such a configuration. Fortunately, the number of new borates with 0D isolated configurations is continuously growing, with ongoing research activities focused on the cause of formation and general building principles to achieve more controllable preparation.

2.4.2. Borates with 1D B−O/F Infinite Chains. In principle, the above isolated B−O/F clusters can further polymerize to 1D infinite chains through corner-sharing and edge-sharing connection models, but very few such 0D clusters experimentally condense to 1D infinite chains in related borates (Table S2 in the SI). According to the composition of a 1D chain, all of the available 1D B−O/F infinite chains in borates can be divided into the following six types: the type **A** chain consists of $[BO_3]$ units, the type **B** chain consists of $[BO_4]$ units, the type **C** chain consists of $[BO_2F_2]$ units, the type **D** chain consists of $[BO_3]$ and $[BO_4]$ units, the type **E** chain consists of $[BO_3]$, $[BO_3F]$, and $[BO_2F_2]$ units, and the type **F** chain consists of $[BO_4]$ and $[BO_3F]$ units (Figure 9). Among them, borates with the structural motif of infinite chains of trigonal $[BO_3]$ groups are the simplest one (type **A**). The $^1[BO_2]_\infty$ chain consisting of $[BO_3]$ triangles was first discovered in CaB_2O_4,[83] in which they are all almost coplanar and further linked by Ca-based polyhedra to form the final 3D crystal structure.

After that, more borates, including α-$LiBO_2$,[151] SrB_2O_4,[152] $REMoBO_6$ (RE = Ce, La),[153] UB_2O_6,[154] $NaBeB_3O_6$,[87] and CeB_2O_4F[155] with the structural motifs similar to CaB_2O_4 are discovered experimentally. The CeB_2O_4F series are obtained under high-pressure driven conditions, showing the first and sole F-containing borate with such structural motifs.[155] Different from the coplanar configurations in CaB_2O_4, the $^1[BO_2]_\infty$ chains in CeB_2O_4F show a wave modulation with the formal wavelength of $\lambda = a$, and the linkage of individual $[BO_3]$ triangles occurs by O(2,3) atoms, whereas the O(1,4) atoms locate on the terminal positions of these chains.[155] Besides the above infinite chains, the type **B** $^1[BO_3]_\infty$ chains solely built up by corner-linked $[BO_4]$ tetrahedra were discovered in $RE_2GeB_2O_8$ (RE = Nd, Sm−Tb),[156] and $REMBO_5$ (RE = La, Pr; M = As, Ge) series.[157] Their structures feature 1D infinite chains of corner-sharing $[BO_4]$ tetrahedra that are further bridged by $[MO_4]$ (M = As, Ge) tetrahedra *via* corner-sharing to form 2D anionic layered frameworks, in which the $[BO_4]$ and $[MO_4]$ (M = As, Ge) tetrahedra are in an alternated arrangement. When all of the terminal O atoms are replaced in the above $^1[BO_3]_\infty$ chains with F atoms, fluorinated type **C** $^1[BOF_2]_\infty$ chains can be formed. Recently, this type of chains were experimentally found in $BaBOF_3$ ($P2_1/c$) for the first time by Pan *et al.*,[70] in which the $[BO_2F_2]$ tetrahedra connect with each other *via* corner-sharing to form a fluorinated $^1[BOF_2]_\infty$ chain. Besides, $BaBOF_3$ ($P2_1/c$) with the wave-like $[Ba_2F_2]$ single-layers can be regarded as the new member of pseudo-Aurivillius type compounds. Structurally, $BaBOF_3$ ($P2_1/c$) is the first crystal that possesses two types of F atoms, therefore it simultaneously possesses the structural characteristic of both borate fluorides and fluorooxoborates.[70]

The type **D** chains consisting of $[BO_3]$ and $[BO_4]$ units can also occur in several borates with difference in the linkage of these basic blocks, and the $^1[B_2O_5]_\infty$ chain in $CaBeB_2O_5$ belongs to this type.[158] The $[B(2)O_4]$ tetrahedra in $MBeB_2O_5$ (M = Ca, Sr)[158,159] closely polymerize into $^1[BO_3]_\infty$ chains *via* sharing O(1) atoms that extend along the b axis. These chains are alternately bridged by sharing vertices O(2) atoms of triangular $[B(1)O_3]$ units to final $^1[B_2O_5]_\infty$ chains along the a axis. We note that REB_3O_6 (RE = Tb, Sm, Pr, Nd)[160] also exhibit the 1D $^1[B_2O_4]_\infty$ chains consisting of four-membered $[B_4O_{12}]$ rings, in which $[BO_3]$ and $[BO_4]$ units are alternately linked, and there is no linkage between $[BO_3]$ and $[BO_3]$ or $[BO_4]$ and $[BO_4]$ units. Besides, $ASeB_3O_7$ (A = Na, K)[90] series are found to possess a type **D** chain that is composed of corner-sharing $[B_3O_7]$ clusters. In the $ASeB_3O_7$ (A = Na, K) phases, the $[B(2,3)O_4]$ and $[B(1)O_4]$ units form a cyclic $[B_3O_7]$ group *via* corner-sharing, and they are interconnected *via* O(5) atoms to build a 1D $^1[B_3O_6]_\infty$ chain along the c axis. With the increase of B−O polymerization, high polymerized type **D** chains are formed. The polymorphisms of (Pb_4O)-

https://dx.doi.org/10.1021/acs.chemrev.0c00796
Chem. Rev. 2021, 121, 1130−1202

$Pb_2B_6O_{14}$[161,162] are found to possess similar type **D** $^1[B_6O_{14}]_\infty$ chains, which consist of two crystallographically different $[B_3O_8]$ rings. The structure of $P\bar{1}$ phase $(Pb_4O)Pb_2B_6O_{14}$ can be described as the centrosymmetric modification of $P1$ phase, forming infinite anti-parallel $^1[B_6O_{14}]_\infty$ chains *via* $[OPb_4]$ tetrahedra and Pb^{2+} cations. The main difference of $^1[B_6O_{14}]_\infty$ chains in the two phases is the different arrangement of the chains in the unit cell: one is anti-parallel and the other is parallel.

Among the six types of 1D chains, two fluorinated chains, namely types **E** and **F**, are the rarest types and can only be observed in fluorooxoborates $Li_2B_3O_4F_3$ (type **E**)[163] and BiB_2O_4F (type **F**),[164] respectively. The $^1[B_3O_4F_3]_\infty$ chains of fluorinated $[B_3O_6F_3]$ rings along the *b* axis in $Li_2B_3O_4F_3$ consist of $[BO_3]$ triangles, $[BO_3F]$, and $[BO_2F_2]$ tetrahedra. The $[B_3O_6F_3]$ rings exhibit a twisted-boat conformation with the maximum dihedral angle of B−O−B−O, which is due to the insertion of tetrahedrally coordinated B atoms and in accordance with the fluorinated B−O/F rings found in other lithium fluorooxoborates. Unlike the type **E** chain in $Li_2B_3O_4F_3$, the type **F** chain in BiB_2O_4F consisting of $[B_3O_8F]$ rings is totally different. The $[B(1)O_4]$ tetrahedra in BiB_2O_4F closely polymerize into $^1[BO_3]_\infty$ chains *via* sharing O(1) atoms extending along the *c* axis. These chains are alternately bridged by sharing O(2) and O(3) vertices of tetrahedral $[B(2)O_3F]$ units to form $^1[B_6O_{10}F_2]_\infty$ infinite helical chains that run along the *c* axis. The Bi^{3+} cations are located within the cavities of the borate helices. In this sense, the structure of BiB_2O_4F can be regarded as a helix of borate chain that captures metal cations. In addition to the above six chain types (**A**−**F**), there are also examples of borates with two or more than two 1D B−O chains. This type of B−O anionic framework was experimentally found in $Li_5A_2B_7O_{14}$ (A = Rb, Cs)[165,166] with two different 1D B−O chains, namely $^1[BO_2]_\infty$ and $^1[B_5O_{11}]_\infty$ chains. Structurally, these chains can be considered as the combination of types **A** and **D** chains. The $^1[BO_2]_\infty$ and $^1[B_5O_{11}]_\infty$ chains are composed of $[B(3)O_3]$ triangles and $[B_5O_{12}]$ units by sharing the vertices of the O(3) and O(8) atoms, respectively. Another interesting example is $ABe_2B_3O_7$ (A = K, Rb).[87] Here, two B−O frameworks with different dimensionality coexist in one single structure. The $ABe_2B_3O_7$ (A = K, Rb) crystals exhibit isolated 0D $[BO_3]$ triangles and 1D $^1[B_3O_6]_\infty$ chains, which is the first and sole case of such a configuration. Different types of 1D chains with varied representative compounds reflect the fact that structurally simple borates have been most studied. To this point, the general current trend is towards the elucidation of borates with increasing complexity and rare structural types, such as borates with type **E**, type **F**, and mixed 1D chains.

2.4.3. Borates with 2D B−O/F Layered Configurations. Generally, borates with layered structures mainly refer to the following two types according to their structural characteristics: (a) The B−O/F anionic groups polymerize into B−O/F layer configurations, such as $Cs_2Na_2B_{10}O_{17}$,[116] $RE_3B_5O_{12}$ (RE = Er−Lu),[167] and LiB_6O_9F,[168] and (b) The B−O/F anionic groups are combined with $[TO_n]$ (T = Be, Al, Zn, Cu, Ni, Mg, *etc.*; *n* = 4, 6) polyhedra to construct M−B−O/F layered configurations, in which T−O bonds show comparatively strong covalence, such as $KBe_2BO_3F_2$ and its derivatives.[27] Thus, in both types, the layers tend to exhibit covalent features. However, in this review, the focus will be on the layers solely built up by B−O/F anionic groups and the following discussions will mainly focus on this type because there are an infinite number of different B−O/F types and also an infinite number of geometrically varied connections of FBBs in layered configurations. The classification and comparison of varied types of B−O/F layered structures will be centered on analyzing structural features of corresponding crystal structures. By analyzing all the available 99 anhydrous borates with layered configurations, three types of 2D layers can be identified according to their structural characteristics, namely single, double, and triple layers (Figure 9 and Table S3 in the SI).

2.4.3.1. Borates with Single-layered Structures. The first borate with single-layers was observed in pentaborate α-CsB_5O_8,[79] which exhibits a novel *zigzag* 2D $^2[B_5O_8]_\infty$ layer built up from $[B_5O_{10}]$ FBBs that consist of four $[BO_3]$ triangles and a $[BO_4]$ tetrahedron, which are then condensed to a double ring *via* a common tetrahedron. The corrugated layers are composed of chains of $[B_5O_{10}]$ FBBs with 2_1 screw axis symmetry paralleling to the *b* axis. It can also be characterized as $5{:}\infty^2[(5{:}4\boldsymbol{\Delta} + \mathbf{T})]$ according to the descriptor, and they are similar in shape to the pentaborates AMB_5O_9 (A = Na, K; M = Ca, Sr, Ba, Pb),[169−172] $MREB_5O_{10}$ (M = Mg, Co, Zn, Ni, Cd; RE = trivalent rare earth metal)[173,174] series, and $La_2CaB_{10}O_{19}$,[36] but they are topologically different. The 2D $^2[B_5O_9]_\infty$ layers in AMB_5O_9 (A = Na, K; M = Ca, Sr, Ba, Pb) series are composed of $[B_5O_{11}]$ FBBs, which consist of two $[BO_4]$ tetrahedra and three $[BO_3]$ triangles and as a result exhibit five terminal oxygens. Four of them are shared with other $[B_5O_{11}]$ FBBs to form a 2D $^2[B_5O_9]_\infty$ layer, and one of them remains as terminal oxygen, while the 2D $^2[B_5O_{10}]_\infty$ layers in $MREB_5O_{10}$ (M = Mg, Co, Zn, Ni, Cd; RE = trivalent rare earth metal) series are composed of $[B_5O_{12}]$ FBBs, which consist of three $[BO_4]$ tetrahedra and two $[BO_3]$ triangles and as a result exhibit six terminal oxygens. Four of them are shared with other $[B_5O_{12}]$ FBBs to form a 2D $^2[B_5O_{10}]_\infty$ layer, and two of them remain as terminal oxygens. In contrast, all of the O atoms in α-CsB_5O_8 are bridging oxygen that are linked to establish 2D $^2[B_5O_8]_\infty$ layers,[79] which is why the number of O atoms in defining 2D layers in α-CsB_5O_8 is one and two fewer than that of other two families, respectively. Compared to these pentaborates, the $^2[B_3O_6]_\infty$ layers in α-BiB_3O_6[26] (*C*2) are built by linear $[B_3O_8]$ FBBs, in which $[BO_3]$ triangles and $[BO_4]$ tetrahedra are in a ratio of 1:2. These FBBs are linked *via* corners to form a 2D network with six-fold coordinated Bi atoms alternating arrangement with $^2[B_3O_6]_\infty$ single layers. With further polymerization, the $^2[B_{26}O_{42}]_\infty$ layers in $Cs_3B_{13}O_{21}$ are formed,[127] which consist of $[B_{26}O_{48}]$ FBBs formed by three kinds of B−O units: $[BO_3]$ triangles, $[B_3O_7]$ rings, and $[B_5O_{10}]$ double rings.

All of the above single-layers are composed of $[BO_3]$ and $[BO_4]$ units. In contrast, layered borates solely built by $[BO_3]$ units are much scarcer. Also, the number of single-layered borates solely built by $[BO_4]$ units is extremely limited. The exception is $Mo_2B_4O_9$, obtained by Huppertz *et al.* under high-pressure and high-temperature conditions.[175] $Mo_2B_4O_9$ achieves three important "first" structural characteristics: the first layered borate with the Mo atoms occurring in the form of tetrahedral metal clusters, the first thoroughly characterized molybdenum borate, and the first compound incorporating transition-metal clusters into an anionic borate crystal structure.[175] A $[B(1)O_4]$ tetrahedron and two $[B(2)O_4]$ tetrahedra in $Mo_2B_4O_9$ condense into a $[B_3O_9]$ ring, and four such rings are further linked by sharing $[BO_4]$ tetrahedra to construct a $[B_8O_{20}]$ "*vierer*" ring. Within the *ab* plane, each

https://dx.doi.org/10.1021/acs.chemrev.0c00796
Chem. Rev. 2021, 121, 1130−1202

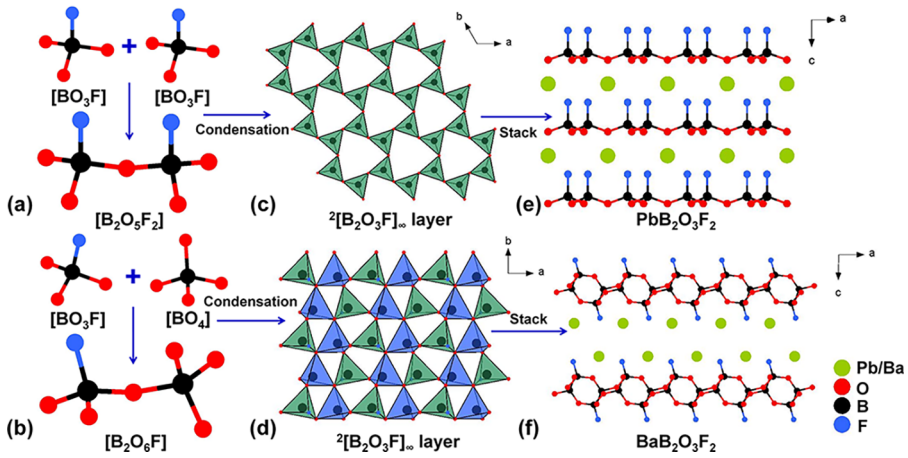

Figure 10. Structural evolution from B−O/F basic units (a,b), FBBs (a,b), single-layers (c,d), to final framework (e,f) of $PbB_2O_3F_2$ and $BaB_2O_3F_2$, respectively. All the structure diagrams were drawn by using the crystallographic information file of $PbB_2O_3F_2$ (ICSD: 263596) in ICSD and $BaB_2O_3F_2$ from ref 71.

ring is linked to four neighboring rings to form a 2D $^2[B_8O_{18}]_\infty$ corrugated layer. Similar to $Mo_2B_4O_9$, the strongly corrugated $^2[B_3O_6]_\infty$ layers in orthorhombic *meta*-oxoborates REB_3O_6 (RE = Dy−Lu)[176] were also built up from corner-sharing $[BO_4]$ tetrahedra. The FBBs in this series are constructed from two three-coordinated O atoms, that is $[OB_3]$, which represent a rare feature of bridging of $[BO_4]$ tetrahedra in oxoborate chemistry.[176]

When F atoms are incorporated into B−O polyanionic architectures, the F atoms can act as depolymerizers to reduce the dimensionality and generate more flexible B−O/F anionic networks. In this way, layered configurations are formed more easily and thus fluorooxoborates exhibit layered structures. LiB_6O_9F is the first fluorooxoborate with layered configuration, which exhibits a fluorinated 2D $^2[B_6O_9F]_\infty$ layer built from $[B_6O_{11}F]$ FBBs that consist of three-membered $[B_3O_6]$ and $[B_3O_6F]$ rings.[168] These strongly corrugated single layers in the *bc* plane with large channels (about 7 Å) are further packed along the *a* axis and interconnected by Li ions. More interestingly, the connectivity of the three-membered B−O/F rings inside the single layers of LiB_6O_9F, as well as the arrangement of these layers, is related directly to the structure of black phosphorus according to the topological analysis.[168] Further research on fluorooxoborate system has revealed that another type of fluorinated single-layer was found in the AB_4O_6F (A = NH_4, Na, Rb, Cs, K/Cs, Rb/Cs) family.[177−180] They feature similar 2D $^2[B_4O_6F]_\infty$ single layers with the A-site cations located between these single layers or filled in the 18-membered ring tunnels. Although all six fluorooxoborates exhibit the similar formula of AB_4O_6F, they possess distinctly different $^2{}_\infty[B_4O_6F]$ layered structures and thus crystallize into a number of different noncentrosymmetric space groups, which can be regarded as the results of regulation by the A-site cations. These space groups change from monoclinic *C*2 in NaB_4O_6F,[180] orthorhombic $Pna2_1$ in AB_4O_6F (A = NH_4, Rb, Cs),[176−179] trigonal *P*321 in $CsKB_8O_{12}F_2$,[178] and hexagonal $P\bar{6}2c$ in $RbCsB_8O_{12}F_2$.[178] The A-site cations affect the arrangement of the B−O/F anionic groups and lead to several configurations. The most notable features are the composition and flatness of the 2D $^2[B_4O_6F]_\infty$ layers. First, all of the single-layers are composed of $[B_4O_8F]$ FBBs, however they are constructed by $[B_3O_6]$ and $[BO_3F]$ units in Cs, K/Cs and Rb/Cs analogues, whereas in NH_4, Na and Rb analogues, they are built up by $[B_3O_6F]$ and $[BO_3]$ units. Second, the flatness value of $^2[B_4O_6F]_\infty$ layers in AB_4O_6F (A = NH_4, Na, Rb, Cs, K/Cs, Rb/Cs) family decreases with the A-site cation size increasing from NH_4^+ to Cs^+,[178] revealing that the $^2[B_4O_6F]_\infty$ layers become flatter as the A-site cations become larger.

A similar fluorinated single-layer was observed in the first alkaline-earth metal fluorooxoborate $BaB_4O_6F_2$ discovered by Höppe *et al.*,[181] which also exhibits a 2D $^2[B_4O_6F_2]_\infty$ layer but differs in its formation. Unlike AB_4O_6F (A = NH_4, Na, Rb, Cs, K/Cs, Rb/Cs) family, the single-layers in $BaB_4O_6F_2$ are built up from $[B_4O_8F]$ FBBs that consist of a $[BO_3]$ triangle and one $[B_3O_6F_2]$ ring. These layers are stacked along the *b* axis with the formation of 18-membered $[B_9O_9]$ rings and the Ba atoms filling in it. When the Ba ions in $BaB_4O_6F_2$ are replaced by its vertical neighbors Sr and Ca elements, the whole structure and the space group remain unchanged.[182] Also in alkaline-earth metal fluorooxoborates, another new type of fluorinated single-layer is found in $MB_5O_7F_3$ (M = Ca, Sr, Pb, Cd)[76,183−186] series, which show completely different structural characteristics compared to above $^2[B_4O_6F_2]_\infty$ single-layers in AB_4O_6F (A = NH_4, Na, Rb, Cs, K/Cs, Rb/Cs) family. The $MB_5O_7F_3$ (M = Ca, Sr, Pb, Cd) famliy features 2D *zigzag* $^2[B_5O_7F_3]_\infty$ layers with the M-site cations residing in the layers. Within them, three different crystallographic $[BO_3]$ and $[BO_3F]$ units are enclosed into $[B_3O_6F_2]$ single rings, and then two such rings further condense into $[B_5O_9F_3]$ double rings by sharing the edged B−O bonds of $[BO_3F]$ tetrahedra. The naphthalene like $[B_5O_9F_3]$ FBBs with near-planar configuration yields the 2D *zigzag* $^2[B_5O_7F_3]_\infty$ single layers. When the $[BO_3]$ triangles in AB_4O_6F (A = NH_4, Na, Rb, Cs, K/Cs, Rb/Cs) and $MB_5O_7F_3$ (M = Ca, Sr, Pb, Cd) series are removed, a simpler fluorinated single-layer solely built up from $[BO_3F]$ units formed in the $MB_2O_3F_2$ (M = Pb, Sn) series.[72,73] The single-layer (see Figures 10c,e) in this family can be expressed as $^2[B_2O_3F]_\infty$, which is constructed by $[B_2O_5F_2]$ FBBs *via* sharing terminal oxygen of the $[BO_3F]$ tetrahedra (Figure 10a). More interestingly, when replacing the Pb and Sn atoms in $MB_2O_3F_2$ (M = Pb, Sn) family with Ba to generate $BaB_2O_3F_2$, the layered configuration shows totally different features.[71] The wave-like 2D $^2[B_2O_3F]_\infty$ layers (Figures 10d,f) in $BaB_2O_3F_2$ include both tetrahedral $[BO_4]$ and $[BO_3F]$ units, which are further linked to form $[B_2O_6F]$ FBBs (Figure 10b). Structurally, $BaB_2O_3F_2$ is analogous to the Aurivillius-type

https://dx.doi.org/10.1021/acs.chemrev.0c00796
Chem. Rev. 2021, 121, 1130−1202

layered oxides, which can be regarded as the results of chemical substitution strategy by taking the classical Aurivillius-type layered Bi_2MoO_6 as a template.[71] That is to say, the layered constituents of $^2[Bi_2O_2]_\infty$ and $^2[MoO_4]_\infty$ in Bi_2MoO_6 were simultaneously replaced by $^2[Ba_2F_2]_\infty$ and $^2[B_2O_3F]_\infty$ in $BaB_2O_3F_2$. It should be noted that several new types of fluorinated 2D single layers can also be found in other fluorooxoborates, and although they are not included in ICSD, we list them here. These examples are the $^2[B_6O_9F_2]_\infty$ single-layers in $Na_2B_6O_9F_2$,[187] the $^2[B_6O_9F_3]_\infty$ layers in $K_3B_6O_9F_3$,[188] the $^2[B_4O_6F]_\infty$ layers in $BaB_8O_{12}F_2$,[189] and the $^2[B_4O_6F_3]_\infty$ layers in $KNiB_4O_6F_3$.[190]

2.4.3.2. Borates with Double-layered Structures. Compared to single-layered borates, the number of borates consisting of double B−O/F layers is limited and only a few cases exhibit such configurations. For example, the structures of $Cs_2A_2B_{10}O_{17}$ (A = Na, K, Tl)[103,116] involve a $^2[B_{10}O_{17}]_\infty$ infinite double layer, which corresponds to the juxtaposition of two pentaborate $[B_5O_{11}]$ groups. As such, a $[B_5O_{11}]$ unit contains six O atoms and five of them are bonded to B atoms, thus five different formulations are possible for the condensation of $[B_5O_{11}]$ groups through the five terminal oxygens. The polymeric $[B_{10}O_{21}]$ FBBs in the $Cs_2A_2B_{10}O_{17}$ (A = Na, K, Tl) family sequester the Cs atoms within the polyborate matrix, whereas the A-site atoms bridge the neighboring $^2[B_{10}O_{17}]_\infty$ double layers. Similar $^2[B_{10}O_{17}]_\infty$ double-layers are observed in $Rb_2Ba_4B_{20}O_{34}Br_2$ and related borate halides,[171] and they all have the same five-connected $[B_5O_{11}]$ FBBs, in which the $[B_5O_{11}]$ units successively stretch in the *ac* plane to form the $^2[B_5O_9]_\infty$ infinite single layers, then the adjacent layers are further linked to form the $^2[B_{10}O_{17}]_\infty$ double layers. As we discussed above that pentaborate AMB_5O_9 (A = Na, K; M = Ca, Sr, Ba, Pb)[169−172] are also built up from $[B_5O_{11}]$ FBBs, however, the difference is the layered configurations that are formed by $[B_5O_{11}]$ FBBs: single-layered configurations in this series and double-layered structures in the $Cs_2A_2B_{10}O_{17}$ (A = Na, K, Tl) and $Rb_2Ba_4B_{20}O_{34}Br_2$ series. That can be seen by analyzing the arrangement between pentaborate blocks axes and layer plane in all of the pentaborates.[10,171] Pan *et al.* proposed that the layered structures of pentaborates are mainly affected by the relationship between the orientation of $[B_5O_{11}]$ FBB's axes and layer plane, and the different number of terminal oxygen in the initial $[B_5O_{11}]$ blocks. That is to say, when the pentaborate blocks axes are parallel to the B−O layers, it can be condensed into double layers, like in $Cs_2A_2B_{10}O_{17}$ (A = Na, K, Tl) series. While when the pentaborate blocks axes are perpendicular to the B−O layers, it can be condensed into single layers, like in AMB_5O_9 (A = Na, K; M = Ca, Sr, Ba, Pb).

Also in polyborates, another type of double layer was found in lanthanum calcium borate by Wu *et al.*[36] The $[B_5O_{12}]$ double-ring groups in $La_2CaB_{10}O_{19}$ are further condensed by five of the six terminal oxygens to form the $[B_{10}O_{23}]$ FBBs and final 2D $^2[B_{10}O_{19}]_\infty$ double layers. The Ca-based polyhedra are sequestered within the polyborate matrix, whereas the La-based polyhedra bridge the neighboring $^2[B_{10}O_{19}]_\infty$ layers. By increasing the content of boron, more borates with double layers can be obtained, such as $A_2M_3B_{16}O_{28}$ (A = Rb, Cs; M = Ca, Cd)[191,192] and $Na_{11}B_{21}O_{36}X_2$ (X = Cl, Br).[193] The two series are both based on polymerized FBBs with a large number of B atoms. The FBB in $A_2M_3B_{16}O_{28}$ (A = Rb, Cs; M = Ca, Cd) series[191,192] is found in a boat-shaped $[B_8O_{18}]$ unit, which contains two $[B_3O_8]$ rings and two $[BO_3]$ units. These FBBs extend in the *bc* plane to form single layers that are further bridged by oxygen to yield the $^2[B_{16}O_{28}]_\infty$ double layers. Another similar B-rich $^2[B_{21}O_{36}]_\infty$ double-layer is observed in two isotopic borate halides $Na_{11}B_{21}O_{36}X_2$ (X = Cl, Br). Four three-membered rings with different crystallographic positions, namely three $[B_3O_7]$ and one $[B_3O_8]$ rings, are bridged by oxygen to form a fan-like $[B_9O_{18}]$ superstructure. Structurally, the $^2[B_{21}O_{36}]_\infty$ double layers in $Na_{11}B_{21}O_{36}X_2$ (X = Cl, Br) are formed by the condensation of $^2[B_6O_{16}]_\infty$ single layers that are composed of $[B_9O_{18}]$ superstructures. The Na atoms with different crystallographic positions reside in holes or between the double layers. Topological analysis reveals that the double layers in $Na_{11}B_{21}O_{36}X_2$ (X = Cl, Br) can be viewed as a graphene-like layer, in which $[B_3O_7]$ and $[B_3O_8]$ rings are equivalent to the C atoms in graphene.[193] With respect to the fluorinated double layers, $Ba_3B_{10}O_{17}F_2{\cdot}0.1KF$[194] with disordered neutral KF is the first and sole example that exhibits unique double-layered B−O/F arrangement. The FBB of $Ba_3B_{10}O_{17}F_2{\cdot}0.1KF$ is determined as the $[B_{10}O_{22}F]$ unit, which consists of four different B−O/F blocks: a $[B_5O_{11}]$ double-ring, a $[B_3O_7F]$ fluorinated ring, a $[BO_3]$ triangle, and a $[BO_4]$ tetrahedron. These FBBs are further linked with neighboring ones to form the 2D corrugated $^2[B_{10}O_{17}F_2]_\infty$ double layers, which are directly separated by the Ba^{2+} cations with the disordered neutral KF salt located within the channels. $Ba_3B_{10}O_{17}F_2{\cdot}0.1KF$ exhibits a shorter interlayer space and the increased bonding force between adjacent layers, which is beneficial to retain reduced structural convergence factors and improved structural stability.

2.4.3.3. Borates with Triple-layered Structures. Compared to the above single- and double-layered borates, the number of triple-layered borates is extremely limited. To the best of our knowledge, $Rb_3B_7O_{12}$,[123] $Cs_3B_7O_{12}$,[128] $K_{11}RbB_{28}O_{48}$,[195] and β-CsB_9O_{14}[196,197] (not included in ICSD) are the exclusive examples that exhibit such rare configurations. Similar to the association of FBBs that build single and double layers, the association of $[B_{14}O_{30}]$, $[B_{63}O_{133}]$, $[B_{28}O_{57}]$, and $[B_9O_{17}]$ FBBs build the complex 2D triple-layers in these alkali metal borates, respectively (Figure 11). These FBBs are common in the formation of the final triple-layered structures, creating

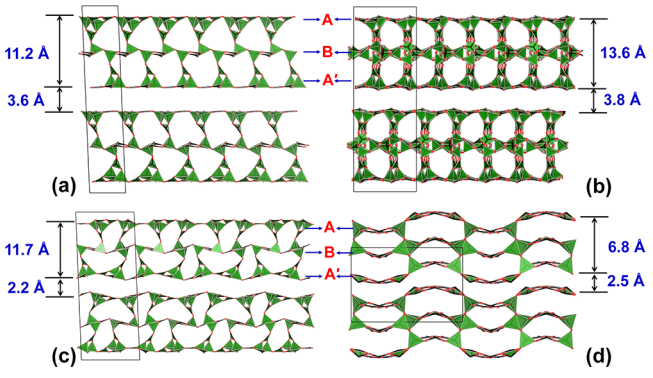

Figure 11. Structural expression and stacking mode of B−O triple-layered structure in (a) $Rb_3B_7O_{12}$, (b) $Cs_3B_7O_{12}$, (c) $K_{11}RbB_{28}O_{48}$, and (d) β-CsB_9O_{14}. The triangle and tetrahedron in green are $[BO_3]$ and $[BO_4]$, respectively. All of the structure diagrams were drawn by using the crystallographic information file of $Rb_3B_7O_{12}$ (ICSD: 412539) in ICSD and $Cs_3B_7O_{12}$, $K_{11}RbB_{28}O_{48}$, and β-CsB_9O_{14} from refs 128,195,197.

https://dx.doi.org/10.1021/acs.chemrev.0c00796
Chem. Rev. 2021, 121, 1130−1202

three types of sublayers, namely **A**, **B**, and **C** single layers, that are bridged and stacked along the *c* axis. In $Rb_3B_7O_{12}$ (Figure 11a),[123] the upper (**A**) and lower (**C**) single layers contain the same pentaborate $[B_5O_{11}]$ units formed by three $[BO_3]$ triangles and two $[BO_4]$ tetrahedra, and layer **C** can be deduced from layer **A** by simply using the two-fold axis. Whereas the intermediate single-layers (**B**) are formed by the alternately connection of the $[BO_4]$ tetrahedra and $[B_3O_7]$ rings. Then the adjacent single layers are further linked along the [001] direction in the −ABA′BA′−(**A′**=**C**) sequence *via* bridging oxygen to generate the final 2D $^2[B_{14}O_{24}]_\infty$ infinite triple layers. The Rb atoms in $Rb_3B_7O_{12}$ locate between the adjacent triple layers or in the cages of these layers.

In the case of $Cs_3B_7O_{12}$ (Figure 11b), it is even more complicated,[128] and it consists of triple layers that are constructed by highly polymerized $[B_{63}O_{133}]$ FBBs, with every oxygen being common to two polyhedra in these FBBs. In $Cs_3B_7O_{12}$, the triple layers are constituted by three sublayers of corner-sharing polyhedra. Sublayers **A** and **C** can be regarded as a quasi-regular arrangement of $[B_5O_{11}]$ groups formed by three $[BO_3]$ triangles and two $[BO_4]$ tetrahedra; similar to that in $Rb_3B_7O_{12}$, the sublayer **C** in $Cs_3B_7O_{12}$ can also be deduced from layer **A** by operating the two-fold axis,[128] whereas the sublayer **B** is complex without the same regularity compared to sublayers **A** and **C**, forming from four distinct B−O units, namely $[B_7O_{16}]$ units constituted by three $[BO_3]$ triangles and four $[BO_4]$ tetrahedra, $[B_5O_{11}]$ units built up by three $[BO_3]$ triangles and two $[BO_4]$ tetrahedra, $[B_5O_{12}]$ units constituted by two $[BO_3]$ triangles and three $[BO_4]$ tetrahedra, as well as mono B−O units ($[BO_3]$ or $[BO_4]$). Then the adjacent sublayers are further linked along the [001] direction in the −ABA′BA′−(**A′**=**C**) sequence *via* bridging oxygen to build the final 2D infinite $^2[B_{63}O_{108}]_\infty$ triple layers. Such a rare layered configuration leads to the occurrence of very large unit cell parameters of a = 59.991 Å, b = 11.520 Å, c = 34.525 Å, and V = 23386.36 Å^3, resulting in a very complex structure. Thus, its total information content is equal to 6062.598 bits/uc.[198]

The B−O anionic framework of $K_{11}RbB_{28}O_{48}$[195] also adopts the −ABA′BA′−(**A′**=**C**) triple-layered arrangement (Figure 11c), in which monolayers **A** and **C** contain $[B_8O_{19}]$ units formed by the condensation of two $[B_3O_7]$ rings and two $[BO_4]$ tetrahedra, whereas the monolayers **B** are composed of another type of $[B_8O_{19}]$ unit that is built up by a $[B_3O_7]$ ring, a $[B_3O_8]$ ring, a $[BO_3]$ triangle, and a $[BO_4]$ tetrahedron. Next four different $[BO_3]$ triangles between these monolayers join them to create a novel $[B_{28}O_{57}]$ FBB and a 2D $^2[B_{28}O_{48}]_\infty$ infinite triple layer arranged parallel to the *ab* plane. With respect to the location of Cs atoms, two distinct groups are observed. The Cs atoms with small displacement parameters locate between the triple layers to insure electrostatic binding. The Cs atoms with high displacement parameters are split and located in tunnels created within these layers. In *β*-CsB_9O_{14},[196,197] it also adopts the −ABCABC−(**C**=**A′**) triple-layered arrangement, there are **A** and **C** monolayers that contain three-membered $[B_3O_7]$ rings, whereas the **B** monolayers are composed of $[B_6O_{12}]$ units that are built up by the condensation of two $[B_3O_7]$ rings *via* edge-sharing $[BO_4]$ tetrahedra (Figure 11d).

2.4.4. Borates with 3D B−O/F Frameworks. The above low-dimensional borates, in principle, can construct various extended high-dimensional structures by condensation reactions with the elimination of nonbonding states of the oxygen in their FBBs under the suitable synthetic conditions forming borates with complicated 3D frameworks. Analysis of 175 available borates with 3D structures (Table S4 in the SI) shows that the frameworks of this class can be classified into the following four types according to the combination mode of the different B−O/F basic blocks: (1) type **A** framework solely consists of $[BO_4]$ tetrahedra, (2) type **B** framework consists of both $[BO_3]$ and $[BO_4]$ units, (3) type **C** framework from $[BO_3]$, $[BO_4]$, and $[BO_3F]$ units, as well as (4) type **D** framework built up by $[BO_3]$, $[BO_4]$, and $[BO_2F_2]$ units. In terms of frequency of occurrence, the first two types are far more common compared to the residual two types and the number of borates in each are 47, 126, 1, and 1 for the four classes. The MB_4O_7 (M = Ca, Sr, Ba, Pb, Sn, *etc.*)[199−203] series with the space group of $Pmn2_1$, $MnB_7O_{13}Br$[204] and its isomorphic phases in cubic $F\bar{4}3c$, SrB_2O_4,[205] and MnB_2O_4[206] and their isomorphic phases with the space group of $P2_1/c$ and $Pa\bar{3}$, as well as the $RE_2B_8O_{15}$ (RE = La, Nd, Pr)[207] series all belong to the type **A** framework. All of them are exclusively constructed by $[BO_4]$ tetrahedra that are strongly interconnected *via* sharing corners to form complicated 3D frameworks that host the M-site cations within the channels formed by B−O anionic frameworks. The majority of them are the new polymorphs of borates with existing formula, which are discovered under extreme experimental conditions of high pressure and high temperature. For example, the $RE_2B_8O_{15}$ (RE = La, Nd, Pr)[207] series were successively obtained by Huppertz *et al.* in a Walker-type multianvil apparatus at high pressure (5.5 GPa) and high temperature (1100 °C) conditions. A new FBB was identified that consists of four $[BO_4]$ tetrahedra and written as $[B_4O_{12}]$ units. In each $[B_4O_{12}]$ FBB, three $[BO_4]$ tetrahedra are condensed to a three-membered ring, and the fourth $[BO_4]$ tetrahedron is bonded to a $[B_3O_9]$ ring *via* the three-fold bridging oxygen. The alternate connectivity of $[B_4O_{12}]$ FBBs through vertices gives rise to a 3D framework with the helical channels running along the *a* axis that are filled by the RE atoms.

Two new polymorphs of BiB_3O_6 are found to possess a similar type **A** 3D framework reported by Lin *et al.*[208] and Huppertz *et al.*,[209] even though they are obtained under different pressure and temperature, namely autogenous pressure at 240 °C for *γ*-BiB_3O_6[208] and high pressure (5.5 GPa) at 820 °C for *δ*-BiB_3O_6.[209] Structurally, *γ*-BiB_3O_6 and *δ*-BiB_3O_6 are the only bismuth borates known so far that contain a 3D borate framework. The FBB of *γ*-BiB_3O_6 is a $[B_3O_9]$ ring consisting of three corner-sharing $[BO_4]$ units,[208] which is further linked by adjacent ones to produce 3D frameworks with three-, four-, six-, and ten-membered borate rings running along the *c* axis. The Bi atoms are coordinated into irregular coordination polyhedra and located within the largest channels formed by the ten-membered rings. While the structure of *δ*-BiB_3O_6 is exclusively built up of $[BO_4]$ tetrahedra,[209] which share common oxygen to form layers and are further interconnected by *zigzag* chains of $[BO_4]$ tetrahedra to generate a 3D network structure with six- and ten-membered borate rings running along the *b* and *c* axes, respectively. Similar to *γ*-BiB_3O_6, the Bi-based irregular polyhedra locate within the channels formed by the ten-membered rings. In both polymorphs, if the lone electron pairs accompanied by the Bi atoms in related structures are included, the Bi-based polyhedra are distorted octahedra rather than pyramidal configurations.

https://dx.doi.org/10.1021/acs.chemrev.0c00796
Chem. Rev. 2021, 121, 1130−1202

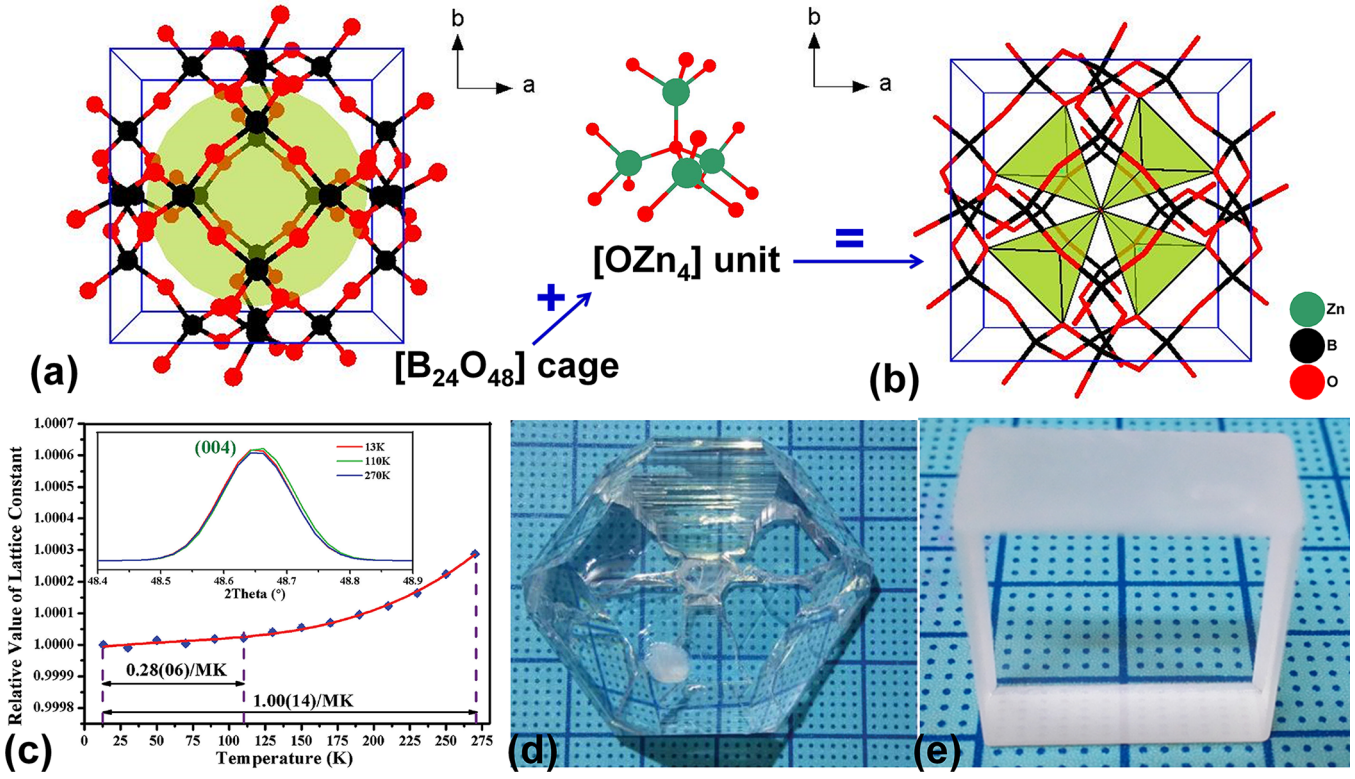

Figure 12. (a,b) The structural evolution from $[B_{24}O_{48}]$ cage to 3D framework in $Zn_4B_6O_{13}$. (c) The variation of the refined cell parameters of $Zn_4B_6O_{13}$ with respect to temperature. Inset: evolution of the cubic (004) peak Bragg reflection as the temperature changes, and the peaks of Kα2 have been removed by Gaussian peak fitting. Reproduced with permission from ref 212. Copyright 2016 John Wiley and Sons. (d,e) The as-grown and fabricated $Zn_4B_6O_{13}$ crystal with the dimensions of 40 × 40 × 18 mm^3 and 20 × 20 × 10 mm^3, respectively. Reproduced with permission from ref 212. Copyright 2016 John Wiley and Sons. Parts a and b were drawn by using the crystallographic information file of $Zn_4B_6O_{13}$ (ICSD: 34085) in ICSD.

$Zn_4B_6O_{13}$ (also written as $Zn_4O[B_6O_{12}]$)[210] also adopts a type **A** 3D framework with sodalite structures, in which $[B_{24}O_{48}]$ sodalite cage (Figures 12a,b) is composed of 24 $[BO_4]$ tetrahedra by sharing O(2) atoms and the whole 3D framework can be extended by sharing the common oxygen in $[B_{24}O_{48}]$ cages. The O(1) atoms are surrounded by four $[ZnO_4]$ tetrahedra to construct a radial $[Zn_4O_{13}]$ cluster that is filled in $[B_{24}O_{48}]$ cages by relatively strong Zn−O covalent bonds. Interestingly, $Zn_4B_6O_{13}$, with the ultramarine structure, shows unprecedented high hardness compared to related ultramarines, which is due to the chemical bond peculiarities in $Zn_4B_6O_{13}$ as follows according to the study of Belokoneva *et al.*[211] The electron density peaks in $[BO_4]$ tetrahedra are higher than usual (~1.2 e/Å^3), which corresponds to strong covalent bonds between the overlapping B sp^3 orbitals in $[BO_4]$ tetrahedra and bridging O(2) p orbitals in the framework. In additions, the oxo-centered $[OZn_4]$ tetrahedra cannot be characterized as nonframework ions because they are bonded with O(2) atoms in the framework. Thus, the bonds can explain the high hardness of $Zn_4B_6O_{13}$ crystals. Lin *et al.* reported the near-zero thermal expansion behavior in $Zn_4B_6O_{13}$ crystals and expanded the near-zero thermal expansion materials family to borate systems for the first time (Figure 12c).[212] As shown in Figures 12d,e, optically perfect $Zn_4B_6O_{13}$ crystals can be easily grown and fabricated as an optical device, indicating the feasibility as a practical near-zero thermal expansion material. First-principles calculations[212] demonstrate that the unprecedented thermal expansion is mainly due to the invariability of the solid $[B_{24}O_{48}]$ truncated cages that are fixed in place by $[Zn_4O_{13}]$ units in $Zn_4B_6O_{13}$.

In comparison, the number of borates in type **B** 3D framework is three times as high as that of borates with type **A**. The $M_2B_5O_9X$ (M = Ca, Sr, Ba, Pb, Sn, Eu; X = Cl, Br, I, *etc.*)[130,213−217] series with the space group of *Pnn*2, $MgB_7O_{13}Cl$,[218] and its isomorphic phases in orthorhombic *Pca*2$_1$, $Na_2Co_2B_{12}O_{21}$,[219] AMB_9O_{15} (A = Li, Na; M = Sr, Ba) series,[112] β-LaB_5O_9,[220] and $A_3B_6O_{10}X$ (A = K, Na, Rb/Na; X = Cl, Br)[221−226] series all belong to the type **B** framework. All are constructed from $[BO_3]$ and $[BO_4]$ groups that are further condensed to complicated 3D frameworks with A- and M-site cations located in the channels or intervals formed by B−O anionic frameworks. Herein, a few with interesting structural features are discussed. For example, $Na_2Co_2B_{12}O_{21}$ with a 3D network was reported by Nazar *et al.*,[219] which is the first infinite borate containing a discernible tunnel structure. The tunnels in $Na_2Co_2B_{12}O_{21}$ are bonded by the 12-membered $[B_{12}O_{24}]$ rings composed of symmetry-related pairs of $[BO_3]$, $[B_3O_7]$, and $[B_4O_9]$ units. These rings are further stacked along the *b* axis to create the tunnel structure with the cross-sectional dimensions up to 4.5 Å × 8.8 Å, and the void spaces and open channels are occupied by Ni^+ and Na^+ cations, respectively. These cations stabilize the void regions within the anion structure by adopting the charge compensating and space filling roles. More importantly, the Na^+ cations in the large tunnels are mobile and are readily exchangeable with the preservation of original crystal structure, which guarantee the feasibility of ion exchange in $Na_2Co_2B_{12}O_{21}$.[219]

https://dx.doi.org/10.1021/acs.chemrev.0c00796
Chem. Rev. 2021, 121, 1130−1202

Another interesting type **B** framework is observed in β-LaB_5O_9 discovered by Lin *et al.*,[220] which contains buckled nine-membered ring layers that are interlinked by $[BO_3]$ triangles to build a 3D framework. Structurally, the 3D structure of β-LaB_5O_9 can be considered as the further polymerization of corresponding 2D layers. The FBB in β-LaB_5O_9 is $[B_5O_{12}]$ consisting of a three-membered $[B_3O_8]$ ring and two $[BO_3]$ triangles, which is totally different from the $[B_5O_{12}]$ double rings in the $MREB_5O_{10}$ (M = Mg, Co, Zn, Ni, Cd; RE = trivalent rare earth metal)[173,174] series, even though they exhibit the same formula for the FBB. Within these $[B_5O_{12}]$ FBBs in β-LaB_5O_9, $[B_3O_8]$ rings link with one of the two $[BO_3]$ triangles to form the $^2[B_4O_8]_\infty$ layers, these single-layers are further condensed by the residual $[BO_3]$ triangles to form the 3D framework. It should be noted that the structure of $Li_2Sr_4B_{12}O_{23}$[227] is an interesting example of two B−O frameworks with different dimensionality coexisted in one structure, namely isolated 0D $[B_2O_5]$ dimers and 3D $^3[B_8O_{18}]_\infty$ framework. Such a configuration is extremely rare and only has been observed in $Li_2Sr_4B_{12}O_{23}$.

Moreover, the symmetrical characteristic type **B** framework formed in the $A_3B_6O_{10}X$ (A = K, Na, Rb/Na, K/Na; X = Cl, Br) series are fine-tuned by different A-sited cations and halogens. The potassium borate bromide $K_3B_6O_{10}Br$ with the space of *R*3*m* is the first member of this family reported by Belokoneva *et al.* in 2006,[221] in which the 3D perovskite-like framework is composed of A-site $[B_6O_{10}]$ FBBs and Br-centered $[BrK_6]$ secondary building blocks (B-site). Thus, when taking the classical perovskite ABX_3 as a template, the formula of $K_3B_6O_{10}Br$ can be represented as $[B_6O_{10}]BrK_3$. Soon afterward, another new member of this family $K_3B_6O_{10}Cl$ which processes the same 3D configurations to its isomorphic $K_3B_6O_{10}Br$ was discovered by Pan and Poeppelmeier *et al.*[222] The NLO properties of $K_3B_6O_{10}X$ (X = Cl, Br), including second-order NLO coefficients, phase matching wavelength, output power, temperature bandwidths, and laser conversion efficiency that mainly rely on its polar architecture, were systematically characterized based on large single crystals.[222,223] All of these results indicate that $K_3B_6O_{10}X$ (X = Cl, Br) series (see section 3.9.1) are excellent NLO crystals, and the perovskite-like frameworks are responsible for such balanced optical properties. Activated by this, more new members, $Na_3B_6O_{10}Cl$,[224] $Na_3B_6O_{10}Br$,[225] $RbNa_2B_6O_{10}Cl$,[224] $RbNa_2B_6O_{10}Br$,[224] and $K_{3-x}Na_xB_6O_{10}Br$,[226] were continuously obtained by Pan *et al.* Interestingly, although these members exhibit similar perovskite-related frameworks, they crystallize with different space groups changing from centrosymmetric *Pnma*, noncentrosymmetric chiral $P2_12_12_1$ to polar *R*3*m*. Such unusual phenomena are found to be related to A-site cations and halogens. For example, the change in $K_{3-x}Na_xB_6O_{10}Br$[226] occurs from the polar framework for the members containing relatively more K^+ content ($\sim x > 0.7$) to the centrosymmetric structure for those with more Na^+ content ($\sim x < 0.7$). The larger radius of K^+ compared to Na^+ cations results in a more flexible $^3[B_6O_{10}]_\infty$ framework and weakens interaction among the $[B_6O_{13}]$ FBBs, allowing the $[B_6O_{13}]$ units to arrange parallel rather than antiparallel to the $[Br(K/Na)_6]$ lattices. Owing to the weak Na−Cl bonds in the $[Cl(Na/Rb)_6]$ octahedra of $Na_3B_6O_{10}X$ and $RbNa_2B_6O_{10}X$ (X = Cl, Br),[224,225] the magnitudes of out-of-center distortion in the $[Cl(Na/Rb)_6]$ octahedra are much larger than those of $[Br(Na/Rb)_6]$ octahedra. These make the connecting angles among the $[X(Na/Rb)_6]$ octahedra different and further influence the overall symmetry of perovskite-related framework in this family. Therefore, the Cl-based members in this series crystallize in the space group of $P2_12_12_1$, whereas the Br-based ones belong to *Pnma*.[224,225]

With respect to the remaining two types, the fluoroxoborates PbB_5O_8F[228] and $Li_2B_6O_9F_2$[229] are the sole borates that are assigned to the types **C** and **D** 3D framework, respectively. PbB_5O_8F was found to be the first lead fluorooxoborate and rationally designed following the strategy of fluorine introduction into borates.[228] The structure of PbB_5O_8F includes two independent interpenetrating 3D networks composed of unprecedented $[B_5O_{10}F]$ FBBs and distorted $[Pb_2O_{14}]$ dimers with the stereochemically active 6*s* lone pairs located in the interstitial voids (Figure 13a).

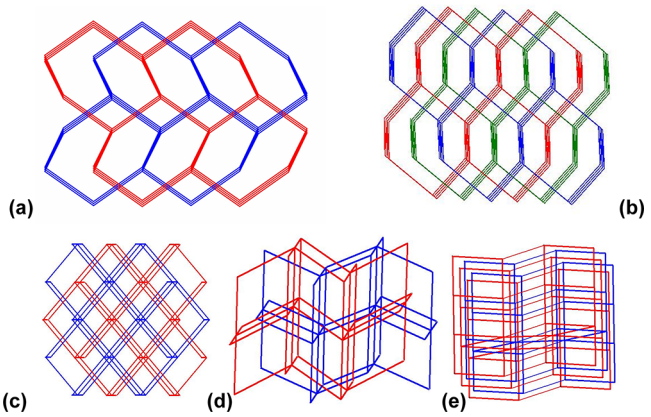

Figure 13. Topological expression of representative borates with two or three independent interpenetrating 3D frameworks, in which the $[B_5O_{10}F]$, $[B_6O_{11}F_2]$, $[B_9O_{19}]$, $[B_9O_{17}]$, and $[B_8O_{13}]$ FBBs are regarded as four, four, six, six, and six-connected nodes for PbB_5O_8F (a), $Li_2B_6O_9F_2$ (b), α-$Na_2B_6O_{10}$ (c), α-CsB_9O_{14} (d), and β-$Na_2B_8O_{13}$ (e), respectively. All of the structure diagrams were drawn by using the crystallographic information file of PbB_5O_8F (ICSD: 256206), $Li_2B_6O_9F_2$ (ICSD: 423435), β-$Na_2B_8O_{13}$ (ICSD: 59748) in ICSD and α-CsB_9O_{14} from ref 197.

$Li_2B_6O_9F_2$ was reported as a new member of lithium fluorooxoborates by Jansen *et al.* in 2011,[229] in which the 3D anionic network is related to the polymeric anion of γ-CsB_5O_8.[230] After substituting one bridging oxygen of $^3[B_5O_8]_\infty$ network in γ-CsB_5O_8 with a $[BO_2F_2]$ tetrahedron, the resulting $^3[B_6O_9F_2]_\infty$ anionic network is identical to the one formed in $Li_2B_6O_9F_2$. Similar to PbB_5O_8F, the topological network of $Li_2B_6O_9F_2$ also exhibits three independent interpenetrating 3D frameworks (Figure 13b). Such configurations are rare, and most of them are polyborates with a relatively high content of B atoms. For example, the B−O anionic framework of α-KB_5O_8,[97] α- and β-$Na_2B_8O_{13}$,[231,232] $Li_2B_4O_7$,[233] α-CsB_9O_{14},[234] and α-LnB_5O_9[220] are 3D networks, formed by two interpenetrating, infinite and separate 3D subframeworks (Figures 13c−e).

2.5. Unconventional Borates with Edge-sharing $[BO_4]$ Tetrahedra

In the terms of structure, the borates are fully characterized by the great variety of connectivity of their FBBs, and the connections of B−O/F basic blocks *via* corner-sharing have long been a main contributor to the structure diversity of borates, thus most borates contain corner-shared clusters or anionic framework. Additionally, the structural characteristics

https://dx.doi.org/10.1021/acs.chemrev.0c00796
Chem. Rev. 2021, 121, 1130−1202

of borates are also supplemented by edge-sharing [BO_4]-tetrahedra. Although borates with such configurations are extremely rare, these unique features lead to a variety of unusual structural arrangements that are not found in any other homonuclear polyoxyanions with the same coordination environment. For compounds built by cation-centered polyhedra, including borates, phosphates, and silicates, *etc.*, sharing edges or faces by two polyhedra may increase the repulsion between adjacent anions and cations, resulting in low stability of the ionic structures according to the Pauling's third and fourth rules as well as the orbital interpretation rules.[235,236] Thus, the corner-shared connection of B−O/F basic blocks is usually more favorable in energy than the edge-shared ones in the structure of borates. With respect to the edge-sharing connection, it only occurs between two [BO_4] tetrahedra in very few borates, and there are still no borates with the linkage of [BO_3] and [BO_3], as well as [BO_3] and [BO_4] *via* edge-sharing. Different synthesis approaches have led to several borates with edge-sharing [BO_4] tetrahedra, for example, high pressure and atmospheric pressure synthesis conditions, which is the classification standard used in the next section.

2.5.1. High Pressure Synthesis of Borates with Edge-sharing [BO_4] Tetrahedra. The first edge-sharing [BO_4] tetrahedra were observed in rare earth borate $Dy_4B_6O_{15}$ by Huppertz and van der Eltz in 2002[131] under the high-pressure and high-temperature conditions of 8.0 GPa and 1000 °C. The anionic framework of $Dy_4B_6O_{15}$ contains a 2D $^2[B_6O_{15}]_\infty$ single-layer built up from [B_6O_{18}] FBBs that exclusively consist of [BO_4] tetrahedra. Within them, the [BO_4] tetrahedra are connected *via* both corner-sharing and edge-sharing, in which two edge-sharing [BO_4] tetrahedra containing [B_2O_6] dimers link with neighboring [BO_4] tetrahedra to form a six-membered [B_6O_{17}] ring. The linkage of these rings by further two corner-sharing [BO_4] tetrahedra leads to ten-membered rings that construct the final corrugated 2D $^2[B_6O_{15}]_\infty$ single layers. Shortly after, isomorphic phase $Ho_4B_6O_{15}$[237] and a new series of rare earth borates with the composition of α-$RE_2B_4O_9$ (RE = Eu, Dy, Sm, Ho, Gd, Tb)[238] were continuously discovered by Huppertz *et al.* between 2003 and 2005, which also possess the edge-sharing [BO_4] tetrahedra. The structures of α-$RE_2B_4O_9$ (RE = Eu, Dy, Sm, Ho, Gd, Tb)[238] family exhibit a complex 3D network of linked [$B_{20}O_{46}$] FBBs, which contain corner-sharing and edge-sharing [BO_4] tetrahedra with the ratio of 18:2. The linkage of the FBBs gives rise to further a 3D network with three different types of infinite channels formed by five-, six- and fourteen-membered rings, respectively. All of the channels along the *b* axis are occupied by crystallographically different RE-site cations. Later on, a new series of edge-sharing [BO_4] tetrahedra containing borates with the composition of high-pressure MB_2O_4 (high pressure = HP; M = Fe, Ni, Co)[239−241] were obtained in a reaction of high pressure and high temperature starting from the stoichiometric mixture of related transition metal oxides and B_2O_3. The biggest highlight of their structural features is that each [BO_4] tetrahedron in HP-MB_2O_4 (M = Fe, Ni, Co) series shares a common edge with a second [BO_4] tetrahedron, and such a connectivity style was previously unknown. The structures of HP-MB_2O_4 (M = Fe, Ni, Co) series are found to have single-layered configurations composed of [BO_4] tetrahedra. Two tetrahedra construct a [B_2O_6] dimer through edge-sharing, and these dimeric units are linked to each other through common vertices to form $^2[B_2O_4]_\infty$ single layers that spread to form in the *bc* plane. These layers stack along the *a* axis and are further condensed by the [MO_6] octahedra to complete the whole structure.

All of the above borates with edge-sharing [BO_4] tetrahedra exclusively consist of tetrahedral [BO_4] units, without involving any [BO_3] triangles. This unique situation changes with the discovery of HP-KB_3O_5 and HP-CsB_5O_8 series by Huppertz *et al.*,[242,243] which exhibits both [BO_3] and [BO_4] motifs. It is noteworthy that HP-KB_3O_5 is the first case that possesses three different possible conjunctions simultaneously, namely, corner-sharing [BO_3] groups, corner-sharing [BO_4] units, and edge-sharing [BO_4] units. The 3D $^3[B_6O_{10}]_\infty$ network contains ribbons composed by [BO_4] tetrahedra along the *c* axis, which are further interconnected by trigonal planar [BO_3] units to form channels with the A-based polyhedra situated in them. It is noteworthy that the B-based precursors for all the above borates are B_2O_3, and only when B_2O_3 is replaced by H_3BO_3 during the synthesis process can more H_2O or OH^- containing hydrated borates with the structural motif edge-sharing [BO_4] units be expected. The discovery of $M_6B_{22}O_{39}\cdot H_2O$ (M = Fe, Co),[244] $Co_7B_{24}O_{42}(OH)_2\cdot 2H_2O$,[245] and $La_3B_6O_{13}(OH)$[246] under high-pressure and high-temperature conditions, as well as α-$Ba_3[B_{10}O_{17}(OH)_2]$[247] under hydrothermal conditions, verifies the earlier assumptions. Interestingly, $M_6B_{22}O_{39}\cdot H_2O$ (M = Fe, Co)[244] and $Co_7B_{24}O_{42}(OH)_2\cdot 2H_2O$[245] are structurally similar, which exhibit the intermediate (the former series) and final (the later one) states in the formation of edge-sharing [BO_4] tetrahedra. Both are constructed by multiple corrugated layers of corner-sharing [BO_4] units, which are interlinked by [BO_3] units. The linking [BO_3] units in $M_6B_{22}O_{39}\cdot H_2O$ (M = Fe, Co)[244] are distorted and very close to the configuration of [BO_4] tetrahedra if the additional O atoms of the neighboring [BO_4] tetrahedra are considered in the coordination sphere. This situation may be considered as an intermediate state on the way to edge-sharing [BO_4] tetrahedra proposed by Huppertz *et al.*[244]

However, the connectivity in the structure of $La_3B_6O_{13}(OH)$[246] exhibits "ideal" edge-sharing [BO_4] tetrahedra, not an intermediate state like the above hydrated borates $M_6B_{22}O_{39}\cdot H_2O$ (M = Fe, Co).[244] The B−O anionic framework of $La_3B_6O_{13}(OH)$ is based on the 2D $^2[B_6O_{13}]_\infty$ single-layers extended in the *bc* plane, which is formed by the polymerization of six-membered rings [B_6O_{17}] FBBs. Both corner-sharing and edge-sharing [BO_4] units are observed in the [B_6O_{17}] FBBs with the ratio of 4:2. Unlike the symmetric feature of overall structure in all of the above edge-sharing [BO_4] units containing borates, $La_3B_6O_{13}(OH)$ adopts a noncentrosymmetric structure with the space group of $P2_1$ (no. 4), which makes $La_3B_6O_{13}(OH)$ the first and sole borate with such edge-sharing [BO_4] tetrahedra that has the potential to be used as an NLO crystal.[246] $La_3B_6O_{13}(OH)$ is also the first borate with different crystalographically B atoms inside these [BO_4] tetrahedra. Another hydrated borate α-$Ba_3[B_{10}O_{17}(OH)_2]$ was synthesized in aqueous solution with hydrothermal approach by Lii *et al.*[247] The synthetic conditions are as follows: raw materials were sealed in a gold ampule to create a condition of 500 Pa (estimated according to the P−T diagram of H_2O) and 500 °C. Such a condition is milder than the high-pressure (~3-10 GPa) and high-temperature (~600-1150 °C) environment set up by Huppertz *et al.* during the synthesis of the above other borates discussed in this section.

https://dx.doi.org/10.1021/acs.chemrev.0c00796
Chem. Rev. 2021, 121, 1130−1202

2.5.2. Atmospheric Pressure Synthesis of Borates with Edge-sharing [BO_4] Tetrahedra. Previously, particularly before 2010, it was generally accepted that edge-sharing [BO_4] tetrahedra containing borates can only be obtained under the extremely conditions of high pressure and high temperature in a sealed atmosphere. Thus, such a rare structural motif of edge-sharing [BO_4] units was found to exist exclusively in few metastable borates obtained under high-pressure conditions. However, $KZnB_3O_6$ with the structural motif of edge-sharing [BO_4] tetrahedra was synthesized under ambient pressure by the two independent groups of Professor Chen and Professor Wu, demonstrating that high pressure is not an indispensable condition to synthesize borates with edge-sharing [BO_4] tetrahedra for the first time.[99,100] $KZnB_3O_6$ exhibits a 0D [B_6O_{12}] hexa-group, in which two [B_3O_7] three-membered rings are further condensed *via* two edge-sharing [BO_4] tetrahedra. The [B_6O_{12}] FBB can be regarded as a six-connected node to link with the closest six [Zn_2O_6] units to form a 3D framework with two channels running along the [$1\bar{1}0$] direction composed of six- and ten-membered rings, and the [KO_9] polyhedra locate in the *zigzag* ten-membered rings. $KZnB_3O_6$ could be preserved from room temperature up to its melting point, indicating the improved thermal stability in $KZnB_3O_6$ compared to high-pressure borates.

Besides, the corner-sharing $KZnB_3O_6$ was established theoretically by Chen *et al.*[100] *via* replacing the Cd with Zn atoms in known $KCdB_3O_6$. Further study shows that edge-sharing $KZnB_3O_6$ is indeed energetically more favorable than another hypothetical structure of $KZnB_3O_6$ with corner-sharing [BO_4] tetrahedra, indicating that the existence of edge-sharing $KZnB_3O_6$ obtained under ambient atmosphere is not an accident but a certain event of energy minimization. To further investigate the origin of the phase stability in edge-sharing $KZnB_3O_6$, theoretical analyses, including molecular dynamics, lattice dynamics, as well as electronic properties of edge-sharing $KZnB_3O_6$ and corner-sharing $KZnB_3O_6$ associated with their structural stabilities were carried out by Zhao *et al.*[248] From the analysis of lattice dynamics in both phases, they believe that the vibrational modes of edge-sharing [BO_4] tetrahedra are dynamically stable and all modes have real frequencies in edge-sharing $KZnB_3O_6$. While in the case of corner-sharing $KZnB_3O_6$, there is a soft mode at the G point with an imaginary frequency, and this dynamically unstable feature has its origin in the linkage of deformed [ZnO_5] polyhedra. Structurally, the [ZnO_5] polyhedra and [BO_3] triangles in corner-sharing $KZnB_3O_6$ repel each other because of steric hindrance and Coulomb repulsion effects, resulting in stretched Zn−O bonds with the smallest covalent nature and the least orbital overlap in deformed [ZnO_5] polyhedra.[248] Such stretched Zn−O bonds lead to a decrease of the force constant, resulting in the soft mode associated with the [ZnO_5] polyhedra in corner-sharing $KZnB_3O_6$. On the basis of the analysis above, it is concluded that the structural instability of corner-sharing $KZnB_3O_6$ is mainly due to the deformed [ZnO_5] polyhedra. The lack of strong corner-sharing competitors could be the key factor that allows this edge-sharing $KZnB_3O_6$ to prevail. However, the origin that is responsible for the formation of the edge-sharing [BO_4] tetrahedra in $KZnB_3O_6$ in an energy-favorable way still remains unclear.

In contrast to the high-pressure metastable edge-sharing borates, $KZnB_3O_6$ can survive up from room temperature to close to its melting point in ambient pressure conditions and also without any detectable phase transition occurring, indicating the rigid feature of its [B_6O_{12}] FBBs and [Zn_2O_6] units. Thus, the thermal expansion property associated with the structural peculiarities and nature of chemical bonds was studied from room temperature to 1013 K by Chen *et al.* for the first time.[249] $KZnB_3O_6$ shows an quasi-unidirectional thermal expansion over the entire measured temperature ranging from 298 to 1013 K. Specifically, it exhibits an area zero thermal expansion of $(-1.06 \pm 0.42) \times 10^{-6}$ K^{-1} and $(0.56 \pm 0.31) \times 10^{-6}$ K^{-1} along the X1 and X2 axes, as well as a very large expansion along the X3 axis of $(44.81 \pm 0.79) \times 10^{-6}$ K^{-1}.[249] Even though it is accepted that borates exbibit large anisotropic thermal expansion compared to other inorganic systems, quasi-unidirectional thermal expansion is extremely rare and peculiar. Theoretical analyses indicate that the unusual thermal expansion in $KZnB_3O_6$ mainly originates from the hinge rotations of [B_6O_{12}] and [Zn_2O_6] rigid units. Further, also by Chen *et al.*,[250] the driving force for the quasi-unidirectional thermal expansion of edge-sharing $K_{1-x}A_xZnB_3O_6$ (A = Na, Rb; $x = 0.5$) was investigated. Partial substitution of K with Na/Rb can regulate the thermal expansion behavior of this family from zero thermal expansion to area negative thermal expansion. The partial density of phonon states in A-site cations of this famliy shows decreased localized harmonic oscillator from $KZnB_3O_6$, $K_{0.5}Rb_{0.5}ZnB_3O_6$ to $K_{0.5}Na_{0.5}ZnB_3O_6$, indicating that the broadening of the low-energy peaks leads to an increase in volume thermal expansion. Thus, we can conclude that the low-energy vibrational modes of A-site alkali metals also play an important role in this unusual quasi-unidirectional thermal expansion behavior.[250]

Subsequently, several new nonpressurized members, including $Ba_4Na_2Zn_4(B_3O_6)_2(B_{12}O_{24})$,[148] with disordered cations, $Li_4Na_2CsB_7O_{14}$,[251] $BaAlBO_4$,[252] and β-CsB_9O_{14},[196,197] have been discovered under atmospheric pressure by Pan's and Chen's groups, which have expanded the number of borates with the structural motif of edge-sharing [BO_4] tetrahedra formed without pressurization. The first three compounds exhibit 0D B−O anionic frameworks, namely isolated [B_3O_6] and [$B_{12}O_{24}$] clusters for $Ba_4Na_2Zn_4(B_3O_6)_2(B_{12}O_{24})$, [$B_{14}O_{28}$] clusters for $Li_4Na_2CsB_7O_{14}$, and [B_4O_{10}] clusters for $BaAlBO_4$, respectively. These clusters are composed of [B_6O_{13}], [B_2O_6], and [B_7O_{15}] intermediates *via* edge-sharing [BO_4] tetrahedra, respectively. In the case of β-CsB_9O_{14}, it possesses the triple-layered structures with the arrangement **−ABCABC−(A═C′)**, in which **B** monolayers consist of [B_6O_{12}] units that are built up by the condensation of two [B_3O_7] rings *via* edge-sharing [BO_4] tetrahedra. Besides, inspired by the unusual thermal expansion behavior in $KZnB_3O_6$, the thermal expansion coefficients of $Li_4Na_2CsB_7O_{14}$ were calculated based on the indexed lattice constants at different measured temperatures. Thermal expansions with the highly anisotropic behavior can be observed with the increased temperatures, and $Li_4Na_2CsB_7O_{14}$ might be used as a thermal expansion material.[251]

Analyses of all of the available edge-sharing [BO_4] tetrahedra containing FBBs in related borates show that these FBBs can be structurally evolved by replacing the four nodes of [B_2O_6] prototype with different B−O blocks (Figure 14).[251] For type **A** model according to the classification by Pan *et al.*, the replaced nodes are the same B−O blocks, like the [B_6O_{12}] FBBs in $KZnB_3O_6$, [B_9O_{17}] FBBs in β-CsB_9O_{14}, [B_6O_{18}] FBBs in $RE_4B_6O_{15}$ (RE = Dy, Ho), and [$B_{20}O_{46}$] FBBs in α-$RE_2B_4O_9$ (RE = Eu, Dy, Sm, Ho, Gd, Tb) family can be extended out by

https://dx.doi.org/10.1021/acs.chemrev.0c00796
Chem. Rev. 2021, 121, 1130−1202

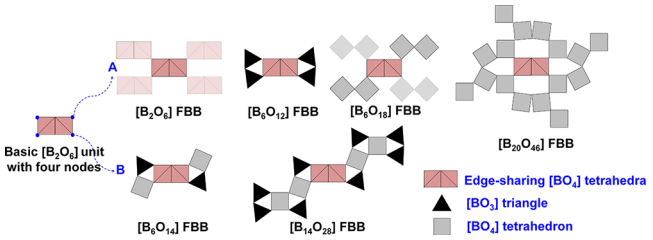

Figure 14. Structural peculiarities of edge-sharing $[BO_4]$ tetrahedra in two types of models. The triangle in black, square in gray, and double-square in jacinth are $[BO_3]$, $[BO_4]$, and edge-sharing $[BO_4]$, respectively. Reproduced with permission from ref 251. Copyright 2019 Royal Society of Chemistry.

replacing the four nodes of $[B_2O_6]$ prototype with identical $[BO_3]$, $[BO_3]$, $[B_2O_7]$, and $[B_4O_{13}]$ units, respectively. In the case of the type **B** model, the replaced nodes are the varied two B−O pairs, such as $[BO_3]$ and $[BO_4]$ units for HP-AB_3O_5 (A = K, Cs) series as well as $[BO_3]$ and $[B_5O_{11}]$ units for $Li_4Na_2CsB_7O_{14}$, respectively.

2.5.3. Identification of the Edge-sharing $[BO_4]$ Tetrahedra. With the increasing of edge-sharing $[BO_4]$ tetrahedra containing borates, the identification of such rare structural motifs seems especially important and urgent. Up to now, several pieces of evidence can be used to confirm the linkage of edge-sharing $[BO_4]$ tetrahedra, covering structural peculiarities and spectral properties.

2.5.3.1. Structural Peculiarities. Although the borates in this subsection were obtained under different syntheses conditions of high pressure and atmospheric pressure, the structural features are highly consistent and share many common features, which can help us identify the edge-sharing $[BO_4]$ tetrahedra. Owing to the effects of like-charges repulsion, the B^{3+} ions with higher valence in the edge sharing $[BO_4]$ tetrahedra will be displaced to minimize the electrostatic potential and thus result in the reduced O−B−O angles and elongated B−O bonds (Figure 15a). Thus, the O−B−O angles within the $[B_2O_2]$ rings are reduced from the ideal tetrahedral value of 109.48° to the region of 92.0-94.4° in these borates with edge sharing $[BO_4]$ tetrahedra, and the B−O bonds are further elongated from the statically averaged B−O bond length of 1.4775 Å (in tetrahedral coordination) up to unprecedented lengths, and the largest B−O bonds can reach to 1.607 Å in $BaAlBO_4$.[252] In addition, significant expansion of the B···B interatomic distances cause a narrowing of the O−B−O angles. Thus, the B···B interatomic distances all fall between 1.9884 and 2.2306 Å (Figure 15b), far longer than the two other undeformed edge-sharing $[BO_4]$ tetrahedra (1.700 Å), such as, $Li_4Na_2CsB_7O_{14}$ (2.0257 Å),[251] α-$Gd_2B_4O_9$ (2.040 Å),[238] $Dy_4B_6O_{15}$ (2.072 Å),[131] $La_3B_6O_{13}(OH)$ (2.077 Å),[246] $KZnB_3O_6$ (2.079 Å),[100] β-FeB_2O_4 (2.083 Å),[240] HP-NiB_2O_4 (2.088 Å),[239] HP-CoB_2O_4, (2.090 Å),[241] $BaAlBO_4$ (2.098 Å),[252] α-$Ba_3[B_{10}O_{17}(OH)_2]$ (2.169 Å),[247] HP-CsB_5O_8 (2.170 Å),[243] and HP-KB_3O_5 (2.210 Å).[242] These structural peculiarities, when taken together, confirm the existence of edge-sharing $[BO_4]$ tetrahedra in a newly determined structure.

2.5.3.2. Spectral Properties. It is possible to make a further confirmation of edge-sharing $[BO_4]$ tetrahedra according to the spectral properties when we have synthesized the polycrystalline samples of target compounds. Up to now, three primary measurement approaches, including infrared spectroscopy, Raman spectroscopy, and solid-state nuclear magnetic resonance (NMR) spectroscopy, have been performed for the experimental confirmation of edge sharing $[BO_4]$ tetrahedra. Generally, there are two observable and characteristic peaks that can be assigned to the modes of edge-sharing $[BO_4]$ tetrahedra in both infrared and Raman spectra. For example, the characteristic peaks at 1271 and 1435 cm^{-1} in $Dy_4B_6O_{15}$[131] (Raman-active), 1253 and 1431 cm^{-1} in α-$Gd_2B_4O_9$ (Raman-active),[238] 1262 and 1444 cm^{-1} in HP-NiB_2O_4 (Raman-active),[239] 1295 and 1438 cm^{-1} in $La_3B_6O_{13}(OH)$ (Raman-active),[246] 1287 and 1445 cm^{-1} in $Li_4Na_2CsB_7O_{14}$ (infrared-active),[251] as well as the 1253 and 1435 cm^{-1} in β-CsB_9O_{14} (infrared-active).[197] By contrast, solid-state NMR is rarely used to identify and characterize the local atomic level environments of borates with edge-sharing $[BO_4]$ tetrahedra. To the best of our knowledge, HT-

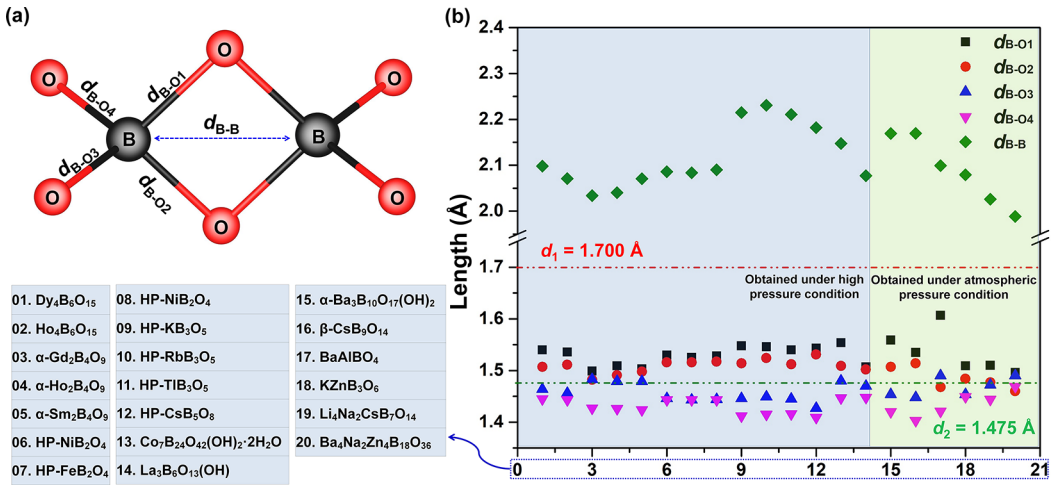

Figure 15. (a) Geometric configuration of edge-sharing $[BO_4]$ tetrahedra. d_{B-B} is the shortest interatomic distance of the two B atoms inside the $[B_2O_2]$ ring, d_{B-O1} and d_{B-O2} represent the B−O distances inside the $[B_2O_2]$ ring, d_{B-O3} and d_{B-O4} represent those outside the ring. (b) Comparison of the bond lengths and interatomic distances inside the edge-sharing $[BO_4]$ tetrahedra of currently representative borates. d_1 (1.700 Å) represents the ideal B···B interatomic distances of two undeformed edge-sharing $[BO_4]$ tetrahedra. d_2 (1.475 Å) represents the statically averaged B−O bond length in $[BO_4]$ tetrahedra.

https://dx.doi.org/10.1021/acs.chemrev.0c00796
Chem. Rev. 2021, 121, 1130−1202

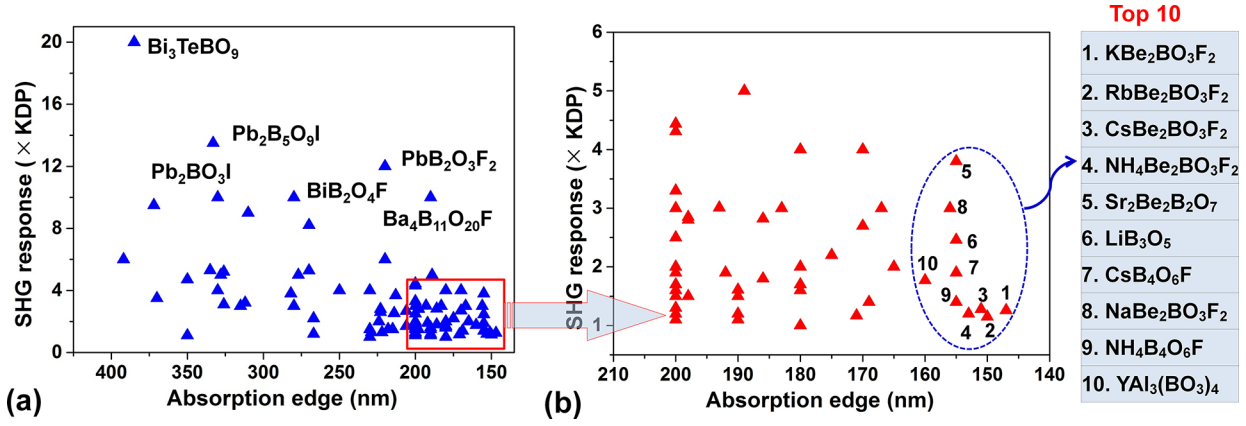

Figure 16. (a,b) Summary of the experimental SHG response and absorption edge of borate-based NLO crystals stored in ICSD. Only those with phase matching SHG response larger than KDP are included here, and when the experimentally effective NLO efficients are available for a crystal, the largest one is selected and the multiple relations are evaluated on the basis of d_{36} (KDP) = 0.39 pm/V.

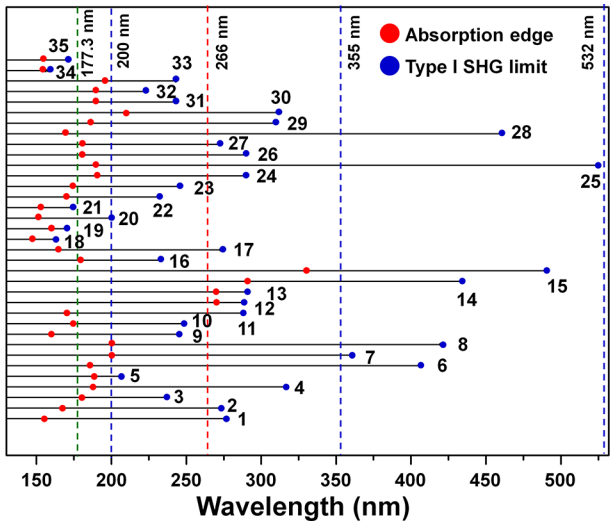

1	LiB_3O_5	18	$KBe_2BO_3F_2$
2	CsB_3O_5	19	$RbBe_2BO_3F_2$
3	$CsLiB_6O_{10}$	20	$CsBe_2BO_3F_2$
4	$LiRbB_4O_7$	21	$NH_4Be_2BO_3F_2$
5	β-BaB_2O_4	22	$NaSr_3Be_3B_3O_9F_4$
6	$NaBaB_9O_{15}$	23	$LiSr_3Be_3B_3O_9F_4$
7	$YCa_4O(BO_3)_3$	24	$Ca_5(BO_3)_3F$
8	$GdCa_4O(BO_3)_3$	25	$Ba_4B_{11}O_{20}F$
9	$YAl_3(BO_3)_4$	26	$K_3B_6O_{10}Br$
10	$GdAl_3(BO_3)_4$	27	$K_3B_6O_{10}Cl$
11	$La_2CaB_{10}O_{19}$	28	$Ca_2B_5O_9Cl$
12	$Na_3La_9O_3(BO_3)_8$	29	$Ba_3Mg_3(BO_3)_3F_3$
13	α-BiB_3O_6	30	$BaCaBO_3F$
14	δ-BiB_3O_6	31	$K_3Ba_3Li_2Al_4B_6O_{20}F$
15	$Bi_2ZnB_2O_7$	32	$K_3Sr_3Li_2Al_4B_6O_{20}F$
16	$BaAl_2B_2O_7$	33	$Rb_3Ba_3Li_2Al_4B_6O_{20}F$
17	$BaAlBO_3F_2$	34	$NH_4B_4O_6F$
		35	CsB_4O_6F

Selected crystals

Figure 17. Summary of absorption edge (a) and type **I** SHG limit (b) of borate-based NLO crystals stored in ICSD. Only those with estimation of type I SHG limit based on the experimentally obtained dispersion equations are included here. Note that where multiple results were available for the same crystals, the most reliable and correct result was selected. The crystals in red and blue are expected or have been used to generate 177.3 and 266 nm light by the sixth (λ = 1064/6 = 177.3 nm) or fourth (λ = 1064/4 = 266 nm) harmonic generation process with the incident lasers of 1064 nm, respectively. Note that a short cutoff edge does not always guarantee a short type **I** SHG limit.

KB_3O_5,[242] $KZnB_3O_6$,[242] and $La_3B_6O_{13}(OH)$[246] are the exclusive examples. The isotropic shifts of 2.4, 1.75, and 2.0 ppm can be assigned to the tetrahedral B atoms of edge-sharing [BO_4] units in HT-KB_3O_5, $KZnB_3O_6$, and $La_3B_6O_{13}(OH)$, respectively. Any of these spectral properties will help to make a further confirmation about the existence of edge-sharing [BO_4] tetrahedra in a new obtained structure.

3. BORATE-BASED NLO MATERIALS

In recent years, there has been continuous research and incremental improvements on the second-order NLO materials associated with laser-driven interference photolithography, precise micromachining, nano- and picosecond pulse generation, as well as laser detection.[253] At the first stage, radiation at the double frequency was first observed when the fundamental light passes through a quartz crystal using a ruby laser.[254] Since then, nonlinear optics have attracted much attention and rapidly become one of the especially important branches of modern optics. However, few natural crystals can cause NLO effects, in this context, new synthetic NLO materials both in organic and inorganic systems with optimized optical properties, continue to be of special interest for many chemists and material scientists. In principle, NLO effects[255] mean that one or two laser beams are directed into suitable materials in which an output beam of the desired frequency is generated, which includes the harmonic generation, sum frequency generation, difference frequency generation, and parametric oscillation. ***In this review, the NLO materials refer to frequency doubling crystals with the NLO effects of SHG, except where noted.*** To date, the most important class of single crystals used in nonlinear optics has been inorganic materials, as it is particularly well-suited to the physics of NLO process. After the discovery of the NLO effects in potassium pentaborate $KB_5O_8{\cdot}4H_2O$ by Dewey *et al.*,[21] the search for new NLO crystals has mainly focused on the borate system, especially suitable for being used in UV and deep-UV spectral regions. The large difference in the electronegativity of B and O is believed to be responsible for the high transmittance in the shorter wavelength region. The conjugated π orbital and high anisotropic distribution of electrons in the B−O/F FBBs

https://dx.doi.org/10.1021/acs.chemrev.0c00796
Chem. Rev. 2021, 121, 1130−1202

of borates is beneficial for a large second-order susceptibility and birefringence. Besides, borates have a wide spectral range of transparency combined with a high laser damage threshold as well as good chemical and mechanical stability. These superiorities make borates crucial materials for the generation of the second harmonic light, and thus borates can be regarded as a rich source of NLO materials, particularly in UV and deep-UV regions (Figures 16 and 17). Therefore, in this section, we will mainly focus on all of the available borate-based NLO crystals stored in ISCD. According to the chemical constituents of borates, this section is divided into nine categories to discuss, and we will start with the consideration of necessary requirements for a practical NLO crystal based on the available experimental and theoretical data revealed in the previous studies.[2,6,7,9,12,20,37,38,43−45,256,257]

3.1. Necessary Requirements for a Practical NLO Material

3.1.1. Crystal Symmetry. Crystallizing into the effective noncentrosymmetric space group is the prerequisite for crystals to be applied as NLO materials.[256] Among all the 21 noncentrosymmetric point groups, the second harmonic coefficients of the crystals that belong to the point groups of 422 and 622 with low dispersion are zero under the restriction of Kleinman symmetry. Also, owing to their isotropic nature, crystals in 23, 432, and $\bar{4}3m$ point groups are excluded because they are all non-phase matchable (see section 3.1.4). Thus, materials that may exhibit practical NLO properties must crystallize in one of the following 16 noncentrosymmetric crystal classes: C_1-1, C_s-*m*, C_2-2, D_2-222, C_{2v}-*mm*2, C_4-4, S-$\bar{4}$, C_{4v}-4*mm*, D_{2d}-$\bar{4}2m$, C_3-3, D_3-32, C_{3v}-3*m*, C_6-6, C_{3h}-$\bar{6}$, C_{3h}-$\bar{6}2m$, and C_{6v}-6*mm*. Studies have shown that the second-order NLO coefficients of crystalline materials are closely related to their structures rather than any particular space group. That is to say, as long as one crystal belongs to one of the above 16 point groups, considerable NLO coefficients can be observed when their basic blocks are in NLO-favorable arrangement. Technically, those NLO crystals that belong to the uniaxial space group (hexagonal, tetragonal, and trigonal) are more favorable when making property characterization and practical application than those in biaxial class (orthorhombic, monoclinic, and triclinic).

3.1.2. Effective Second-order NLO Coefficients. The light−light frequency conversion efficiency is proportional to the square of effective second-order NLO coefficient (d_{eff}), thus NLO materials should exhibit large NLO coefficients in order to have high efficiency in frequency doubling conversion. With respect to those NLO materials that are used in different wavelength from UV and deep-UV, visible light, to infrared spectral region, the corresponding d_{eff} coefficients need to be larger than that of KH_2PO_4 (KDP, 0.39 pm/V), $KTiOPO_4$ (4.3 pm/V), and $AgGaS_2$ (13.4 pm/V), respectively. In principle, the d_{eff} coefficient can be derived once the individual NLO coefficients (d_{ij}) are experimentally obtained for a crystal. Individual d_{ij} coefficients can be measured by both Maker Fringe technique and phase matching method by using indexed and polished single-crystal plates. It should be noted that the largest d_{ij} coefficients are meaningless if they are not included in the formula of d_{eff} coefficients.[6,7,9] When sizable single crystals are not available to test the d_{ij} and d_{eff} coefficients, the powder SHG measurements with the Kurtz and Perry[258] method are usually taken to initially evaluate the NLO properties.

3.1.3. Transparency Range. Different types of materials are capable of producing the coherent light from deep-UV to far-infrared spectral ranges. Thus, the NLO crystals should have high transparency under both fundamental and doubling frequency light. For example, the transparency ranges of deep-UV NLO materials are always required to blue-shift to less than 200 nm and also retain high transparency in UV region at the same time. In the case of infrared NLO materials, the infrared absorption edges should exceed 10 μm. Generally, the transparency ranges determined by spectral properties are controllable and predictable by analyzing the chemical bonding behavior and chemical constituents of NLO materials. For example, alkali, alkaline-earth, and partial rare-earth metals without *d*−*d* or *f*−*f* electronic transitions are beneficial for good transparency in the UV and deep-UV region; NLO crystals without terminal dangling bonds of O atoms are more blue-shifted than those with the dangling bonds; the chemical constituents of infrared NLO materials are free of oxygen to aviod the characteristic absorbing of M−O (M = Metal) vibrations in the infrared spectral region. As shown in Figure 17, a short absorption edge does not guarantee a short SHG limit.

3.1.4. Birefringence. One of the most important features for a practical NLO material is the phase matching behavior, which is mainly determined by the birefringence with the possible contributions from atomic dispersion and symmetry of structures.[257] Thus, a moderate birefringence is required for phase matching, an optical direction in the material where the refractive indices are equal, *i.e.*, $n(\omega) = n(2\omega)$. When the birefringence of NLO materials is too small or too large, the non-phase matching behavior and walk-off effects will occur. For UV and deep-UV NLO materials, birefringence of Δn = 0.05−0.10 at 1064 nm is suitable to ensure phase matching and retain small walk-off angles. As shown in Figure 17, owing to the small birefringence, vew few borate crystals can achieve the phase matching in UV region below 266 nm. Therefore, birefringence, as the shortest plank, severely restricts the SHG phase matching of borates in the UV and deep-UV region. Exactly how the birefringence impacts the phase matching behavior of NLO materials is discussed by Halasyamani *et al.*[257]

3.1.5. Crystal Growth Habit and Optical Quality. Growing large size single crystals with high quality and homogeneity is extremely important and it is also the most paramount and hardest challenge. Thus, easy growth of sizeable bulk single crystals with high optical quality and favorable growth habit is required, particularly no strong layering tendency. The optical quality of a crystal can be identified by conoscopic interference and X-ray diffraction patterns. The full-width at half maximum on crystal plate should not exceed 100 arc-seconds; of course, less is better. Technically, those congruently melting NLO crystals are easy to grow from their stoichiometric ratios by the Czochralski method, Bridgman method, and Kyropoulos growth method, *etc.*

3.1.6. Laser Damage Threshold and Stability. NLO materials experience long exposure to laser light, thus the ability to resist to laser damage is required. Studies have shown that the laser damage thresholds of NLO crystals are closely related to their bandgaps and optical homogeneity. A crystal with larger bandgaps and high optical quality is beneficial to achieve sufficiently high laser damage thresholds. For high-power NLO applications in UV and deep-UV region, a high

https://dx.doi.org/10.1021/acs.chemrev.0c00796
Chem. Rev. 2021, 121, 1130−1202

laser damage threshold of 5 GW/cm^2 with a nanosecond pulse at 1064 nm is required, and of course, higher is better. More importantly, NLO crystals should be chemically and physically stable before, during, and after operation in a laser system, and also the mechanical and thermal stability are important factors to be included. These require that NLO materials should be hard to crack, not decompose, or deliquesce during operation.

3.2. Alkali Metal and Alkaline-earth Metal Borates

3.2.1. Alkali Metal Borates. *3.2.1.1. LiB_3O_5.* LiB_3O_5 is one of the most well investigated NLO materials and is commercially available. The crystal structure of LiB_3O_5 was determined by Konig *et al.* in 1978, with the space group of $Pna2_1$ (no. 33).[259] It shows that a 3D $^3[B_3O_5]_\infty$ anionic framework consists of $[B_3O_7]$ FBBs, which contains ten-membered ring tunnels running along the *c* axis that are occupied by Li^+ ions (Figures 18a,b). The potential application

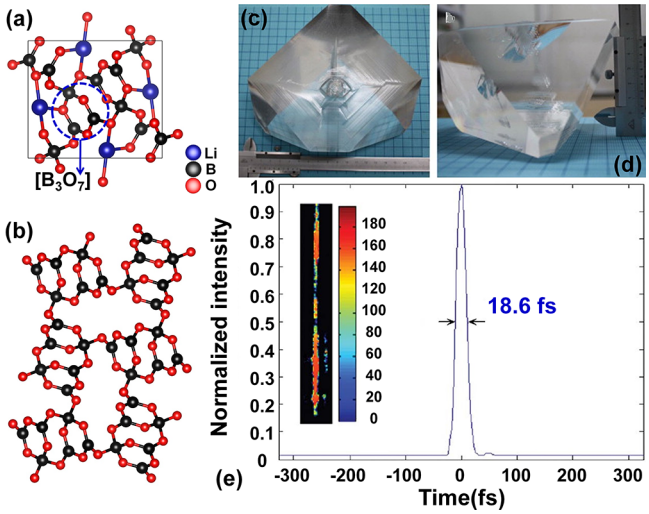

Figure 18. (a,b) Crystal structure of LiB_3O_5. Top (c) and side (d) view of the as-grown LiB_3O_5 crystal at 2 kg-level in $Li_2O-B_2O_3-MoO_3$ ternary system with the dimensions up to 160 × 150 × 77 mm^3. Reproduced with permission from ref 267. Copyright 2011 Elsevier. (e) Pulse shape of the output laser measured by an autocorrelator with the pulse width of 18.6 fs after Gaussian profile fitting based on the all OPCPA technique with LiB_3O_5 crystal. Reproduced with permission from ref 269. Copyright 2017 Optical Society. Parts a and b were drawn by using the crystallographic information file of LiB_3O_5 (ICSD: 1585) in ICSD.

of LiB_3O_5 used as an NLO crystal was first found and demonstrated by Chen *et al.* in 1989[23] with the guidance of anionic group theory. In their works, sizable LiB_3O_5 crystals with dimensions up to 30 × 30 × 15 mm^3 have been grown by high-temperature solution top-seeding method. The high-quality crystals allow them to obtain the basic linear and NLO properties based on the indexed and polished LiB_3O_5 crystal plates. LiB_3O_5 exhibits a relatively large angular acceptance bandwidth which permits effective frequency doubling of multimode laser radiation.[23] On the other hand, LiB_3O_5 crystal possesses the highest optical damage threshold amongst known NLO crystals and stronger nonlinearity than KDP. Stated thus, it should be noted that LiB_3O_5 crystal is a very useful NLO material, especially for SHG of high-intensity laser radiation, intracavity SHG, deep-UV sum-frequency generation (SFG), and OPO applications. In the same year, the NLO characteristics of LiB_3O_5 crystals were investigated by Chen *et al.* in great detail. The independent NLO coefficients are measured to be d_{31} = ±2.51 (1 ± 0.09) × d_{36}(KDP), d_{32} = ±2.69 (1 ± 0.12) × d_{36} (KDP), d_{33} = ±0.15 (1 ± 0.10) × d_{36} (KDP) according to type **I** Maker fringes with maximum envelope functions at normal incidence, which can get better results than that of type **II** Maker fringes with vanishing envelope functions.[260] The broad temperature-tuned noncritical phase matching ability of LiB_3O_5 crystals are demonstrated, with the tuning range from 273 to −9 °C for temperature and 0.95 to 1.34 μm for wavelength, respectively.

With respect to crystal growth, LiB_3O_5 crystal melts incongruently and can be grown by the flux method under the deviated stoichiometric ratio. In the early research of 1990s, B_2O_3 is the most commonly used self-flux, and thus centimeter crystals can be grown by optimizing the crystal growth parameters, including the ratio for LiB_3O_5/flux, rotation, pulling and cooling rate, temperature distribution, as well as selected seed direction.[261−263] Unfortunately, the high viscosity of flux system often leads to a low growth rate, entrapment of the solution, and the inclusion of unknown phases, and therefore, the as-grown LiB_3O_5 crystals are extremely limited in size and optical quality. The growth of LiB_3O_5 crystals in molybdenum oxide fluxes has brought considerable progress in LiB_3O_5 growth technology. It has been demonstrated that the addition of MoO_3 to the flux system largely decreases the viscosity of $LiB_3O_5-B_2O_3$ high temperature solution and therefore enables the growth of optically perfect LiB_3O_5 crystals with much larger size.[264,265] With these fluxes, high-quality crystals were grown from crucibles of 80−100 mm in diameter by the Kyropoulos method with the weight less than 300 g.

In 2010, Kokh *et al.* proved that the Kyropoulos method can substantially improve the as-grown LiB_3O_5 crystals in size and optical quality by controlling the heat field symmetry and its rotation. On the basis of this, a large LiB_3O_5 single crystal with the dimensions of 148 × 130 × 89 mm^3 has been grown and its weight reached 1379 g.[266] Frequency doubler was cut based on the above as-grown LiB_3O_5 crystal for either or both types **I** and **II** phase matching directions. Efficiencies over 90% were obtained using a 53 mm collimated top-hat beam in a LiB_3O_5 crystal (φ 65 mm × 12 mm) with an average intensity of 900 MW/cm^2. High-energy NLO experiments based on this sample show the ability to produce 115 J of green light (λ = 527 nm) with the high efficiency of 85%.[266] Further analysis of the viscosity in the $Li_2O-B_2O_3-MoO_3$ system by Hu *et al.* enabled the growth of LiB_3O_5 crystal with the dimensions up to 160 × 150 × 77 mm^3 (Figures 18c,d), and its weight was close to 2000 g.[267] The as-grown LiB_3O_5 crystals with very large size of high quality manufactured samples are proven to be optically perfect with high optical homogeneity (3.8 × 10^6 cm^{-1}), high transmittance (over 90%) from the wavelength region of 200 to 380 nm, and a sufficiently high laser damage threshold (11.2 GW/cm^2 under 1064 nm and 7.5 ns).

The breakthrough of crystal growth on wide-aperture crystals enables the application of LiB_3O_5 crystals in ultrafast laser systems. The gain bandwidth of LiB_3O_5 crystal is broader than 70 nm, approximately 800 nm in wavelength, allowing the amplification of large bandwidth stretched pulses recompressible to the sub 20 fs pulse duration. In the last year, LiB_3O_5 crystals with clear apertures of more than 100 mm in diameter were grown. Under these conditions, Xu *et al.* constructed a high-energy and high-conversion-efficiency broadband parametric chirped-pulse amplification (OCPCA) laser system by

https://dx.doi.org/10.1021/acs.chemrev.0c00796
Chem. Rev. 2021, 121, 1130−1202

using a manufactured wide-aperture (100 × 100 × 17 mm^3) LiB_3O_5 crystal in 2015.[268] Within this system, an amplified energy of 45.3 J was achieved with the efficiency of 26.3% and the peak power was as high as 1.02 PW with a compressed duration of 32 fs, which is the first reported OCPCA peak power higher than 1 PW.[268] Furthermore, the large bandwidth stretched laser pulses at 800 nm, 3 ns pulse duration, was successfully amplified up to 168.7 J, 105 mm × 105 mm beam size, 65 nm spectral bandwidth,[269] in an OPCPA laser system based on two type **I** phase matching wide-aperture LiB_3O_5 crystals with the dimensions of 165 × 120 × 10 mm^3 and 130 × 130 × 10 mm^3, respectively. A compressed pulse shorter than 20 fs is achieved in a PW-class laser facility for the first time (Figure 18e). The maximum output peak power of the all OPCPA system is 4.9 PW, and in principle the output power can be furthered increased with the increase of the effective diameter of wide-aperture LiB_3O_5 crystals.[269] In 2015, Naftaly *et al.* expanded the application wavelength of LiB_3O_5 crystals to terahertz range.[270] Dispersion equations for the entire transparency range of LiB_3O_5 crystals were developed for the first time, and the birefringence of Δn = 0.42 under measured terahertz region was measured in LiB_3O_5 crystals at the same time. The estimation of phase matching for terahertz down-conversion was done based on the established dispersion equations, which makes LiB_3O_5 crystal one of the most promising crystals for terahertz generation by down-conversion from near-infrared.[270]

3.2.1.2. CsB_3O_5. Both lattice parameters and single crystal structure of CsB_3O_5 were determined by Krogh-Moe *et al.* in 1958 and 1974, respectively.[196,271] CsB_3O_5 crystallizes in the space group of $P2_12_12_1$ (no. 19), and it shows a 3D $^3[B_3O_5]_\infty$ anionic framework that is composed of $[B_3O_7]$ FBBs with Cs^+ ions located in the ten-membered ring tunnels. The NLO capabilities of CsB_3O_5 were confirmed first by Chen *et al.* in 1989,[23] and they theoretically analyzed the NLO coefficients of CsB_3O_5 together with LiB_3O_5 crystals. In 1993, also by Chen *et al.*, large size CsB_3O_5 crystals have been grown and subjected to linear and NLO properties characterization in great detail.[24] The CsB_3O_5 crystal is transparent far into the deep-UV region (167−3400 nm) and can be phase matchable for both type **I** and type **II** SHG or third harmonic generation (THG) of 1064 nm. The large effective NLO coefficient for type **II** THG of 1064 nm and laser damage threshold under 10 ns pulses at 1053 nm are found to be d_{eff} = 1.15 pm/V and 26 GW/cm^2, respectively, which can be comparable to those of LiB_3O_5 crystals.

The CsB_3O_5 crystals melt congruently, and as such bulk large size single crystals were obtained from stoichiometric melts with Czochralski and Kyropoulos techniques by many groups.[272,273] Further studies have shown that slight enrichment of Cs_2O flux melt can make improvement of as-grown crystal in optical quality and size. The UV light of 355 nm was generated by using a type **II** 8 mm long CsB_3O_5 crystal as a sum frequency of 1064 and 532 nm light.[274] The output power of 3.0 W was obtained at a repetition rate of 31 kHz and the conversion efficiency of this process reached 30%, which was 1.5 times higher than that obtained with a type **II** LiB_3O_5 crystal under the same laser system.[274] In 2016, a higher 355 nm laser was produced by THG process of an acousto-optic Q-switched quasicontinuous wave of 1064 nm laser in CsB_3O_5 crystal by Xu *et al.*[275] The 28.3 W UV laser has been achieved by a 30 mm long type **II** CsB_3O_5 crystal through the sum frequency of fundamental light (1064 nm) and second harmonic (532 nm) of a nanosecond Nd:YVO_4 laser. The conversion efficiency from the fundamental light to the third harmonic laser reaches 13.5%, which is even higher than that obtained with a type **II** LiB_3O_5 crystal under the same experimental conditions.[275] It should be noted that the temperature bandwidth is much broader than that of LiB_3O_5 crystals. Thus, CsB_3O_5 is superior to LiB_3O_5 in the sense of conversion efficiency and temperature sensitivity for THG of 355 nm laser. Unfortunately, CsB_3O_5 crystal is hygroscopic at room temperature and in an air atmosphere, which extremely limits its further applications.

3.2.1.3. α-RbB_3O_5 and TlB_3O_5. RbB_3O_5 polymorphism was studied for a long time and low temperature modification of α-RbB_3O_5 refined by the Rietveld method was found to be isostructural to CsB_3O_5 with the space group of $P2_12_12_1$ (no. 19).[276] The anionic framework of α-RbB_3O_5 is constructed by three-membered $[B_3O_7]$ rings, which are further linked to form infinite channels with the Rb-based polyhedra filling the channels. Whereas TlB_3O_5[277] is also isostructural to CsB_3O_5 and α-RbB_3O_5 with the slight differences in the oxygen coordination of Rb, Cs, and Tl atoms because of the size effects of the A-site (A = Rb, Cs, and Tl) cations. Although the experimental NLO properties of α-RbB_3O_5 and TlB_3O_5 are not known, according to the anionic group theory[20] and analysis of structure−property relationship, equally or comparable excellent NLO performance of α-RbB_3O_5 and TlB_3O_5 can be expected once the sizable crystals are grown.

3.2.1.4. $CsLiB_6O_{10}$ and β-$CsLiB_6O_{10}$. $CsLiB_6O_{10}$ is one of the most well investigated NLO materials and is commercially available. It was determined first by Mori *et al.* in 1995 and then immediately shown to be a very promising NLO material.[25] $CsLiB_6O_{10}$ is a negative uniaxial crystal and belongs to a tetragonal space group $I\bar{4}2d$ (no. 122), which is different from the biaxial LiB_3O_5 ($Pna2_1$) and CsB_3O_5 ($P2_12_12_1$) crystals. The molecular formula of $CsLiB_6O_{10}$ can be regarded as the combination of LiB_3O_5 and CsB_3O_5, and its anionic configuration is similar to them and can be derived from the full condensation of the simple three-membered $[B_3O_7]$ rings by sharing vertices. Sites in channels extending along the *a* and *c* axes are occupied by the $[CsO_8]$ and $[LiO_4]$ polyhedra.

$CsLiB_6O_{10}$ crystals melt congruently, and as such bulk large size single crystals can be obtained by either stoichiometric melt or from solution. In the same year of 1995, a large and high quality $CsLiB_6O_{10}$ single crystal with the dimensions of 140 × 110 × 110 mm^3 was grown within three weeks by the top-seeded Kyropoulos method by Mori *et al.*[25] The transmission range of $CsLiB_6O_{10}$ single crystals was determined to be 180−2750 nm, which makes $CsLiB_6O_{10}$ a relatively high bulk laser-induced damage threshold of 26 GW/cm^2 at 1064 nm with a 1.1 ns pulse width. Fourth harmonic and fifth harmonic generations of 1064 nm Nd:$Y_3Al_5O_{12}$ (Nd:YAG) laser radiation with type **I** phase matching were realized in 1995 by Mori *et al.*[25] The Sellmeier equations of $CsLiB_6O_{10}$ crystals were reported and revised, then based on type **I** and **II** phase matching conditions, the shortest type **I** and **II** phase matching wavelengths were shown to be 236.5 and 318 nm, respectively. The blue-shifted phase matching wavelengths of $CsLiB_6O_{10}$ compared with those of LiB_3O_5 and CsB_3O_5 crystals are due to the enlarged birefringence (Δn = 0.050@1064 nm). The NLO coefficients of $CsLiB_6O_{10}$ crystal have been determined and updated for visible-to-ultraviolet second-harmonic wavelengths in 2001 by Shoji *et al.*[278] The d_{36} coefficients of $CsLiB_6O_{10}$ crystal are found to be 0.92, 0.83,

https://dx.doi.org/10.1021/acs.chemrev.0c00796
Chem. Rev. 2021, 121, 1130−1202

and 0.74 pm/V under 532, 852, and 1064 nm, respectively. Thus, the corresponding effective NLO coefficients are determined to be 0.82, 0.48, and 0.38 pm/V under 532, 852, and 1064 nm, respectively.

Owing to these superior properties, $CsLiB_6O_{10}$ crystal is considered as a highly promising NLO crystal, and thus more attention has been paid to the generation of short wavelength UV radiation. For example, high pulse energies of nanosecond-level fourth- and fifth-harmonic generation of an Nd:YAG laser have been obtained with a $CsLiB_6O_{10}$ crystal by Sasaki *et al.* in 1996.[279] Thus, stable 266 and 213 nm lasers with the high pulse energies of 500 and 230 mJ have been realized. The corresponding conversion efficiencies of the initial fundamental input energy reach 50 and 10.4%, respectively.[279] In 2000, Sakuma *et al.* proved that $CsLiB_6O_{10}$ crystals can be used to generate the high power, narrow-bandwidth, deep-UV radiation below 200 nm as well as around 242 nm by sum-frequency mixing method. They obtained the UV radiation of greater than 3 W at 241.6 nm, which was subsequently mixed with the residual 1047 nm light to produce the deep-UV radiation of 1.5 W at 196.3 nm.[280] Turčičová *et al.* used $CsLiB_6O_{10}$ crystals to generate deep-UV light with the pulses shorter than 10 ps for the first time, and they obtained a 6 W laser at 257.5 nm by fourth harmonic generation (FHG) with high conversion efficiency of 10%. Owing to the smaller walk-off effects of $CsLiB_6O_{10}$ crystals, the deep-UV laser beam quality is effectively improved (Figure 19a).[281] In 2015, Sakuma *et al.* reported a deep-UV laser output at 193.4 nm with an estimated line width less than 200 kHz by using $CsLiB_6O_{10}$ crystals.[282] The source is based on the frequency conversion of three single-mode and single-frequency fiber amplifiers. The generated maximum output power is about 120 mW, which is the highest solid-state continuous-wave 193 nm laser to date. In addition, they demonstrated that the SHG → FHG conversion in the $CsLiB_6O_{10}$ crystal is even higher than that in the β-BaB_2O_4 crystal with closely spaced FHG spectral bandwidths of 0.22 and 0.20 nm for two crystals, respectively (Figures 19b,c).

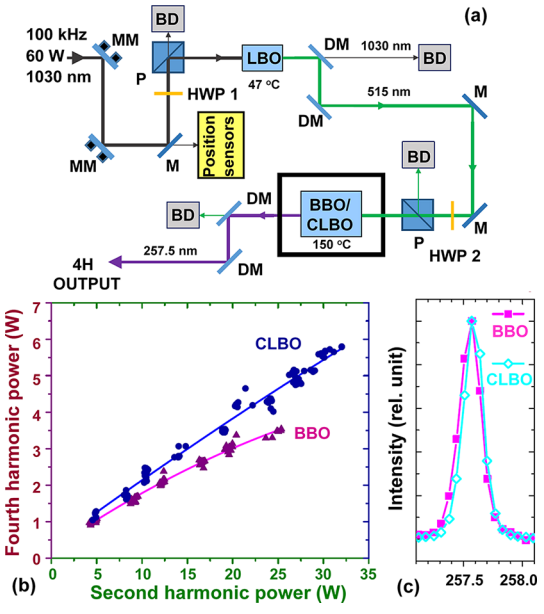

Figure 19. (a) Optical scheme of the SHG and FHG setup, in which the MM, M, BD, DM, HWP, and P refer motorized mirror, mirror, beam dump, dichroic mirror, half-wave plate, and polarizer, respectively. (b) FHG output power dependence on the SHG in β-BaB_2O_4 (BBO, coated) and $CsLiB_6O_{10}$ (CLBO, without coated) crystals. The input pulse energy tuning was done by the first half-wave plate, **HWP 1**. (c) Relevant FHG spectra for β-BaB_2O_4 and $CsLiB_6O_{10}$. Reproduced with permission from ref 281. Copyright 2016 Optical Society.

In addition, the high average output power of 40 W at the wavelength of 266 nm was obtained by Sasaki *et al.* by using $CsLiB_6O_{10}$ crystals in high-power Nd:YAG laser at 1064 nm through SHG process.[283] Yoshimura *et al.* generated 355 nm UV laser in $CsLiB_6O_{10}$ crystal by the sum frequency process, and the maximum output power of 30.9 W has been achieved from the fundamental source of 64 W at a repetition rate of 300 kHz.[284] The remarkable conversion efficiency of 48.3% could be reached, which is about 1.2 times higher than that using LiB_3O_5 crystal. Interestingly, a reversible and partial transition to a new modification, β-$CsLiB_6O_{10}$, was observed during cooling crystalline and moist samples of $CsLiB_6O_{10}$ to −25 °C. The new phase β-$CsLiB_6O_{10}$ belongs to the orthorhombic $P222_1$ (no. 17),[285] in which four nonequivalent triborate rings $[B_3O_7]$ constitute the B−O framework with Li- and Cs-based polyhedra located in positions similar to those in $CsLiB_6O_{10}$ crystal.

3.2.1.5. γ-$LiBO_2$ and $TlBO_2$. In the early work at Bell Telephone Laboratories, M. Marezio and J. P. Remeika discovered that the centrosymmetric α-$LiBO_2$ can be converted to the noncentrosymmetric phase of γ-$LiBO_2$ in pressure of 15 kbar at 950 °C with a flux of LiCl. γ-$LiBO_2$ is a negative uniaxial crystal and belongs to a tetragonal space group of $I\bar{4}2d$ (no. 122).[84] The structure of γ-$LiBO_2$ consists of an infinite 3D framework of tetrahedral $[BO_4]$ and $[LiO_4]$ units, and the stacking of these tetrahedra is the same as one of the zinc-blende structure. In 2008, the convenient hydrothermal synthesis and growth of sizable γ-$LiBO_2$ single crystals at a moderate temperature and pressure were achieved by Kolis *et al.*[286] By using the as-grown and polished γ-$LiBO_2$ crystals, the UV transparency measurement was performed. The γ-$LiBO_2$ crystal exhibits high transmittance for all the measured wavelengths with an extremely short cutoff edge of 135 nm, corresponding to a large bandgap over 9.19 eV.[286] Such a short absorption is shorter than those of almost all the borate-based optical materials. The SHG efficiency for 1064 nm radiation is approximately 250 times that of a quartz standard with non-phase matching behavior. This is not surprising for γ-$LiBO_2$ because borates that contain only $[BO_4]$ tetrahedra generally have a birefringence that is too small to ensure the phase matching behavior. In the case of $TlBO_2$ with the non-centrosymmetric space group $P4_1$ (no. 76, ICSD: 36404), experimentally optical and NLO properties are still missing.

3.2.1.6. $AA'B_4O_7$ (A = Li, Na; A′ = Li, Na, K, Rb). All the mixed-alkali metal borates with the similar formula of $AA'B_4O_7$ (A = Li, Na; A′= Li, Na, K, Rb), including $Li_2B_4O_7$, $Na_2B_4O_7$, $LiKB_4O_7$, $LiRbB_4O_7$, and $LiNaB_4O_7$ adopt the noncentrosymmetric space groups but exhibit different structural features which are fine-tuned by A-site cations. The lithium tetraborate $Li_2B_4O_7$ with the space group of $I4_1cd$ (no. 110) is the first member of this series reported by Krogh-Moe *et al.* in 1962.[233] The structure of $Li_2B_4O_7$ is formed by two interpenetrating, infinite, and separated 3D $^3[B_4O_7]_\infty$ subframeworks with ten-membered ring tunnels running along the *c* axis that are occupied by Li^+ ions. The FBB of $Li_2B_4O_7$ is a twisted $[B_4O_9]$ double ring consisting of two triangular $[BO_3]$ and two tetrahedral $[BO_4]$ units. $Li_2B_4O_7$ crystal is proved to be a

https://dx.doi.org/10.1021/acs.chemrev.0c00796
Chem. Rev. 2021, 121, 1130−1202

promising NLO material for frequency conversion including the fourth- and fifth-harmonic generation of the Nd:YAG laser. Large $Li_2B_4O_7$ crystals with diameter of 2.0−2.5 inches were successfully grown by the Czochralski method by Komatsu *et al.* in 1997.[287] $Li_2B_4O_7$ crystals were optically transparent to 170 nm, which can be comparable to those of other lithium borates. The $Li_2B_4O_7$ crystal is uniaxial and optically negative, and the shortest SHG wavelength was found to be 243.8 nm for the phase matching angle (90°). On the basis of this, the fourth- and fifth-harmonic generations were obtained successfully with the output power of 160 and 70 mJ, respectively. The laser damage threshold of $Li_2B_4O_7$ crystals was 40 GW/cm^2 under the radiation of Nd:YAG laser (1.5 J, 10 Hz, 10 ns), even higher than those of any other borate-based NLO materials. Unfortunately, $Li_2B_4O_7$ crystals suffer from low NLO output responses and the effective NLO coefficient d_{eff} is only 0.16 pm/V at 532 nm, which is much lower than those of other borate-based NLO materials and thus limits its application.[288]

In 2000, Komatsu *et al.* reported two new isostructural members of this series, $LiKB_4O_7$ and $LiRbB_4O_7$, with the space group of $P2_12_12_1$ (no. 19).[109] Both crystals exhibit totally different structural features compared to $Li_2B_4O_7$. Both $LiKB_4O_7$ and $LiRbB_4O_7$ possess similar 3D $^3[B_8O_{14}]_\infty$ frameworks with alkali metal cations in the channels or intervals formed by condensing of $[B_3O_8]$ and $[B_5O_{10}]$ units. The three-membered $[B_3O_8]$ rings construct the infinite spiral chains parallel to the *a* axis and are interconnected by sharing O atoms with $[B_5O_{10}]$ units to form final 3D anionic framework. Optical measurements show that the as-grown $LiRbB_4O_7$ crystal exhibits an absorption edge of 187 nm, a birefringence of 0.03 is across the visible region, the shortest type **I** SHG wavelength of 317 nm, and an NLO coefficient d_{14} of 0.45 pm/V.[289] In the case of $LiKB_4O_7$, it shows comparable or superior properties compared with isostructural $LiRbB_4O_7$.[290] Experimentally, the SHG radiation of Nd:YAG continuous laser power of 8 W has been observed on a manufactured $LiKB_4O_7$ crystal with an aperture and thickness of 4 mm.[290] Another new member of this series, $LiNaB_4O_7$ with the space group of *Fdd*2 (no. 43), was obtained first by Mączka in 2007,[291] which exhibits similar structure and optical properties compared with $Li_2B_4O_7$, although they are not isostructural. For example, $LiNaB_4O_7$ shows an interpenetrating $^3[B_4O_7]_\infty$ framework composed of $[B_4O_9]$ FBBs, an optical absorption edge lower than 180 nm, and a relatively low SHG signal of 0.15 × KDP@1064 nm.[291] The new polymorph of sodium tetraborate HP-$Na_2B_4O_7$ was obtained under high-pressure/high-temperature conditions by Huppertz *et al.* in 2012.[292] It crystallizes in the trigonal chiral space group of $P3_221$ (no. 154), and its 3D anionic framework was constructed by the interconnected "sechser" rings of alternating corner-sharing $[BO_3]$ and $[BO_4]$ groups. The channels along the *c* axis in anionic framework are occupied by sodium ions. There is no further work, however, that concerns its NLO properties to date.

3.2.1.7. $Li_xA_{x-1}B_{2x-1}O_{4x-2}$ (A = Cs, Rb, x = 3, 4, 6). Six noncentrosymmetric mixed-alkali metal borates, including $Li_5Rb_2B_7O_{14}$,[165] $Li_5Cs_2B_7O_{14}$,[166] $Li_4Rb_3B_7O_{14}$,[293] $Li_4Cs_3B_7O_{14}$,[102] $Li_6Rb_5B_{11}O_{22}$,[118] and $Li_3Cs_2B_5O_{10}$,[294] were continuously discovered by Pan *et al.* from 2011 to 2015, which can be reduced to a general formula of $Li_xA_{x-1}B_{2x-1}O_{4x-2}$ (A = Cs, Rb, *x* = 3, 4, 6). The varied structural characteristics are tuned by the A-site cations, and the dimensionality of B−O anionic framework changes from 1D in the first two compounds to 0D in the other four structures. Among them, $Li_5Rb_2B_7O_{14}$ and $Li_5Cs_2B_7O_{14}$ are isostructural and belong to the orthorhombic *Ama*2 (no. 40).[165,166] Both of them feature 1D anionic frameworks that are composed of two different 1D infinite chains of $^1[BO_2]_\infty$ and $^1[B_5O_{11}]_\infty$ along the *c* axis, which are sequestered by Li and Rb/Cs atoms. In the case of $Li_4Rb_3B_7O_{14}$ and $Li_4Cs_3B_7O_{14}$,[102,293] they crystallize in the trigonal space group of $P3_121$ (no. 152) with 0D isolated $[B_7O_{14}]$ FBBs. Whereas $Li_6Rb_5B_{11}O_{22}$ crystallizes in the monoclinic space group *C*2 (no. 5) with a 0D highly polymerized $[B_{11}O_{22}]$ FBB that is constructed by five continuously linked three-membered rings.[118] Similarly, the structure of $Li_3Cs_2B_5O_{10}$ is also built by 0D $[B_5O_{10}]$ FBBs, but differently, it crystallizes in the orthorhombic $C222_1$ (no. 20) compared to the above borates.[294] In terms of optical performance, the absorption edges of above compounds are all reported to be below 200 nm, but more exact values were not given owing to the lack of optically perfect single crystals for the transmittance test. All of them exhibit exceedingly small macroscopic SHG coefficients, which are much less than KDP under 1064 nm. That is because the unfavorable arrangements of the $[BO_3]$ and $[BO_4]$ NLO active units in their FBBs and structures weaken their SHG effect. To further identify the spatial distribution of the electronic states dominating the SHG responses, the SHG density method was utilized by Pan *et al.* for this family. The results reveal that the "charge-transfer excitation" from the non-bonding 2*p* occupied states of O atoms to the *p** and 2*p* unoccupied states of $[BO_3]$ substructures in their FBBs is the key mechanism of NLO properties of this series.[293]

3.2.1.8. $Na_8AB_{21}O_{36}$ (A = Rb, Cs), α-CsB_9O_{14}, and K_2LiBO_3. Owing to their congruently melting features, two boron-rich mixed-alkali metal borates, namely, $Na_8RbB_{21}O_{36}$ and $Na_8CsB_{21}O_{36}$, have been synthesized from their stoichiometric melts by Pan *et al.* in 2017.[126] They are isostructural and belong to the same asymmetric space group of $I\bar{4}$(no. 82). Their FBBs are found to be the unprecedented $[B_{21}O_{36}]$ units, co-templated by four-connected $[BO_4]$ and five-connected $[B_5O_{11}]$ units. The terminal O atoms of $[B_{21}O_{36}]$ FBBs act as linkers to yield the 3D B−O anionic framework with two types of channels running along the *c* axis, which are filled with the Rb/Cs and Na atoms. Although they are all UV transparent with short deep-UV absorption edges about 200 nm, their SHG intensities are only about 1/10 that of KDP. Obviously, the $[BO_3]$ NLO-active units in $Na_8AB_{21}O_{36}$ (A = Rb, Cs) adopt the opposite orientations and lead to the weakened SHG responses, which is quite low for NLO application. Furthermore, although α-CsB_9O_{14} and K_2LiBO_3 are reported to crystallize in the noncentrosymmetric space group of $P222_1$ (no. 17) and *C*2 (no. 5) with interpenetrating 3D $^3[B_9O_{14}]_\infty$ frameworks and 0D $[BO_3]$ units, respectively, the linear and NLO properties are not reported.[234,295] However, the calculated SHG coefficients of K_2LiBO_3 are given by Li *et al.*[296] Thus, it remains to be seen if the above two compounds can be used for NLO applications.

3.2.2. Alkaline-earth Metal Borates. *3.2.2.1. β-BaB_2O_4.* β-BaB_2O_4 is one of the most well investigated NLO materials and is commercially available. The crystal structure of low temperature phase β-BaB_2O_4 was reported by Liebertz *et al.* in 1983.[297] During the crystallization of BaB_2O_4 melts, two phases appear, namely α- and β-BaB_2O_4. The melting point of BaB_2O_4 is 1095 ± 5 °C and α−β phase transition occurs at 925 ± 5 °C.[22] The high (α-BaB_2O_4)[28] and low (β-BaB_2O_4)[22]

https://dx.doi.org/10.1021/acs.chemrev.0c00796
Chem. Rev. 2021, 121, 1130−1202

temperature phase crystallize in centrosymmetric $R\bar{3}c$ (no. 167) and noncentrosymmetric $R3c$ (no. 161), respectively. Both phases exhibit 0D isolated $[B_3O_6]$ FBBs that are separated by the Ba-based polyhedra (Figure 20a,b). The

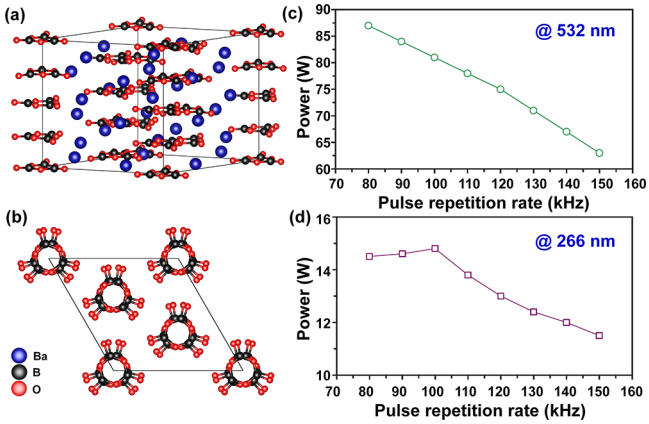

Figure 20. (a,b) Crystal structure of β-BaB_2O_4. (c,d) Power output of the 532 and 266 nm laser at high pulse repetition frequency, in which type **I** phase matching LiB_3O_5 and β-BaB_2O_4 crystals were used as the extracavity frequency doubled and quartered crystal, respectively. Reproduced with permission from ref 310. Copyright 2008 Institute of Physics. Parts a and b were drawn by using the crystallographic information file of β-BaB_2O_4 (ICSD: 30885) in ICSD.

potential of β-BaB_2O_4 as an NLO material was determined first by Chen *et al.* in 1985 and then immediately became a very promising NLO material.[22] They grew large transparent β-BaB_2O_4 crystals with the dimensions up to Φ 30 mm × 10 mm by the high-temperature solution top-seeded method. Using these crystals, the transmission region (189−3500 nm), birefringence (0.1140@1079 nm), effective SHG coefficients ($3.5 \pm 0.187 \times d_{36}$(KDP), and $4.23 \pm 0.56 \times d_{36}$ (KDP) were measured by two different methods), laser damage threshold (2 GW/cm^2 under 1064 nm, 150 mJ, 7.5 ns) were obtained, demonstrating that β-BaB_2O_4 is an excellent crystal for NLO applications.

For this purpose, large size and optically perfect β-BaB_2O_4 crystals are in great demand and thus many techniques have been proposed over the past 35 years. Several techniques have been used in order to optimize the crystal growth process of β-BaB_2O_4 crystal, including Czochralski, top-seeded solution, laser-heated pedestal, optical floating zone, traveling solvent-zone melting, and immersion-seeded solution crystal growth technique.[298−305] Among them, the top-seeded solution growth method is more appropriate, in particular, for the growth of large size β-BaB_2O_4 crystals without inclusions. Most of above method should involve suitable flux system, and thus there are a number of fluxes that have been applied with different advantages for the growth of β-BaB_2O_4 crystals up to now.[298−305] For example, monocomponential B_2O_3, Li_2O, Na_2O, NaF, and BaF_2 as well as dicomponential Na_2O-NaF and Na_2O-B_2O_3 are the most common fluxes used for growing β-BaB_2O_4 crystals. The growth process in boron-enriched systems, for example, self-flux B_2O_3, is hindered by the high viscosity of the solution. This results in the constitutional undercooling and related cellular growth, preventing the formation of large high-quality crystals. By contrast, the flux with fluoride can decrease viscosity of the solution and become one of the most suitable options. For example, a large β-BaB_2O_4 crystal with the dimensions up to Φ 100 mm × 40 mm has been grown by high-temperature solution top-seeded method with the NaF flux by Wang *et al.* in 2003.[304] The as-grown crystal is free of inclusions and has a high transmissivity from 190 to 2800 nm, indicating its high optical quality. Poeppelmeier *et al.* demonstrated that the thermal decomposition of the incongruently melting phase $LiBa_2B_5O_{10}$ can be used to grow β-BaB_2O_4 crystals with different scales in 2007.[305] By 2019, Simonova *et al.* reported the growth of β-BaB_2O_4 crystal by using the solvent of LiF and Li_2O with low volatility, providing an optional method for growing β-BaB_2O_4 bulk single crystals.[303]

With respect to the application of β-BaB_2O_4 crystal in laser system, Cheng *et al.* reported the OPO technology of β-BaB_2O_4 crystal first in the visible and near infrared spectral region in 1988.[306] The stable oscillation tuning from 0.45 to 1.68 μm has been achieved with a 354.7 nm pumped β-BaB_2O_4 OPO, and the maximum total energy conversion efficiency reached 9.5%.[306] Later on, Cheng *et al.* also demonstrated that a new two-crystal, walk-off compensated device can significantly improve the conversion efficiency of β-BaB_2O_4 OPO.[307] The oscillator is pumped at 354.7 nm, and the stable oscillation tuning from 0.42 to 2.3 μm has been achieved with the overall conversion efficiencies as high as 32%. It should be noted that this approach can be used for any other critically phase matching frequency conversion process, leading to the large improvements on corresponding conversion efficiency.[307] In the same year of 1989, Imai *et al.* reported the first cascading THG by light from an alexandrite laser using β-BaB_2O_4 crystals.[308] The UV light generation in the wavelength region of 244−259 nm has been achieved with the maximum efficiency of 24% by using type **I** mixing. In 1998, long-term operation of more than 1000 h of a 266 nm all-solid-state laser at 100 mW continuous wave output has been achieved in β-BaB_2O_4 crystals by Kondo *et al.*[309] The β-BaB_2O_4 crystals are used to double the 532 nm light which was produced by an intracavity frequency-doubled of Nd:YVO_4 laser (Figure 20c). Even higher 14.8 W UV laser of 266 nm was obtained at the pulse repetition rate of 100 kHz with the conversion efficiency of 18.3% from green to UV light by Liu *et al.* (Figure 20d).[310] The highest peak power of 21 kW has also been achieved at 80 kHz with the average output power of 14.5 W.[310]

Moreover, β-BaB_2O_4 crystals can also be used to generate shorter light through sum frequency generation. For example, in 1999, the tunable pulse generation from 192 to 197 nm at 7 kHz repetition-rate inside the β-BaB_2O_4 crystals employing all-solid-state lasers was demonstrated first by Masuda *et al.*, even though it was very close to the absorption edge (189 nm) of β-BaB_2O_4 crystals.[311] The average power generation at 196 and 193.3 nm are 31 and 10 mW, respectively. In 2001, also by Masuda *et al.* they demonstrated an all-solid-state, continuous wave laser operating at less than 200 nm by SFG of a frequency-quadrupled Nd:YAG laser at 266 nm with a Ti:sapphire laser at 745 nm. The generated power in the β-BaB_2O_4 crystal is about 3 mW with the bandwidth of 0.84 pm at about 195 nm, which is the highest power of continuous wave light below 200 nm.[312] In 2018, Nikolaev *et al.* studied the optical properties of β-BaB_2O_4 crystals in the terahertz range.[313] It was found that at long wavelengths, β-BaB_2O_4 crystals possess low optical absorption coefficient, and it is phase matchable for downconversion of near infrared lasers into this range. Thus, accounting other well-known attractive

https://dx.doi.org/10.1021/acs.chemrev.0c00796
Chem. Rev. 2021, 121, 1130−1202

physical properties of β-BaB_2O_4 crystal, wide application in terahertz technique can be forecasted.[313] Very recently, Dai *et al.* established a narrow line width OPO with a 452 nm signal radiation output, and pumped by a 355 nm single frequency Nd:YAG laser.[314] The OPO is built up by two β-BaB_2O_4 crystals with arrangement in a linear cavity configuration. The maximum output pulse energy realized for the 452 nm signal is 11 mJ with the pump energy of 45 mJ. Unfortunately, β-BaB_2O_4 crystal suffers from the large walk-off angles that limit the nonlinear interaction length.

3.2.2.2. α-SrB_4O_7, β-SrB_4O_7, and β-CaB_4O_7. The structure of α-SrB_4O_7 was determined first to belong to the space group of $Pmn2_1$ (no. 31) in 1964 by Krogh-Moe.[200] Its structure is exclusively constructed by the $[BO_4]$ tetrahedra that are strongly interconnected *via* sharing corners to form a 3D $^3[B_4O_7]_\infty$ framework that hosts the Sr cations within the channels. The needle-shaped α-SrB_4O_7 single crystals were grown from the stoichiometric melts with Czochralski and Kyropolus method. Since then, α-SrB_4O_7 crystals have been attracting much attention as an NLO crystal with the following benefits: a transparency down to 120 nm, the highest damage threshold, and no hygroscopicity.[315,316] The decrease of the SHG intensity with the increasing of the particle size confirms the absence of phase matching for SHG under 1064 nm laser with α-SrB_4O_7 crystals, which is due to its small birefringence of 0.0021@1064 nm.[315,316] Although it is non-phase matchable, Petrov *et al.* demonstrated a practical application of α-SrB_4O_7 crystals for diagnostics of femtosecond UV pulses by non-phase matching SHG within the coherence length. In this process, femtosecond pulses can be converted to wavelengths as low as 125 nm, which is very close to the transparency limit of α-SrB_4O_7 crystals.[317] By 2016, also by Petrov *et al.*, the tunable coherent radiation is successfully generated in the vacuum UV down to 121 nm using random quasi-phase matching method in α-SrB_4O_7 crystals, which is the shortest wavelength ever produced with a second-order NLO process in a solid-state material.[318] Meanwhile, they obtained unexpectedly four orders of magnitude enhancement compared with the non-phase matching case. The obtained SHG conversion efficiency of 10^{-5} starting with an amplified femtosecond Ti:sapphire laser system result in single pulse energies on the nJ level at 133 nm (sixth harmonic).[318]

By 2010, a new noncentrosymmetric polymorph of strontium tetraborate β-SrB_4O_7 with the space group of $P3$ (no. 143) was determined first by Vasiliev *et al.*[319] Within the structure, pairs of $[BO_3]$ triangles and $[BO_4]$ tetrahedra are linked *via* common corners to form chains that are further constructed to form a 3D framework with the channels running along the *c* axis, and the Sr^{2+} ions reside in the channels and exhibit strongly distorted polyhedra. Owing to the introduction of $[BO_3]$ triangles in its structure, the birefringence is enhanced to 0.030 compared with orthorhombic α-SrB_4O_7 (0.0021@1064) in $Pmn2_1$ (no. 31),[320] which might result in different phase matching behavior, but there is no further work reported on its NLO properties to date. In the case of β-CaB_4O_7, it was obtained first under high-pressure and high-temperature conditions by Huppertz *et al.* in 2014.[199] β-CaB_4O_7 is isomorphic to α-SrB_4O_7 with $Pmn2_1$ (no. 31) and shows similar framework that is solely built up by $[BO_4]$ units. To date, the related NLO properties have not been reported.

3.2.2.3. CaB_2O_4, $Ca_2(B_2O_5)$ and $CaMg(B_2O_5)$. The high pressure phase CaB_2O_4 was obtained first by Marezio *et al.* in 1965 under the conditions of 20 kbar and 900 °C.[321] CaB_2O_4 crystal belongs to $Pna2_1$ (no. 33) and exhibits a 3D $^3[B_6O_{12}]_\infty$ framework that is composed of $[B_6O_{17}]$ FBBs. The orthorhombic phases of $Ca(B_2O_5)$ and $CaMg(B_2O_5)$ are shown to crystallize in the noncentrosymmetric space group of $P2_12_12_1$ (no. 19) and $Pca2_1$ (no. 29), respectively, which show 0D framework of isolated $[B_2O_5]$ FBBs that are separated by M-site anions.[322,323] As of yet, SHG properties of the above three borates have not been reported, and thus it remains to be seen whether they have the potential in NLO applications.

3.2.2.4. BaB_8O_{13}, $Ba_5(BO_3)_2(B_2O_5)$ and $Sr_4B_{14}O_{25}$. Although BaB_8O_{13} belongs to the noncentrosymmetric space group of $P4_122$ (no. 91),[51] the SHG coefficients of BaB_8O_{13} with low dispersion are zero under the restriction of Kleinman symmetry. This implies that the BaB_8O_{13} crystals are unable to be used as an NLO material. Another barium borate $Ba_5(BO_3)_2(B_2O_5)$ was reported by Furmanova *et al.* in 2006,[324] which contains two different isolated $[BO_3]$ and $[B_2O_5]$ units with the symmetry of $P2_12_12_1$ (no. 19). At present, NLO properties information about $Ba_5(BO_3)_2(B_2O_5)$ is still unknown. Later on, a new noncentrosymmetric member of SrO-B_2O_3 system, $Sr_4B_{14}O_{25}$, has been synthesized by Kudrjavtcev *et al.* in 2003.[325] It belongs to $Cmc2_1$ (no. 36) and possesses a 3D framework consisting of three-membered $[B_3O_8]$ rings. The $Sr_4B_{14}O_{25}$ crystals with sizes up to 20−25 mm in diameter and 10 mm in length were obtained by top-seeded solution growth method. The UV absorption edge of $Sr_4B_{14}O_{25}$ was determined to be less than 190 nm.[325] But, $Sr_4B_{14}O_{25}$ is metastable and decomposes, on long-term storage, into strontium di- and metaborate, thus the further optical characterizations are still untaken.

3.2.2.5. $Sr_2Be_2B_2O_7$. $Sr_2Be_2B_2O_7$ was considered first as a potential deep-UV NLO material by Chen *et al.* in 1995.[3] $Sr_2Be_2B_2O_7$ crystal belongs to the space group of $P\bar{6}2c$ (no. 190) and features NLO-favorable $^2[Be_2B_2O_7]_\infty$ double-layers (Figures 21a,b), in which the isolated NLO-active $[BO_3]$ triangles aligned optimally (Figure 21c), and the $[BeO_4]$ units eliminate the dangling bonds of $[BO_3]$ units and also provide stronger interlayer interactions. The SHG response of $Sr_2Be_2B_2O_7$ is observed to be 3.8 × KDP under 1064 nm laser radiation. The $Sr_2Be_2B_2O_7$ crystals are transparent down to 155 nm with the suitable birefringence (cal. 0.062@589 nm), which might allow $Sr_2Be_2B_2O_7$ crystals to produce the coherent light below 200 nm by the direct SHG process. Although the optically perfect $Sr_2Be_2B_2O_7$ crystals can be easily

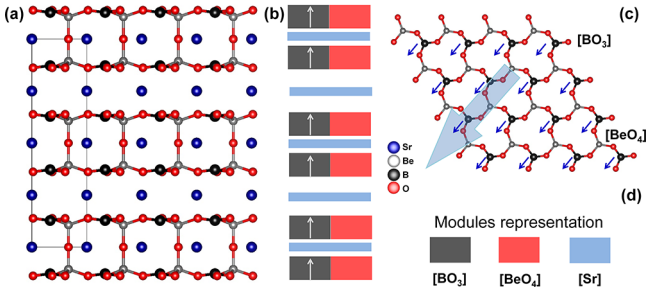

Figure 21. (a) Crystal structure of $Sr_2Be_2B_2O_7$. (b) Modular description of the arrangement of $[BO_3]$ and $[BeO_4]$ modules in $Sr_2Be_2B_2O_7$. (c) Optimally aligned arrangement of $[BO_3]$ NLO active units in $Sr_2Be_2B_2O_7$. (d) Representation of $[BO_3]$, $[BeO_4]$, and [Sr] modules. Parts a and c were drawn by using the crystallographic information file of $Sr_2Be_2B_2O_7$ (ICSD: 79025) in ICSD.

https://dx.doi.org/10.1021/acs.chemrev.0c00796
Chem. Rev. 2021, 121, 1130−1202

grown to 3 mm in the thickness, the cohesion forces between the $^2[Be_2B_2O_7]_\infty$ layers cannot be eliminated or weakened,[326] which make the structure of $Sr_2Be_2B_2O_7$ crystal unstable and extremely limit its further applications.

3.3. Mixed Alkali Metal and Alkaline-earth Metal Borates

3.3.1. $AMBO_3$ and $AM_4(BO_3)_3$ (A = Na, K, Rb, Cs; M = Mg, Ca, Sr). The 0D structures of both series are composed of isolated $[BO_3]$ triangles that are further separated by A- and M-site cations (Figures 22a,b). The noncentrosymmetric

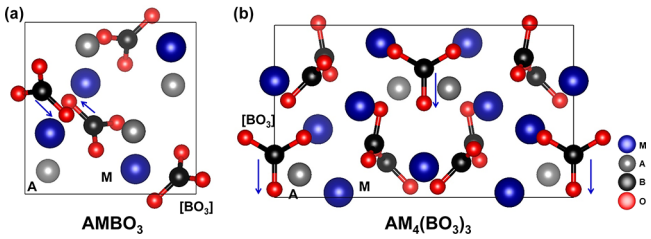

Figure 22. (a,b) The crystal structures of $AMBO_3$ and $AM_4(BO_3)_3$ (A = Na, K, Rb, Cs; M = Mg, Ca, Sr) series. Parts a and b were drawn by using the crystallographic information file of $KMgBO_3$ (ICSD: 174336) and $KCa_4(BO_3)_3$ (ICSD: 171422) in ICSD.

mixed metal borates in the above two series include cubic $KMgBO_3$,[327] $RbMgBO_3$,[328] $CsCaBO_3$,[329] and $RbCaBO_3$[330] as well as orthorhombic $KCa_4(BO_3)_3$, $KSr_4(BO_3)_3$, and $NaCa_4(BO_3)_3$.[330] The crystallized space groups for the two series are determined to be $P2_13$ (no. 198) and $Ama2$ (no. 40), respectively. The birefringence of crystals crystallizing in $P2_13$ is zero because of their isotropic nature, which also makes them non-phase matchable. Thus, $AMBO_3$ (A = K, R, Cs; M = Mg, Ca) series in this class is incapable of being used as NLO materials, even though they are transparent down to the UV spectral region. By contrast, the crystals in $AM_4(BO_3)_3$ (A = K, Na; M = Ca, Sr) series are reported to be phase matchable, with the SHG responses ranging from 1/3 to 2/3 × KDP under 1064 nm laser radiation.[330] It should be noted that the $[BO_3]$ triangles in these phases are distributed in a parallel manner along six different lattice planes (Figure 22b), thus most of the anisotropic polarizations are cancelled, which is consistent with the observed SHG coefficients. However, large crystals of this series have not been grown, thus the SHG coefficients, birefringence, and related optical data have not been reported.

3.3.2. $NaBeB_3O_6$, β-$KBe_2B_3O_7$, γ-$KBe_2B_3O_7$, $RbBe_2B_3O_7$, $Na_2Be_4B_4O_{11}$, $Na_2CsBe_6B_5O_{15}$, and $LiNa_5Be_{12}B_{12}O_{33}$. Motivated by the positive effects of $[BeO_4]$ tetrahedra with strong relatively strong covalence on eliminating the non-bonding states of O atoms in B−O units and shifting the absorption edges to deeper regions, a series of beryllium borates have been obtained as new types of NLO materials (Table 4). Among them, $NaBeB_3O_6$ ($Pna2_1$, no. 33),[87] β-$KBe_2B_3O_7$ ($Pmn2_1$, no. 31),[87] γ-$KBe_2B_3O_7$ ($P2_1$, no. 4),[87] $RbBe_2B_3O_7$ ($Pmn2_1$, no. 31),[87] and $Na_2CsBe_6B_5O_{15}$ ($C2$, no. 5)[331] were continuously discovered by Ye *et al.* in 2010 and 2011, respectively, whereas $Na_2Be_4B_4O_{11}$ ($P1$, no. 1)[144] and $LiNa_5Be_{12}B_{12}O_{33}$ (Pc, no. 7)[144] were obtained by Chen *et al.* in 2013. They exhibit low dimensional (0D and 1D) B−O anionic frameworks that are solely composed of $[BO_3]$ triangles in different arrangement. The linear $[B_3O_7]$ FBBs built up by three $[BO_3]$ triangles in $NaBeB_3O_6$ further condense into 1D infinite $^1[B_3O_6]_\infty$ chains. Whereas in isostructural β-$KBe_2B_3O_7$ and $RbBe_2B_3O_7$, in addition to $^1[B_3O_6]_\infty$ chains, they also have isolated 0D $[BO_3]$ triangles, which make them the first and sole borate that achieves the coexistence of 0D and 1D B−O units in one structure. In contrast, the residual five beryllium borates in this class only contain 0D isolated units, such as $Na_2CsBe_6B_5O_{15}$ with $[BO_3]$ triangles, $Na_2Be_4B_4O_{11}$ and $LiNa_5Be_{12}B_{12}O_{33}$ with $[BO_3]$ and $[B_2O_5]$ units, as well as γ-$KBe_2B_3O_7$ with $[BO_3]$ and $[B_3O_6]$ units. All of them only exhibit π-conjugated $[BO_3]$ or $[B_3O_6]$ units with the coplanar configuration, which make them exhibit strong anisotropy resulting from their differentiated polarizabilities in different directions. Therefore, benefiting from the NLO favorable configuration, they exhibit considerable NLO effects.

SHG measurements at 1064 nm on the powder samples indicate that $NaBeB_3O_6$, β-$KBe_2B_3O_7$, γ-$KBe_2B_3O_7$, $RbBe_2B_3O_7$, $Na_2Be_4B_4O_{11}$, $Na_2CsBe_6B_5O_{15}$, and $LiNa_5Be_{12}B_{12}O_{33}$ are all phase matching crystals, with the observed SHG coefficients of approximately 1.60, 0.75, 0.68, 0.79, 1.3, 1.17, and 1.4 times as large as that of KDP, respectively (see Table 4).[87,144,331] The difference among them is due to the density of NLO active $[BO_3]$ groups and their alignment. For example, the enhanced NLO effects have been achieved in $Na_2Be_4B_4O_{11}$ and $LiNa_5Be_{12}B_{12}O_{33}$ through cationic structural design, in which the flexible $[B_2O_5]$ groups are used as connections to construct the compact crystal structure. The absorption edges for all seven beryllium borates are reported to be below 200 nm; more accurate values await large single crystals.[87,144,331] Only both $Na_2Be_4B_4O_{11}$ and $LiNa_5Be_{12}B_{12}O_{33}$ have been grown to sizeable crystals. On the basis of transmittance spectra measurements, the UV short-wavelength absorption edges of $Na_2Be_4B_4O_{11}$ and $LiNa_5Be_{12}B_{12}O_{33}$ are reported to be 171 and 169 nm, respectively.[144] They also exhibit high transmittance (>70%) in the measured region of 190−380 nm. More tests for SHG

Table 4. Structural Information and Optical Properties of $NaBeB_3O_6$, β-$KBe_2B_3O_7$, γ-$KBe_2B_3O_7$, $RbBe_2B_3O_7$, $Na_2Be_4B_4O_{11}$, $Na_2CsBe_6B_5O_{15}$, and $LiNa_5Be_{12}B_{12}O_{33}$[a]

formula	space group	anionic framework	SHG response	cutoff edge
$NaBeB_3O_6$	$Pna2_1$	1D $^1[B_3O_6]_\infty$	1.60×KDP	<200 nm
β-$KBe_2B_3O_7$	$Pmn2_1$	0D $[BO_3]$ + 1D $^1[B_3O_6]_\infty$	0.75×KDP	<200 nm
γ-$KBe_2B_3O_7$	$P2_1$	0D $[BO_3]$ + 0D $[B_3O_6]$	0.68×KDP	<200 nm
$RbBe_2B_3O_7$	$Pmn2_1$	0D $[BO_3]$ + 1D $^1[B_3O_6]_\infty$	0.79×KDP	<200 nm
$Na_2CsBe_6B_5O_{15}$	$C2$	0D $[BO_3]$	1.3×KDP	<200 nm
$Na_2Be_4B_4O_{11}$	$P1$	0D $[BO_3]$ + 0D $[B_2O_5]$	1.17×KDP	171 nm
$LiNa_5Be_{12}B_{12}O_{33}$	Pc	0D $[BO_3]$ + 0D $[B_2O_5]$	1.4×KDP	169 nm

[a]All the data were collected from refs 87,144,331.

https://dx.doi.org/10.1021/acs.chemrev.0c00796
Chem. Rev. 2021, 121, 1130−1202

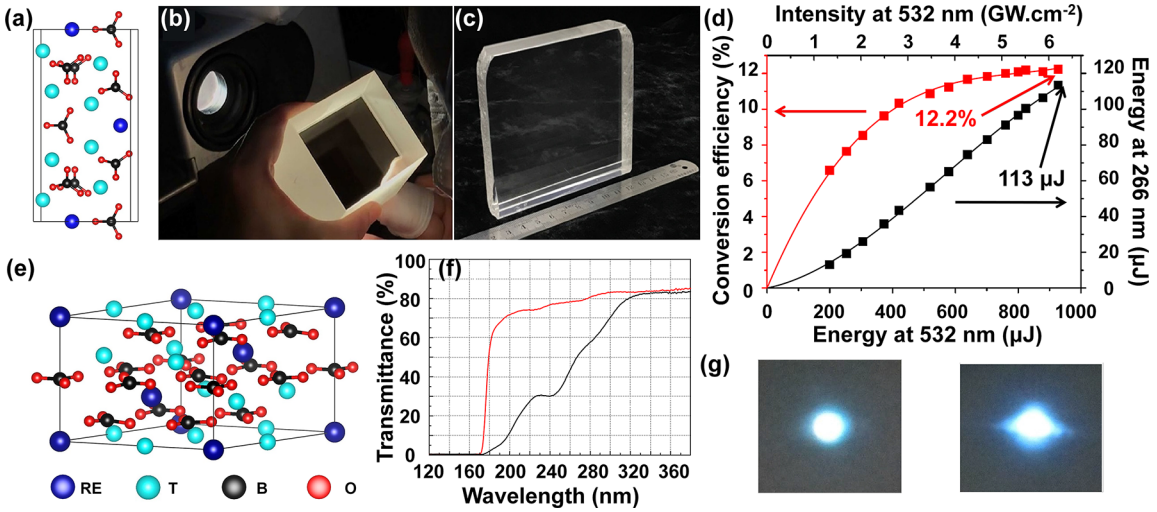

Figure 23. (a) Crystal structure of $REM_4O(BO_3)_3$ (RE = rare-earth metal; M = Ca, Cd) series. (b,c) Photographs of large aperture $YCa_4O(BO_3)_3$ crystal elements with the size of 80 × 60 × 50 mm^3 and 102 × 100 × 18 mm^3. Reproduced with permission from ref 344. Copyright 2020 Elsevier. (d) Conversion efficiency from 532 to 266 nm (red line) and output energy at 266 nm versus input energy and intensity at 532 nm (black line). The FHG at 266 nm was achieved by using a type **I** $YAl_3(BO_3)_4$ crystal from a Q-switched microchip laser Nd:YAG/Cr^{4+}:YAG frequency doubled with a LiB_3O_5 crystal. Reproduced with permission from ref 355. Copyright 2014 The Optical Society (e) Crystal structure of $RET_3(BO_3)_4$ series (RE = rare-earth metal; T = Al, Ga). (f) Transmittance spectra of $YAl_3(BO_3)_4$ crystal that is grown in both non-oxygen atmosphere (red line) and open air (black line). Reproduced with permission from ref 353. Copyright 2012 Elsevier. (g) Photographs of two UV beams at 266 nm in $YAl_3(BO_3)_4$ crystal with two different positions. Reproduced with permission from ref 355. Copyright 2014 The Optical Society. Parts a and e were drawn by using the crystallographic information file of $Ca_4SmO(BO_3)_3$ (ICSD: 66369) and $YAl_3(BO_3)_4$ (ICSD: 20223) in ICSD.

coefficients and birefringence data have not been reported for these beryllium borate crystals.

3.3.3. AMB_9O_{15} (A = Li, Na; M = Ba, Sr) and $K_2BaB_{16}O_{26}$. Three isostructural polyborates $LiBaB_9O_{15}$, $NaBaB_9O_{15}$, and $LiSrB_9O_{15}$ exist in two different phases, namely noncentrosymmetric *R*3*c* (no. 161) and centrosymmetric $R\bar{3}c$ (no. 167). The noncentrosymmetric phases are discussed here as they might exhibit NLO effects.[112] The structures consist of 3D $^3[B_9O_{15}]_\infty$ frameworks that are formed by the juxtaposition of three-member $[B_3O_7]$ units. Every $[B_3O_7]$ ring is further condensed around the three-fold through sharing the vertex of one $[BO_4]$ tetrahedron from the first $[B_3O_7]$ ring and one $[BO_3]$ triangle from the second $[B_3O_7]$ ring, and the 3D frameworks form with the channels running along the *c* axis that are occupied by A- and M-site anions. The $NaBaB_9O_{15}$ crystals with dimensions up to Φ 17 mm × 50 mm have been grown through Czochralski pulling method by Xu *et al.* in 2009.[332] The as-grown crystals are chemically stable and are not hygroscopic. The UV absorption edge for $NaBaB_9O_{15}$ crystals occurs slightly below 185 nm. The birefringence is only 0.02@589 nm, which can only satisfy the type **I** phase matching conditions under or near the 1064 nm and the shortest SHG type **I** wavelength is determined to be 406 nm. $NaBaB_9O_{15}$ possesses a very weak effective NLO coefficient, smaller than 0.25 pm/V, which makes it not competitive compared to other borate-based NLO materials.[332] Similarly, $LiBaB_9O_{15}$ and $LiSrB_9O_{15}$ crystals show similar performance compared with their isostructural $NaBaB_9O_{15}$. Another polyborate $K_2BaB_{16}O_{26}$ is obtained by Pan *et al.* in 2017 with noncentrosymmetric space group of $C222_1$ (no. 20).[105] It shows a 3D $^3[B_8O_{13}]_\infty$ framework with three different types of channels, in which two of them are filled with the Ba−O and K−O based polyhedra. $K_2BaB_{16}O_{26}$ possesses a short deep-UV absorption edge blow 190 nm, but the opposite orientations of NLO-active units in $K_2BaB_{16}O_{26}$ seriously weaken the SHG intensities to only 1/5 × KDP, which is quite low for NLO application.[105]

3.3.4. $CsBaB_3O_6$. The structure of $CsBaB_3O_6$ was determined first by Wu *et al.* in 2007.[333] $CsBaB_3O_6$ exhibits the similar structure to BaB_2O_4 series but crystallizes in different space group of *P*321 (no. 150), in which the isolated $[B_3O_6]$ units are perpendicular to the three-fold axis and tilting in the *ab* plane. The Cs and Ba atoms alternately locate between the $[B_3O_6]$ pseudo-sheets and form layers constructed by Cs- and Ba-based polyhedra. The UV short-wavelength absorption edge of $CsBaB_3O_6$ is reported to be 190 nm, which is quite close to that of the BaB_2O_4 series with similar configurations. However, the SHG efficiencies are much lower than those of β-BaB_2O_4 crystal, and no second-harmonic signal was detected during the SHG test.[333] This can be explained by the following structural aspects: the $[B_3O_6]$ units in two neighboring pseudo-layers are almost in opposite arrangements, which completely offsets the NLO effects in $CsBaB_3O_6$.

3.3.5. $Li_4Sr(BO_3)_2$. The $Li_4Sr(BO_3)_2$ crystal was obtained first by Luo *et al.* in 2014 with the low symmetry of *Cc* (no. 9; not included in ICSD).[334] The 0D anionic framework of $Li_4Sr(BO_3)_2$ is composed of isolated $[BO_3]$ triangles that are further separated by Li and Sr cations. $Li_4Sr(BO_3)_2$ crystals without layering tendency were initially grown by the top-seeded solution growth method from the self-flux system. A deep-UV absorption edge of 186 nm has been measured based on $Li_4Sr(BO_3)_2$ powders. Owing to the optically aligned of the NLO-active anionic groups in the structure of $Li_4Sr(BO_3)_2$, the SHG efficiencies of $Li_4Sr(BO_3)_2$ powders are detected to be ∼2.0 × KDP and 1/3 × β-BaB_2O_4 under incident laser at 1064 and 532 nm, respectively.[334] The derived birefringence is 0.056@532 nm for $Li_4Sr(BO_3)_2$, and it is sufficient for the phase matching in the SHG process of 1064 and 532 incident laser, which is in good agreement with the SHG measurements.[334] Attributable to the lack of large single crystals, the

https://dx.doi.org/10.1021/acs.chemrev.0c00796
Chem. Rev. 2021, 121, 1130−1202

SHG coefficients, laser damage threshold, and experimental birefringence have not yet been reported.

3.4. Rare-earth Metal Borates

In rare-earth metal borates, the structural characteristics of B−O and RE−O groups determine their UV transparency, high polarizability, and capability of resisting against radiation-induced damage, which implies that many rare-earth metal borates are attractive candidates for laser hosts and NLO materials with enhanced nonlinearities activated by the distorted RE-based polyhedra. Thus, many studies have been focused on the searching of NLO candidates in rare-earth metal−borate system. Therefore, rare-earth metal borates, closely approach 100 cases, with the general formulas of $RECa_4O(BO_3)_3$, $Na_3RE_9O_3(BO_3)_8$, $RE(BO_3)$, RE_3BWO_9, $RET_3(BO_3)_4$, $RE_2M_3(BO_3)_4$, $Na_3RE_2(BO_3)_3$, $A_3RE_2(BO_3)_3$, $REM_3(BO_3)_3$, and $A_7MRE_2(B_5O_{10})_3$, *etc.*, have been discovered, in which RE is a trivalent rare-earth metal, A is monovalent alkali metal, M is divalent alkaline-earth metal, and T is trivalent metal (Tables S1−S4 in the SI), but only the crystal chemistry or fluorescence properties of above substantial rare-earth metal borates are concerned rather than their NLO properties. Herein, in this section, we will discuss several representative candidates for NLO applications.

3.4.1. $RECa_4O(BO_3)_3$ (RE = Rare-earth Metal). Rare-earth calcium oxyborate family with the general formula of $RECa_4O(BO_3)_3$ (RE = Rare-earth metal) is one of the commonly used rare-earth metal borates for NLO and laser applications. The first member of this family with the chemical composition of $SmCa_4O(BO_3)_3$ was obtained and structurally determined by Khamaganova *et al.* in 1991.[335] The subsequent studies on this family prompt the discovery of other $RECa_4O(BO_3)_3$ members with RE = Y, La, Gd, Nd and Lu, *etc.*[35,336,337] Structurally, $RECa_4O(BO_3)_3$ crystals belong to the monoclinic *Cm* (no. 8) with 0D anionic framework of isolated $[BO_3]$ triangles (Figure 23a). They contain two sets of isolated $[BO_3]$ units, which are roughly parallel to *ab* plane for one $[BO_3]$ triangle and are skewed by approximately 30° for the other one. All of the $[BO_3]$ units will almost fully add their contributions to the total NLO properties of this family. The RE- and Ca-based octahedra locate in the mirror plane. By replacing the Ca with Cd atoms with polar displacement, three new cadmium rare earth oxyborates, $Cd_4REO(BO_3)_3$ (Re = Y, Gd, Lu; not included in ICSD), have been synthesized by Ye *et al.* in 2012.[338] They exhibit the similar 0D anionic framework of $[BO_3]$ units with above $RECa_4O(BO_3)_3$ series. The SHG measurements indicate that the phase matching SHG responses are approximately 5.2, 5.0, and 5.3 × KDP at 1064 nm for Y-, Gd-, and Lu-phases, respectively. They have wide transparent regions ranging from UV to near IR with the absorption edges of 328, 326, and 335 nm, respectively.[338] The $RECa_4O(BO_3)_3$ series are attractive NLO candidates for frequency conversion as they possess large NLO coefficients, high laser damage threshold, moderate birefringence, and favorable growth habit.

Now in this section, we choose the most commonly studied $YCa_4O(BO_3)_3$ and $GdCa_4O(BO_3)_3$ as representatives to discuss the potential NLO applications of this family. The $YCa_4O(BO_3)_3$ and $GdCa_4O(BO_3)_3$ crystals melt congruently with the melting points of 1510 and 1480 °C, respectively, which were conventionally grown by Czochralski and Bridgman methods.[35,337,339,340] $YCa_4O(BO_3)_3$ is a biaxial monoclinic crystal with the measured birefringence of 0.041 at 1064 nm, which is larger than that of its isostructural $GdCa_4O(BO_3)_3$ (0.033@1064 nm). Owing to the enhanced birefringence, it follows that the shorter fundamental wavelength limit for type **I** SHG along the Y axis is 720 nm for $YCa_4O(BO_3)_3$ and 840 nm for $GdCa_4O(BO_3)_3$, respectively.[35] The deep-UV transmittance spectra for both crystals indicate that the absorption edges are all near 200 nm, which facilitate their applications in the UV spectral range.[35,337,339,340] Because $RECa_4O(BO_3)_3$ (RE = Y, Gd) crystals belong to the low symmetric system of *Cm*, which exhibit six independent NLO coefficients, and two independent quadrants are needed to determine the completely distribution of the effective coefficients (d_{eff}). Thus, several sets of (θ, φ) angles in $RECa_4O(BO_3)_3$ (RE = Y, Gd) crystals have been proposed by Shao *et al.* under the laser emission of 1064 nm. $|d_{eff}(\theta, \varphi)|$ with varied orientations change from 0.42−1.73 pm/V for $YCa_4O(BO_3)_3$ and 0.44−1.68 pm/V for $GdCa_4O(BO_3)_3$, respectively.[340] It is obvious that the maximum $d_{eff}(\theta, \varphi)$ is not in the principal plane or the first quadrant, but in the second quadrant. The maximum $|d_{eff}(\theta, \varphi)|$ are measured to be 1.73 and 1.68 pm/V with (θ, φ) = (67, 143.5°) and (66.8, 132.6°) for $YCa_4O(BO_3)_3$ and $GdCa_4O(BO_3)_3$ crystals, respectively. On the basis of these, the SHG efficiencies reach 41.5 and 48% for 5 mm long $YCa_4O(BO_3)_3$ (113.2, 47.4°) and 6 mm long $GdCa_4O(BO_3)_3$ crystals (113, 36.5°), respectively.[340]

The continuous wave SHG output power of 2.35 W was generated in the phase matching direction of (θ, φ) = (64.5, 35.5°) with the conversion efficiency of 18.1% in $YCa_4O(BO_3)_3$ crystals by Liu *et al.* in 2000.[341] In the case of $GdCa_4O(BO_3)_3$ crystals, similar laser system gave the $GdCa_4O(BO_3)_3$ crystals the continuous wave SHG output power of 2.81 W with the conversion efficiency of 18.7%.[342] The high output SFD power of 245 mW at 530 nm was achieved in Nd_3:$YCa_4O(BO_3)_3$ by Hammons *et al.* in 2000.[343] The power scaling is achieved by diode pumping using a novel technology of combining the output of up to four high-brightness laser diodes. Very recently, $YCa_4O(BO_3)_3$ crystals were grown by the Bridgman method to 102 × 100 × 18 mm^3, which is the largest grown aperture up to now (Figures 23b,c).[344] By using it, the highest SHG conversion efficiency of 73% was obtained from the fundamental source with 2 Hz repetition rate and 50 ps pulse duration at 1053 nm in a 10 mm long crystal.[344]

3.4.2. $RET_3(BO_3)_4$ (RE = Rare-earth Metal; T = Trivalent Metal). The first series of $RET_3(BO_3)_4$ family were synthesized by Ballman in 1962,[345] which were classified as the part of huntite family with space group of *R*32 (no. 155). The subsequent studies on this family prompt the discovery of other new members with varied noncentrosymmetric structures of *C*2 (no. 5), *Cc* (no. 9), and $P3_121$ (no. 154).[345−349] Studies have shown that rare earth borates with huntite type structure, including their derivatives, are very attractive for NLO applications due to their favorable physicochemical properties, for example, good stability, high transparency, high thermal coefficient, and in particular very high NLO coefficients. Among them, $YAl_3(BO_3)_4$ crystal with hexagonal *R*32 polytype appears to be an excellent NLO material, and we will discuss it in this class. The $YAl_3(BO_3)_4$ crystal was discovered first by Ballman in 1962, and it exhibits 0D anionic framework of isolated $[BO_3]$ triangles with the Y and Al ions occupying the local D_3 point symmetry and octahedral sites, respectively (Figure 23e).[345] The $YAl_3(BO_3)_4$ crystal melts

https://dx.doi.org/10.1021/acs.chemrev.0c00796
Chem. Rev. 2021, 121, 1130−1202

incongruently at 1280 °C, and it can be only grown from flux solutions. Up to now, several flux systems, like $K_2Mo_3O_{10}$-B_2O_3−KF, $Na_2B_4O_7$, $Li_2B_4O_7$−B_2O_3, PbO-B_2O_3, and Li_2CO_3−B_2O_3 have been used to grow the large size $YAl_3(BO_3)_4$ crystals.[349−353,355] On the basis of the as-grown optically perfect crystals, $YAl_3(BO_3)_4$ is proved to be an excellent NLO crystal with extremely short absorption edges from 160 to 170 nm depending on the quality of as-grown crystals, a highly effective coefficient of d_{eff} = 0.69 pm/V, a suitable large birefringence (0.0684@1064 nm) to ensure the generation of 532 and 266 nm harmonic light within 1064 nm laser, a small walk-off angle of 1.9°, and a high laser damage threshold. The FHG of a frequency doubled Nd:YAG laser, from 532 to 266 nm, was carried out with $YAl_3(BO_3)_4$ crystals doubler for the first time by Hu *et al.* in 2010.[352] The average output power of 2.4 mW was obtained at 266 nm with the conversion efficiency of 15.6%. Later on, the average power of 266 nm UV laser is increased to 5.05 W at 65 kHz pulse repetition frequency by Liu *et al.*[354] by using the type **I** phase matching $YAl_3(BO_3)_4$ crystal, the conversion efficiency from 532 to 266 nm is reported to be about 12.3%. In 2014, the 240 kW peak power at 266 nm with a mean conversion efficiency of 12.2% from 532 to 266 nm has been obtained by using a 2.94 mm thick type **I** phase matching $YAl_3(BO_3)_4$ crystal by Loiseau *et al.* (Figures 23d,g).[355] But, the $YAl_3(BO_3)_4$ crystals grown in the open system tend to have serious absorption in the UV region of 200−300 nm, which seriously reduces the conversion efficiency. Thus, non-oxygen atmosphere is used to grow $YAl_3(BO_3)_4$ crystals without UV absorption by Liu *et al.* (Figure 23f),[353] which indeed has removed the abnormal absorption in UV region.

3.4.3. $La_2CaB_{10}O_{19}$. A new lanthanum calcium borate $La_2CaB_{10}O_{19}$ was discovered to crystallize in the monoclinic space group of *C*2 (no. 5) by Wu *et al.* in 2001.[36] The $[B_5O_{12}]$ double rings in $La_2CaB_{10}O_{19}$ condense to form the 2D $^2[B_{10}O_{19}]_\infty$ double-layers by sharing five of the six terminal oxygens in $[B_5O_{12}]$ units. The Ca-based polyhedra are sequestered within the polyborate matrix, and the La-based polyhedra bridge the neighboring $^2[B_{10}O_{19}]_\infty$ layers. $La_2CaB_{10}O_{19}$ crystal exhibits an optical SHG effect about twice as large as that of KDP, and its effective coefficient is 1.05 pm/V.[356] The absorption edge for $La_2CaB_{10}O_{19}$ crystal is 170 nm, and the high laser damage threshold of >8 GW/cm^2 under 35 ps and 1064 nm is also observed. A suitable birefringence of Δn = 0.053@1064 nm shifts the type **I** shortest SHG wavelengths to 288 nm.[356] More importantly, extremely large crystals, over centimeter level, have been grown by top-seeded growth method.[357] Thus, $La_2CaB_{10}O_{19}$ crystal is a promising NLO material for high power frequency conversion. For the first time, Wu *et al.* performed the THG experiments by using types **I** and **II** $La_2CaB_{10}O_{19}$ crystals in 2011.[358] The 355 nm UV light output of 5.0 and 3.5 mW with conversion efficiencies of 28.3 and 21.1% was generated under a picosecond Nd:YAG laser by types **I** and **II** $La_2CaB_{10}O_{19}$ crystals.[358] By 2014, the maximum output power of 5.3 W of 355 nm UV laser was obtained from 1064 nm fundamental laser with optical conversion efficiency 15.1% from 1064 to 355 nm.[359]

3.4.4. $Na_3La_2(BO_3)_3$ and $Na_3La_9O_3(BO_3)_8$. The $Na_3La_2(BO_3)_3$ crystal was reported in 1983 by Mascetti *et al.*[360] and was discovered to be NLO active in 2001 by Zhang *et al.*[361] $Na_3La_2(BO_3)_3$ crystallizes in orthorhombic *Amm*2 (no. 38) with 0D anionic framework of isolated $[BO_3]$ triangles that are separated by Na and La atoms (Figures 24a,b). Sizable

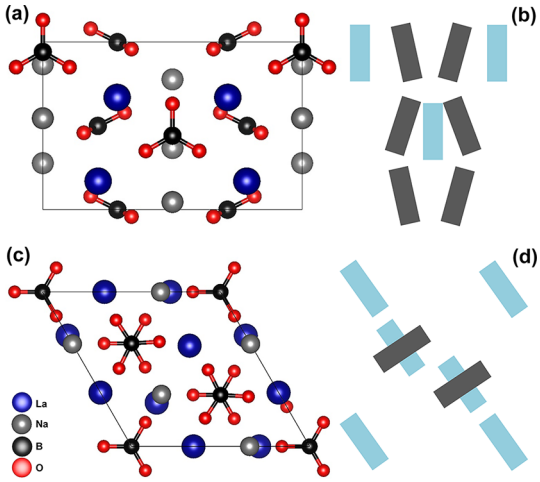

Figure 24. (a,c) Crystal structures of $Na_3La_2(BO_3)_3$ and $Na_3La_9O_3(BO_3)_8$. (b,d) Modular descriptions of the arrangement of $[BO_3]$ modules in $Na_3La_2(BO_3)_3$ and $Na_3La_9O_3(BO_3)_8$. Different color represents varied crystallographic positions of $[BO_3]$ units, namely $[B(1)O_3]$ and $[B(2)O_3]$ units in light-black and light-blue. Parts a and c were drawn by using the crystallographic information file of $Na_3La_2(BO_3)_3$ (ICSD: 151884) and $Na_3La_9O_3(BO_3)_8$ (ICSD: 245228) in ICSD.

$Na_3La_2(BO_3)_3$ crystals have been grown by top-seeded solution growth method and subjected to performance measurements. $Na_3La_2(BO_3)_3$ crystal possesses a short UV absorption edge at 213 nm with the effective coefficient d_{eff} for type **I** phase matching reaching 1.44 pm/V, which is even larger than that of LiB_3O_5 crystal.[362] Theoretical analyses indicate that such large SHG effects mainly originate from the synergistic effects of π-conjugated $[BO_3]$ units and La-centered polyhedra with large polar displacement. Owing to the relatively small birefringence in$Na_3La_2(BO_3)_3$ (Δn = 0.023@ 1014 nm) and its isostructural derivatives, the generation of shorter harmonic light like 355 and 266 nm is limited.[362]

Another ternary borate of sodium and rare earth metal, $Na_3La_9O_3(BO_3)_8$, was discovered by Pechev *et al.* in 2002[363] and was reported to be an NLO crystal by Zhang *et al.* in 2005.[364] $Na_3La_9O_3(BO_3)_8$ belongs to the space group of $P\bar{6}2m$(no. 189) with three types of crystallographically independent isolated $[BO_3]$ units paralleling to the *ab* plane that are interlinked by Na and La atoms (Figures 24c,d). The absorption edge of approximately 270 nm[364] was determined for $Na_3La_9O_3(BO_3)_8$ crystal, which is thought to be attributable to the full connectivity of $[BO_3]$ units with terminal oxygen atoms. The Sellmeier equations fitted by the least squares fitting method reveal that $Na_3La_9O_3(BO_3)_8$ crystal has a large birefringence of Δn = 0.086@1064 nm, which shift the shortest type **I** SHG phase matching wavelength (288 nm) to very close to its absorption edge.[365] That means that the THG of Nd:YAG laser could be realized in $Na_3La_9O_3(BO_3)_8$ crystals. The sole non-zero independent SHG coefficient, *i.e.*, d_{22}, was found to be d_{22} = (5.925 ± 0.171) × d_{36}(KDP) = (2.31 ± 0.07) pm/V, which is even larger than those of β-BaB_2O_4 and LiB_3O_5.[366] With respect to the effective NLO coefficients d_{eff}, they range from 0 to 2.06 pm/V and 0 to 1.44 pm/V for types **I** and **II** SHG process, respectively, which are related to the angles of (θ, φ). The energy conversion efficiency of 58.3% for SHG at 532 nm was obtained for $Na_3La_9O_3(BO_3)_8$ crystal,[366] however for LiB_3O_5

https://dx.doi.org/10.1021/acs.chemrev.0c00796
Chem. Rev. 2021, 121, 1130−1202

with at the same incident power intensity, it was only 21.5%. Similarly, the 355 nm light was obtained by THG process with $Na_3La_9O_3(BO_3)_8$ crystal for the first time by Wu *et al.* in 2012. A 355 nm UV light output of 1.9 mW was obtained successfully under a picosecond Nd:YAG laser by using type I $Na_3La_9O_3(BO_3)_8$ crystal, corresponding to the conversion efficiency of 9.3%.[367] More importantly, both SHG and THG conversion efficiencies can be increased if the larger $Na_3La_9O_3(BO_3)_8$ crystals are utilized.

3.4.5. $A_7MRE_2(B_5O_{10})_3$ (A = Alkali Metal; M = Divalent Metal; RE = Rare-earth Metal). A series of mixed-metal rare earth borates with the general formula of $A_7MRE_2(B_5O_{10})_3$ were continually reported by many groups,[368−373] in which A represents mono-alkali metal or mixed alkali metals, M site can be alkaline-earth metal or divalent post-transition metal (like Zn, Cd, Pb, *etc.*), and RE refers rare-earth metal. The number of this family is continually increasing due to the easy achievement of substitution and co-substitution in cognate atoms. All of the $A_7MRE_2(B_5O_{10})_3$ crystals belong to trigonal *R*32 (no. 155) with the 0D isolated $[B_5O_{10}]$ clusters. For those mixed alkali and alkaline-earth metal members consisting of the RE atoms with closed-shell electronic configurations or half-occupied 4*f* orbitals, *i.e.*, Y, Sc, La, Gd, and Lu, they can be transparent down to 190 nm.[368−373,373] Their SHG responses range from 0.4 to 2.1 × KDP under 1064 nm, which is tuned by different A-, M-, and RE-sites anions, but such NLO effects are not competitive compared with those of other rare earth NLO materials.[368−373] It should be noted that more borates can be obtained by chemical substitution and co-substitution strategy based on the template of $A_7MRE_2(B_5O_{10})_3$, which provides a good model to study the effects of A-site metal cation on structure and property. At present, large single crystals of this family have not been grown, as such birefringence, SHG coefficients, and laser damage threshold have not been measured or determined experimentally.

3.5. Borates with SOJT Distorted Cations

3.5.1. $Pb_4O(BO_3)_2$ and $(Pb_4O)Pb_2B_6O_{14}$. By introducing Pb^{2+} cations with stereoactive lone pair into borates, two novel lead oxyborates, $Pb_4O(BO_3)_2$,[374] and $(Pb_4O)Pb_2B_6O_{14}$,[161] were discovered to be NLO active by Pan *et al.* in 2012 and 2016, respectively. They crystallize in the noncentrosymmetric space groups of *Aba*2 (no. 41) and *P*1 (no. 1) with 0D and 1D B−O anionic frameworks, respectively. The isolated $[B_2O_5]$ and $[BO_3]$ units in $Pb_4O(BO_3)_2$ are in a parallel arrangement in *bc* plane and alternately stack along the *a* axis. Among them, $[BO_3]$ triangles are optimally aligned with the same orientations to produce large optical anisotropies. In the case of $(Pb_4O)Pb_2B_6O_{14}$, it features 1D parallel spiral $^1[B_6O_{14}]_\infty$ infinite chains that are composed of $[B_6O_{15}]$ FBBs. In the highly distorted $[PbO_n]$ (n = 3-5) and $[PbO_n]$ (n = 6-9) polyhedra in $Pb_4O(BO_3)_2$ and $(Pb_4O)Pb_2B_6O_{14}$, respectively, all of the O atoms fall within the same hemisphere around Pb, suggesting the stereoactive features of Pb^{2+} cation in the opposite direction. The isolated $[Pb_4O]$ tetrahedra are observed first in $(Pb_4O)Pb_2B_6O_{14}$. The SHG efficiencies of approximately 3.0 and 3.5 × KDP were determined for $Pb_4O(BO_3)_2$ and $(Pb_4O)Pb_2B_6O_{14}$ powders,[161,374] which are thought to be attributable to the synergistic effects of the $[PbO_n]$ polyhedra with stereoactive feature and B−O units. However, the 6*s* → 6*p* electronic transitions in both lead borates give rise to an intense absorption in the UV region, thus relatively high absorption edges of 280 and ∼370 nm were observed in $Pb_4O(BO_3)_2$ and $(Pb_4O)Pb_2B_6O_{14}$.[161,374] At present, large single crystals of this family have not been grown, as such birefringence, SHG coefficients, and laser damage threshold have not been measured or determined experimentally.

3.5.2. PbB_4O_7 and β-SnB_4O_7. The structures of PbB_4O_7 and β-SnB_4O_7 are all reported to be isomorphic to α-SrB_4O_7 with the space group of $Pmn2_1$ (no. 31),[201,202,315] which are solely constructed by $[BO_4]$ tetrahedra that are interconnected to form 3D $^3[B_4O_7]_\infty$ frameworks with Pb^{2+} and Sn^{2+} cations located within the channels. PbB_4O_7 melts congruently with a low melting point of 782 °C, which was conventionally grown by top-seeded growth technique. PbB_4O_7 crystal has a absorption edge of 240 nm and the laser damage threshold was found to be ∼20 GW/cm^2 for 17 ns Nd:YAG (1064 nm) laser radiation, but the extremely small birefringence of 0.0064@1064 nm was observed in PbB_4O_7 crystal, which is ultimately responsible for the absence of angle phase matching.[315] In the case of β-SnB_4O_7, it was obtained first under high-pressure and high-temperature conditions by Huppertz *et al.* in 2007.[202] To date, the related NLO properties have not been reported.

3.5.3. α-BiB_3O_6, δ-BiB_3O_6, and BiB_3O_6 (*P*1). The bismuth triborate of α-BiB_3O_6 was discovered first in 1962 by Levin *et al.*[375] from the Bi_2O_3−B_2O_3 binary phase diagram. The single crystals were grown in 1982[376] by Liebertz and its monoclinic (*C*2, no.5) crystal structure was solved by Fröhlich *et al.* in 1984 for the first time.[377] By 1998, α-BiB_3O_6 was recognized as an excellent NLO material by Hellwig *et al.*[26] α-BiB_3O_6 melts congruently with the melting point of 826 °C, which was conventionally grown by top-seeded growth technique.[378] α-BiB_3O_6 features the 2D $^2[B_3O_6]_\infty$ layers that are built up by linear $[B_3O_8]$ FBBs, in which the $[BO_3]$ triangles and $[BO_4]$ tetrahedra are in a ratio of 1:2 (Figure 25a). These FBBs are linked *via* corners to form a 2D network with six-fold coordinated Bi atoms alternating arrangement with $^2[B_3O_6]_\infty$ single-layers. α-BiB_3O_6 crystals possess high transmittance above 80% and wide transparency ranges covering the visible and near-infrared regions with a short absorption edge of 270 nm. The laser damage threshold of α-BiB_3O_6 crystals is

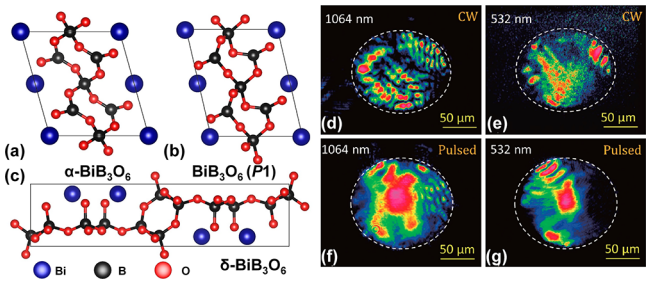

Figure 25. (a−c) Crystal structures of α-BiB_3O_6, BiB_3O_6 (*P*1), and δ-BiB_3O_6. (d,e) Modal profiles of fundamental and second harmonic continuous wave light at 1064 and 532 nm from α-BiB_3O_6 optical cladding waveguide. Reproduced with permission from ref 382. Copyright 2012 Japan Society of Applied Physics. (f,g) Modal profiles of pulsed fundamental and second-harmonic light at 1064 and 532 nm from α-BiB_3O_6 optical cladding wave guide. The dashed lines indicate the spatial location of the wave guide. Reproduced with permission from ref 382. Copyright 2012 Japan Society of Applied Physics. Parts a−c were drawn by using the crystallographic information file of α-BiB_3O_6 (ICSD: 48025), BiB_3O_6 (*P*1) (ICSD: 173746), and δ-BiB_3O_6 (ICSD: 416822) in ICSD.

https://dx.doi.org/10.1021/acs.chemrev.0c00796
Chem. Rev. 2021, 121, 1130−1202

comparable to that of high-quality LiB_3O_5 crystal. The exceptionally large NLO coefficient and birefringence are measured to be d_{eff} = 3.2 pm/V for a type **I** SHG process and Δn = 0.1605 at 1014 nm, which are higher than those of most borate-based NLO crystals.[26,379]

The wide tuning range of phase matching directions together with the monoclinic symmetry allows a broad variety of applications, and therefore, α-BiB_3O_6 crystals have been used to generate harmonic light with varied different wavelengths. For example, the continuous wave SHG output power of 364 mW was generated by using α-BiB_3O_6 crystals at the type **I** phase matching direction of (θ, φ) = (168.9°, 90°) by Du *et al.* in 2001,[380] and the corresponding effective intracavity SHG efficiency is as high as 32.4%. Besides, Ishii *et al.* demonstrated the octave-spanning optical parametric amplification of infrared pulses in the range from 1100 to 2200 nm by using a α-BiB_3O_6 crystal and 800 nm pump pulses.[381] In 2012, the guided-wave SHG at 532 nm green light has been achieved by Chen *et al.* under continuous and pulsed wave pump at 1064 nm within the type **I** birefringent phase matching configuration of α-BiB_3O_6 crystals with the conversion efficiencies of 0.083 and 25%, respectively.[382] They also demonstrate the multimodal of fundamental and second-harmonic light (Figures 25d–g). Very recently, Huang *et al.* measured the refractive index and absorption coefficient in the terahertz frequency range and predicted that α-BiB_3O_6 crystal can be an efficient terahertz radiation generator under intense laser pumping.[383]

Two new noncentrosymmetric polymorphs of BiB_3O_6, namely, BiB_3O_6 ($P1$, no. 1) and δ-BiB_3O_6 ($Pca2_1$, no. 29) were reported by Dinnebier *et al.*[384] and Huppertz *et al.*,[209] respectively. BiB_3O_6 ($P1$) can be obtained by pressurizing to 6.86–11.6 GPa on the phase of α-BiB_3O_6. On closer inspection of the 2D layered anionic configurations in BiB_3O_6 ($P1$) and α-BiB_3O_6, differences can be seen in the small reorientations of the $[BO_3]$ and $[BO_4]$ units (Figures 25a,b) and in the higher coordination of Bi cations between two phases. But, to date, the related linear and NLO properties of BiB_3O_6 ($P1$) have not be given, thus it remains to be seen if BiB_3O_6 ($P1$) can be used for NLO applications. In the case of δ-BiB_3O_6, it is exclusively built up of $[BO_4]$ tetrahedra, which share common oxygen to form layers and are further interconnected by *zigzag* chains of $[BO_4]$ tetrahedra to generate a 3D network structure (Figure 25c).[209] Its single crystals and optical properties have been grown and measured by Aleksandrovsky *et al.* The transmission range (50% transmission level) of δ-BiB_3O_6 crystal is from 315 nm to more than 3500 nm. The effective NLO coefficient and birefringence are measured to be d_{eff} = 1.2 pm/V and Δn = 0.0756 at 1014 nm, which are smaller than those of monoclinic phase α-BiB_3O_6.[385] These results indicate that δ-BiB_3O_6 crystal is suitable for doubling the laser with a wavelength 1.32 μm, especially as the concentrated SFD laser crystal for this wavelength.

3.5.4. $CaBi_2B_2O_7$, $SrBi_2B_2O_7$, $Bi_2B_8O_{15}$, $Bi_2Cu_5B_4O_{14}$, and Bi_3TeBO_9. Two new borates, $CaBi_2B_2O_7$ and $SrBi_2B_2O_7$, were discovered first during the exploratory syntheses in the corresponding ternary systems by Barbier *et al.* in 2006.[386] Although they share similar formula, they are not isostructural and crystallize into the different space groups of $Pna2_1$ (no. 33) and $P6_3$ (no. 173) for Ca and Sr analogues, respectively. Both structures, however, are constructed by the stacking of pseudo-layers that match the stoichiometry of the compound built of corner-sharing $[BO_3]$ triangles and $[MO_6]$ trigonal prisms with the Bi atoms located in the six-membered rings (Figures 26a,b). The measurement of the powder SHG efficiency for

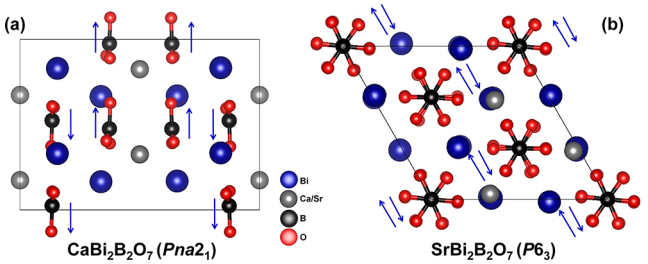

Figure 26. (a,b) The crystal structures of $CaBi_2B_2O_7$ and $SrBi_2B_2O_7$. All of the $[BO_3]$ units adopt opposite arrangement, therefore the polarization of the $[BO_3]$ units were largely cancelled and thus made small contribution for the SHG response. Parts a–c were drawn by using the crystallographic information file of $CaBi_2B_2O_7$ (ICSD: 245016) and $SrBi_2B_2O_7$ (ICSD: 245017) in ICSD.

$CaBi_2B_2O_7$ reveals a value of 2.0 ×KDP under 1064 nm,[387] while for $SrBi_2B_2O_7$, it is expected to display a moderate SHG efficiency, but no exact results are given. The structure difference betweent them is that all of the $[BO_3]$ units in $SrBi_2B_2O_7$ adopt opposite arrangement (Figures 26a,b), which make the polarization of $[BO_3]$ units largely cancel each other and thus make a small contribution to the SHG response. Therefore, the SOJT distorted Bi^{3+} cations are responsible for the considerable SHG responses in both $CaBi_2B_2O_7$ and $SrBi_2B_2O_7$.

The bismuth tri-borate of $Bi_2B_8O_{15}$ was discovered first in 1962 by Levin *et al.* from the Bi_2O_3–B_2O_3 binary phase diagram.[375] Large crystals were grown by Becker *et al.* with a top-seeded solution growth method.[387] $Bi_2B_8O_{15}$ crystallizes in the space group of $P2_1$ (no. 4) and it shows 2D $^2[B_8O_{15}]_\infty$ layers built from $[B_8O_{18}]$ FBBs with the Bi atoms located between the layers. Optical measurements of $Bi_2B_8O_{15}$ reveal that the UV absorption edge is 267 nm, and the powder SHG response is about 1.2 times that of KDP.[388] The structure of $Bi_2Cu_5B_4O_{14}$ was initially thought to crystallize in the centrosymmetric space group of $P\bar{1}$(no. 2),[389] but this was re-determined to a new non-centrosymmetric class, $P1$(no. 1), by Poeppelmeier *et al.*[390] in 2008. The SHG efficiency of $Bi_2Cu_5B_4O_{14}$ crystal, using 1064 nm radiation, is only about one half time that of KDP. Another new borate Bi_3TeBO_9 with different types of second-order Jahn–Teller distorted cations, *i,e.*, Pb^{2+} and Te^{4+}, was reported by Lin and Li *et al.* in 2016.[391] Bi_3TeBO_9 crystallizes in a polar hexagonal space group of $P6_3$ (no. 173) and exhibits 0D anionic of isolated $[BO_3]$ triangles. The additive contribution from $[BiO_6]$, distorted $[TeO_6]$ octahedra, and π-orbital planar $[BO_3]$ units results in an extremely large powder SHG response of approximately 20 times that of KDP in Bi_3TeBO_9, which is the largest value and sets a new record among borates.[391]

3.5.5. ATB_2O_6 (A = K, Rb, Cs, Tl; T = Nb, Ta), $ASbB_2O_6$ (A = K, Rb), and $K_3T_3B_2O_{12}$ (T = Nb, Ta). The first members of mixed borates in ATB_2O_6 (A = K, Rb, Cs, Tl; T = Nb, Ta) family with A = Rb, Tl and T = Nb, Ta, were reported first by Baucher *et al.* in 1975.[392] More members of this crystal family have continuously been discovered by many laboratories. All present 0D anionic framework of isolated $[B_2O_5]$ units, which approximately reside in the *bc* plane and further interlinked by adjacent octahedral chains that lie approximately along the *a*

https://dx.doi.org/10.1021/acs.chemrev.0c00796
Chem. Rev. 2021, 121, 1130–1202

axis. Owing to the flexibility [TO_6] octahedra and [B_2O_5] units, the member of family is reported to crystallize into the different noncentrosymmetric space groups ranging from the monoclinic *Pc* (no. 7) to orthorhombic $Pmn2_1$ (no. 31), and $Pna2_1$ (no. 33).[393−395] The crystals of $KNbB_2O_6$ and $CsNbB_2O_6$ have been grown by top-seeded solution growth method and subjected to performance measurement.[394,395] The absorption edges of $KNbB_2O_6$ and $CsNbB_2O_6$ crystal occur at 274 and 277 nm, respectively, considerably shorter than those of $LiNbO_3$ (350 nm) and $KNbO_3$ (400 nm). Both crystals were found to have SHG responses about five times that of KDP under 1064 nm but differ in their phase matchability. The SHG with $KNbB_2O_6$ crystal is not critically phase matchable at the fundamental wavelength of 1064 nm, while for $CsNbB_2O_6$, it is phase matchable.[394,395] Birefringence is key when considering the main factor influencing the phase matching wavelength, *i.e.* the $CsNbB_2O_6$ crystal with a larger birefringence (Δn = 0.044@632.8 nm) than $KNbB_2O_6$ crystal (Δn = 0.028@632.8 nm) can result in shorter phase matching wavelength.[394,395]

The $ASbB_2O_6$ (A = K, Rb) crystals were obtained by Mao *et al.* with the space group of *Cc* (no. 9).[89,396] Their structures feature 0D configuration of isolated [B_2O_5] units that are separated by 1D infinite chains of corner-sharing [SbO_6] octahedra, but these phases exhibit very weak SHG responses, which is caused by the small distortion of [SbO_6] octahedra and opposite arrangement of [B_2O_5] units in $ASbB_2O_6$ (A = K, Rb) crystals. The structures of $K_3T_3B_2O_{12}$ (T = Nb, Ta) with the space groups of $Pmc2_1$ (no. 26) and $P\bar{6}2m$ (no. 189) are reported to be NLO active,[397] however, no exact values were given.

3.5.6. $Se_2B_2O_7$, $Zn_8Se_2(BO_2)_{12}$, $PbAsBO_5$, and $Pb_6(AsO_4)(B(AsO_4)_4)$. A newselenite borate $Se_2B_2O_7$ with the symmetry of $P2_12_12_1$ (no. 19) was obtained first by Mao *et al.*, and it was immediately shown to be a promising NLO material.[86] The structure of $Se_2B_2O_7$ features a 0D anionic network with isolated [B_2O_7] units that are interconnected by Se atoms. The SHG measurements reveal that $Se_2B_2O_7$ powder exhibits a moderate SHG efficiency of about 2.2 times that of KDP under 1064 nm. Other crystals in this subsection, including $Zn_8Se_2(BO_2)_{12}$,[398] $PbAsBO_5$,[399] and $Pb_6(AsO_4)B(AsO_4)_4$[399] adopt noncentrosymmetric space groups of $I\bar{4}3m$ (no. 217), $P3_1$ (no. 144), and $P\bar{4}$ (no. 81), respectively, but the related optical properties, including SHG coefficients, transmission spectra, and birefringence have not been reported.

3.6. Borates with d^{10} Transition Metals

3.6.1. $BaZn_2(BO_3)_2$, $Ba_2Zn(BO_3)_2$, and $Ba_5Zn_4(BO_3)_6$. Two new borates, $BaZn_2(BO_3)_2$ and $Ba_2Zn(BO_3)_2$, have been prepared by Smith *et al.* in 1992 and 1994, respectively.[400,401] They belong to the orthorhombic systems of $P2_12_12_1$ (no. 19) and $Pca2_1$ (no. 29). Both form a 0D anionic framework consisting of isolated [BO_3] units that are interlinked by [ZnO_4] tetrahedra (Figures 27a,b). Both experimental and theoretical results confirm that the SHG efficient for $BaZn_2(BO_3)_2$ is quite small and to be only approximately 10% of that of KDP. In contrast, $Ba_2Zn(BO_3)_2$ crystal is theoretically predicted to be NLO active with d_{24} = 0.61 pm/V.[400] In 2016, $Ba_2Zn(BO_3)_2$ crystals were grown by the top-seeded solution growth method under the optimized conditions by Halasyamani *et al.*[402] The $Ba_2Zn(BO_3)_2$ crystal has an absorption edge of 230 nm. The powder SHG measurements reveal the type **I** phase matching behavior under both 1064 and 532 nm laser radiations with the efficiencies of approximately 1.5 × KDP@1064 nm and 0.58 × β-BaB_2O_4@532 nm, respectively.[402] A new member of mixed zincborate $Ba_5Zn_4(BO_3)_6$ has been obtained by Li *et al.* (Figure 27c) in 2017, with the 0D anionic framework of isolated [BO_3] units.[403] It belongs to the acentric space group, *Pc* (no. 7), and its structure is composed of the stacking of [$Zn_4(BO_3)_4O_6$] layers along the *c* axis. The smaller interlayer spacing and stronger bond between these neighboring layers provide $Ba_5Zn_4(BO_3)_6$ a better growth habit without a strong tendency to layer. The absorption edge of $Ba_5Zn_4(BO_3)_6$ crystal is below 223 nm and the SHG efficiency is about 2.6 × KDP at 1064 nm. Such a large SHG response is attributed to the synergistic effects of [ZnO_4] and [BO_3] units.[403] As shown in Figures 27d−f, the [BO_3] NLO active units in these three compounds adopt different arrangements, and they exhibit different SHG efficiencies ranging from 0.1 × KDP in $BaZn_2(BO_3)_2$, 1.5 × KDP for $Ba_2Zn(BO_3)_2$, and 2.6 × KDP in $Ba_5Zn_4(BO_3)_6$.

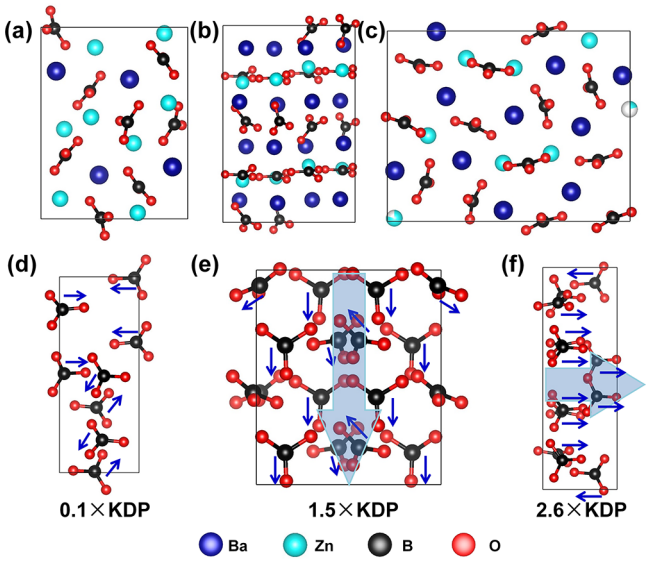

Figure 27. (a−c) Crystal structures of $BaZn_2(BO_3)_2$, $Ba_2Zn(BO_3)_2$, and $Ba_5Zn_4(BO_3)_6$. (d−f) The arrangement of [BO_3] NLO active units in $BaZn_2(BO_3)_2$, $Ba_2Zn(BO_3)_2$, and $Ba_5Zn_4(BO_3)_6$. All of the structure diagrams were drawn by using the crystallographic information file of $BaZn_2(BO_3)_2$ (ICSD: 72193), $Ba_2Zn(BO_3)_2$ (ICSD: 75606), and $Ba_5Zn_4(BO_3)_6$ (ICSD: 254298) in ICSD.

3.6.2. $Cs_3Zn_6B_9O_{21}$ and $CsZn_2B_3O_7$. In 2014, two new noncentrosymmetric zincborates, $Cs_3Zn_6B_9O_{21}$ and $CsZn_2B_3O_7$, were synthesized independently by Pan's and Luo's groups.[404,405] They are the same compounds with a different expression of formula depending on the determintion of *Z* value. Their space group is orthorhombic $Cmc2_1$ (no. 36). They present 0D B−O configurations of isolated planar [BO_3] and [B_3O_6] units that are interlinked by the [ZnO_4] tetrahedra to construct the whole framework with two 1D channels running along the *a* and *c* axes. $Cs_3Zn_6B_9O_{21}$ is transparent down to the UV spectral region with short absorption edges at about 200−218 nm and is phase matchable with powder SHG efficiencies of 1.5−3.3 × KDP at 1064 nm.[404,405] Theoretical analyses reveal that the large SHG effects in $Cs_3Zn_6B_9O_{21}$ originate from the synergistic effects of co-parallel [BO_3] triangles and distorted [ZnO_4] tetrahedra in the $^2[Zn_2BO_3O_2]_\infty$ layers. However, the lack of large crystals

https://dx.doi.org/10.1021/acs.chemrev.0c00796
Chem. Rev. 2021, 121, 1130−1202

makes it difficult for accurate evaluation of its optical properties and applications.

3.6.3. $CdZn_2(BO_3)_2$ and $Cd_3Zn_3(BO_3)_4$. Two new borates, $CdZn_2(BO_3)_2$ and $Cd_3Zn_3(BO_3)_4$, were initially discovered in the ternary phase diagram by Harrison *et al.* in 1959[406] and Whitaker *et al.* in 1993,[407] respectively. Both crystals were recognized to be NLO active by Shen *et al.*[408,409] Both crystals crystallize in the trigonal system, *R*3*c* (no. 161), and exhibit isolated $[BO_3]$ units that are separated by $[ZnO_4]$ and $[CdO_4]$ tetrahedra, in which the coplanar $[BO_3]$ triangles are perpendicular to the *c* axis and tilted in the *ab* plane. The $[BO_3]$ units in two neighboring pseudo-layers orient in almost the same direction and only slightly rotate around the threefold axis. The self-flux system is ideal for the growth of $CdZn_2(BO_3)_2$ and $Cd_3Zn_3(BO_3)_4$ crystals at the temperature below their decomposition points of 834 and 750 °C.[408,409] As large crystals have not been grown large enough, NLO coefficients of 1.04 and 0.96 pm/V have been evaluated from the powder SHG test under 1064 nm laser radiation for $CdZn_2(BO_3)_2$ and $Cd_3Zn_3(BO_3)_4$ compounds, respectively.[408,409]

3.6.4. α-$LiCdBO_3$ and $CsCdBO_3$. The α-$LiCdBO_3$ crystal was reported first in 1978 by Kazanskaya *et al.*[410] and was discovered to be NLO active in 1985 by Chen *et al.*[411] α-$LiCdBO_3$ crystal crystallizes in hexagonal $P\bar{6}$ (no. 174) with 0D anionic framework of isolated $[BO_3]$ triangles with nearly coplanar and aligned arrangement. Powder SHG test confirms the asymmetric structure of α-$LiCdBO_3$, and the SHG effect is estimated to be ~3 × KDP at 1064 nm.[411] In the case of $CsCdBO_3$,[412] it is isostructural to the above $AMBO_3$ (A = K, Rb, Cs; M = Mg, Ca) series with $P2_13$ (no. 198) and shows similar non-phase matching behavior owing to its isotropic nature ($\Delta n = 0$).

3.6.5. $Na_2ZnB_6O_{11}$, $Zn_4B_6O_{13}$, and $Cd_{12}Ge_{17}B_8O_{58}$. $Na_2ZnB_6O_{11}$, a novel hexaborate, has been synthesized and determined structurally by Liang *et al.* in 2010.[413] The compound crystallizes in the monoclinic space group *Cc* (no. 9) with 2D $^2[B_6O_{11}]_\infty$ layers built up from $[B_6O_{12}]$ FBBs. The hexagonal $[B_6O_{12}]$ double-ring is formed by the polymerization of two three-membered $[B_3O_7]$ single rings. Although $Na_2ZnB_6O_{11}$ is reported to have a noncentrosymmetric structure, its NLO properties have not been reported and still need to be further studied. Cubic $Zn_4B_6O_{13}$ is reported to belong to the space group of $I\bar{4}3m$ (no. 217).[210] $Zn_4B_6O_{13}$ (also written as $Zn_4O[B_6O_{12}]$) adopts a 3D $^2[B_6O_{13}]_\infty$ framework with sodalite structures, in which $[B_{24}O_{48}]$ sodalite cage is composed of 24 $[BO_4]$ tetrahedra by sharing O(2) atoms and the whole 3D framework can be extended by sharing the common oxygens in $[B_{24}O_{48}]$ cages. Similar to the other borates in cubic system, $Zn_4B_6O_{13}$ is predicted to be non-phase matchable because of its isotropic nature ($\Delta n = 0$). A new borogermanate, $Cd_{12}Ge_{17}B_8O_{58}$, was obtained by Mao *et al.* in 2011.[414] It belongs to the acentric space group, $P\bar{4}$ (no. 81), and its structure is composed of 0D $[B_2O_7]$ units that are interlinked by 1D $^1[Ge_4O_{16}]_\infty$ chains to form 1D tunnels of five-, six-, and seven-membered rings along the *c* axis that are occupied by the Cd^{2+} cations. But, $Cd_{12}Ge_{17}B_8O_{58}$ shows a very weak SHG response (0.1 × KDP@1064 nm),[414] which is due to the antiparallel arrangements of $[BO_4]$ tetrahedra. Such configuration makes the polarization of $[BO_4]$ units largely cancel with each other and is unfavorable with respect to a large macroscopic polarization.

3.6.6. β-HgB_4O_7, NiB_4O_7, CdB_2O_4, $Ag_3B_5O_9$, Ag_3BO_3, AgB_3O_5, and $Ag_2CsB_{15}O_{24}$. The utilization of high-pressure and high-temperature conditions with Walker-type multianvil apparatuses led to the discovery of three new high pressure borates β-HgB_4O_7,[203] NiB_4O_7,[415] and CdB_2O_4,[416] starting from their corresponding stoichiometric mixtures of oxides by Huppertz *et al.* All three phases are exclusively built up from corner-sharing $[BO_4]$ tetrahedra, forming layers which are interconnected to form final 3D networks. Among them, β-HgB_4O_7[203] is isostructural to the known ambient pressure phases MB_4O_7 (M = Sr, Pb) and the high-pressure phase β-CaB_4O_7 crystallizes in the space group of $Pmn2_1$ (no. 31). In the case of NiB_4O_7 and CdB_2O_4 crystals, they belong to the varied hexagonal space groups of $P6_522$ (no. 179) and $P6_3$ (no. 173), respectively.[415,416] These four silver borates were deduced to be NLO active because they all belong to the noncentrosymmetric space group of $P2_12_12_1$ (no. 19) for $Ag_3B_5O_9$, *R*32 (no. 155) for Ag_3BO_3, $Pna2_1$ (no. 33) for AgB_3O_5, and $P2_12_12$ (no. 18) for $Ag_2CsB_{15}O_{24}$, respectively.[417−420] Unfortunately, all of the above compounds were only subjected to structural chemical analysis without evaluation of NLO characteristics.

3.7. Borates with Mixed d^{10} Transition Metals and SOJT Distorted Cations

3.7.1. $Cd_4BiO(BO_3)_3$. A new mixed metal borate, $Cd_4BiO(BO_3)_3$, has been prepared using the high temperature solid-state reaction by Cheng *et al.* in 2010.[421] The $Cd_4BiO(BO_3)_3$ crystal is isostructural to the $RECa_4O(BO_3)_3$ (RE = rare earth metal) family with the same monoclinic space group of *Cm* (no. 8). Its structure exhibits 0D anionic framework of $[BO_3]$ units that are interconnected *via* corner- or edge-sharing with distorted $[BiO_6]$ and $[CdO_n]$ (n = 6, 7) polyhedra (Figure 28a). One of the most excellent properties of $Cd_4BiO(BO_3)_3$ crystal is its NLO effect. An extremely large, phase matchable SHG intensity of 6.0 × KDP is observed at 1064 nm, much larger than in its isostructural compounds.[421] Such a strong SHG response can be attributed to the cooperative effects of three different NLO chromophores, namely π-delocalized $[BO_3]$ groups (Figure 28b), $[BiO_6]$ octahedra with second-

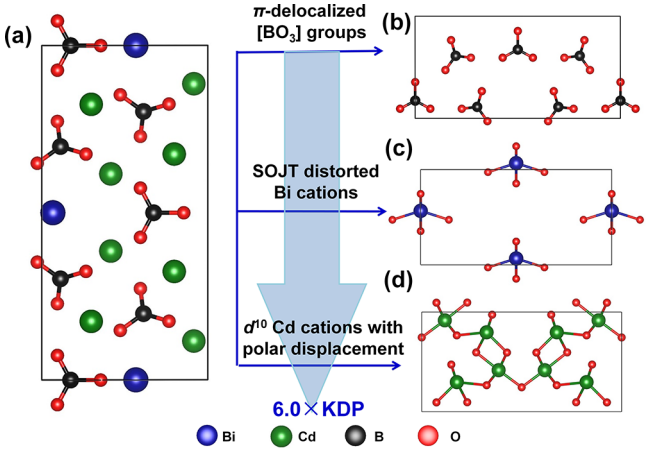

Figure 28. Crystal structure $Cd_4BiO(BO_3)_3$ (a) and the arrangement of its three NLO active chromophores, π-delocalized $[BO_3]$ units (b), $[BiO_6]$ octahedra with SOJT distorted Bi cations (c), and $[CdO_n]$ polyhedra with a polar displacement of d^{10} Cd cations (d). All of the structure diagrams were drawn by using the crystallographic information file of $Cd_4BiO(BO_3)_3$ (ICSD: 248027) in ICSD.

https://dx.doi.org/10.1021/acs.chemrev.0c00796
Chem. Rev. 2021, 121, 1130−1202

order Jahn−Teller (SOJT) distorted Bi cations (Figure 28c), and [CdO_n] polyhedra with a polar displacement of d^{10} Cd cation (Figure 28d),[421] but the related optical properties, including SHG coefficients, transmission spectra, and birefringence, have not been given owing to lack of sufficient large single crystals.

3.7.2. $Bi_2ZnB_2O_7$. A new ternary bismuth borate $Bi_2ZnB_2O_7$ was reported first in 1991 by Liebertz *et al.*[422] and was considered as a potential NLO material in 2005 by Barbier *et al.*[423] The compound crystallizes in the orthorhombic space group of *Pba*2 (no. 32) with 0D anionic framework of isolated [BO_3] triangles. The structure of $Bi_2ZnB_2O_7$ can be regarded as an alternating stacking of $^2[ZnB_2O_7]_\infty$ and $^2[Bi_2O_8]_\infty$ layers along the *c* axis. All of the O atoms directly bond with B atoms, except for O(2) atoms, As a result, $Bi_2ZnB_2O_7$ is an oxyborate with the formula of $Bi_2ZnOB_2O_6$. The [BiO_6] polyhedra in $Bi_2ZnB_2O_7$ are indeed significantly more asymmetric and thus lead to a reduced cancellation of Bi−O bond polarizabilities and a large SHG response of approximately 4.0 × KDP at 1064 nm. $Bi_2ZnB_2O_7$ crystals melt congruently at 692 °C and thus have been grown using a top seeded growth method from stoichiometric melt by Pan *et al.*[424,425] A wide transmission range from 330 to 3000 nm is observed in $Bi_2ZnB_2O_7$ crystals. $Bi_2ZnB_2O_7$ has been proved to be a positive biaxial optical crystal with a large birefringence (Δn = 0.0906@546.1 nm) and wide SHG phase matchable range (~490−2260 nm).[424] The independent NLO coefficients of $Bi_2ZnB_2O_7$ crystal are measured to be d_{31} = (2.34 ± 0.05) × d_{36}(KDP), d_{32} = (7.90 ± 0.16) × d_{36}(KDP), and d_{33} = (2.60 ± 0.06) × d_{36}(KDP) by the Maker fringes method at 1064 nm.[425] Unfortunately, the largest NLO coefficient d_{32} is not included in the effective NLO coefficient formula and cannot be used to improve the SHG conversion efficiency. Theoretical analyses indicate that the contributions of [BiO_6] and [B_2O_5] NLO-active units are dominant in $Bi_2ZnB_2O_7$ crystals for producing the large microscopic second-order susceptibilities.[426]

3.7.3. α-, β-, and γ-$Pb_2Ba_4Zn_4B_{14}O_{31}$. The first examples of a borate with all polar polymorphs were achieved in the $Pb_2Ba_4Zn_4B_{14}O_{31}$ family by Pan and Halasyamani *et al.* in 2015.[427] These three polar polymorphs, α-, β-, and γ-$Pb_2Ba_4Zn_4B_{14}O_{31}$, were structurally solved to belong to the polar space group of triclinic *P*1 (no. 1), monoclinic *Cc* (no. 9), and trigonal $P3_2$ (no. 145), respectively. All of them are constructed by two types of 0D isolated units, [B_2O_5] and [B_6O_{13}]. Their whole structures can be formed by alternating stacking of $^2[Pb_2B_2O_5]_\infty$ and $^2[Zn_4B_{12}O_{26}]_\infty$ layers along the *c* axis. In $^2[Pb_2B_2O_5]_\infty$ layers, all the isolated [B_2O_5] units possess the same orientation that are interconnected by the [PbO_n] polyhedra. In the case of $^2[Zn_4B_{12}O_{26}]_\infty$ layers, there are two types of [B_6O_{13}] units with different orientations that are further connected by [ZnO_4] tetrahedra and dimeric [Zn_2O_6] units. The experimental and theoretical evaluations of SHG properties reveal that three polar polymorphs exhibit moderate SHG efficiency of about 0.6−1.1 times that of KDP.[427] The [PbO_n] polyhedra were shown to give greater contribution to SHG response than other asymmetric units.

3.8. Borates with Other Metals

3.8.1. $BaAl_2B_2O_7$ and $SrAl_2B_2O_7$. A new barium aluminum borate $BaAl_2B_2O_7$ with trigonal space group *R*32 (no. 155) was initially reported by Chen *et al.* in 1998 and immediately shown to be a novel NLO material.[428] The crystal structure of $BaAl_2B_2O_7$ is characterized by $^2[Al_2B_2O_7]_\infty$ double-layers built from isolated [BO_3] triangles and [AlO_4] tetrahedra with Ba cations between those layers for charge balance. $BaAl_2B_2O_7$ crystals melt incongruently and thus have been grown by the top seeded flux method. Optical measurement on $BaAl_2B_2O_7$ crystals reveals a short UV absorption edge of 180 nm. The powder SHG response is about 1.7 times that of KDP at 1064 nm, and d_{11} was measured to be 0.75 pm/V.[429] The derived birefringence is 0.05 at 1064 nm for $BaAl_2B_2O_7$ crystal and which is sufficient for the phase matching in the SHG process with a 1064 nm incident laser, which is in good agreement with the powder SHG measurements. The structure of $SrAl_2B_2O_7$ is reported to be isostructural to that of $BaAl_2B_2O_7$, but no more optical properties have been given.

3.8.2. $K_2Al_2B_2O_7$, β-$Rb_2Al_2B_2O_7$, $K_2T_2B_2O_7$ (T = Ga, Fe), and β-$SrGaBO_4$. The structure of $K_2Al_2B_2O_7$ was redetermined nearly simultaneously as NLO active trigonal *P*321 (no. 150) rather than a hexagonal space group by both the Chen's[429] and Hu's[430] groups independently. Similar to $BaAl_2B_2O_7$, $K_2Al_2B_2O_7$ has $^2[Al_2B_2O_7]_\infty$ double-layers that are stacked along the *c* axis, in which the [BO_3] groups are in a coplanar arrangement, extending in the *ab* plane with their three terminal oxygen atoms linked with [AlO_4] tetrahedra. $K_2Al_2B_2O_7$ crystals have been grown by the top-seeded solution growth method with NaF as a flux. The $K_2Al_2B_2O_7$ crystal is transparent far into the deep-UV region (180−3600 nm), which can be phase matchable for both type **I** SHG and FHG at 1064 nm due to the large birefringence of Δn = 0.070@1064 nm.[431] The shortest wavelength of type **I** SHG is calculated to be 232.5 nm using the derived Sellmeier equations. The NLO coefficient and laser damage threshold are found to be d_{11} = 0.45 pm/V and 15 GW/cm^2 under 10 ns pulses at 1064 nm, respectively.[431] The UV beam at 266 nm was obtained by FHG of 1064 nm Nd:YAG laser radiation through a $K_2Al_2B_2O_7$ crystal for the first time with a optical conversion efficiency of 13%.[432] Unfortunately, for a long time, $K_2Al_2B_2O_7$ crystal is shown to exhibit abnormal UV absorption around 230 nm, which is proved to be caused by Fe impurities and thus reduce the conversion efficiency from 532 to 266 nm. Faced with this, large and optically perfect $K_2Al_2B_2O_7$ crystals were grown in a non-oxygen atmosphere by Chen *et al.* in 2011 for the first time,[433] which effectively eliminated the abnormal absorption in UV spectral region. By using the as-grown $K_2Al_2B_2O_7$ crystal, a 280 mW average output power was obtained through FHG with a conversion efficiency as high as 33.4%,[433] which is much higher than the above values.

β-$Rb_2Al_2B_2O_7$ was reported to exhibit a similar structure to its isostructural $K_2Al_2B_2O_7$ by Halasyamani *et al.* in 2017.[434] The β-$Rb_2Al_2B_2O_7$ polycrystalline exhibits a wide transparency window with a short absorption below 200 nm. Powder SHG tests of β-$Rb_2Al_2B_2O_7$ using 1064 and 532 nm radiation revealed stronger SHG efficiencies of approximately 2 × KDP and 0.4 × β-BaB_2O_4, respectively.[434] The enhancement of SHG response in β-$Rb_2Al_2B_2O_7$ compared with $K_2Al_2B_2O_7$ is interpreted as the results of two factors: (1) the more eclipsed and planar arrangement of [BO_3] NLO active units and (2) the greater cation variance.[434] To date, the SHG coefficients and birefringence of β-$Rb_2Al_2B_2O_7$ are still unknown, only the theoretical values are given.

Although $K_2T_2B_2O_7$ (T = Ga, Fe) crystals are isostructural with $K_2Al_2B_2O_7$, there are still no further reports on their crystal growth and optical properties.[435,436] The SHG response

https://dx.doi.org/10.1021/acs.chemrev.0c00796
Chem. Rev. 2021, 121, 1130−1202

Table 5. Structural Information and Optical Properties of a Series of Mixed Alkali Metal Borogermanates[a]

formula	sace group	anionic framework	SHG response (×KDP)	bandgap
$Rb_2GeB_4O_9$	$P2_1$	0D [B_4O_9]	2.0	5.54 eV
$Cs_2GeB_4O_9$	$I\bar{4}$	0D [B_4O_9]	2.8	6.26 eV
$K_2Ge_3B_2O_{10}$	$C2$	0D [BO_4]	weak	5.38 eV
$Rb_4Ge_3B_6O_{17}$	Cc	0D [B_3O_7]	1.3	5.42 eV
$RbGeB_3O_7$	$Pna2_1$	0D [B_3O_7]	1.3	5.58 eV
$CsGeB_3O_7$	$Pna2_1$	0D [B_3O_7]	1.5	5.76 eV
KGe_2BO_6	$P2_12_12_1$	0D [BO_4]	N/A	N/A
$Ca_{10}Ge_{16}B_6O_{51}$	$Pba2$	0D [BO_4] + 0D [B_2O_7]	weak	5.47 eV
$Ca_{12}Ge_{17}B_8O_{58}$	$P\bar{4}$	0D [B_2O_7]	weak	N/A

[a]All the data were collected from refs 92,414,441−445. N/A means not given in the related reference.

of $K_2Fe_2B_2O_7$ is reduced to only about 0.4 times that of KDP,[435] which is due to the opposite arrangement of [BO_3] NLO active units between the adjacent layers of $K_2Fe_2B_2O_7$. Besides, a new compound, β-$SrGaBO_4$, has been obtained through the solid phase transition from α-$SrGaBO_4$ at high temperatures by Yang *et al.* in 2002.[437] Owing to the lack of suitable single crystals, the crystal structure of β-$SrGaBO_4$ was determined using powder X-ray diffraction techniques. It has an orthorhombic space group of $P2_12_12$ (no. 18) with 0D isolated [BO_3] units. The powder SHG measurement confirms its noncentrosymmetric feature and the corresponding efficiency is only about 0.5 × KDP at 1064 nm.

3.8.3. $BaZr(BO_3)_2$, $BaHf(BO_3)_2$, $Al_5(BO_3)O_6$, and $Ba_3Ti_3O_6(BO_3)_2$. Two isostructural borates with 0D anionic framework of isolated [BO_3] units, $BaZr(BO_3)_2$ and $BaHf(BO_3)_2$, have been prepared.[438] They crystallize in the trigonal system of $R3c$ (no. 161), and show the dolomite-like structure doubled in the c direction, which is built up by alternating layers of [HfO_6] octahedra and [BaO_6] distorted trigonal prisms that are further linked by [BO_3] triangles. Structural analyses show that the deviations from centrosymmetric structure are small for both crystals, which indicate the SHG effects of them might be weak, but no exact values are given.[438] $Al_5(BO_3)O_6$ crystallizes in the polar noncentrosymmetric space group, $Cmc2_1$ (no. 36), with 0D isolated [BO_3] units that are linked by distorted [AlO_n] (n = 4-6) polyhedra. The SHG intensity of $Al_5(BO_3)O_6$ crystal is observed to be only 0.2 times that of KDP and is not phase matchable, which is due to the relatively small birefringence (cal. Δn = 0.02).[439]

The $Ba_3Ti_3O_6(BO_3)_2$ crystal has been reformulated from previously reported $Ba_2Ti_2B_2O_9$ by Barbier *et al.* in 2003.[440] The crystal structure has been re-determined to a hexagonal system of $P\bar{6}2m$ (no. 189). Its structure consists of 0D isolated [BO_3] groups which are interlinked by [TiO_6] octahedra. The Ba cations locate in the irregular pentagonal tunnels parallel to the c axis. All of the [BO_3] triangles in $Ba_3Ti_3O_6(BO_3)_2$ exhibit a strictly planar, regularly triangular geometry and are parallel to [100] and [110] two-fold axes of the structure with only a small twist angle of 3.1°, such a configuration is favorable for inducing large SHG coefficients. The SHG efficiency of $Ba_3Ti_3O_6(BO_3)_2$ is found to be about 0.95 × $LiNbO_3$ at 1064 nm.[440] Apart from the [BO_3] NLO active units, the asymmetrical Ti−O bonds in the [TiO_6] octahedra also contribute to the large SHG efficiency of $Ba_3Ti_3O_6(BO_3)_2$.

3.8.4. $A_2GeB_4O_9$, $AGeB_3O_7$, $Rb_4Ge_3B_6O_{17}$, $K_2Ge_3B_2O_{10}$, KGe_2BO_6, $Ca_{10}B_6Ge_{16}O_{51}$, $Ca_{12}Ge_{17}B_8O_{58}$, and $LiGeBO_4$ (A = Rb, Cs). Six noncentrosymmetric alkali metal borogermanates have been obtained *via* the high-temperature solid-state reactions by Mao *et al.* from 2008 to 2013.[92,441,442] They crystallize into the varied noncentrosymmetric space groups, monoclinic $P2_1$ (no. 4) for $Rb_2GeB_4O_9$,[92] $C2$ (no. 5) for $K_2Ge_3B_2O_{10}$,[441] Cc (no. 9) for $Rb_4Ge_3B_6O_{17}$,[92] orthorhombic $Pna2_1$ (no. 33) for $AGeB_3O_7$ (A = Rb, Cs),[92] and tetragonal $I\bar{4}$ (no. 82) for $Cs_2GeB_4O_9$,[442] respectively (Table 5). Their structures are all characterized by 0D B−O anionic frameworks of [BO_3] triangles, [BO_4] units, [B_3O_7] three-membered rings, and [B_4O_9] double-rings for different borogermanates. They are all transparent down to the UV region, with the large bandgaps ranging from 5.38 to 6.26 eV, corresponding to the absorption edges from 230 to 198 nm (Table 5).[92,441,442] The powder SHG measurements at 1064 nm revealed the type **I** phase matching behavior and efficiencies of approximately 1.3 × KDP for $RbGeB_3O_7$ and $Rb_4Ge_3B_6O_{17}$, 1.5 × KDP for $CsGeB_3O_7$, 2.0 × KDP for $Rb_2GeB_4O_9$, and 2.8 × KDP for $Cs_2GeB_4O_9$, respectively,[92,441,442] whereas the SHG signal of $K_2B_2Ge_3O_{10}$ is very weak to be detected. The difference among them is due to the alignment of varied B−O anionic clusters and also their density in unit cell. Other members of borogermanates, namely, KGe_2BO_6 ($P2_12_12_1$, no. 19),[443] $Ca_{10}B_6Ge_{16}O_{51}$ ($Pba2$, no. 32),[414] $Ca_{12}Ge_{17}B_8O_{58}$ ($P\bar{4}$, no. 81),[444] and $LiGeBO_4$ ($I\bar{4}$, no. 82)[445] were also reported to exhibit noncentrosymmetric structures, but they all show weak or non-phase matching SHG efficiencies (Table 5).

3.8.5. $Li_6CuB_4O_{10}$. The extensive search in the unexplored Li_2O-CuO-B_2O_3 ternary system has led to the discovery of $Li_6CuB_4O_{10}$ by Poeppelmeier *et al.* in 2006.[446] $Li_6CuB_4O_{10}$ crystallizes in the noncentrosymmetric space group $P1$ (no. 1) and contains isolated pseudo-symmetric [CuB_4O_{10}] polyanions which are interconnected by [LiO_4] polyhedra. $Li_6CuB_4O_{10}$ crystal melts congruently and as such bulk single crystals can, in principle, be grown from its stoichiometric melts. Because $Li_6CuB_4O_{10}$ lacks a center of symmetry, it exhibits distinct NLO efficiency which is similar to that of KDP and is also phase matchable under 1064 nm.[446] The SHG coefficients and birefringence have not been reported due to the lack of large $Li_6CuB_4O_{10}$ crystals, but the Cu atom has a serious absorption in the UV spectral region, which limits its application as UV NLO materials.

3.8.6. Borates without Evaluation of NLO Properties. In this subsection, there are still several noncentrosymmetric metal borates, to our best knowledge, which are not to be given NLO performance characterization. Regardless of the extensive study on the synthetic methods and structural features, their NLO properties are poorly examined (Tables S1−S4 in the SI). They include CuB_2O_4 ($I\bar{4}2d$, no. 122, ICSD: 9087), PdB_2O_4 ($I\bar{4}2d$, no. 122, ICSD: 32539), Fe_2BO_4 (Pc, no. 7, ICSD: 417972), $LiMnBO_3$ ($P\bar{6}$, no. 174, ICSD: 94318), $CaAlBO_4$ ($Ccc2$, no. 37, ICSD: 27647), $CaGaBO_4$ ($Ccc2$, no.

https://dx.doi.org/10.1021/acs.chemrev.0c00796
Chem. Rev. 2021, 121, 1130−1202

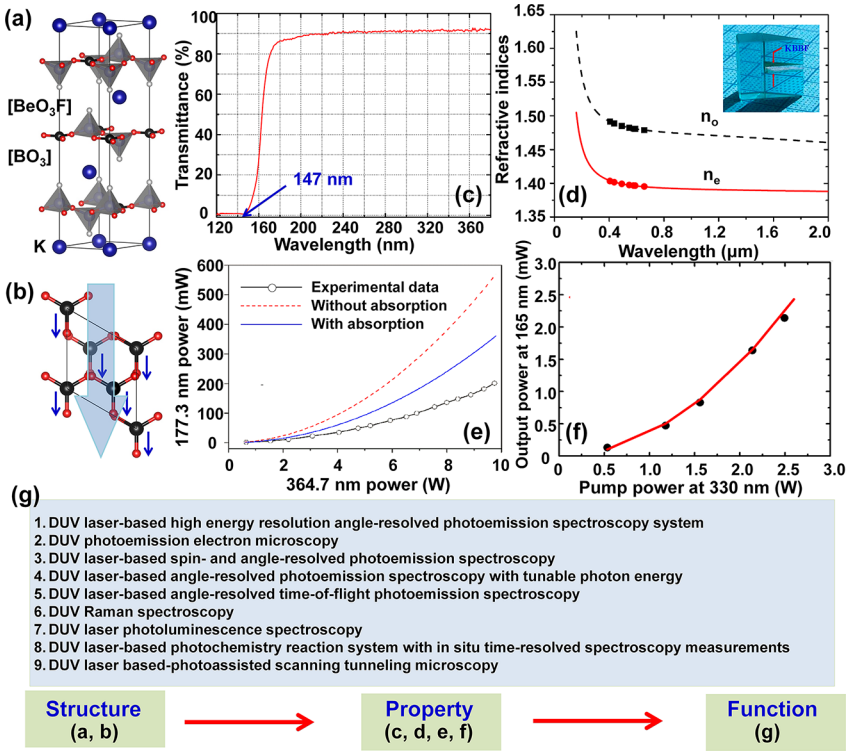

Figure 29. Diagrammatic sketch from structure (a,b), property (c–f) to function (g) by taking the classic $KBe_2BO_3F_2$ NLO crystal as a representative. (a) Crystal structure of $KBe_2BO_3F_2$. (b) Optimally aligned arrangement of $[BO_3]$ NLO active units in $KBe_2BO_3F_2$. (c) Transmittance spectrum of $KBe_2BO_3F_2$ crystal in the UV spectral region from 120 to 380 nm. Reproduced with permission from ref 27, Copyright 2009 Springer-Verlag. (d) Dispersion of the refractive indices (n_o and n_e). Insert gives the photograph of the $KBe_2BO_3F_2$-based prism. Reproduced with permission from ref 27, Copyright 2009 Springer-Verlag. (e) Output power of six-harmonic generation at 177.3 nm versus the 354.7 nm pump power for $KBe_2BO_3F_2$ crystal (1.58 mm in thickness). The pulse width and repetition rate are 10 ps and 1 MHz, respectively. Reproduced with permission from ref 457, Copyright 2015 Springer-Verlag. (f) Deep-UV output power at 165 nm versus pump power at 330 nm for $KBe_2BO_3F_2$ crystal with an effective length of 2.7 mm. The experimental and simulated data are shown in black and red, respectively. Reproduced with permission from ref 458, Copyright 2016 Institute of Physics. (g) Nine advanced instruments based on the deep-UV diode pumped solid-state laser that is generated by $KBe_2BO_3F_2$ crystals. Parts a and b were drawn by using the crystallographic information file of $KBe_2BO_3F_2$ (ICSD: 77277) in ICSD.

37, ICSD: 93390), $CaB_2U_2O_{10}$ (*C*2, no. 5, ICSD: 62751), $AsBO_4$ polymorphs ($I\bar{4}$, no. 82, ICSD: 26891; $P3_221$, no. 154, ICSD: 413436), $BaAsBO_5$ ($P3_1$, no. 144, ICSD: 404439), UB_2O_6 (*C*2, no. 5, ICSD: 248127), $Co_4B_6O_{13}$ ($I\bar{4}3m$, no. 217, ICSD: 96561), $CsAl_4Be_4B_{12}O_{28}$ ($P\bar{4}3m$, no. 215, ICSD: 17018), $BaCuB_2O_5$ (*C*2, no. 5, ICSD: 84683), and $SrCu_2B_2O_6$ polymorphs (*I*4*cm*, no. 108, ICSD: 247206; $I\bar{4}2c$, no. 120, ICSD: 247205; $I\bar{4}2m$, no. 121, ICSD: 80592).

3.9. Halide containing Metal Borates

3.9.1. Borate Halides. *3.9.1.1. $ABe_2BO_3F_2$ (A = Na, K, Rb, Cs, Tl, NH_4).* The structures of $ABe_2BO_3F_2$ (A = K, Rb, Cs) were thought initially to crystallize in monoclinic *C*2 (no. 5),[447,448] but this was corrected to trigonal *R*32 (no. 155) by Chen *et al.*[27] Except Na analogue in *C*2 (no. 5),[448,449] other members in this family with the composition of A = K, Rb, Cs, Tl, NH_4 belong to trigonal *R*32 (no. 155).[27,450−452] All of them exhibit 0D isolated $[BO_3]$ units that are linked by the fluorinated $[BeO_3F]$ tetrahedra to form $^2[Be_2BO_3F_2]_\infty$ single layers with the A-site cations resided between the layers, in which the weak A−F (A = Na, K, Rb, Cs) or N−H bonds serve as linkers to connect the adjacent single layers (Figure 29a). The strong layering tendency in $ABe_2BO_3F_2$ (A = Na, K, Rb, Cs, Tl, NH_4) family is observed, and the largest thickness of as-grown $KBe_2BO_3F_2$ crystals with high optical quality is reoported to be only 3.7 mm.[453] More importantly, the $[BO_3]$ triangles in this family are aligned optimally (Figure 29b), which is beneficial to obtain large optical anisotropy and hyper-polarizability, corresponding to a large birefringence (Figure 29d) and high NLO coefficients. Besides, the dangling bonds of $[BO_3]$ triangles in them are effectively eliminated by the rigid $[BeO_3F]$ tetrahedra, which can help to obtain the blue-shifted deep-UV absorption edges (Figure 29c). Thus, the $ABe_2BO_3F_2$ (A = Na, K, Rb, Cs, Tl, NH_4) family possess excellent linear and NLO properties, including short deep-UV absorption edges (147−155 nm), moderate SHG efficiencies (1.15−1.5 × KDP at 1064 nm), large birefringence (Δn = 0.057−0.077), and short type **I** SHG phase matching wavelengths (161−202 nm).[27,449−452] These excellent optical properties make this family promising candicates that could produce UV or deep-UV coherent light by the direct SHG process.

Thus, the quasi-continuous wave output has been achieved by using optically contacted, prism-coupled $KBe_2BO_3F_2$ crystals by Togashi *et al.* The maximum output power of this process is about 2.5 mW in 2003 and is increased to 12.95 mW in 2008 by optimizing the laser system and conditions.[454,455] Meanwhile, they also achieved the second harmonic generation with a frequency-doubled laser at 172.5 nm and sum-frequency mixing laser at 163.3 nm. Soon after that, an average output power as much as 1.2 W at 200 nm by using $KBe_2BO_3F_2$

https://dx.doi.org/10.1021/acs.chemrev.0c00796
Chem. Rev. 2021, 121, 1130−1202

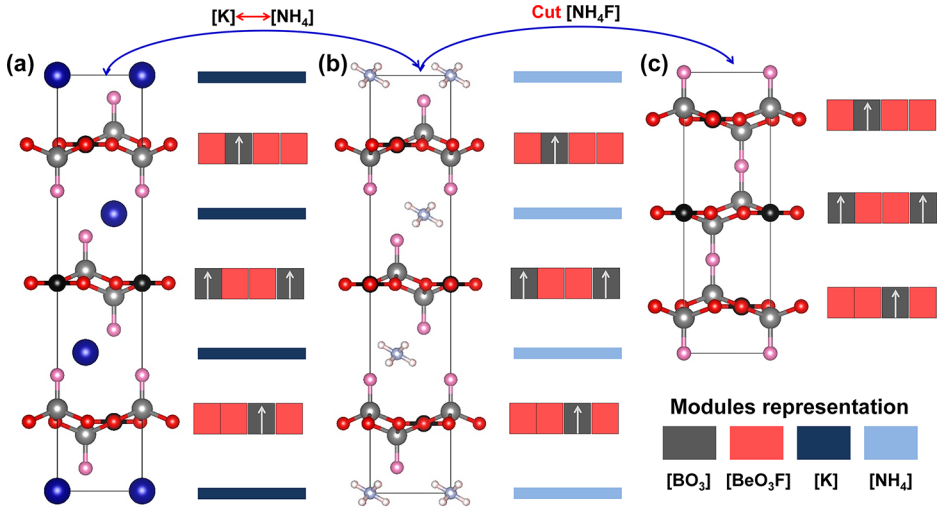

Figure 30. Structural evolution from (a) $KBe_2BO_3F_2$ to (b) $NH_4Be_2BO_3F_2$ to (c) γ-Be_2BO_3F. The modular descriptions are given on the right side of each crystal structure. Parts a–c were drawn by using the crystallographic information file of $KBe_2BO_3F_2$ (ICSD: 77277) in ICSD. $NH_4Be_2BO_3F_2$ and γ-Be_2BO_3F from ref 452

crystals has been generated by Kanai *et al.* in 2009.[456] Watt-level tunable average-power was generated in the deep-UV region from 185 to 200 nm. Then the output power of 200 mW at 177.3 nm has been generated by Lin *et al.* in 2015, which is the highest power at 177.3 nm ever generated in any NLO crystals (Figure 29e).[457] In the case of $RbBe_2BO_3F_2$ crystal, a high average power was achieved with the tunable wavelengths ranging from 180 to 232.5 nm by Wang *et al.* in 2008. The output power over the whole wavelength range exceeds 2 mW, the highest being 43.3 mW at 202.5 nm. For the deeper region, emission below 170 nm was demonstrated first in 2015 and then a 165 nm laser was generated with the output power of mW level by the eighth harmonic generation process within the 1319 nm Nd:YAG laser by Xu *et al.* in 2016 by $KBe_2BO_3F_2$ crystal (Figure 29f).[458] Thus, we can come to the conclusion that, currently, as an NLO material, $KBe_2BO_3F_2$ crystal is probably the best in all of its deep-UV applications. More importantly, several laser systems and advanced instruments have been developed based on $KBe_2BO_3F_2$ crystals (Figure 29g), which lead to the observation of various new phenomena and the amassment of new data in the fields of high temperature superconductivity, topological electronics, Fermi semi-metals, and so forth.[459]

3.9.1.2. $NaCaBe_2B_2O_6F$, $ASr_3Be_3B_3O_9F_4$ (A = Li, Na), $BaBe_2BO_3F_3$, and Be_2BO_3F Polymorphs. To obtain new competitive NLO candidates with improved growth habit and structural stability, studies have been concentrated on the beryllium borate fluorides by Chen *et al.* and Ye *et al.* Several new noncentrosymmetric beryllium borate fluorides, including $NaCaBe_2B_2O_6F$ (*Cc*, no. 9),[460] $ASr_3Be_3B_3O_9F_4$ (A = Li, Na; Li analogue is not included in ICSD) (*R*3*m*, no. 160),[461,462] $BaBe_2BO_3F_3$ ($P6_3$, no. 173),[463] and Be_2BO_3F (*C*2, no. 5 and *R*32, no. 155 for α and γ phases; γ phase is not included in ICSD)[452,464] polymorphs, have been prepared, which show $KBe_2BO_3F_2$- or $Sr_2Be_2B_2O_7$-like structures. All of them present 0D anionic framework of isolated $[BO_3]$ units that are connected by fluorinated $[BeO_3F]$ tetrahedra to form varied framework, *i.e.*, $^2[Be_3B_3O_6F_3]_\infty$ double-layers in NaCa-$Be_2(BO_3)_2F$,[460] $^3[Be_3B_3O_9F]_\infty$ framework in $ASr_3Be_3B_3O_9F_4$ (A = Li, Na),[461,462] $^2[Be_2BO_3F_2]_\infty$ single layers in $BaBe_2BO_3F_3$,[463] and $^2[Be_2BO_3F_2]_\infty$ single layers in Be_2BO_3F polymorphs.[452,464]

The $[BO_3]$ NLO active units in $ASr_3Be_3B_3O_9F_4$ (A = Li, Na) and γ-Be_2BO_3F are nearly coplanar and aligned with the same orientations to produce large optical anisotropies and SHG responses of 4, 2.2, and 2.3 × KDP at 1064 nm, respectively,[461,462] whereas in α-Be_2BO_3F and NaCa-$Be_2(BO_3)_2F$, they adopt opposite orientations. Thus, these two compounds possess discrepant SHG intensities compared with other crystals in this subsection with low SHG efficiencies of 0.1 and 0.4 × KDP for $BaBe_2BO_3F_3$[463] and NaCa-$Be_2(BO_3)_2F$,[460] respectively. Besides, all the crystals in this class also have a wide transparent range with deep-UV absorption edges far from 200 nm, *i.e.*, $NaCaBe_2B_2O_6F$ (190 nm),[460] $NaSr_3Be_3B_3O_9F_4$ (170 nm),[461] $LiSr_3Be_3B_3O_9F_4$ (175 nm),[462] $BaBe_2BO_3F_3$ (<185 nm),[463] and γ-Be_2BO_3F (<190 nm).[452] Structurally, γ-Be_2BO_3F (Figure 30) can be regarded as the derivative of successive evolution from $KBe_2BO_3F_2$, which retains the NLO favorable configuration of $KBe_2BO_3F_2$ and also the layering tendency was greatly improved. Among them, large size $NaSr_3Be_3B_3O_9F_4$ crystals were grown and subjected to linear and NLO properties characterization in great detail by Liu *et al.*,[465] indicating that $NaSr_3Be_3B_3O_9F_4$ crystal does allow achieving 266 nm UV light by simple frequency doubling of second harmonic from the fundamental laser at 1064 nm. On the basis of this, the 266 nm laser output in $NaSr_3Be_3B_3O_9F_4$ crystal by the FHG process has been generated for the first time by Liu *et al.* in 2017.[466] Within this process, a 280 μJ 266 nm UV laser was obtained with the conversion efficiency of 35.9%. Soon after, also by Liu *et al.*, they obtained higher output power of 1.6 W at the wavelength of 266 nm with the conversion efficiency of 10.3% by using $NaSr_3Be_3B_3O_9F_4$ crystals.[467]

3.9.1.3. $M_5(BO_3)_3X$ (M = Ca, Sr, Ba, Pb, Cd, Eu; X = F, Cl, Br). The first apatite-type borate, $Ca_5(BO_3)_3F$, was obtained by Lei *et al.* in 1989 with noncentrosymmetric space group *Cm* (no. 8).[468] Its structure consists of 0D isolated $[BO_3]$ units that are further linked by $[CaO_4F_2]$ octahedra to form a 3D network. All the planar $[BO_3]$ triangles lie approximately parallel to *ab* plane with the same orientation and thus can produce large optical anisotropy. Structurally, $Ca_5(BO_3)_3F$

https://dx.doi.org/10.1021/acs.chemrev.0c00796
Chem. Rev. 2021, 121, 1130–1202

crystal is isostructural to $RECa_4O(BO_3)_3$ (RE = rare earth metals) series and it can be considered as the derivative from $RECa_4O(BO_3)_3$ because RE is substituted by Ca and partial O atoms are replaced by F to preserve the electroneutrality. Contrarily to $RECa_4O(BO_3)_3$ series, $Ca_5(BO_3)_3F$ crystal does not present a congruent melting behavior, and thus it can be grown by top seeded solution method with 10−20 wt % of LiF as a flux. A wide transmission range is observed in as-grown $Ca_5(BO_3)_3F$ crystals with the UV cutoff wavelength near 190 nm, which is shorter than those of the $RECa_4O(BO_3)_3$ family. The $Ca_5(BO_3)_3F$ crystal is a negative biaxial optical crystal with a large birefringence of 0.053 at 589 nm, which shifts the shortest type **I** SHG wavelength to 289 nm.[469,470] That indicates that $Ca_5(BO_3)_3F$ crystal cannot be used to generate 266 nm UV light by simple frequency doubling from the second harmonic of fundamental laser at 1064 nm. The largest second-order NLO coefficient d_{eff} (0.63 pm/V) locates in the XY plane for type **II** process.[469,470]

Since then, borates with apatite family are considered as a new source of NLO materials, thus, more members with the formula of $M_5(BO_3)_3X$ (M = Ca, Sr, Ba, Cd, Eu; X = F, Cl, Br) have been characterized. The compounds in this family are very similar in their architectures but are distinct in a crystallized noncentrosymmetric space group and cation coordinates. For example, $Mg_5(BO_3)_3F$ with orthorhombic $Pna2_1$ (no. 33),[471] $M_5(BO_3)_3X$ and $Pb_2Ba_3(BO_3)_3X$ (M = Sr, Ba; X = Cl, Br) with orthorhombic $C222_1$ (no. 20),[472−476] and $Ca_5(BO_3)_3F$ with monoclinic Cm (no. 8).[468] The SHG effects in this family are quite distinct, varying from 0.5 × KDP in $Ba_5(BO_3)_3Cl$ to 3.8 × KDP in $Ca_5(BO_3)_3F$, that are tuned by the M and X site atoms. It is worth noting that the phase matching SHG efficiencies of $Pb_2Ba_3(BO_3)_3X$ (X = Cl, Br) series are found to be 3.2 and 3.1 times that of KDP at 1064 nm, respectively,[474,475] and as high as six times that of isomorphic $Ba_5(BO_3)_3Cl$. The enhanced SHG response mainly originates from a unique edge-sharing connection between Pb−O and $[BO_3]$ NLO-active units.[474]

3.9.1.4. $M_3B_6O_{11}F_2$ (M = Sr, Ba, Pb) and $Ba_4B_{11}O_{20}F$. Three fabianite-like borate fluorides with different templating cations were synthesized by Kolis *et al.*[477] and Pan *et al.*[478−480] in 2012. They are isostructural and belong to the same monoclinic $P2_1$ (no. 4) with the 3D $^3[B_6O_{11}]_\infty$ anionic framework that is built up by $[B_6O_{14}]$ FBBs.[477−480] The F atoms are coordinated to $[FM_3]$ secondary building blocks that are further linked to form 2D $[F_2M_3]$ infinite layers with the same orientation. The phase matching SHG efficiencies of this family are detected to be approximately 2.5, 3.0, and 4.0 × KDP under the incident lasers at 1064 nm for Sr, Ba, and Pb analogues, respectively[477−480] The absorption edges for the three borate fluorides are reported to be below 230 nm without given accurate values due to lack of large size crystals. The positive roles of F atoms on absorption edges and SHG effects were confirmed *via* theoretical approaches. Attributable to the lack of large single crystals, SHG coefficients and birefringence have not been reported in the experiment for the $M_3B_6O_{11}F_2$ (M = Sr, Ba, Pb) series.

$Ba_4B_{11}O_{20}F$ with a polar structure ($Cmc2_1$, no. 36, not included in ICSD) was designed and synthesized by Pan *et al.* in 2013.[481] It features 3D B−O open framework constructed by $[B_{21}O_{24}]$ FBBs with the Ba−F−Ba infinite chains filled in the tunnels and Ba-based polyhedra situated in the periphery of tunnels. The $Ba_4B_{11}O_{20}F$ crystals with high optical homogeneity were grown at the optimal conditions by Pan *et al.* and Halasyamani *et al.*[482] $Ba_4B_{11}O_{20}F$ crystal fully achieves the coexistence a short absorption edge (190 nm) and large SHG coefficients (d_{31} = 1.57, d_{32} = 0.27, and d_{33} = 0.46 pm/V),[482] but, its relatively low birefringence of Δn = 0.0146@ 1064 nm makes $Ba_4B_{11}O_{20}F$ incapable of producing outout shorter wavelength, like 266 and 355 nm or lower than that, within the direct SHG method.

3.9.1.5. Pb_2BO_3X and $M_2B_5O_9X$ (M = Ca, Sr, Ba, Pb, Eu; X = Cl, Br, I). The first member in the Pb_2BO_3X(X = Cl, Br, I) family, Pb_2BO_3Cl, was discovered by Ok *et al.* in 2016.[483] It crystallizes in the trigonal polar space group $P321$ (no. 150) with 0D anionic framework of isolated $[BO_3]$ units. The planar $[BO_3]$ triangles are linked by $[PbO_3]$ trigonal pyramids to build honeycomb-like $^2[Pb_2BO_3]_\infty$ single layers in the *ab* plane with the Cl^- anions resided in the interlayer space. The remarkably strong and type **I** phase matching SHG response of about 9.0 × KDP is detected in Pb_2BO_3Cl crystal,[483] which is mainly activated by the p−π interactions between Pb and $[BO_3]$ triangles. Soon after, the Br and I analogues, Pb_2BO_3Br and Pb_2BO_3I, were obtained by Ye *et al.*[484] and Halasyamani *et al.* in 2018.[485] Both members are found to be isostructural to Pb_2BO_3Cl with trigonal $P321$ (no. 150) and exhibit similar structural features. The SHG efficiencies are observed to slightly increase to 9.5 and 10 × KDP for Br and I analogues, respectively, and thus the nonlinearity in the Pb_2BO_3X (X = Cl, Br, I) family is considered to be equivalent (Table 6).[484,485]

Table 6. Basic Properties of Two Isostructural Series, Pb_2BO_3X and $Pb_2B_5O_9X$ (X = Cl, Br, I)[a]

formula	space group	anionic framework	SHG response (× KDP)	bandgap (eV)
Pb_2BO_3Cl[483]	$P321$	0D $[BO_3]$ units	9.0	3.99
Pb_2BO_3Br[484]	$P321$	0D $[BO_3]$ units	9.5	3.33
Pb_2BO_3I[485]	$P321$	0D $[BO_3]$ units	10.0	~3.45
$Pb_2B_5O_9Cl$[130]	$Pnn2$	3D $^3[B_5O_9]_\infty$ network	0.7	3.33
$Pb_2B_5O_9Br$[130]	$Pnn2$	3D $^3[B_5O_9]_\infty$ network	4.7	3.54
$Pb_2B_5O_9I$[130]	$Pnn2$	3D $^3[B_5O_9]_\infty$ network	13.5	3.72

[a]All the data were collected from refs 130,483−485.

Whereas in the $M_2B_5O_9X$ (M = Ca, Sr, Ba, Pb, Eu; X = Cl, Br, I) family with the space group of $Pnn2$ (no. 34),[130,213−217] that is utterly different. For example, great divergent of nonlinearity in three Pb-based isomorphic $Pb_2B_5O_9X$ (X = Cl, Br, I) is observed, with the SHG efficiencies ranging from 0.7 × KDP in $Pb_2B_5O_9Cl$, 4.7 × KDP in $Pb_2B_5O_9Br$ to 13.5 × KDP in $Pb_2B_5O_9I$.[130] The large enhancement of SHG efficiency originates from not only the lone pairs on Pb^{2+} cations but also the bonding state of halogen anions. Although the reported SHG efficiency varies in this family, a general rule could be observed that the SHG response increases along the isostructural $M_2B_5O_9X$ (M = Ca, Sr, Ba, Pb, Eu; X = Cl, Br, I) family with the following order: Ca < Sr < Ba < Pb for M site cations and Cl < Br < I for X site anions. Very recently, large $Ca_2B_5O_9Cl$ and $Sr_2B_5O_9Cl$ crystals have been grown by Long *et al.*[486] by the high temperature solution method in a sealed silica tube. Their absorption edges locate at about 170 nm with high transmittance in the UV spectral region. The moderate SHG responses were found to be 0.84 (Ca) and 0.54 (Sr) × KDP at 1064 nm, with phase matching for Ca, and non-phase matching for Sr analogue, which is due to the larger

https://dx.doi.org/10.1021/acs.chemrev.0c00796
Chem. Rev. 2021, 121, 1130−1202

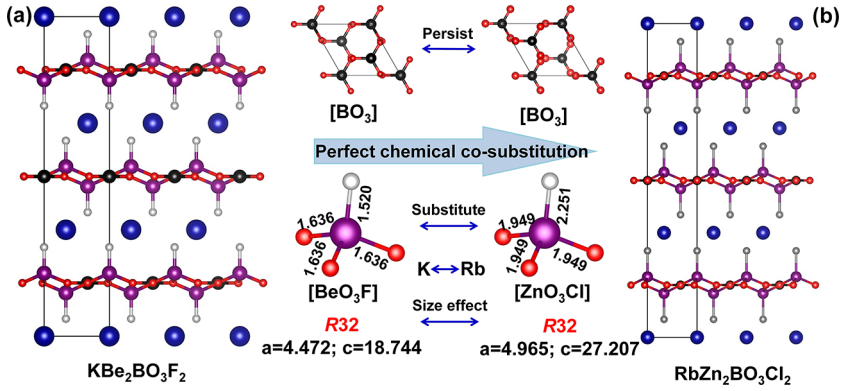

Figure 31. (a,b) Perfect chemical co-substitution strategy performed from $KBe_2BO_3F_2$ to $RbZn_2BO_3Cl_2$ by replacing the $[BeO_3F]$ units in $KBe_2BO_3F_2$ by $[ZnO_3Cl]$ tetrahedra. Parts a and b were drawn by using the crystallographic information file of $KBe_2BO_3F_2$ (ICSD: 77277) and $RbZn_2BO_3Cl_2$ (ICSD: 253579) in ICSD.

birefringence in Ca than Sr analogue.[486] Thus, motivated by the similar or divergent properties in the isostructural structures, one should be noted that the contribution of anions on optical properties is not negligible. Even the same combinations, the differentiation might be obvious or small depending on different system, like the nonlinearity in Pb_2BO_3X and $Pb_2B_5O_9X$ series (X = Cl, Br, I).

3.9.1.6. $AZn_2BO_3X_2$(A = NH_4, Na, K, Rb; X = Cl, Br) and $ABa_{12}(BO_3)_7F_4$ (A = Li, Na). A new natural mineral borate chloride, $KZn_2BO_3Cl_2$, was found in the sublimates of active fumaroles by Pekov and Zubkova in 2015.[487] Soon after, a series of novel beryllium-free NLO crystals, $AZn_2BO_3X_2$ (A = NH_4, Na, K, Rb; X = Cl, Br), with $KBe_2BO_3F_2$-like structure, were reported nearly simultaneously by Li *et al.* and Ye *et al.* in 2016.[488,489] All of the members in the family are isostructural to $KBe_2BO_3F_2$ and crystallize into chiral space group *R*32 (no. 155). Thus, from a chemical point of view, this series can be regarded as derivatives of the chemical co-substitution strategy based on $KBe_2BO_3F_2$ crystal by replacing $[BeO_3F]$ by $[ZnO_3X]$ tetrahedra (Figures 31a,b). The high consistency in space group, lattice parameters, and crystallographic positions of corresponding units further confirms the isostructural behavior in $KBe_2BO_3F_2$ and $AZn_2BO_3X_2$ (A = NH_4, Na, K, Rb; X = Cl, Br) series. All of them present 0D anionic framework of isolated $[BO_3]$ units that are connected by the fluorinated $[ZnO_3X]$ tetrahedra to form $^2[Zn_2BO_3X_2]_\infty$ single layers, in which $[BO_3]$ units align with same orientation and fully add their contributions to the total NLO properties. The powder SHG measurements reveal the considerable higher efficiencies than that of KDP at 1064 and 532 nm.[488,489] They are transparent down to the UV spectral region and exhibit short absorption edges from 190 to 209 nm. These results indicate that $AZn_2BO_3X_2$ (A = NH_4, Na, K, Rb; X = Cl, Br) family has potential to generate the 266 nm coherent light by a direct FHG process once the crystals are grown to large size.[488,489] Thus, the next step will be to grow large crystal and verify the capacity for generating 266 nm coherent light. Noncentrosymmetric modification of two barium borate fluorides, $ABa_{12}(BO_3)_7F_4$ (A = Li, Na), were reported by Bekker *et al.* in 2016.[490] Although they crystallize in the noncentrosymmetric tetragonal system, $P4_2bc$ (no. 106), the SHG efficiencies have not given.

3.9.1.7. $BaMBO_3F$ (M = Ca, Mg, Zn) and $Ba_3Mg_3(BO_3)_3F_3$ Polymorphs. The structure of $BaCaBO_3F$ crystal was determined first by Keszler *et al.* in 1993.[491] $BaCaBO_3F$ belongs to the space group of $P\bar{6}2c$ (no. 190) and features 0D isolated $[BO_3]$ triangles that are linked with $[CaO_5F_2]$ polyhedra to form $^2[CaO_2F_2BO_3]_\infty$ single layers with Ba cations situated between the layers. It was found that $BaCaBO_3F$ crystal undergoes a reversible phase transition at about 242 °C, that is, α-$BaCaBO_3F$ (*R*3, no. 146) ⇆ β-$BaCaBO_3F$ ($P\bar{6}2c$, no. 190).[492] The β-$BaCaBO_3F$ crystals melt congruently with the melting point of 1096 °C and thus were grown by Czochralski pulling method. Its UV absorption edge occurs at about 210 nm with the effective NLO coefficient (d_{eff}) for type **I** SHG process of 0.23 pm/V.[493,494] Better yet, β-$BaCaBO_3F$ crystal allows UV generation at 355 nm by THG of an Nd:YAG laser operating at 1064 nm.[494]

In the case of $BaMBO_3F$ (M = Mg, Zn) series, they were synthesized first and determined structurally by Li *et al.* in 2010.[495] Their structures exhibit strong structural relations to above $BaCaBO_3F$ polymorphs but belong to different noncentrosymmetric space groups, *i.e.*, *Cc* (no. 9) for Mg analogue and $P\bar{6}$ (no. 174) for Zn analogue. The changes in coordination environments of M site cations have great influences on the arrangement of the $[BO_3]$ NLO active units and therefore the SHG effects. That can be confirmed by the distinctive SHG response in $BaZnBO_3F$ (2.8 × KDP) and $BaMgBO_3F$ (0.1 × KDP).[495] In 2016, $BaZnBO_3F$ crystals have been grown with BaF_2−NaF flux by Li *et al.* and its UV absorption edge occurs at 223 nm.[496] The continued study in this family has led to two new noncentrosymmetric phases of $BaMgBO_3F$, namely orthorhombic $Pna2_1$ (no. 33) and hexagonal $P\bar{6}2m$ (no. 189) polymorphs of $Ba_3Mg_3(BO_3)_3F_3$.[497] It was found that $Ba_3Mg_3(BO_3)_3F_3$ crystal undergoes a reversible phase transition at about 450 °C, that is, $Pna2_1$ ⇆ $P\bar{6}2m$. The two new $Ba_3Mg_3(BO_3)_3F_3$ polymorphs show much larger SHG intensities (1.8 and 2.0 × KDP) than above monoclinic $BaMgBO_3F$. Detailed descriptions of its growth, phase transition, linear, and NLO properties have been discussed elsewhere by Pan *et al.*[497]

3.9.1.8. $BaAlBO_3F_2$, $Rb_3Al_3B_3O_{10}F$, $Ba_{4-x}Sr_{3+x}(BO_3)_{4-y}F_{2+3y}$, and $Li_3Ca_9(BO_3)_7{\cdot}2[LiF]$. The structure of $BaAlBO_3F_2$ was initially thought to be isotopic with that of $BaGaBO_3F_2$ and crystallizes in the centrosymmetric $P6_3/m$ (no. 176) by Park *et al.* in 2000,[498] but this was finally corrected to the noncentrosymmetric class $P\bar{6}2c$ (no. 190) by Hu *et al.* in 2011.[499] $BaAlBO_3F_2$ crystal consists of isolated $[BO_3]$ triangles that are fully connected with $[AlO_3F_2]$ trigonal bipyramids to from $^2[AlBO_3F_2]_\infty$ layers (Figure 32a). The $BaAlBO_3F_2$ crystal was

https://dx.doi.org/10.1021/acs.chemrev.0c00796
Chem. Rev. 2021, 121, 1130−1202

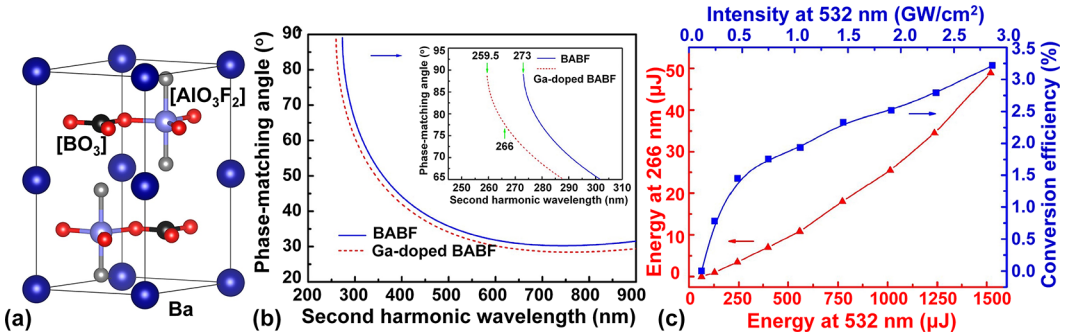

Figure 32. (a) Crystal structure of $BaAlBO_3F_2$. (b) Phase matching angle curves for type **I** SHG as a function of the second-harmonic wavelength in $BaAlBO_3F_2$ (shortened as BABF in figure) and Ga-doped $BaAlBO_3F_2$ crystals. Inset: amplified curves with the second-harmonic wavelength varied from 245 to 310 nm. (c) Output energy at 266 nm versus input energy at 532 nm, and the optical conversion efficiency of Ga-doped $BaAlBO_3F_2$ crystal from 532 to 266 nm. Reproduced with permission from ref 501. Copyright 2016 The Optical Society of America Publishing. Part a was drawn by using the crystallographic information file of $BaAlBO_3F_2$ (ICSD: 421141) in ICSD.

found to have a high phase matching SHG efficiency of 2.0 × KDP and its absorption edge shifts to the deep-UV region (165 nm). Large $BaAlBO_3F_2$ crystals were grown with optimized LiF-NaF-B_2O_3 flux system and thus NLO coefficient (d_{22} = 1.24 pm/V), birefringence (Δn = 0.0418@1064 nm), and laser damage threshold (6.25 GW/cm^2 under 7.5 ns, 1064 nm) were determined by using the as-grown crystals.[500] Thus, $BaAlBO_3F_2$ crystal can be used to generate 532 and 355 nm light, but incapable of generating 266 nm light by direct FHG due to its small birefringence. However, in 2016, Hu *et al.*[501] demonstrated that the birefringence of $BaAlBO_3F_2$ crystal can be effectively increased by doping the Ga ions, then blue-shift the shortest type **I** wavelength to below 266 nm. Thus, the FHG of UV light at 266 nm was achieved for the first time in Ga:$BaAlBO_3F_2$ crystals with the optical conversion efficiency of 3.2% from 532 to 266 nm (Figures 32b,c).[501] Further research needs to be done to improve the output power and conversion efficiency of 266 nm light in this process.

Another aluminum borate $Rb_3Al_3B_3O_{10}F$ has been reported in trigonal *P*31*c* (no. 159, not included in ICSD) with a framework structure that preserves the NLO favorable structural merits of $KBe_2BO_3F_2$ by Luo *et al.* in 2015.[502] Thus, $Rb_3Al_3B_3O_{10}F$ possesses comparable optical properties to $KBe_2BO_3F_2$ in SHG response (1.2 × KDP). Better yet, the strong Al−O/F bonds in $Rb_3Al_3B_3O_{10}F$ crystals make it exhibit a remarkably stronger bonding interaction than that in $KBe_2BO_3F_2$ crystals, and thus no layering single-crystal growth tendency was observed.[502] But the optical properties relating to its buck crystals are still unrevealed.

Two new noncentrosymmetric orthoborate fluorides with isolated $[BO_3]$ units, $Ba_7(BO_3)_3F_5$ and $Ba_3Sr_4(BO_3)_3F_5$, with the general formula of $Ba_{4-x}Sr_{3+x}(BO_3)_{4-y}F_{2+3y}$ were obtained first by Keszler *et al.* in 1993.[490] They are isostructural and belong to the hexagonal $P6_3mc$ (no. 186) with moderate SHG intensities (~1/3 and 1/2 × KDP) and short cutoff wavelengths (190 and 210 nm). The low SHG effects are not competitive, and the SHG coefficients and birefringence have not been reported. The single crystals of a new salt-inclusion borate fluoride $Li_3Ca_9(BO_3)_7{\cdot}2[LiF]$ were obtained *via* spontaneous crystallization by Pan *et al.* in 2013.[503] It crystallizes into the triclinic crystal system of *P*1 (no. 1) space group with the 0D isolated $[BO_3]$ units. The SHG signal of $Li_3Ca_9(BO_3)_7{\cdot}2[LiF]$ was found to be about 1.0 × KDP, and it can achieve the phase matching behavior.[503] Theoretical calculations analyses reveal that the optically active region near the Fermi level is mainly derived from the O 2*p* orbitals and B 2*p* states, whereas the F 2*p* states locate far from the Fermi level, resulting in contribution less to the optical properties, which is quite different from the above-discussed borate fluorides and this phenomenon is similar to that in $Ca_5(BO_3)_3F$. Thus, the coplanar $[BO_3]^{3-}$ units are the major NLO-active units without more direct or indirect effects of fluorine on NLO properties. Attributable to the lack of large single crystals, SHG coefficients and birefringence of $Li_3Ca_9(BO_3)_7{\cdot}2[LiF]$ have not been reported.

3.9.1.9. $A_3M_3Li_2T_4B_6O_{20}F$, $Ba_2TB_4O_9Cl$, and $Na\text{-}Ba_4(TB_4O_9)_2X_3$ (A = K, Rb; M = Ba, Sr; T = Ga, Al; X = Cl, Br). The first member in the $A_3M_3Li_2Al_4B_6O_{20}F$ (A = K, Rb; M = Ba, Sr) family, $K_3Ba_3Li_2Al_4B_6O_{20}F$, was reported with a framework structure that preserves the structural merits of $Sr_2Be_2B_2O_7$ double-layer configuration by Luo *et al.* in 2016.[504] It crystallizes in the hexagonal $P\bar{6}2c$ (no. 190) with 0D anionic framework of isolated $[BO_3]$ units. The planar $[BO_3]$ triangles are linked by tetrahedral coordinated $[AlO_4]$ and $[LiO_3F]$ units to form the $^2[Li_2Al_4B_6O_{20}F]_\infty$ double layers in the *ab* plane. Better yet, $K_3Ba_3Li_2Al_4B_6O_{20}F$ crystal exhibits a deep-UV absorption edge of 190 nm, a sufficiently large SHG response of 1.5 × KDP and a suitable birefringence (Δn = ~0.068@852.1 nm), which make it have the potential to generate the 266 nm coherent light by a direct FHG process.[505] In 2017, two more new members in this family, $K_3Sr_3Li_2Al_4B_6O_{20}F$ and $Rb_3Ba_3Li_2Al_4B_6O_{20}F$, were reported nearly simultaneously by Luo *et al.* and Halasyamani *et al.*[506−509] They exhibit a similar structure with KBa analogue but crystallize in a distinctive space group, *i.e.*, *R*32 (no. 155) for KSr analogue and $P\bar{6}2c$ (no. 190) for RbBa (not included in ICSD) analogue. Both crystals exhibit absorption edges below 200 nm, moderate birefringence (Δn = 0.0637 and 0.057@ 1064 nm), and shortest type **I** SHG wavelengths below 266 nm (224 and 243 nm). Thus, together with KBa analogue, they are all potential candidates to generate 266 nm radiation by direct FHG method.[506−509] Xia *et al.* obtained two Ga-based new members,[510] $A_3Ba_3Li_2Ga_4B_6O_{20}F$ (A = K and Rb), with space group of $P\bar{6}2c$ (no. 190; not included in ICSD). They show weaker SHG responses of 0.7 and 0.5 × KDP than other members.[510] For the above crystals in this subsection, the next step will be to verify the capacity for generating of 266 nm coherent light.

Two new mixed borate chlorides, $Ba_2TB_4O_9Cl$ (T = Ga, Al), were obtained first by Barbier *et al.* in 2007[511] with the

https://dx.doi.org/10.1021/acs.chemrev.0c00796
Chem. Rev. 2021, 121, 1130−1202

tetragonal system ($P4_2nm$, no. 102, not included in ICSD). Only the powder SHG efficiency of $Ba_2GaB_4O_9Cl$ is given to about 0.95 × KDP.[511] A new mixed borate chloride $NaBa_4Al_2B_8O_{18}Cl_3$, that is similar to the $Ba_2TB_4O_9Cl$ (T = Ga, Al) series, was obtained by Wu *et al.* in 2012 with the tetragonal system, $P4_2nm$ (no. 102).[512] The crystal structure of $NaBa_4Al_2B_8O_{18}Cl_3$ is characterized by the 3D $^3[B_8O_{18}]_\infty$ anionic framework that is built up from $[B_4O_9]$ FBBs. The $NaBa_4Al_2B_8O_{18}Cl_3$ crystals have been grown to centimeter level from the NaF-LiCl or NaF-NaCl flux systems by the top-seeded solution growth method.[512,513] The absorption edge of $NaBa_4Al_2B_8O_{18}Cl_3$ crystal was initially reported to occur at 230 nm, and then it was improved to 183 nm by using the as-grown $NaBa_4Al_2B_8O_{18}Cl_3$ crystals without Fe^{3+} impurity.[513] More optical properties have also been obtained in great detail based on the optically perfect crystals, such as birefringence (Δn = 0.017@808 nm), NLO coefficients (d_{15} = 0.49 pm/V, d_{33} = 0.88 pm/V), and thermal-expansion coefficients (α_a =1.6 × 10^{-6}/°C and α_c = 4.5 × 10^{-6}/°C).[511] Later on, three more compounds, $NaBa_4Al_2B_8O_{18}Br_3$, $NaBa_4Ga_2B_8O_{18}Cl_3$, and $NaBa_4Ga_2B_8O_{18}Br_3$, were obtained by Pan *et al.*,[514,515] which are isostructural with $NaBa_4Al_2B_8O_{18}Cl_3$ crystals. Thus, all of the four crystals show similar structures and closely optical properties. The relatively low birefringence of ~0.01 in this famliy restricts them to outout shorter wavelength, like 266 and 355 nm or lower than that, within the direct SHG method.

3.9.1.10. $A_3B_6O_{10}X$, $Na_3B_4O_7X$, $M_3B_7O_{13}X$, $Li_4B_7O_{12}X$, and (A = K, Na, Na/Rb, K/Na; M = Mg, Zn, Fe, Mn, Co, Cr, Ni; X = Cl, Br, I). A series of perovskite-like borate halides with the general formula of $A_3B_6O_{10}X$ (A = K, Na, Rb/Na, K/Na; X = Cl, Br) have been continuously obtained by Belokoneva *et al.*[221] and Pan *et al.*[222−224,226] They show rich structural diversity that we have discussed in section 2.4.4, thus, in this category, only their properties are compared and reviewed. Among them, attributable to ease of growth of large crystals with high optical quality, $K_3B_6O_{10}Cl$ and $K_3B_6O_{10}Br$ crystals have been fully investigated in great detail. The powder SHG efficiencies of them are given to about 3.0 (Br) and 4.0 (Cl) × KDP at 1064 nm. $K_3B_6O_{10}Cl$ is a uniaxial crystal with the measured birefringence of 0.0503 at 404 nm, which is larger than that in its isostructural $K_3B_6O_{10}Br$ (Δn = 0.046@1064 nm).[223,516,517] Owing to the enhanced birefringence, it follows that the shorter wavelength limits for type **I** SHG is 272 nm for Cl analogue and 289 nm for Br analogue, respectively. The deep-UV transmittance spectra for both crystals indicate that the absorption edges are all near 180 nm, which facilitate their applications in the UV spectral range, but owing to the use of PbO as a flux, the absorption in UV region of as grown crystals is ineluctable and thus new PbO free flux need to be introduced. Even so, both $K_3B_6O_{10}Cl$ and $K_3B_6O_{10}Br$ crystals still can generate 532 and 355 nm UV light by SHG and THG methoda from 1064 nm lasers.[223,516,517] The maximum average power of 19.3 W 355 nm light has been achieved by using type **I** cut $K_3B_6O_{10}Br$ crystals with the corresponding conversion efficiency of 16.3% by Li *et al.*[518] Pan *et al.* have demonstrated a 1.21 W 532 nm picosecond green laser *via* SHG process of type **I** $K_3B_6O_{10}Cl$ crystals.[519] For the 10 Hz picosecond laser, the output at 532 nm was 1.78 mJ/pulse with an optical conversion efficiency of 36.0%. Detailed descriptions of the output of different wavelengths and important applications of $K_3B_6O_{10}Cl$ and $K_3B_6O_{10}Br$ crystals have been discussed.[518,519]

Whereas for the $Na_3B_4O_7X$, $M_3B_7O_{13}X$, and $Li_4B_7O_{12}X$ (A = K, Na, Na/Rb, K/Na; M = Mg, Zn, Fe, Mn, Co, Cr, Ni; X = Cl, Br, I) series, all of them crystallize into the non-centrosymmetric crystal system but show poor non-phase matching or unreported SHG properties due to the unfavorable arrangement of B−O anionic framework. Although $M_3B_7O_{13}X$ (M = Mg, Mn, Co, Cr, Ni; X = Cl, Br) series with orthorhombic $Pca2_1$ (no. 29)[104,204,218] are shown to have small birefringence that is insufficient to achieve phase matching at 1064 nm. But they are capable of generating UV coherent light *via* a quasi-phase matching technique with a periodically poling method. For example, Long *et al.*[520] have grown the $Mg_3B_7O_{13}Cl$ crystals and achieved the generation of deep-UV lights by avoiding the limitation of birefringence and walk-off effect *via* quasi-phase matching technique, which provides an effective method to generate deep-UV coherent light by using non-phase matching NLO materials.[520]

3.9.2. Fluorooxoborates. *3.9.2.1. $Li_2B_3O_4F_3$, LiB_6O_9F, and $Li_2B_6O_9F_2$.* Three new lithium fluorooxoborates were initially reported and investigated as novel ionic conductors and NLO materials by Jansen *et al.*[163,168,229] They belong to the noncentrosymmetric space group of $P2_12_12_1$ (no. 19), $Pna2_1$ (no. 33), and Cc (no. 9) with 1D $^1[B_3O_4F_3]_\infty$ chain, 2D $^2[B_6O_9F]_\infty$ layer, and 3D $^3[B_6O_9F_2]_\infty$ anionic framework for $Li_2B_3O_4F_3$, LiB_6O_9F, and $Li_2B_6O_9F_2$, respectively (see Figure 33).[163,168,229] The bandgap, birefringence and largest SHG

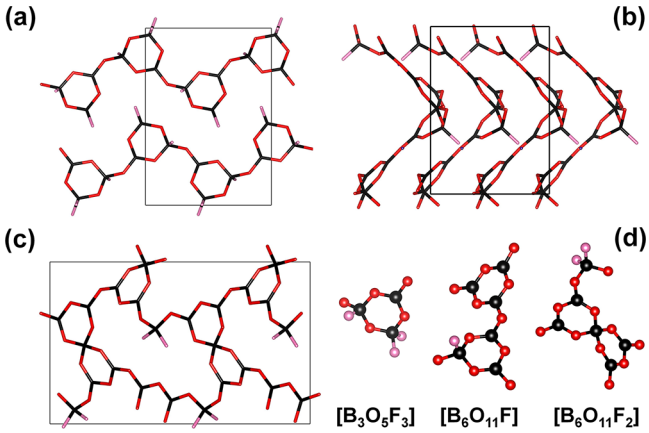

Figure 33. Crystal structure (a−c) and FBB (d) of $Li_2B_3O_4F_3$, LiB_6O_9F, and $Li_2B_6O_9F_2$. All of the figures were drawn by using the crystallographic information file of $Li_2B_3O_4F_3$ (ICSD: 423661), LiB_6O_9F (ICSD: 420286), and $Li_2B_6O_9F_2$ (ICSD: 423435) in ICSD.

tensors were calculated to be 8.425 eV, 0.05@1064 nm and d_{14} = 0.088 pm/V for $Li_2B_3O_4F_3$, 8.37 eV, 0.06@1064 nm and d_{24} = 0.161 pm/V for LiB_6O_9F, 8.05 eV, 0.07@1064 nm and d_{13} = -0.536 pm/V for $Li_2B_6O_9F_2$, respectively.[521] The difference among these can be explained by the varied orientation of B−O/F units. Among them, $Li_2B_6O_9F_2$ crystal was highlighted by Pan *et al.*, as it possesses even superior performances in SHG response (0.9 × KDP) and absorption edge (<190 nm) than other two compounds and the shortest type **I** phase matching wavelength (192 nm) is down to the deep-UV spectral region.[521] Unfortunately, all of the three lithium fluorooxoborates exhibit very low decomposition temperature (~500°) due to the easy break of B−F bonds, which increase the difficulty of growing large size crystals. Thus, the SHG coefficients and birefringence are still unknown in experimental study.

3.9.2.2. AB_4O_6F (A = NH_4, Na, Rb, Cs, K/Cs, Rb/Cs). This family is one of the most promising NLO candidates, and they

https://dx.doi.org/10.1021/acs.chemrev.0c00796
Chem. Rev. 2021, 121, 1130−1202

Table 7. Comparison of Structural Chemistry and Optical Properties among Three Fluorooxoborates Series, AB_4O_6F (A = NH_4, Na, Rb, Cs, K/Cs, Rb/Cs), $MB_5O_7F_3$ (M = Ca, Sr, Pb, Cd), and $MB_2O_3F_2$ (M = Pb, Sn, Ba) Series[a]

formula	AB_4O_6F	$MB_5O_7F_3$	$MB_2O_3F_2$
space group	varied symmetries from $C2$, $Pna2_1$, $P321$ to $P\bar{6}2c$	fixed class of $Cmc2_1$	varied symmetries from $P2_1$ to $P3_2$
FBBs	same formula of $[B_4O_8F]$ units but shows different formation: type A ($[B_3O_6]$ + $[BO_3F]$) and type B ($[B_3O_6F]$ + $[BO_3]$)	same formula of $[B_5O_7F_3]$ with same formation	different formula of $[B_2O_3F_2]$ ($[BO_3F]$ + $[BO_3F]$) and $[B_2O_5F_2]$ ($[BO_4]$ + $BO_3F]$)
anionic framework	2D $^2[B_4O_6F]_\infty$ single-layer	2D $^2[B_5O_7F_3]_\infty$ single-layer	2D $^2[B_2O_3F_2]_\infty$ single-layer
position of metal anion	between the layers or in the layers	in the layers	between the layers
birefringence	large	moderate	small
SHG response	large	large	extremely large for Pb and Sn phases
phase matching wavelength	all can be down to the deep-UV region	can be down to deep-UV region with the composition of M = Ca and Sr	cannot be down to deep-UV region with the composition of M = Pb and Sn

[a]All the data were collected from refs 72,73,76,177−180 and 183−186.

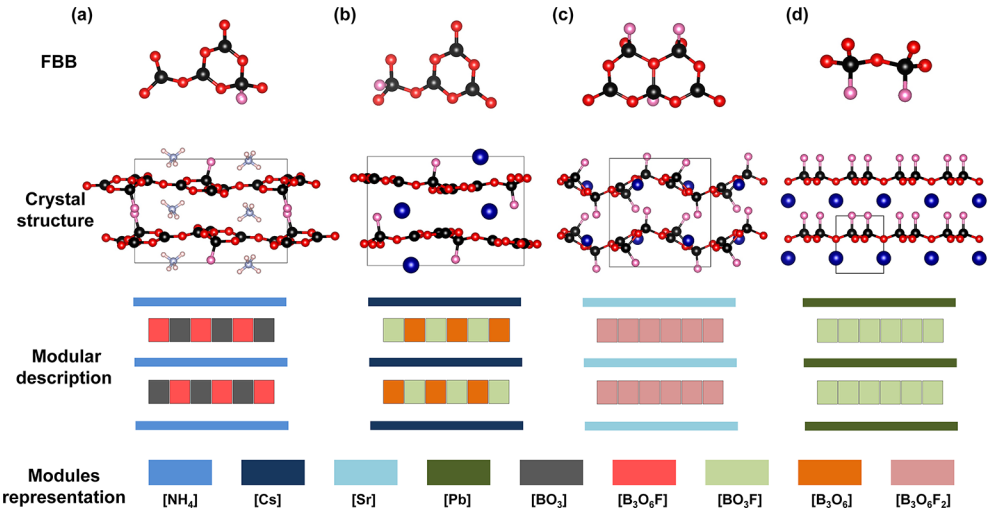

Figure 34. FBB, crystal structure, and modular description of $NH_4B_4O_6F$ (a), CsB_4O_6F (b), $SrB_5O_7F_3$ (c), and $PbB_2O_3F_2$ (d). The modules representation of different atoms or units are given in the last line. Parts a−d were drawn by using the crystallographic information file of $NH_4B_4O_6F$ (ICSD: 254160), $SrB_5O_7F_3$ (ICSD: 263469), and $PbB_2O_3F_2$ (ICSD: 263596) in ICSD and CsB_4O_6F from ref 179

were all reported first by Pan *et al.* in the period of 2017−2019 and then immediately shown to be very promising deep-UV NLO materials (Table 7).[177−180] Although all of the six fluorooxoborates take the similar formula of AB_4O_6F, they crystallize in the different noncentrosymmetric space groups, *i.e.*, monoclinic $C2$ (no. 5) for NaB_4O_6F,[180] orthorhombic $Pna2_1$ (no. 33) for AB_4O_6F (A = NH_4, Rb, Cs, Figures 34a,b),[177−179] trigonal $P321$ (no. 150) for $CsKB_8O_{12}F_2$,[178] and hexagonal $P\bar{6}2c$(no. 188) for $RbCsB_8O_{12}F_2$,[178] respectively. This family is reported to have a framework structure that preserves the structural merits of $KBe_2BO_3F_2$ crystal. Better yet, the as-grown crystals of AB_4O_6F (A = NH_4, Cs) show no strong layer growth tendency,[177,179] which has obviously been improved compared with $KBe_2BO_3F_2$ crystal. Carefully structural comparisons reveal that the layer spacing is largely reduced from 6.25 Å in $KBe_2BO_3F_2$ to 3.81−3.96 Å in AB_4O_6F (A = NH_4, Na, Rb, Cs, K/Cs, Rb/Cs) family.[45] This was also confirmed by the calculation of binding energy in the neighboring layers, which indicates that the magnitude of binding energy in this family is 5−6 times larger than that in $KBe_2BO_3F_2$ crystal. With respect to the optical properties of AB_4O_6F (A = NH_4, Na, Rb, Cs, K/Cs, Rb/Cs) family, covering experimental and theoretical results, all of them exhibit suitable sufficiently large powder SHG efficiencies (0.9−3.0 × KDP@ 1064 nm), suitable large birefringence (Δn = 0.098−0.12@ 1064 nm), short deep-UV absorption edges (all lower than 180 nm), as well as the short deep-UV SHG phase matching wavelengths (cal. 158−172 nm). These strongly suggest that AB_4O_6F series are outstanding deep-UV NLO materials and have great potential to generate deep-UV light once they are grown to sizable crystals.[177−180] Detailed descriptions about the comparison of structure and properties in AB_4O_6F (A = NH_4, Na, Rb, Cs, K/Cs, Rb/Cs) family and their potential as competitive deep-UV candidates have been discussed elsewhere.[45] If necessary, please refer to the recent review entitled "Emergent Deep-Ultraviolet Nonlinear Optical Candidates".[45]

3.9.2.3. $MB_5O_7F_3$ (M = Ca, Sr, Pb, Cd). A series of alkaline-earth metal fluorooxoborates with the general formula of $MB_5O_7F_3$ (M = Ca, Sr, Pb, Cd) are one of the recently discovered competitive NLO crystals by Pan *et al.* and Ye *et al.* (Table 7).[76,183−186] They are all isostructural and belong to the same orthorhombic $Cmc2_1$ (no. 36). The $MB_5O_7F_3$ (M = Ca, Sr, Pb, Cd) family feature 2D *zigzag* $^2[B_5O_7F_3]_\infty$ single layers with the M site cations resided in the layers (Figure 34c). The Sr and Ca analogues are the first members in this family. It is interesting to note that the naphthalene liked FBBs without dangling bonds of $[B_5O_9F_3]$ show a more delocalized π-electron, which leads to the large SHG intensities of ∼1.6−2.5 times that of KDP, short absorption edges below 180 nm, and large birefringence of cal. 0.070 at 1064 nm.[76,183,184] Thus,

https://dx.doi.org/10.1021/acs.chemrev.0c00796
Chem. Rev. 2021, 121, 1130−1202

both $CaB_5O_7F_3$ and $SrB_5O_7F_3$ crystals would be the very outstanding NLO crystals for generating the deep-UV light below 200 nm once their large optically perfect crystals are obtained. Recent studies, including experimental and theoretical, have shown that the SHG response and birefringence can be improved to 2−3 times that of its isotropic phases by replacing the M site cations with Pb and Cd (Table 7),[185,186] but the sacrifice of optical transparency windows is inevitable at the same time. Similarly to the other fluorooxoborates family, there is also a pressing need for large $MB_5O_7F_3$ crystals (M = Ca, Sr, Pb, Cd), only once that is satisfied can they be expected to generate UV and deep-UV coherent light.

3.9.2.4. BiB_2O_4F and $MB_2O_3F_2$ (M = Pb, Sn, Ba). The extensive search in bismuth borates with boric acid flux at low temperature system has led to BiB_2O_4F by Lin *et al.* in 2005.[164] BiB_2O_4F crystallizes in the trigonal space group $P3_2$ (no. 145) and contains 1D $^1[B_6O_{10}F_2]_\infty$ infinite helical chains along the *c* axis. The Bi^{3+} cations locate within the cavities of the borate helices. Investigation on the optical properties on BiB_2O_4F, together with its isotropic BiB_2O_4OH reveals that BiB_2O_4F is a phase matching crystal with exceptionally large SHG responses of more than ∼10 and ∼4 times that of KDP and BiB_2O_4OH, respectively. Cong *et al.*[522] demonstrated that the incorporation of fluorine into BiB_2O_4F leads to a synergistic enhancement of local polarizations in $[BiO_5]$ and $[BO_3F]$ polyhedra and, hence, a very strong SHG efficiency. Two new fluorooxoborates, $PbB_2O_3F_2$ and $SnB_2O_3F_2$, were obtained by Ye *et al.*[72] through molecular engineering design from classic $Sr_2Be_2B_2O_7$ crystal. They are isostructural and belong to the same noncentrosymmetric space group of $P3_1m$ (no. 157). Their anionic frameworks are based on the $^2[B_2O_3F]_\infty$ single layers that are further linked by M site cations with lone pair electrons (Figure 34d). More interestingly, $MB_2O_3F_2$ (M = Pb, Sn) series are reported to exhibit widely divergent SHG responses, *i.e.*, 13 × and 4 × KDP for $PbB_2O_3F_2$ and $SnB_2O_3F_2$, respectively (Table 7).[72] Ye *et al.* demonstrated that the different electrons' activities on M site cations are responsible for this discrepancy of NLO effects. Meanwhile, $SnB_2O_3F_2$ was also reported by Höppe *et al.* with the same structural features.[73] The absence of an inversion center and B−F bonds in the structure of $SnB_2O_3F_2$ was proven by SHG experiments and solid-state NMR spectroscopy.[73] When replacing the Pb and Sn atoms in the $MB_2O_3F_2$ (M = Pb, Sn) family with Ba to generate $BaB_2O_3F_2$, layered configuration shows totally different features with different space group of $P2_1$ (no. 4, not included in ICSD)[71] but show much weaker SHG response to be detected than Pb and Sn analogues. But, to date, large crystals of $MB_2O_3F_2$ (M = Pb, Sn, Ba) series have not been grown, which makes SHG coefficients and birefringence still unknown in experimental study.

4. BORATE-BASED SFD LASER CRYSTALS

The compact all-solid-state light sources, including tunable visible, UV, and near-infrared lasers, can be directly generated when the upconversion lasers emitted shorter wavelength than the pump source. Studies have shown that an alternative to upconversion lasing is frequency conversion by the NLO method. The most effective material for this purpose is SFD laser crystal, in which laser effects and NLO process of frequency doubling occur simultaneously in the same crystal.[17,523,524] That is why SFD laser crystal can be considered as a multifunctional crystal with both laser and frequency doubling properties. The SFD laser crystals can combine their laser emission of optically active ions (Yb^{3+} and Nd^{3+}) with host NLO materials and thus lead to certain laser radiation by SFD. The first SFD laser was realized in Tm doped $LiNbO_3$ crystal by Johnson and Ballman in 1969.[525] SFD candidates were expanded to a borate system in 1981 with the development of the $Nd:Al_3(BO_3)_4$ SFD laser crystal by Dorozhkin *et al.*[526] Presently, borates, particularly rare earth borates, are intensively investigated as novel candidates for SFD laser crystals because the rare earth compositions can be easily substituted by lasing ions without modification of the acentric host lattice. Meanwhile, the superiorities of linear and NLO properties in borates are reserved when they are incorporated as SFD laser crystals. Thus, it is worth examining the state of art in classical borate-based SFD laser crystals and highlighting the multifunctionality of the borates system. In this section, we still start with the consideration of necessary requirements for a practical SFD laser crystal based on the available experimental and theoretical data revealed in the related literature.

4.1. Necessary Requirements for a SFD Laser Crystal

As we mentioned that SFD laser crystal is a type of multifunctional material, a combination of laser and NLO crystal, and therefore they should simultaneously satisfy the criteria that are required for both laser and NLO applications. Thus, the SFD laser crystal should first be an NLO crystal and satisfy all the requirements that we have discussed in section 3.1. Many different demands are being placed on SFD laser crystals as far as the laser properties are concerned:[17,523,524] (1) The SFD laser crystals must accept the fluorescent doping (most usually with Yb or Nd), which require that lattice of the NLO host materials is suitable for doping with active ions. Also, the broadband absorption with a large absorption peak for the emission of diodes is indispensable for SFD laser crystals. To obtain a highly efficient laser system with high beam quality, additional laser properties are also required for SFD laser crystals, including long fluorescence lifetime, high radiative quantum efficiency, large emission cross sections, and low photon energy. (2) The requirements on the thermal properties for SFD laser crystals are rather strict, such as a large effective thermal conductivity to enable the efficient extraction of heat from the host materials, low thermal focal effects to minimize the negative effects of heat on the refractive indices and thermal induced loss, and low thermal expansion anisotropy to facilitate the crystal growth process.

4.2. Active Ions Doped Rare-earth Borates

4.2.1. Active Ions Doped $REAl_3(BO_3)_4$ (RE = Rare-earth Metals) Crystals. $YAl_3(BO_3)_4$ crystal with high NLO coefficients, a large laser damage threshold, and favorable mechanical and thermal properties (the detail parameters are available in section 3.4) can be considered as the ideal host materials for SFD laser generation when doped with active ions. The Nd doped $YAl_3(BO_3)_4$ crystal was developed first and identified as a new SFD laser crystal by Dorozhki *et al.* in 1981.[526] The SFD red laser of 660 nm pumped by a flash lamp was generated in $Nd:YAl_3(BO_3)_4$ crystal, which is the first SFD laser obtained by borate-based NLO host crystal.[526] After that, many studies have been fully carried out to obtain different light sources with improved output power by using the active ions doped $YAl_3(BO_3)_4$ SFD crystals. Early in 1981, the experimental realization of SFD green laser from 1060 to 530 nm by $Nd:YAl_3(BO_3)_4$ crystal was difficult owing to the strong absorption of Nd ions at 530 nm,[526] but this was achieved with

https://dx.doi.org/10.1021/acs.chemrev.0c00796
Chem. Rev. 2021, 121, 1130−1202

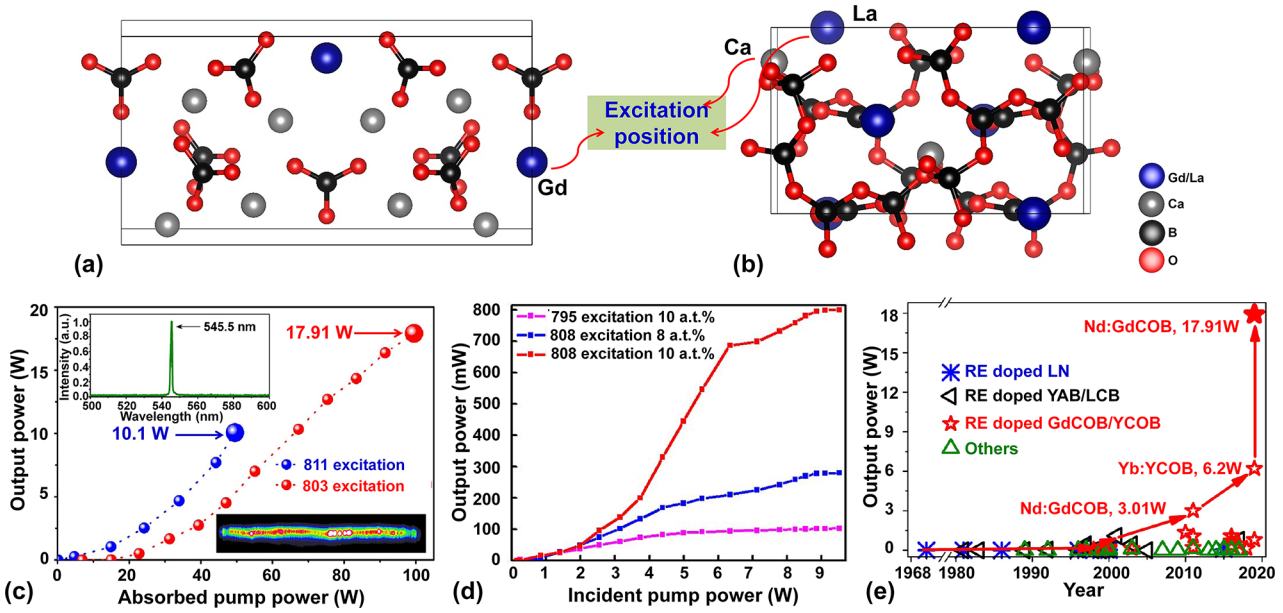

Figure 35. (a,b) Crystal structures of $GdCa_4O(BO_3)_3$ and $La_2CaB_{10}O_{19}$. The excitation position means the crystallographic sites that are doped and occupied by active ions. (c) Nd:$GdCa_4O(BO_3)_3$ laser output power versus absorbed pump power. Inset: Nd:$GdCa_4O(BO_3)_3$ SFD laser spectrum at the center of 545.5 nm and its beam profile at the output power of 1 W. Reproduced with permission from ref 541. Copyright 2020 The Optical Society of America. (d) Output powers of Nd:$La_2CaB_{10}O_{19}$ SFD green laser with different excitation wavelengths (795 and 808 nm) and different doping concentrations (8 and 10 at %) versus incident pump power. Reproduced with permission from ref 545. Copyright 2017 The Optical Society of America. (e) Summary of the SFD lasers output power (generated by different host crystals) versus time. Reproduced with permission from ref 541. Copyright 2020 The Optical Society of America. Parts a and d were drawn by using the crystallographic information file of $GdCa_4O(BO_3)_3$ (ICSD: 39716) and $La_2CaB_{10}O_{19}$ (ICSD: 92866) in ICSD.

the first generation of SFD green laser from 1060 to 530 nm in Nd:$YAl_3(BO_3)_4$ crystal with the optimized ratios of Nd:Y by Lu *et al.*[527] But the threshold energy is measured to be less than 2 mJ and the output energy of green light is only 5 mJ with the conversion efficiency of 12.5%.[527] Later on, an output of 10 mW at 532 nm was achieved by Schütz *et al.*,[528] indicating that SFD diode pumped Nd:$YAl_3(BO_3)_4$ crystal laser can be a simple laser system for the generation of green continuous wave laser radiation, but the above 532 green light output levels are extremely low compared with a continuous wave SFD Nd:YAG laser pumped at the same power level. As a result of substantial improvements on crystal optical quality and available diode power, approximately 51 mW 531 laser output was achieved with optical-to-optical conversion efficiency of 4% from the Nd:$YAl_3(BO_3)_4$ crystal by Hemmati in 1992.[529] Better yet, the optimized laser system allows to generate the SFD Nd:$YAl_3(BO_3)_4$ green laser output of 225 mW with the efficiency of 14% when pumped by the combined beams of two 20-stripe diode arrays.[530] A high 531 nm output of up to 450 mW with conversion efficiency of 20% has been realized by using the diffraction-limited output of a Ti:sapphire laser as a pump source.[530]

All the above $YAl_3(BO_3)_4$ host materials work well with the same Nd active ions, however, more attractive SFD laser crystals can also be obtained using Yb as the active ions. However, the use of trivalent Yb as the alternate active ions to replace Nd is especially advantageous for 1 μm laser applications using $YAl_3(BO_3)_4$ SFD crystals.[531] The simple two-state energy level scheme of Yb, that is, $^2F_{7/2}$ ground state and $^2F_{5/2}$ excited state, avoids the detrimental effects of luminescence concentration quenching, upconversion losses and excited state absorption that normally exist in Nd-based laser media. Improvement in the optical conversion efficiencies are due to the lack of any absorption lines in the visible spectral region. Besides, the thermal loads for Yb lasers are far lower than that of Nd lasers, which can avoid reducing the second harmonic output power. The Yb doped crystals also exhibit longer radiative lifetimes than Nd doped counterparts. Therefore, Yb:$YAl_3(BO_3)_4$ SFD laser crystals were reported. In 1998, the longer lifetime, negligible visible absorption, and better crystal optical quality of Yb:$YAl_3(BO_3)_4$ SFD laser crystals compared with Nd doped counterparts were experimentally verified by Dawes *et al.*[532] The continuous wave SFD green laser and wavelength tenability over 33 nm (tunable from 513.0 to 545.8 nm) in the visible from diode-pumped Yb:$YAl_3(BO_3)_4$ have been achieved for the first time by Dawes *et al.*[532] The maximum green output power of 160 mW was obtained with the pump−green conversion efficiency of 11.3%.[532] Soon after, the higher continuous wave SFD green laser of 1.1 W was realized in Yb:$YAl_3(BO_3)_4$ crystals by Dekker *et al.* under the pump power of 11 W with the wavelength of 977 nm in 2001.[533] The diode-to-green conversion efficiency is as high as 10%. They also reported the plano−plano microchip operation of Yb:$YAl_3(BO_3)_4$ crystal and an infrared output of more than 4.3 W at 1042 was achieved, corresponding to the diode-to-infrared conversion efficiency of 36%. For a microchip style cavity, the SDF green laser with output power of 600 mW was also obtained with the diode-to-green conversion efficiency of 5.5%.[533] A much anticipated highlight is that the related conversion efficiencies can be improved by decreasing the intracavity mode size and narrowing the infrared line width.

The SFD properties of other members in $REAl_3(BO_3)_4$ (RE = rare-earth metals) crystals were also studied. For example, $GdAl_3(BO_3)_4$ crystals have a wide optical transparency window (310−3450 nm), a large effective NLO coefficient (d_{eff} = 1.186

https://dx.doi.org/10.1021/acs.chemrev.0c00796
Chem. Rev. 2021, 121, 1130−1202

pm/V), and a small dispersion angle (2.396°). Thus, it too can be a promising host material for the generation of green and red SFD lasers when doped with active ions. The SFD green laser with the maximum power of 119.5 μJ/pulse for a 2.75 mJ/pulse pump was obtained in Nd:$GdAl_3(BO_3)_4$ crystals by Brenier *et al.*,[534] corresponding to the conversion efficiency of 4.3%. Further, also by Brenier *et al.*, the SFD laser operation of Nd:$GdAl_3(BO_3)_4$ crystals near 1338 nm was reported. The red SFD laser at 669 nm was detected with the maximum power of about 19 μJ/pulse for a 4.65 mJ/pulse pump.[535] The value ican be increased by changing the phase matching orientation. Detailed descriptions about the output of different wavelengths, including yellow, blue, and UV laser by a self-sum-frequency mixing method in Nd:$GdAl_3(BO_3)_4$ crystals were discussed elsewhere.[534,535]

4.2.2. Active Ions Doped $RECa_4O(BO_3)_3$ (RE = Rare-earth Metals) Crystals. The calcium rare earth oxyborates $RECa_4O(BO_3)_3$ (RE = rare-earth metals) were shown to be the excellent NLO crystals with better optical properties in practical use (the detail parameters are available in section 3.4). This family offers the opportunity of suitable sites for activator ions emitting around 1 μm. Among them, Nd:$GdCa_4O(BO_3)_3$ has already been proved to be an efficient SFD material with either Ti:sapphire or diode pumping. The unique combination of exceedingly good NLO properties with favorable mechanical performance makes Nd:$GdCa_4O(BO_3)_3$ an excellent crystal for low cost microchip lasers. Thus, in this section, we will take Nd:$GdCa_4O(BO_3)_3$ as representative of this efficient family SFD material to discuss and analyze (Figure 35a). Nd:$GdCa_4O(BO_3)_3$ crystal was recognized as a SFD material by Aka *et al.* in 1996,[337] and thus a 530 nm green laser was observed by using an Nd (4%) doped $GdCa_4O(BO_3)_3$ crystal that is fabricated in the XZ plane with (θ, φ) = (90, 46°).[536] The Nd:$GdCa_4O(BO_3)_3$ SFD crystal shows even greater advantages compared with above Nd:$YAl_3(BO_3)_4$ crystal, such as congruent melting behavior and small absorption coefficient at 530 nm. Later, in 1998, the first SFD diode-pumped Nd:$GdCa_4O(BO_3)_3$ laser was obtained. The output of 21 mW continuous wave green laser radiation at 530.5 nm has been obtained for an absorbed pump power of 820 mW under laser diode pumping.[537] An efficient SFD has been reported in a diode-pumped microchip configuration by Lucas-Leclin *et al.*[538] They optimized the laser cavity and replaced the Ti:sapphire laser with a pump laser diode to maximize the output power of 115 mW at 545 nm.[538] The lasting operation of Nd:$GdCa_4O(BO_3)_3$ crystal in a plano−plano cavity offers an highest output power of 22 mW at 545 nm.

In the SFD Nd:$GdCa_4O(BO_3)_3$ laser system, the doped concentration of Nd in $GdCa_4O(BO_3)_3$ crystal and its crystal length are significant parameters that determine the SFD output power and optical conversion efficiency. Thus, in principle, the optimization of above two parameters can help us obtain higher output power and conversion efficiency. After that, the highest SFD green power sets new records. Wang *et al.*[539] obtained the watt-level SFD lasers in 2010 with Nd:$GdCa_4O(BO_3)_3$ crystals. The output power is as high as 1.35 W with the maximum optical conversion efficiency of 17%. They also found that much improvement on output power compared with its isomorphic Nd:$YCa_4O(BO_3)_3$ is related to the direction of crystals that cut.[539] In 2011, the maximum output power of 3.01 and 1.32 W SFD lasers at the wavelengths of 545 and 530 nm were realized also by Wang *et al.*[540] by optimizing the laser configuration and cut orientation of Nd:$GdCa_4O(BO_3)_3$ crystals. The corresponding optical conversion efficiencies are as high as 20.7 and 6.5%, respectively.[540] Very recently, by employing a partially end-pumped slab structure and optimized laser-diode pump wavelength by Yu *et al.*[541] pushed the SFD output power to an unprecedented of 17.91 W at the wavelength of 545.5 nm in Nd:$GdCa_4O(BO_3)_3$ laser crystals (Figures 35c,e), which represents the highest output power in SFD lasers. The corresponding optical conversion efficiency reached 20% at the same time.[541] On the basis of this, Nd:$GdCa_4O(BO_3)_3$ is confirmed to be an excellent SFD laser crystal, but a relatively low thermal conductivity has been proved to be the sole drawback of Nd:$GdCa_4O(BO_3)_3$ crystals.[542] Thus, to obtain the highest possible laser output power, special attention to the cooling process is required.

Owing to the superiority of Nd:$GdCa_4O(BO_3)_3$ crystal in SFD green laser generation, it has been manufactured as the core device in the green laser pointer and also is being brought to market in China. Currently, the combination of Nd:YVO_4 and $KTiOPO_4$ is the most commonly used model in a commercialized green laser pointer, but it still has some disadvantages, such as the laser system is a complex which needs two independent crystals (Nd:YVO_4 and $KTiOPO_4$) to achieve the function of laser and SHG. The extra optical attenuator was also needed to decrease the output power to eye-safe region ($\leq$ 1 mW). However, the green laser pointer made with Nd:$GdCa_4O(BO_3)_3$ crystals can effectively overcome the above problems.[524] First, Nd:$GdCa_4O(BO_3)_3$ crystal with high optical quality can be easily grown in a short time with the commercial Czochralski method. Moreover, Nd:$GdCa_4O(BO_3)_3$ crystal has a smaller emission cross-section and NLO coefficient compared to Nd:YVO_4 and $KTiOPO_4$, respectively, which offers the tunable absorbed pumped power range that is easier to decrease the output power to eye-safe region ($\leq$ 1 mW). Furthermore, Nd:$GdCa_4O(BO_3)_3$ crystals are expected to have potential for applications in laser displays and self-mode-locking laser devices.

4.2.3. Active Ions Doped $La_2CaB_{10}O_{19}$ and $LaBGeO_5$ Crystals. $La_2CaB_{10}O_{19}$ crystal is a novel NLO crystal with a highly effective NLO coefficient (d_{eff} = 1.05 pm/V), a wide transmission range (185−3000 nm), and favorable mechanical and thermal properties (detailed parameters are available in section 3.4). Thus, it is possible to dope this borate with active ions to create an Nd:$La_2CaB_{10}O_{19}$ SFD crystal. The Nd ions occupy the crystallographic positions of La and Ca atoms in the $La_2CaB_{10}O_{19}$ host crystal and split the emission spectra. Thus, the SFD properties in two laser channels have been investigated by Brenier *et al.*,[543] which correspond to the spectral wavelength peaked at 1343 and 1322 nm for $^4F_{3/2} \rightarrow {}^4F_{13/2}$ as well as 1051 and 1069 nm for $^4F_{3/2} \rightarrow {}^4F_{11/2}$. On the basis of this, SFD green and red lasers have been obtained, but the maximum output power of 525 nm laser is still limited to be only about 100 mW in Nd:$La_2CaB_{10}O_{19}$ SFD crystal,[544] which is quite low compared with those in Nd:$GdCa_4O(BO_3)_3$ and Yb:$YAl_3(BO_3)_4$ crystals. However, the maximum output power of 801 mW SFD laser in Nd:$La_2CaB_{10}O_{19}$ crystal has been obtained by Yu *et al.* (Figure 35d);[545] this occurs by exciting the Nd ions in the Ca crystallographic positions (Figure 35b) in $La_2CaB_{10}O_{19}$. These studies also confirmed that the selective excitation of active ions can result in a large difference in the output power. For example, the maximum

https://dx.doi.org/10.1021/acs.chemrev.0c00796
Chem. Rev. 2021, 121, 1130−1202

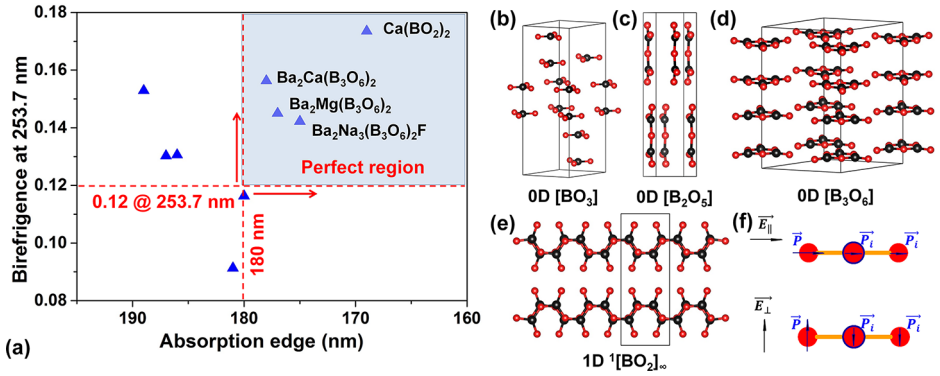

Figure 36. (a) Summary of available borate-based deep-UV birefringent materials concerning on the two critical properties of absorption edge and birefringence in deep-UV spectral region of 253.7 nm. All of the listed birefringent data are collected from their experimental results at 253.7 nm or derived from the corresponding Sellmeier equations. (b–e) Four different types of B–O anionic framework (0D $[BO_3]$, $[B_2O_5]$, $[B_3O_6]$ units, and 1D $^1[BO_2]_\infty$ chains) with coplanar arrangement. (f) Dipole–dipole interaction model. Adapted with permission from ref 33. Copyright 2018 The American Chemical Society. Parts b–e were drawn by using the crystallographic information file of $Ca_3(BO_3)_2$ (ICSD: 23664), α-BaB_2O_4 (ICSD: 14376), $Ca(BO_2)_2$ (ICSD: 34641) in ICSD, and $Li_2Na_2B_2O_5$ from ref 560.

output power of 801 mW was achieved with the SFD laser at the wavelength of 533 nm with the citation of Nd ions in the Ca positions,[545] however, the enhancement of output power was as large as 7.8 time greater than by excitation of Nd ions in the La positions.

The $REBGeO_5$ (RE = rare-earth metals) family exhibits two different types of structures depending on the ionic size of the rare-earth metals, namely stillwellite- and datolite-type structures. We were concerned in this section with the former one because of its acentric and polar with the trigonal space group $P3_1$ (no. 144), while the later one belongs to the centrosymmetric space group $P2_1/c$.[546] The stillwellite-type $REBGeO_5$ family features 1D chains of corner-sharing $[BO_4]$ tetrahedra along the c axis that are capped by the $[GeO_4]$ tetrahedra. Among them, $LaBGeO_5$ crystal was investigated in great detail on its ferroelectric, NLO, and laser properties. $LaBGeO_5$ crystals melt congruently at the melting point of 1200 °C, and thus it can be grown by the Czochralski method.[547] $LaBGeO_5$ crystals are transparent in the spectral region from 190 to 4500 nm. The derived birefringence is 0.0372 at 1064 nm, which is sufficient for the phase matching required by the SHG process of 1064 nm incident laser.[547] More than 300 mW of 355 nm generation was confirmed by a cascaded configuration from 1064 nm in a $LaBGeO_5$ crystal by Hirohashi *et al.*[548] Furthermore, $LaBGeO_5$ crystals can also be easily incorporated with Nd active ions and thus can serve as SFD materials. In 1998, Capmany *et al.* obtained the SFD green laser radiation first at 524 nm using the fundamental laser line at 1048 nm in type **I** phase matching Nd:$LaBGeO_5$ crystals.[549] The output power is extremely limited and less than 100 μW, which is due to the low NLO coefficients of $LaBGeO_5$ crystals.[549] The $^4F_{3/2} \rightarrow {}^4F_{13/2}$ laser channel of Nd ions in Nd:$LaBGeO_5$ crystals makes it possible to perform laser radiation at 1314 and 1386 nm, corresponding to the π and δ polarization.[550] Thus, the SFD red laser generation of 657 nm radiation is demonstrated with an output power of approximately 0.8 mW in Nd:$LaBGeO_5$ crystals by Capmany *et al.*[550] Overall, the SFD performance of Nd:$LaBGeO_5$ crystals is too weak to stay competitive compared to other crystals for practical SFD laser applications.

4.3. Active Ions Doped Borate Fluorides

4.3.1. Active Ions Doped $Ca_5(BO_3)_3F$ Crystal. As discussed in section 3.9.1, $Ca_5(BO_3)_3F$ crystal was characterized as a promising NLO material, consequently, its SFD properties were investigated first by Li *et al.* in 2012.[551] An Nd ions (2%) doped $Ca_5(BO_3)_3F$ crystal with sizes up to 51 × 48 × 8 mm^3 has been grown by top seeded solution growth method with the Li_2O–B_2O_3–LiF flux system, in which Nd occupied the Ca sites with simultaneously substituting partial O with F to preserve the electroneutrality. Thus, the formula was determined to be $(Nd_{0.02}Ca_{0.98})_5(BO_3)_3F_{0.9}O_{0.1}$. The Nd:$Ca_5(BO_3)_3F$ crystal shows long fluorescence lifetime of 51.8 μs with the quantum efficiency reaching 9.09%, which is slightly smaller but about equal with other famous borate-based SFD crystals.[551] Thus, Nd:$Ca_5(BO_3)_3F$ crystal may be a new SFD material once the output of a stable SFD laser can be achieved with high power and optical conversion efficiency.

4.3.2. Active Ions Doped $BaCaBO_3F$ Crystal. The potential of Yb:$BaCaBO_3F$ crystal for both lasing at 1034 nm and self-doubling the laser light to generate 517 nm is particularly attractive because the Yb ions do not exhibit an absorption loss at the frequency of the doubled light. Thus, the spectroscopic analyses and laser-pumped laser experiments of Yb:$BaCaBO_3F$ crystal were performed first by Schaffers *et al.* in 1996.[552] The Yb:$BaCaBO_3F$ crystals were grown by the Czochralski technique, in which the Yb ions were used to occupy the Ca sites instead of the Ba positions because the size of the Yb ion is most closely suited to the seven-coordinated Ca sites. The Yb:$BaCaBO_3F$ laser has been demonstrated with a measured slope efficiency of 38% for the fundamental laser output and threshold output power of near 100 mW.[552] The polarized spectroscopic properties of Yb:$BaCaBO_3F$ crystal were studied by Zhao *et al.* in 2011,[553] indicating the absorption cross sections of 1.5 × 10^{-20} cm^2 at 534 nm for δ polarization, which is much larger than those of Nd:$YAl_3(BO_3)_4$ and Nd:$GdCa_4O(BO_3)_3$ SFD laser crystals. But, in the meanwhile, such a large absorption at 534 nm is the most probable obstacle to realizing SFD output for Yb:$BaCaBO_3F$ crystal at 534 nm. Thus, there is no report on its output of 534 nm green laser to date.

https://dx.doi.org/10.1021/acs.chemrev.0c00796
Chem. Rev. 2021, 121, 1130–1202

5. BORATE-BASED BIREFRINGENT MATERIALS

Birefringent materials that can modulate the polarization of light are essential components of modern optical materials as they can be utilized as prism polarizers, phase compensators, and beam displacers, *etc.*[16,554,555] The availability of short wavelength polarization light, including the UV and deep-UV spectral regions, has greatly facilitated the work of academic and industrial to requirements. To date, several commercial birefringent materials are available, including $CaCO_3$, YVO_4, TiO_2, MgF_2, and α-BaB_2O_4 crystals. Among them, only MgF_2 and α-BaB_2O_4 crystals can be used for light polarization in the deep-UV spectral region. However, the birefringence of MgF_2 is fairly small (0.0136@193 nm) and the absorption edge of α-BaB_2O_4 (189 nm) is very close to the boundary value of deep-UV region (200 nm), which hinders their utility for light polarization in the deep-UV region. Therefore, high-performance birefringent materials in the deep-UV region are still urgently needed, and thus many borate-based birefringent crystals have been continuously discovered, studied, and characterized with large birefringence and deep-UV absorption edges (Figure 36a). Therefore, in this section, we will mainly focus on the deep-UV borate-based birefringent crystals that are characterized by large as-grown crystals. We believe that these selected crystals provide an idea of the current status and future opportunities for researchers interested in the field of optical devices that require deep-UV birefringent materials. Similarly, we will start with the consideration of necessary requirements for a practical deep-UV birefringent material.[16,28−33,557−566]

5.1. Necessary Requirements for a Practical Birefringent Material

First, crystallizing into the effective non-cubic crystal system is the prerequisite for crystals to be applied as a birefringent material. These structures in cubic systems are excluded here because their birefringence is zero owing to their isotropic nature. In addition, those uniaxial crystals in hexagonal, tetragonal, and trigonal systems with two independent refractive indexs (n_o and n_e) are more favorable in practical use than biaxial crystals in orthorhombic, monoclinic, and triclinic systems with three independent refractive indexs (n_x, n_y, and n_z). Second, a sufficiently large birefringence of more than 0.10 at 589 nm is required for deep-UV birefringent materials. Third, the absorption edges of deep-UV birefringent materials are always required to blue-shift to as far as possible below 200 nm (the lower, the better) and also retain high transparency (>70%, the higher, the better) in the UV region at the same time. Fourth, large crystals should be grown easily (>cm^3) with high quality, and also the favorable growth habit is extremely important. Birefringent materials should also possess favorable thermal expansion coefficients. The tremendous anisotropy among different axes can cause the as-grown crystals to crack along the cleavage face when the tension stress is larger than the critical stress. Generally, the possible cleavage face can be predicted by analyzing its structure and also can be avoided by choosing the appropriate orientation of seed crystals. For example, the *c* axis is the sole main axis of α-BaB_2O_4 crystal, thus the main section perpendicular to the *c* axis is its cleavage face. Thus, α-BaB_2O_4 crystals without cracking can be grown from the direction that is perpendicular to the *c* axis. Technically, those congruent melting crystals are easier to grow starting from their stoichiometric ratios by the Czochralski and Bridgman method. Last but not least, the ideal deep-UV birefringent materials should have high laser damage threshold and high chemical, physical, and mechanical stabilities. Thus, a birefringent crystal should be chemically and physically stable before, during, and after operation in a laser system, and also the beneficially mechanical and thermal stability are important factors to be included. These require birefringent crystals hard to crack, do not decompose, and deliquesce during operation.

5.2. Borate-based Birefringent Materials with 0D B−O Anionic Groups

5.2.1. Borate-based Birefringent Materials with 0D [BO_3] Units. *5.2.1.1. $Ca_3(BO_3)_2$.* The structure of $Ca_3(BO_3)_2$ was solved and reported for the first time by Schuckmann and re-determined by Vegas *et al.*[556] The compound crystallizes in the trigonal space group $R\bar{3}c$ (no. 167) and contains 0D [BO_3] triangles. The structure was constructed by the cation-centered polyhedra, with eight-coordinated Ca located at the center of a distorted square antiprism and [BO_3] units. All the coplanar [BO_3] triangles are perpendicular to the *c* axis and expand in the *ab* plane. The behavior of the corresponding electron configuration is markedly different when the electrical field direction of an incident light wave is within or perpendicular to the planes formed by coplanar [BO_3] triangles. Thus, a large birefringence in $Ca_3(BO_3)_2$ crystal can be predicted because [BO_3] triangles are all in planes perpendicular to the optical axis. The $Ca_3(BO_3)_2$ crystal melts congruently (1479 °C) and was grown by the Czochralski method. As-grown $Ca_3(BO_3)_2$ crystals are likely to cleavage along the *ab* plane, however, the use of seed crystals with [001] direction can avoid the cleavage phenomena. Thus, colorless and transparent $Ca_3(BO_3)_2$ crystal with dimensions of 30 × 30 × 15 mm^3 has been grown successfully by Zhang *et al.*[29] The absorption edge of $Ca_3(BO_3)_2$ crystal occurs at 180 and 3800 nm for UV and infrared spectral region, respectively, accompanying with a high transparency (>70%) in the region of 280−2500 nm. The ordinary (n_o) and extraordinary (n_e) refractive indices were measured at 12 different wavelengths between 404.7 and 1068 nm *via* the minimum deviation method, which reveals that $Ca_3(BO_3)_2$ crystal has a large birefringence of Δn = 0.0927−0.1020 at the measured region.[29] Meanwhile, the Sellmeier dispersion equations have been fit from the measured refractive indices. The thermal expansion coefficients for *c* and *b* axes of $Ca_3(BO_3)_2$ crystal are measured to be 4.690 × 10^{-5} and 1.367 × 10^{-5} K^{-1}, respectively.[557] The expansion difference (α_c/α_b = 3.43) is obviously smaller than that of benchmark α-BaB_2O_4 (9.0) crystal, which indicates that $Ca_3(BO_3)_2$ crystal exhibits a favorable anisotropic thermal expansion, which will effectively protect the crystals from cracking. Thus, $Ca_3(BO_3)_2$ crystal is a promising deep-UV birefringent material. To date, its laser damage threshold and physicochemical stability are still unknown.

5.2.1.2. $Ba_2Mg(BO_3)_2$. The buetschliite-type borate, $Ba_2Mg(BO_3)_2$, was initially reported as a luminescent material by Keszler *et al.* in 1995.[558] It belongs to trigonal space group $R\bar{3}m$ (no. 166) and exhibits isolated 0D [BO_3] units that are interconnected *via* corner- or edge-sharing Ba- and Mg-based polyhedra. The pseudo-layers of [BO_3] triangles extend orthogonal to the crystallographic *c* axis (Figure 36b). Interleaved between these pseudo-layers are double-layers of Ba sites and single-layers of Mg sites, respectively. The $Ba_2Mg(BO_3)_2$ crystal was proposed first to be a potential negative birefringent material with theoretical studies by Li *et*

https://dx.doi.org/10.1021/acs.chemrev.0c00796
Chem. Rev. 2021, 121, 1130−1202

al. in 2011.[16] $Ba_2Mg(BO_3)_2$ crystals melt congruently at 1247 °C and were recently grown to large size by Lu *et al. via* the Kyropoulos technique.[559] Similar to $Ca_3(BO_3)_2$ crystal, a [001]-oriented seed crystal was also used to grow $Ba_2Mg(BO_3)_2$ crystals, and thus a optically perfect single crystal with the dimensions up to 37 × 25 × 17 mm^3 was obtained. The 1 mm thick and double-side polished $Ba_2Mg(BO_3)_2$ crystal is shown to exhibit a high transmittance larger than 80% in the spectral range of 300−3000 nm with the UV absorption edge located at about 187 nm.[559] The as-grown $Ba_2Mg(BO_3)_2$ crystal was cut as a right-angle prism with an apex angle of 30.12° to measure the refractive indices at 13 different spectral lines changing from 253.7 to 1529.6 nm, which reveals the typical negative feature ($n_o > n_e$) with relatively high birefringence (Δn = 0.0834−0.1302) at measured wavelengths.[559] Therefore, the large birefringence combined with a short deep-UV cutoff edge of $Ba_2Mg(BO_3)_2$ make it a potential birefringent crystal in UV and deep-UV region. However, its thermal, chemical, physical, and mechanical stabilities are still unknown to date.

5.2.2. Borate-based Birefringent Materials with 0D [B_2O_5] Units. *5.2.2.1. $Li_2Na_2B_2O_5$.* A new mixed alkali metal borate, $Li_2Na_2B_2O_5$, was recently obtained by Pan *et al.*[560] and was immediately shown to be a promising deep-UV birefringent material. $Li_2Na_2B_2O_5$ crystallizes in the orthorhombic space group *Cmcm* (no. 63) and shows 0D isolated [B_2O_5] FBBs. The coplanar [B_2O_5] dimers extend in the *bc* plane and are further stacked along the *a* axis, which are further linked by $^1[LiO_2]_\infty$ chains constructed from edge-sharing [LiO_4] tetrahedra to form 3D framework that hosts the [NaO_n] (n = 5, 8) polyhedra within the channels. Interestingly, the dihedral angle in [B_2O_5] units is zero, indicating that two [BO_3] triangles in the [B_2O_5] units is strictly coplanar (Figure 36c). This type of configuration is very rare in borates and has only been observed in few borates (Tables S1−S4 in the SI), for example $Er_2B_2O_5Cl_2$, $MgUO_2(B_2O_5)$, $Li_2Sr_4B_{12}O_{23}$, and $Sr_2Sc_2(BO_3)_2(B_2O_5)$.[560] Compared with coplanar [BO_3] triangles, [B_2O_5] units with such alignment exhibit more highly localized valence electrons and anisotropy polarizability and thus is more likely to cause a large birefringence. $Li_2Na_2B_2O_5$ crystal melts incongruently and thus has been grown by the top seeded growth method with a self-flux system. As a result, a $Li_2Na_2B_2O_5$ crystal with size of 35 × 15 × 5 mm^3 was obtained.[560] The average thermal expansion coefficients are 47.72 × 10^{-6}, 8.54 × 10^{-6}, and 9.01 × 10^{-6} K^{-1} for three axes, respectively. The expansion difference of $Li_2Na_2B_2O_5$ crystal is determined to be α_a/α_b = 5.6, which will effectively protect the crystal from cracking. $Li_2Na_2B_2O_5$ crystal exhibits a high transparency (>60%) in the range of 187−3500 nm with a deep-UV absorption edge of 181 nm and its optical quality is high enough, which make it possesses a high laser damage threshold of ∼7.5 GW/cm^2 at the radiation conditions of 1064 nm, 10 ns, and 10 Hz. The refractive indices at only five different spectral lines ranging from 405.0 to 1546.7 nm were obtained *via* (001) plate of $Li_2Na_2B_2O_5$ crystal, which gives a large birefringence of Δn = 0.08441−0.09849.[560] Better yet, this work indicates that the [B_2O_5] units, particularly those in coplanar alignment, can serve as an alternative unit that can be used to design deep-UV birefringent materials. To date, the chemical, physical, and mechanical stabilities of $Li_2Na_2B_2O_5$ crystal have not been reported.

5.2.3. Borate-based Birefringent Materials with 0D [B_3O_6] Units. *5.2.3.1. α-BaB_2O_4.* The high temperature phase, α-BaB_2O_4, is one of the most well investigated and commercialized birefringent crystals.[28] α-BaB_2O_4 crystallizes in the trigonal space group $R\bar{3}c$ (no. 167) and contains 0D [B_3O_6] triangles that are separated by Ba^{2+} cations, in which the nearly coplanar [B_3O_6] rings are perpendicular to the *c* axis. Structurally, the [B_3O_6] groups in α-BaB_2O_4 arrange in coplanar alignment, thus the optical anisotropy along and vertical to the B−O planes is further enhanced to lead to a reasonably large birefringence. The α-BaB_2O_4 crystal melts congruently at 1095 ± 5 °C and 1 atm. Different methods have been used to obtain large size α-BaB_2O_4 crystals from both stoichiometric melts and high-temperature solutions, including the Czochralski, Bridgman, and Kyropoulos methods. Studies have shown that the α-BaB_2O_4 crystal is likely to crack along the (001) cleavage face during the crystal growth if the seed orientation is parallel to *a* or *b* axis. On the contrary, if the seed orientation is parallel to its sole optical *c* axis, the optically perfect α-BaB_2O_4 crystals can be obtained. The as-grown crystals can reach 80 mm in diameter and 70 mm in length. The wide transmission range is observed in the as-grown α-BaB_2O_4 crystal with the UV cutoff wavelength located at 189 nm. The α-BaB_2O_4 crystal is a negative uniaxial crystal with a large birefringence of 0.1222 at 532 nm.[28] The thermal expansion of the α-BaB_2O_4 crystal is anisotropic, and the average thermal expansion coefficient for the *c* axis is measured to be 36.3 × 10^{-6} K^{-1}, which is about nine times larger than that of *a* (= *b*) axis (9.0 × 10^{-6} K^{-1}). The tremendous anisotropy of the thermal expansion can cause α-BaB_2O_4 crystal to bend along the *c* axis during the crystal growth process.

5.2.3.2. $Ba_2Na_3(B_3O_6)_2F$. The extensive search in the BaB_2O_4−NaF phase diagram led to the discovery of $Ba_2Na_3(B_3O_6)_2F$ by Bekker *et al.* in 2009.[561] It belongs to the hexagonal space group $P6_3/m$ (no. 176), and its FBBs are determined as [B_3O_6] units (Figure 36d), which perfectly arrange in parallel in the *ab* plane that are further condensed with [BaO_{10}] polyhedra to form $^2[Ba_2B_6O_{12}]_\infty$ double layers. The Na-based polyhedra locate between these layers. The single crystals of $Ba_2Na_3(B_3O_6)_2F$ were grown by Bekker *et al.* from the high-temperature solution of BaB_2O_4:NaF = 1:1 in 2009,[562] whereas the potential of $Ba_2Na_3(B_3O_6)_2F$ crystal to be a deep-UV birefringent material was recognized first by Li *et al.* and Pan *et al.* in 2014.[563,564] Compared to α-BaB_2O_4, $Ba_2Na_3(B_3O_6)_2F$ exhibits superior or comparable optical properties in several pivotal aspects:[563,564] (1) $Ba_2Na_3(B_3O_6)_2F$ crystal has a high transparency (>80%) in the range of 300−3000 nm with short absorption edges of 186 or 175 nm, depending on the quality of as-grown crystals, which is shorter than that of α-BaB_2O_4 (189 nm). This makes $Ba_2Na_3(B_3O_6)_2F$ crystal be more effective for applications in the deep-UV spectral region. (2) $Ba_2Na_3(B_3O_6)_2F$ is a negative uniaxial optical crystal and exhibits a large birefringence of 0.0937−0.1300 at the measured region of 253.7−2325.0 nm, which is comparable to those of α-BaB_2O_4 crystal. (3) The average thermal expansion coefficients along the *a* (= *b*) and *c* axes are measured to be 12.1 × 10^{-6} and 27.6 × 10^{-6} K^{-1}, respectively. The expansion difference (α_c/α_a = 2.27) of $Ba_2Na_3(B_3O_6)_2F$ crystal is much smaller than that of α-BaB_2O_4 crystal (α_c/α_a = 9.0), indicating a favorable anisotropy that can keep the crystal from cracking. (4) The laser damage threshold of $Ba_2Na_3(B_3O_6)_2F$ crystal is measured to be 108 GW/cm^{-2} at

https://dx.doi.org/10.1021/acs.chemrev.0c00796
Chem. Rev. 2021, 121, 1130−1202

1064 nm, 30 ps, and 10 Hz, which is much higher than that of α-BaB_2O_4 crystal in the same conditions. (5) $Ba_2Na_3(B_3O_6)_2F$ crystal melts congruently with no first-order phase transition occurring from room temperature to its melting point (820 °C), which is also lower than that of α-BaB_2O_4 crystal. (6) The optical measurements indicate that the Glan type polarizer constructed by $Ba_2Na_3(B_3O_6)_2F$ crystal exhibits good performance with the extinction ratio of 2.8×10^4:1, which is in the same level of α-BaB_2O_4 crystal (3.9×10^4:1). Besides, $Ba_2Na_3(B_3O_6)_2F$ crystal possesses nonhygroscopic feature, a suitable Mohs hardness (4.5), and good mechanical stability, indicating that $Ba_2Na_3(B_3O_6)_2F$ crystal is a competitive birefringent candidate for deep-UV region.

5.2.3.3. $Ba_2M(B_3O_6)_2$ (M = Mg, Ca). Two isomorphic mixed alkaline-earth borates, $Ba_2Mg(B_3O_6)_2$ and $Ba_2Ca(B_3O_6)_2$, were initially obtained and reported by Liebertz *et al.* in 1984.[565] They were both proposed first to be potential birefringent materials with theoretical studies by Li *et al.* in 2011.[16] After that, Li *et al.* obtained sizable crystals and evaluated the optical properties in 2012 for the Mg analogue and 2016 for Ca analogue, respectively.[31,32] Both structures crystallize in the centrosymmetric space group $R\bar{3}$ (no. 148) with 0D FBBs of $[B_3O_6]$ rings. These coplanar rings are parallel to each other and stack along the *c* axis in the unit cell, with Ba and M site atoms alternately located between the $[B_3O_6]$ pseudo-sheets and forming 2D layers constructed by Ba- and Mg-based polyhedra. Differential scanning calorimetry and melting experiments confirm the congruent melting feature of $Ba_2Mg(B_3O_6)_2$ and $Ba_2Ca(B_3O_6)_2$ crystals with the corresponding melting points of 1000 and 1116 °C, respectively.[31,32] In principle, they can be grown from their stoichiometric melts, while the lower growth temperature is more preferred. Thus during the earlier growth of both crystals, the high-quality $Ba_2Mg(B_3O_6)_2$ and $Ba_2Ca(B_3O_6)_2$ crystals were obtained by top seeded solution growth with H_3BO_3 and NaF as fluxes. The as-grown crystals show high optical quality with the sizes up to $40 \times 40 \times 7$ mm^3 and $40 \times 28 \times 10$ mm^3 for Mg and Ca analogues, respectively. Both crystals are characterized by short cutoff edges (177 and 178 nm), large birefringence (0.0914−0.1455 and 0.1001−0.1563 in the measured region of 253.7−2325.4 nm), and small expansion difference (α_c/α_a = 4.89 and 4.67).[31,32] On the basis of this, Li *et al.* designed and manufactured Glan−Taylor type polarizers with $Ba_2Mg(B_3O_6)_2$ and $Ba_2Ca(B_3O_6)_2$ crystals (Figure 37a). The optical tests indicate that the polarizers have the extinction ratios of 7.1×10^4:1 for Mg and 3.1×10^4:1 for Ca analogues (Figure 37b), respectively, which are in the same level of extinction ratio ($\sim 10^4$) with that made of commercial α-BaB_2O_4 crystals. Besides, the measured refractive indices at different temperatures from 24 to 140 °C show the good thermal stability of $Ba_2Mg(B_3O_6)_2$ crystals as the reflective indices' differences are minor at different temperatures.[566] Therefore, $Ba_2Mg(B_3O_6)_2$ and $Ba_2Ca(B_3O_6)_2$ crystals are competitive deep-UV birefringent materials for practical applications.

5.3. Borate-based Birefringent Materials with 1D B−O Anionic Groups

5.3.1. Borate-based Birefringent Materials with 1D $^1[BO_2]_\infty$ Chains. *5.3.1.1. $Ca(BO_2)_2$.* As early as in 1932, the structure of $Ca(BO_2)_2$ (also written as CaB_2O_4) crystal was determined by Zachariasen *et al.*[83] It belongs to the orthorhombic system with a centrosymmetric space group of

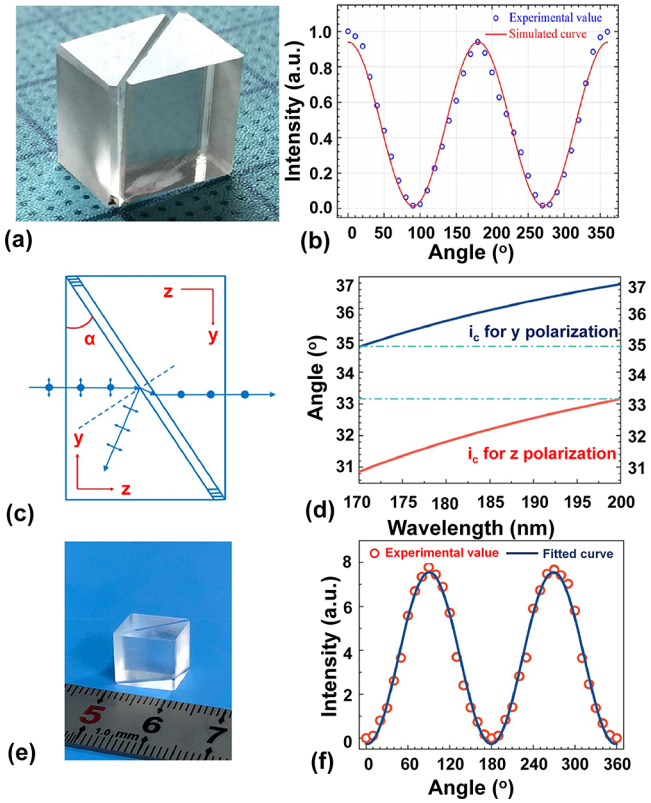

Figure 37. (a) Glan−Taylor polarizer fabricated by $Ba_2Ca(B_3O_6)_2$ crystals. (b) Tested transmitted beam intensity versus rotating angle of $Ba_2Ca(B_3O_6)_2$ based Glan−Taylor polarizer. For the extinction ratio measurement, a 633 nm He−Ne laser light beam passed through a Glan−Taylor polarizer made of $CaCO_3$, and then the light was sent into a second Glan−Taylor polarizer fabricated by $Ba_2Ca(B_3O_6)_2$ crystal. (c) Schematic design representation of a $Ca(BO_2)_2$ crystal-based Glan polarizer. (d) Critical angle of total internal reflection (i_c) for x and y polarization versus deep-UV spectral region from 170 to 200 nm. (e) The Glan polarizer fabricated by $Ca(BO_2)_2$ crystals. (f) The tested transmitted light energy versus rotating angle of a $Ca(BO_2)_2$ based Glan polarizer. For the extinction ratio measurement, a 193 ArF laser light beam passed through a commercial MgF_2 Rochon polarizer, and then the light was sent into a second $Ca(BO_2)_2$ based Glan polarizer. Reproduced with permission from refs 31 and 33. Copyright 2017 and 2018 The American Chemical Society.

Pbcn (no. 60). $Ca(BO_2)_2$ presents 1D anionic framework of $^1[BO_2]_\infty$ chains (Figure 37e) constructed by $[BO_3]$ triangles which are in almost coplanar configuration and further linked by neighboring $^2[CaO_4]_\infty$ layers to form the final 3D crystal structure. According to the dipole−dipole interaction model (Figure 36f), the polymerization of $[BO_3]$ triangles within the same plane can enhance the average anisotropy of polarizabilities. As a consequence, the highly polymerized $^1[BO_2]_\infty$ chains are expected to have larger average anisotropic polarizabilities than those of isolated $[BO_3]$ groups and resulting in a larger birefringence.[33] Thus, the crystal of $Ca(BO_2)_2$ was grown and subjected to physicochemical property characterizations, and based on this, $Ca(BO_2)_2$ crystal is highlighted as a novel deep-UV birefringent material for light polarization as it shows great advantages in the following aspects:[33] (1) $Ca(BO_2)_2$ crystal melts congruently without a first-order phase transition occuring in the region from room temperature to its melting point (1152 °C) at atmospheric pressure, and thus the $Ca(BO_2)_2$ crystal can be easily grown

https://dx.doi.org/10.1021/acs.chemrev.0c00796
Chem. Rev. 2021, 121, 1130−1202

from its stoichiometric melts *via* high-efficiency Bridgman, Czochralski, heat exchange, and Kyropoulos methods. Accordingly, optically perfect $Ca(BO_2)_2$ crystals with the maximum dimensions up to 50 × 41× 22 mm^3 have been obtained by Pan and Poeppelmeier *et al.*[33] with the Czochralski method. (2) The $Ca(BO_2)_2$ crystal posseses three vital "best" properties among the available borate-based deep-UV birefringent material (Figures 36,37a), including a shortest UV cutoff edge (169 nm), a largest birefringence (Δn = 0.1230−0.1735 in the measured region of 253−1529 nm), and a highest laser-induced damage threshold (~3.1× α-BaB_2O_4). (3) The $Ca(BO_2)_2$ crystal is more likely to achieve practical applications as it has a relatively low growth temperature (1152 °C), much lower production costs, and high production yields. More importantly, the first Glan polarizer for deep-UV light polarization has been fabricated and characterized by using the as-grown $Ca(BO_2)_2$ crystals (Figures 37c−f), and also the extinction ratio of the as-fabricated $Ca(BO_2)_2$ polarizer was determined to be 1.1 × 10^4:1, which can satisfy the practical requirements. Thus, the $Ca(BO_2)_2$ crystal can be expected to be used in a wide field of applications, ranging from 193 nm lithography to complex laser systems of spectroscopy, and also the highly polymerized $^1[BO_2]_\infty$ chains can be regarded as a new birefringence-active unit to design novel deep-UV birefringent materials, which can be further confirmed by achieving extremely short absorption edges and large birefringence in $[BO_2]_\infty$ chains containing borates, like $Sr(BO_2)_2$ and $LiBO_2$ crystal.[33]

6. CONCLUSIONS AND PERSPECTIVES

Borates have achieved impressive progress over the past several decades and entered into a very exciting era, with recent discoveries laying the groundwork for further development of solid-state chemistry and advanced optical materials. In this context, there is a good reason to investigate the structural chemistry of borate and its functionality as novel optical materials. Studies related to newly discovered borates with rich structural diversity allow a deeper understanding of their structure−property relationship, paving the way for related inorganic systems with increased complexity and functional capabilities. In this review, we have surveyed the currently available anhydrous borates and analyzed the recent advances in their structural chemistry with special emphasis on the relations between structural architectures and optical properties. On the basis of this, we provide an overview on the state of art in borate-based optical materials, for this purpose, NLO, SFD, and birefringent materials are taken as representative examples to the area of borate-based optical materials that lie at the current frontier of knowledge. Several borates with unique structural characteristics have been discovered, and also many new borates show great potential as the irreplaceable optical materials. Overall, the future appears to look rather bright for borate chemistry and its optical materials. Even though many issues still remain and great challenges also exist, which need to be carefully considered and addressed to make borates show greatest advantage as the study subjects of solid-state chemistry and also a rich source of optical materials. We enumerate the thoughts here and look forward to many discoveries to come in borate chemistry and to address these challenges and issues to promote the academic and industrial applications.

6.1. Challenges to the Unrevealed Mechanism

Knowledge of the structure chemistry is crucial to our understanding of how the B−O/F anionic units are formed and then affect the optical performance of borates. Given this, several theories and rules have been intensively developed to analyze the structural features and also to get the correlation between microstructure and observed optical properties in borates. For example, the inherent rules for the occurrence of polyborate anion types proposed by Becker offer the possibility of inferring the possible B−O units' type of borates according to the ratios of cation and boron.[135] The anionic group theory developed by Chen *et al.*[20] indicates that the certain types of B−O anionic groups make the main contribution to the SHG coefficients, which make it possible to search the prospective borates by analyzing the arrangement of their B−O NLO active units. Besides, the extended [redacted] theory introduced by Belokoneva[10] offers a new tool to crystal chemical analysis of borates. These theories or rules are useful and indeed make considerable contribution in certain borate chemistry. However, some unrevealed mechanisms reflected by the unique structural features of borates still remain and need to be addressed:

(a) How does the flux promote the crystallization and crystal growth process of borates?

(b) What is the theoretical basis for the formation of unique structural rearrangements such as edge-sharing $[BO_4]$ tetrahedra, polymorphism, and highly polymerized B−O/F FBBs, *etc.*?

(c) How to distinguish the real contribution of independent atoms or units on optical properties in the experiment.

(d) How do we test the generalization ability of non-π-conjugated system on optical properties?

(e) Why are all of the $[B_3O_6]$ units in the borates with only such isolated units align in coplanar arrangement?

Most borates melt incongruently, and therefore it is apparent that in the course of growing borate crystals, the suitable flux system needs to be carefully chosen and well-controlled, as otherwise the improper choice of flux may prove to be caused to the unfavorable absorption but a serious impact will be brought on the optical quality of borates. Generally, the flux growth utilizes a high-temperature solution of borates as the solvent for crystallization. To date, the early stages of crystallization and crystal growth process can be investigated from high-temperature solutions by the *in situ* approaches, but what exactly goes on in the solution is still unknown and leading the limited understanding of borates' crystal growth mechanism.[567] The analysis of LiB_3O_5−$Li_2Mo_3O_{10}$ high-temperature solution reveals the solvent−solute interactions reflected by the transformation from the initial states ($^1[B_3O_6]_\infty$ chains + $[Mo_3O_{10}]$ clusters) to transition states ($^1[B_3O_6$−$MoO_3]_\infty$ chains + $[Mo_2O_7]$ clusters).[568] But, how exactly the flux promotes the crystallization and crystal growth process of borates is still unable to give a quantitative analysis due to the lack of approaches to routinely study these processes.

Besides, as we have discussed in section 2.5, formation of edge-sharing $[BO_4]$ tetrahedra in borates is quite unconventional and only observed in a few borates. Although theoretical studies in terms of lattice dynamics and electronic-structure calculations indicate that the vibrational modes of edge-sharing $[BO_4]$ tetrahedra are dynamically stable and all modes have real frequencies.[248] Certainly, the high pressure-driven

https://dx.doi.org/10.1021/acs.chemrev.0c00796
Chem. Rev. 2021, 121, 1130−1202

condition is known to be more favorable in the forms of such an unconventional connection. The real origin, however, responsible for the formation of edge-sharing [BO_4] tetrahedra in related borates, covering those obtained under high pressure and atmospheric pressure conditions, in energy- and structure-favorable way associated with their structural stabilities still remains unrevealed.

Structurally, the B−O/F FBBs of borate structures are generally small, with most of them which contain the B atoms less than six (see sections 2.3 and 2.4).[135] There are still some exceptions to this rule, the structure of which are based on the FBBs containing far more B atoms, and to date, the largest one reaches 63 in the [$B_{63}O_{133}$] FBBs of $Cs_3B_7O_{12}$.[128] Studies have shown that the decrement of cation/boron ratio is beneficial to generate the highly polymerized B−O/F FBBs, and also, almost all of the borates with high-polymeric FBBs contain cations with large ionic radii (like Rb and Cs), which tend to make the whole construction more stable and closer and thus resulting in the increased polymerization of B−O/F FBBs. Still, owing to the absence of mechanism to guide the rational synthesis of borates with target structures, the formation of high-polymerized B−O/F FBBs still remains elusive.

With respect to the analysis of structure−property relationships, especially for linear (birefringence) and NLO (SHG coefficients) properties, several theoretical approaches have been employed,[16,20,569−574] such as the anionic group theory, real-space atom-cutting technique, SHG-weighted charge density analysis tool, Born effective charges analysis, and atomic response theory, which enable us to quantitatively or qualitatively analyze the contribution of the individual ions (or groups) to the optical properties. It turns out that we are very successful at predicting and evaluating the theoretical results of birefringence and SHG coefficients with relative mean errors less than 5% compared with experimental data[16] but find it significantly more difficult to distinguish the contribution of individual atoms or units on optical properties in experiment. Yet, it is likely that these difficulties mainly come from the infeasibility of separating the atoms of whole crystal structure in experiments, which may hold the key in the endeavor of realizing their experimental verifications. Likewise, to what extent the UV transparent non-π-conjugated units[8,575−578] can also lead to the improvement of birefringence and SHG coefficients, while undoubtedly important, is not well understood to date. Hence, the researcher must always perform some degree of exploratory work to identify the contribution of π- and non-π-conjugated units in theory and experiment.

6.2. Opportunities to Prediction and Simulation

For most borate-based optical materials, their discovery has followed the traditionally inductive paradigm between experimental and computational chemistry, in which the experimental approaches enable the acquirement of new structures with assigned molecular formula, and then computational methods were used to clarify the structure−property relationships. Better yet, such a combination model has been updated with the participation of theoretical search and prediction methods, which largely accelerate the discovery of new borates with target properties. There are three major approaches that have been used to theoretically search and predict new borate structures:[579−583] (1) making structural regulation on the known structures *via* substitution or co-substitution to predict new competitive borates; (2) making high-throughput screen based on large quantities of known structures to discover the potential borates with high optical performance, and (3) searching the local minimum or global minimum on a potential energy surface *via* systematic global structure optimization method to predict several undiscovered structures with assigned molecular formula. The former two methods request a suitable prototype or descriptor to facilitate the process of structural design, and also the predicted structures are usually limited in quantity and type, whereas the newly introduced systematic global structure optimization method to predict borate-based optical materials might enable us to obtain several experimentally undiscovered phases that are assigned to certain chemical constituents or molecular formulas. Thus, the desire to facilitate synthetic discovery with the help of above methods toward more likely chemical compositions has been omnipresent in the search of borate-based optical materials.

Simply put, the process of structure prediction includes two main steps, the structure with assigned crystallographic information should be obtained first and then further verification of its possibility to be formed. The early attempt at introducing the systematic global structure optimization method in ternary and quaternary borate system generate the $NaBeBO_3$ and Be_2BO_3F series with serval energy-favorable phases,[581,582] but unfortunately, they have not yet experimentally obtained to date. These approaches have enabled us to predict new structures with limited atomic numbers in unit cells, but they still face several challenges. Theoretically, the polyphyletic borate system with heavier elements or strongly correlated electrons is more time-consuming and complicated than binary ionic compounds, and also, the prediction of optical properties is more complicated than that of physical properties, as it describes not only a single state but also constantly changing states, and their calculation requires extensive and expensive sampling.[583] Experimentally, the number of generated structures by structure prediction method is usually extremely high, depending on the given accuracy, even though several thermodynamically stable structures with relatively small and closely formation enthalpies will be picked out to guide the experimental synthesis. They always show close structures with slight difference in crystallographic position of individual atoms, which make it hard to obtain one of the target compounds. We also noted that the deep-learning technique can be applied to crystallography from large repositories of crystallographic data,[584] which can effectively guide the synthetic efforts in the discovery of new structures and materials, especially in the case of systems composed of three or more chemical elements. However, there are still no borate-based optical materials, which have been predicted *via* deep-learning technique. It is expected that the prediction model in deep-learning is more effective than others once they are applied to predict potential optical materials in borate systems.

6.3. Toward the Limits and Elevation

The discovery of new borate structures and associated desirable properties has been a driving force behind solid-state chemistry and materials science for several decades. This review has distinctly shown the great optimism of studies on the structural chemistry of borates and their applications as multiple optical materials. It seems that these borates are approaching their limits on structure and optical performance parameters. Until now, structurally, the largest FBBs and maximum polymorphism are observed in $Cs_3B_7O_{12}$[128] with

https://dx.doi.org/10.1021/acs.chemrev.0c00796
Chem. Rev. 2021, 121, 1130−1202

$[B_{63}O_{133}]$ units and BiB_3O_6 series with six different phases.[585] In the case of three critical parameters for optical application, the limits of the strongest powder SHG response, the shortest absorption edge, and the largest birefringence are experimentally determined as 20 × KDP@1064 nm in Bi_3TeBO_9,[391] 120 nm in SrB_4O_7,[315] and 0.290@546 nm in SbB_3O_6,[586] respectively, but thinking optimistically, this is far from reaching the real limits of borates in structural aspects and properties. It was also apparent that most borates discussed in this review are composed of traditional $[BO_3]$ and $[BO_4]$ units, and few borates contain fluorinated $[BO_{4-x}F_x]$ tetrahedra. Recently, the discovery of linear $[BO_2]$ units in $K_5Ba_2(B_{10}O_{17})_2(BO_2)$ provide more useful information to push the current limits of borates to a new height.[587] We can imagine that the introduction of linear $[BO_2]$ units in the structures of currently available B−O/F anionic framework will cause more interesting FBBs and configuration. More importantly, the polarizability anisotropy of $[BO_2]$ units is found to be larger than those of traditional $[BO_3]$ and $[BO_4]$ units (Table 1), hence, theoretically designed KBO_2 exclusively composed of $[BO_2]$ units is predicted to have a large birefringence of 0.18@1064 nm, preliminarily prove that the idea of new $[BO_2]$ functional units can generate new limits in properties. Even better, when the terminal O atoms of $[BO_3]$ and $[B_3O_6]$ units are further linked by $[BO_2]$ units to form highly conjugated $[B_4O_6]$ and $[B_6O_9]$ units (Figure 38), much more enhacement on the polarizability anisotropy and hyperpolarizability can be expected and proved theoretically, which is more conducive to lead to the improvement of birefringence and NLO susceptibilities and thus creates new limits in properties. This virtuous circle of "new unit → new property → new limit" may also occur once more new units in borates being discovered. Like fluorinated $[BO_{3-x}F_x]$ triangles, face-sharing $[BO_{3-x}F_x]$ triangles, or $[BO_{4-x}F_x]$ tetrahedra. We admitted that the synthesis of such unprecedented units is extremely intractable, especially adopting the traditional preparation approaches, and thus for achieving this purpose, any reasonable guidance of synthetic efforts becomes highly valuable.

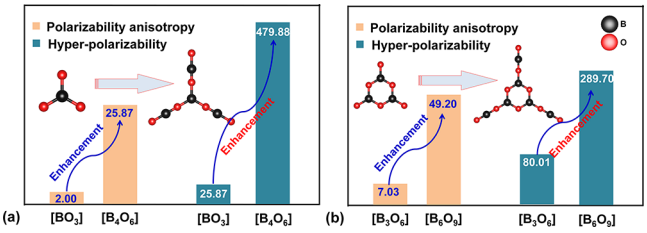

Figure 38. (a,b) Polarizability anisotropy and largest hyper-polarizability tensor of $[BO_3]$, $[B_4O_6]$, $[B_3O_6]$, and $[B_6O_9]$ units. These values were caculated by buliding the ideal geometric models of corresponding units.

ASSOCIATED CONTENT

Supporting Information

The Supporting Information is available free of charge at https://pubs.acs.org/doi/10.1021/acs.chemrev.0c00796.

Tabulated formulae, symmetry information, structural units, and ICSD codes for 0D, 1D, 2D, and 3D borates (PDF)

AUTHOR INFORMATION

Corresponding Authors

Kenneth R. Poeppelmeier − *Department of Chemistry, Northwestern University, Evanston, Illinois 60208-3113, United States;* orcid.org/0000-0003-1655-9127; Phone: 847-491-3505; Email: krp@northwestern.edu

Shilie Pan − *Key Laboratory of Functional Materials and Devices for Special Environments, Xinjiang Technical Institute of Physics and Chemistry, Chinese Academy of Sciences; Xinjiang Key Laboratory of Electronic Information Materials and Devices, Urumqi 830011, China; Center of Materials Science and Optoelectronics Engineering, University of Chinese Academy of Sciences, Beijing 100049, China;* orcid.org/0000-0003-4521-4507; Email: slpan@ms.xjb.ac.cn

Author

Miriding Mutailipu − *Key Laboratory of Functional Materials and Devices for Special Environments, Xinjiang Technical Institute of Physics and Chemistry, Chinese Academy of Sciences; Xinjiang Key Laboratory of Electronic Information Materials and Devices, Urumqi 830011, China; Center of Materials Science and Optoelectronics Engineering, University of Chinese Academy of Sciences, Beijing 100049, China;* orcid.org/0000-0002-1331-0185

Complete contact information is available at: https://pubs.acs.org/10.1021/acs.chemrev.0c00796

Notes

The authors declare no competing financial interest.

Biographies

Miriding Mutailipu received his B.S degree in Materials Science and Engineering from Hunan University in 2014. He then joined Professor Shilie Pan's research group as a Ph.D. student at University of Chinese Academy of Sciences. He completed his Ph.D. in Material Physics and Chemistry in 2019. In the same year, he started his independent career at Xinjiang Technical Institute of Physics and Chemistry of CAS (XTIPC, CAS). He is currently focusing on the borate chemistry and borate-based optical materials.

Kenneth R. Poeppelmeier is the Charles E. and Emma H. Morrison Professor in the Department of Chemistry at Northwestern University. He received his Ph.D. from Iowa State University (1978). His research covers several subjects in the field of inorganic solid-state chemistry, growth of single crystals, and the synthesis of new metal oxides and oxide fluorides, which emphasizes the connections between the synthesis and structure of new materials, the physical properties of new materials, and the technological advances that result from these discoveries.

Shilie Pan received his B.S. degree in Chemistry from Zhengzhou University in 1996. He completed his Ph.D. at the University of Science and Technology of China in 2002. From 2002 to 2004, he was a post-doctoral fellow at the Technical Institute of Physics and Chemistry, CAS. From 2004 to 2007, he was a post-doctoral fellow at Northwestern University. From 2007, he worked as a full professor at XTIPC, CAS. His current research interests include the design, synthesis, crystal growth, and evaluation of new optoelectronic functional materials.

https://dx.doi.org/10.1021/acs.chemrev.0c00796
Chem. Rev. 2021, 121, 1130−1202

ACKNOWLEDGMENTS

We gratefully acknowledge the National Natural Science Foundation of China (61835014, 51972336), Xinjiang Tianshan Youth Program-Outstanding Young Science and Technology talents (2019Q026), National Key Research Project (2016YFB0402104), the International Partnership Program of CAS (1A1365KYSB20200008), the Western Light Foundation of CAS (grant no. Y92S191301), CAS President's International Fellowship Initiative (PIFI, 2020DC0006), the Instrument Developing Project of CAS, the Science and Technology Service Network Initiative of CAS (KFJ-STS-QYZD-130), the Fujian Institute of Innovation, CAS, and the U.S. National Science Foundation (DMR-1904701).

ABBREVIATIONS

0D = zero-dimensional
1D = one-dimensional
2D = two-dimensional
3D = three-dimensional
B−O = boron−oxygen
B−O/F = boron−oxygen/fluorine
FBBs = fundamental building blocks
UV = ultraviolet
NLO = nonlinear optical
SFD = self-frequency-doubling
ICSD = Inorganic Crystal Structure Database
CSD = Cambridge Structural Database
SHG = second harmonic generation
pH = potential of hydrogen
HOMO = highest occupied molecular orbital
LUMO = lowest unoccupied molecular orbital
HP = high pressure
NMR = nuclear magnetic resonance
d_{eff} coefficient = effective second-order nonlinear optical coefficient
KDP = KH_2PO_4
Nd:YAG = $Nd:Y_3Al_5O_{12}$
SFG = sum-frequency generation
OPO = optical parametric oscillation
OCPCA = parametric chirped-pulse amplification
THG = third harmonic generation
FHG = fourth harmonic generation
SOJT = Second-order Jahn−Teller

REFERENCES

(1) Trofimenko, S. Recent Advances in Poly(pyrazolyl)borate (scorpionate) Chemistry. *Chem. Rev.* **1993**, *93*, 943−980.
(2) Becker, P. Borate Materials in Nonlinear Optics. *Adv. Mater.* **1998**, *10*, 979−992.
(3) Chen, C. T.; Wang, Y. B.; Wu, B. C.; Wu, K. C.; Zeng, W. L.; Yu, L. H. Design and Synthesis of an Ultraviolet-transparent Nonlinear Optical Crystal $Sr_2Be_2B_2O_7$. *Nature* **1995**, *373*, 322−324.
(4) Lin, Z. E.; Yang, G. Y. Oxo Boron Clusters and Their Open Frameworks. *Eur. J. Inorg. Chem.* **2011**, *2011*, 3857−3867.
(5) Keszler, D. A. *Borates: Solid State Chemistry. In Encyclopedia of Inorganic Chemistry*; King, R. B., Ed.; John Wiley & Sons: Chichester, 1994, *1*, 318−327.
(6) Chen, C. T.; Liu, G. Z. Recent Advances in Nonlinear Optical and Electro-optical Materials. *Annu. Rev. Mater. Sci.* **1986**, *16*, 203−243.
(7) Chen, C. T.; Sasaki, T.; Li, R. K.; Wu, Y. C.; Lin, Z. S.; Mori, Y.; Hu, Z. G.; Wang, J. Y.; Uda, S.; Yoshimura, M. et al. *Nonlinear Optical Borate Crystals: Principles and Applications*. Wiley-VCH: Weinheim. 2012.
(8) Mutailipu, M.; Zhang, M.; Yang, Z. H.; Pan, S. L. Targeting the Next Generation of Deep-Ultraviolet Nonlinear Optical Materials: Expanding from Borates to Borate Fluorides to Fluorooxoborates. *Acc. Chem. Res.* **2019**, *52*, 791−801.
(9) Sasaki, T.; Mori, Y.; Yoshimura, M.; Yap, Y. K.; Kamimura, T. Recent Development of Nonlinear Optical Borate Crystals: Key Materials for Generation of Visible and UV Light. *Mater. Sci. Eng., R* **2000**, *30*, 1−54.
(10) Belokoneva, E. L. Borate Crystal Chemistry in Terms of the Extended OD Theory: Topology and Symmetry Analysis. *Crystallogr. Rev.* **2005**, *11*, 151−198.
(11) Cheng, L.; Wei, Q.; Wu, H. Q.; Zhou, L. J.; Yang, G. Y. $Ba_3M_2[B_3O_6(OH)]_2[B_4O_7(OH)_2]$ (M = Al, Ga): Two Novel UV Nonlinear Optical Metal Borates Containing Two Types of Oxoboron Clusters. *Chem. - Eur. J.* **2013**, *19*, 17662−17667.
(12) Tran, T. T.; Yu, H. W.; Rondinelli, J. M.; Poeppelmeier, K. R.; Halasyamani, P. S. Deep Ultraviolet Nonlinear Optical Materials. *Chem. Mater.* **2016**, *28*, 5238−5258.
(13) Huang, H. W.; He, Y.; Lin, Z. S.; Kang, L.; Zhang, Y. H. Two Novel Bi-Based Borate Photocatalysts: Crystal Structure, Electronic Structure, Photoelectrochemical Properties, and Photocatalytic Activity under Simulated Solar Light Irradiation. *J. Phys. Chem. C* **2013**, *117*, 22986−22994.
(14) Shen, K. K.; Kochesfahani, S.; Jouffret, F. Zinc Borates as Multifunctional Polymer Additives. *Polym. Adv. Technol.* **2008**, *19*, 469−474.
(15) Yu, Y. X.; Zhao, J.; Bayly, A. E. Development of Surfactants and Builders in Detergent Formulations. *Chin. J. Chem. Eng.* **2008**, *16*, 517−527.
(16) Qin, F. L.; Li, R. K. Predicting Refractive Indices of the Borate Optical Crystals. *J. Cryst. Growth* **2011**, *318*, 642−644.
(17) Aka, G.; Brenier, A. Self-frequency Conversion in Nonlinear Laser Crystals. *Opt. Mater.* **2003**, *22*, 89−94.
(18) Wang, S. A.; Alekseev, E. V.; Ling, J.; Liu, G. K.; Depmeier, W.; Albrecht-Schmitt, T. E. Polarity and Chirality in Uranyl Borates: Insights into Understanding the Vitrification of Nuclear Waste and the Development of Nonlinear Optical Materials. *Chem. Mater.* **2010**, *22*, 2155−2163.
(19) Wang, E. R.; Huang, J. H.; Yu, S. J.; Lan, Y. Z.; Cheng, J. W.; Yang, G. Y. An Ultraviolet Nonlinear Optic Borate with 13-Ring Channels Constructed from Different Building Units. *Inorg. Chem.* **2017**, *56*, 6780−6783.
(20) Chen, C. T.; Wu, Y. C.; Li, R. K. The Anionic Group Theory of the Non-linear Optical Effect and its Applications in the Development of New High-quality NLO Crystals in the Borate Series. *Int. Rev. Phys. Chem.* **1989**, *8*, 65−91.
(21) Dewey, C. F.; Cook, W. R.; Hodgson, R. T.; Wynne, J. J. Frequency Doubling in $KB_5O_8{\cdot}4H_2O$ and $NH_4B_5O_8{\cdot}4H_2O$ to 217 nm. *Appl. Phys. Lett.* **1975**, *26*, 714−716.
(22) Chen, C. T.; Wu, B. C.; Jiang, A. D.; You, G. M. A New Ultraviolet SHG Crystal β-BaB_2O_4. *Sci. Sin., Ser. B* **1985**, *18*, 235−243.
(23) Chen, C. T.; Wu, Y. C.; Jiang, A. D.; Wu, B. C.; You, G. M.; Li, R. K.; Lin, S. J. New Nonlinear-optical Crystal: LiB_3O_5. *J. Opt. Soc. Am. B* **1989**, *6*, 616−621.
(24) Wu, Y. C.; Sasaki, T.; Nakai, N.; Yokotani, A.; Tang, H. G.; Chen, C. T. CsB_3O_5: A New Nonlinear Optical Crystal. *Appl. Phys. Lett.* **1993**, *62*, 2614−2615.
(25) Mori, Y.; Kuroda, I.; Nakajima, S.; Sasaki, T.; Nakai, S. New Nonlinear Optical Crystal: Cesium Lithium Borate. *Appl. Phys. Lett.* **1995**, *67*, 1818−1820.
(26) Hellwig, H.; Liebertz, J.; Bohatý, L. Exceptional Large Nonlinear Optical Coefficients in the Monoclinic Bismuth Borate BiB_3O_6 (BIBO). *Solid State Commun.* **1998**, *109*, 249−251.
(27) Chen, C. T.; Wang, G. L.; Wang, X. Y.; Xu, Z. Y. Deep-UV Nonlinear Optical Crystal $KBe_2BO_3F_2$ —Discovery, Growth, Optical

https://dx.doi.org/10.1021/acs.chemrev.0c00796
Chem. Rev. 2021, 121, 1130−1202

Properties and Applications. *Appl. Phys. B: Lasers Opt.* **2009**, *97*, 9−25.
(28) Zhou, G. Q.; Xu, J.; Chen, X. D.; Zhong, H. Y.; Wang, S. T.; Xu, K.; Deng, P. Z.; Gan, F. X. Growth and Spectrum of a Novel Birefringent α-BaB_2O_4 Crystal. *J. Cryst. Growth* **1998**, *191*, 517−519.
(29) Zhang, S. Y.; Wu, X.; Song, Y. T.; Ni, D. Q.; Hu, B. Q.; Zhou, T. Growth of Birefringent $Ca_3(BO_3)_2$ Crystals by the Czochralski Method. *J. Cryst. Growth* **2003**, *252*, 246−250.
(30) He, M.; Chen, X. L.; Sun, Y. P.; Liu, J.; Zhao, J. T.; Duan, C. $YBa_3B_9O_{18}$: A Promising Scintillation Crystal. *Cryst. Growth Des.* **2007**, *7*, 199−201.
(31) Jia, Z.; Zhang, N. N.; Ma, Y. Y.; Zhao, L. W.; Xia, M. J.; Li, R. K. Top-seeded Solution Growth and Optical Properties of Deep-UV Birefringent Crystal $Ba_2Ca(B_3O_6)_2$. *Cryst. Growth Des.* **2017**, *17*, 558−562.
(32) Li, R. K.; Ma, Y. Y. Chemical Engineering of a Birefringent Crystal Transparent in the Deep UV Range. *CrystEngComm* **2012**, *14*, 5421−5424.
(33) Chen, X. L.; Zhang, B. B.; Zhang, F. F.; Wang, Y.; Zhang, M.; Yang, Z. H.; Poeppelmeier, K. R.; Pan, S. L. Designing an Excellent Deep-Ultraviolet Birefringent Material for Light Polarization. *J. Am. Chem. Soc.* **2018**, *140*, 16311−16319.
(34) Filimonov, A. A.; Leonyuk, N. I.; Meissner, L. B.; Timchenko, T. I.; Rez, I. S. Nonlinear Optical Properties of an Isomorphic Family of Crystals with a Yttrium-Aluminum Borate (YAB) Structure. *Krist. Tech.* **1974**, *9*, 63−66.
(35) Iwai, M.; Kobayashi, T.; Furuya, H.; Mori, Y.; Sasaki, T. Crystal Growth and Optical Characterization of Rare-Earth (Re) Calcium Oxyborate $ReCa_4O(BO_3)_3$ (Re = Y or Gd) as New Nonlinear Optical Material. *Jpn. J. Appl. Phys.* **1997**, *36*, L276−L279.
(36) Wu, Y. C.; Liu, J. G.; Fu, P. Z.; Wang, J. X.; Zhou, H. Y.; Wang, G. F.; Chen, T. C. A New Lanthanum and Calcium Borate $La_2CaB_{10}O_{19}$. *Chem. Mater.* **2001**, *13*, 753−755.
(37) Yao, W. J.; He, R.; Wang, X. Y.; Lin, Z. S.; Chen, C. T. Analysis of Deep-UV Nonlinear Optical Borates: Approaching the End. *Adv. Opt. Mater.* **2014**, *2*, 411−417.
(38) Keszler, D. A. Borates for Optical Frequency Conversion. *Curr. Opin. Solid State Mater. Sci.* **1996**, *1*, 204−208.
(39) Wang, S. S.; Yang, G. Y. Recent Advances in Polyoxometalate-Catalyzed Reactions. *Chem. Rev.* **2015**, *115*, 4893−4962.
(40) Rong, C.; Yu, Z. W.; Wang, Q.; Zheng, T. S.; Pan, C. Y.; Deng, F.; Yang, G. Y. Aluminoborates with Open Frameworks: Syntheses, Structures, and Properties. *Inorg. Chem.* **2009**, *48*, 3650−3659.
(41) Bubnova, R.; Volkov, S.; Albert, B.; Filatov, S. Borates—Crystal Structures of Prospective Nonlinear Optical Materials: High Anisotropy of the Thermal Expansion Caused by Anharmonic Atomic Vibrations. *Crystals* **2017**, *7*, 93−125.
(42) Zhou, J.; Fang, W.; Rong, C.; Yang, G. Y. A Series of Open-Framework Aluminoborates Templated by Transition-Metal Complexes. *Chem. - Eur. J.* **2010**, *16*, 4852−4863.
(43) Shen, Y. G.; Zhao, S. G.; Luo, J. H. The Role of Cations in Second-order Nonlinear Optical Materials Based on π-conjugated $[BO_3]^{3-}$ Groups. *Coord. Chem. Rev.* **2018**, *366*, 1−28.
(44) Gong, P. F.; Liu, X. M.; Kang, L.; Lin, Z. S. Inorganic Planar π-conjugated Groups in Nonlinear Optical Crystals: Review and Outlook. *Inorg. Chem. Front.* **2020**, *7*, 839−852.
(45) Mutailipu, M.; Pan, S. L. Emergent Deep-Ultraviolet Nonlinear Optical Candidates. *Angew. Chem., Int. Ed.* **2020**, *59*, 20302−20317.
(46) Zachariasen, W. H. The Crystalline Structure of Hambergite, $Be_2BO_3(OH)$. *Z. Kristallogr. - Cryst. Mater.* **1931**, *76*, 289−302.
(47) *Inorganic Crystal Structure Database* National Institute of Standards and Technology, 2020.
(48) The Cambridge Structural Database; Cambridge Crystallographic Data Centre.
(49) Touboul, M.; Amoussou, D. Structure Cristalline de $TlBO_2$. *Rev. Chim. Miner.* **1978**, *15*, 223−232 in French.
(50) Kaduk, J. A.; Satek, L. C.; Mckenna, S. T. Crystal Structures of Metal Aluminum Borates. *Rigaku J.* **1999**, *16*, 17−30.
(51) Krogh-Moe, J.; Ihara, M. On the Crystal Structure of Barium Tetraborate, $BaO(B_2O_3)_4$. *Acta Crystallogr., Sect. B: Struct. Crystallogr. Cryst. Chem.* **1969**, *B25*, 2153−2154.
(52) Maleki, L. The Optoelectronic Oscillator. *Nat. Photonics* **2011**, *5*, 728−730.
(53) Pan, S. L.; Wang, Y.; Poeppelmeier, K. R. Frequency-Doubling Oxide Fluorides, Borate Fluorides, and Fluoroxoborates. *In Photonic and Electronic Properties of Fluoride Materials*; Elsevier: Amsterdam, 2016, Chapter 15, 311−354.
(54) Han, G. P.; Wang, Y.; Zhang, B. B.; Pan, S. L. Fluorooxoborates: Ushering in a New Era of Deep Ultraviolet Nonlinear Optical Materials. *Chem. - Eur. J.* **2018**, *24*, 17638−17650.
(55) Depmeier, W.; Schmid, H.; Haenssler, F. PdB_2O_4, the First Palladium Borate. *Naturwissenschaften* **1980**, *67*, 456.
(56) Stojanovska, M.; Petruševski, V. M.; Šoptrajanov, B. The Concept of Sublimation − Iodine as an Example. *Educ. Quim.* **2012**, *23*, 171−175.
(57) Hu, C. L.; Mao, J. G. Recent Advances on Second-order NLO Materials Based on Metal Iodates. *Coord. Chem. Rev.* **2018**, *288*, 1−17.
(58) Höppe, H. A. $Gd_4(BO_2)O_5F$ − A Gadolinium Borate Fluoride Oxide Comprising a Linear BO_2 Moiety. *Z. Naturforsch., B: J. Chem. Sci.* **2015**, *70*, 769−774.
(59) Alvo, C.; Ggiaxi, R. Linear Metaborate Anions, BO^{2-}, in Apatitic Phosphates. *J. Chem. Soc., Chem. Commun.* **1974**, *17*, 714−715.
(60) Calvo, C.; Faggiani, R.; Krishnamachari, N. The Crystal Structure of $Sr_{9.402}Na_{0.209}(PO_4)B_{0.996}O_2$ - A Deviant Apatite. *Acta Crystallogr., Sect. B: Struct. Crystallogr. Cryst. Chem.* **1975**, *B31*, 188−192.
(61) Ci, Z.; Sun, Q.; Sun, M.; Jiang, X.; Qin, S.; Wang, Y. The Structure, Photoluminescence and Thermal Properties of Ce^{3+}, Mn^{2+} Co-doped Phosphosilicate $Sr_7La_3[(PO_4)_{2.5}(SiO_4)_3(BO_4)_{0.5}](BO_2)$ Emission-tunable Phosphor. *J. Mater. Chem. C* **2014**, *2*, 5850−5856.
(62) Chen, S.; Hoffmann, S.; Carrillo-Cabrera, W.; Akselrud, L.; Prots, P.; Schwarz, U.; Zhao, J.; Kniep, R. $Sr_{10}[(PO_4)_{5.5}(BO_4)_{0.5}]$-$(BO_2)$: Growth and Crystal Structure of Astrontium Phosphate Orthoborate Metaborate Closely Related to the Apatite-type Crystal Structure. *J. Solid State Chem.* **2010**, *183*, 658−661.
(63) Gutsev, G. L.; Boldyrev, A. I. The Electronic Structure of Superhalogens and Superalkalies. *Russ. Chem. Rev.* **1987**, *56*, 519−531.
(64) Huppertz, H. Multianvil High-pressure / High-temperature Synthesis in Solid State Chemistry. *Z. Kristallogr.* **2004**, *219*, 330−338.
(65) Bubnova, R. S.; Filatov, S. K. High-temperature Borate Crystal Chemistry. *Z. Kristallogr.* **2013**, *228*, 395−428.
(66) Kageyama, H.; Hayashi, K.; Maeda, K.; Attfield, J. P.; Hiroi, Z.; Rondinelli, J. M.; Poeppelmeier, K. R. Expanding Frontiers in Materials Chemistry and Physics with Multiple Anions. *Nat. Commun.* **2018**, *9*, 772.
(67) Harada, J. K.; Charles, N.; Poeppelmeier, K. R.; Rondinelli, J. M. Heteroanionic Materials by Design: Progress Toward Targeted Properties. *Adv. Mater.* **2019**, *31*, 1805295.
(68) Chackraburtty, D. M. The Structure of $BaBOF_3$. *Acta Crystallogr.* **1957**, *10*, 199−200.
(69) Mallouk, T. E.; Rosenthal, G. L.; Mueller, G.; Brusasco, R.; Bartlett, N. Fluoride Ion Affinities of Germanium Tetrafluoride and Boron Trifluoride from Thermodynamic and Structural Data for $(SF_3)_2GeF_6$, ClO_2GeF_5, and ClO_2BF_4. *Inorg. Chem.* **1984**, *23*, 3167−3173.
(70) Jiang, D. W.; Wang, W.; Li, H.; Yang, Z. H.; Pan, S. L. $BaBOF_3$: a New Aurivillius-like Borate Containing Two Types of F Atoms. *Dalton Trans.* **2018**, *47*, 5157−5160.
(71) Huang, C. M.; Zhang, F. F.; Li, H.; Yang, Z. J.; Yu, H. H.; Pan, S. L. $BaB_2O_3F_2$: A Barium Fluorooxoborate with a Unique $[B_2O_3F]^-$ Layer and Short Cutoff Edge. *Chem. - Eur. J.* **2019**, *25*, 6693−6697.
(72) Luo, M.; Liang, F.; Song, Y. X.; Zhao, D.; Ye, N.; Lin, Z. S. Rational Design of the First Lead/Tin Fluorooxoborates $MB_2O_3F_2$ (M = Pb, Sn), Containing Flexible Two-Dimensional $[B_6O_{12}F_6]_\infty$

https://dx.doi.org/10.1021/acs.chemrev.0c00796
Chem. Rev. 2021, 121, 1130−1202

Single Layers with Widely Divergent Second Harmonic Generation Effects. *J. Am. Chem. Soc.* **2018**, *140*, 6814−6817.
(73) Jantz, S.G.; Dialer, M.; Bayarjargal, L.; Winkler, B.; van Wüllen, L.; Pielnhofer, F.; Brgoch, J.; Weihrich, R.; Höppe, H. A. $Sn[B_2O_3F_2]$-The First Tin Fluorooxoborate as Possible NLO Material. *Adv. Opt. Mater.* **2018**, *6*, 1800497.
(74) Frisch, M. J.; Trucks, G. W.; Schlegel, H. B.; Scuseria, G. E.; Robb, M. A.; Cheeseman, J. R.; et al. *Gaussian09*, revision D.01; Gaussian, Inc.: Wallingford, CT, 2009.
(75) Haines, J.; Chateau, C.; Leger, J. M.; Bogicevic, C.; Hull, S.; Klug, D. D.; Tse, J. S. Collapsing Cristobalitelike Structures in Silica Analogues at High Pressure. *Phys. Rev. Lett.* **2003**, *91*, 015503.
(76) Mutailipu, M.; Zhang, M.; Zhang, B. B.; Wang, L. Y.; Yang, Z. H.; Zhou, X.; Pan, S. L. $SrB_5O_7F_3$ Functionalized with $[B_5O_9F_3]^{6-}$ Chromophores: Accelerating the Rational Design of Deep-Ultraviolet Nonlinear Optical Materials. *Angew. Chem., Int. Ed.* **2018**, *57*, 6095−6099.
(77) Yuan, G.; Xue, D. F. Crystal Chemistry of Borates: The Classification and Algebraic Description by Topological Type of Fundamental Building Blocks. *Acta Crystallogr., Sect. B: Struct. Sci.* **2007**, *B63*, 353−362.
(78) Christ, C. L.; Clark, J. R. A Crystal-chemical Classification of Borate Structures with Emphasis on Hydrated Borates. *Phys. Chem. Miner.* **1977**, *2*, 59−87.
(79) Krogh-Moe, J. The Cation Distribution in Some Crystalline and Vitreous Cesium Borates. *Ark. Kemi.* **1959**, *14*, 451−459.
(80) Burns, P. S.; Grice, J. D.; Hawthorne, F. C. Borate Minerals. I. Polyhedral Clusters and Fundamental Building Blocks. *Can. Miner.* **1995**, *33*, 1131−1151.
(81) Strunz, H. Classification of Borate Minerals. *Eur. J. Mineral.* **1997**, *9*, 225−232.
(82) Touboul, M.; Penin, N.; Nowogrocki, G. Borates: A Survey of Main Trends Concerning Crystal-chemistry, Polymorphism and Dehydration Process of Alkaline and Pseudo-alkaline Borates. *Solid State Sci.* **2003**, *5*, 1327−1342.
(83) Zachariasen, W. H.; Ziegler, G. E. The Crystal Structure of Calcium Metaborate, CaB_2O_4. *Z. Kristallogr. - Cryst. Mater.* **1932**, *83*, 354−361.
(84) Marezio, M.; Remeika, J. P. Polymorphism of $LiMO_2$ Compounds and High-pressure Single-crystal Synthesis of $LiBO_2$. *J. Chem. Phys.* **1966**, *44*, 3348−3353.
(85) Ju, J.; Yang, T.; Li, G. B.; Liao, F. H.; Wang, Y. X.; You, L. P.; Lin, J. H. PKU-5: An Aluminoborate with Novel Octahedral Framework Topology. *Chem. - Eur. J.* **2004**, *10*, 3901−3906.
(86) Kong, F.; Huang, S. P.; Sun, Z. M.; Mao, J. G.; Cheng, W. D. $Se_2(B_2O_7)$: A New Type of Second-Order NLO Material. *J. Am. Chem. Soc.* **2006**, *128*, 7750−7751.
(87) Wang, S. C.; Ye, N.; Li, W.; Zhao, D. **A** lkaline Beryllium Borate $NaBeB_3O_6$ and $ABe_2B_3O_7$ (A = K, Rb) as UV Nonlinear Optical Crystals. *J. Am. Chem. Soc.* **2010**, *132*, 8779−8786.
(88) Yan, D.; Hu, C. L.; Mao, J. G. $A_2SbB_3O_8$ (A = Na, K, Rb) and β-$RbSbB_2O_6$: Two Types of Alkali Boroantimonates with 3D Anionic Architectures Composed of SbO_6 Octahedra and Borate Groups. *CrystEngComm* **2016**, *18*, 1655−1664.
(89) Ren, M.; Lin, J. H.; Dong, Y.; Yang, L. Q.; Su, M. Z.; You, L. P. Structure and Phase Transition of $GdBO_3$. *Chem. Mater.* **1999**, *11*, 1576−1580.
(90) Zhang, J. H.; Kong, F.; Yang, B. P.; Mao, J. G. A Series of Boroselenite-based Open Frameworks Mediated by the Cationic Sizes of the Alkali Metals. *CrystEngComm* **2012**, *14*, 8727−8733.
(91) Rousse, G.; Baptiste, B.; Lelong, G. Crystal Structures of $Li_6B_4O_9$ and $Li_3B_{11}O_{18}$ and Application of the Dimensional Reduction Formalism to Lithium Borates. *Inorg. Chem.* **2014**, *53*, 6034−6041.
(92) Zhang, J. H.; Hu, C. L.; Xu, X.; Kong, F.; Mao, J. G. New Second-Order NLO Materials Based on Polymeric Borate Clusters and GeO_4 Tetrahedra: A Combined Experimental and Theoretical Study. *Inorg. Chem.* **2011**, *50*, 1973−1982.
(93) Haberer, A.; Kaindl, R.; Huppertz, H. $Gd_4B_4O_{11}F_2$: Synthesis and Crystal Structure of a Rare-earth Fluoride Borate Exhibiting a New "Fundamental Building Block" in Borate Chemistry. *J. Solid State Chem.* **2010**, *183*, 471−478.
(94) Brachtel, G.; Jansen, M. Silber(I)-metaborat, $AgBO_2$. *Z. Anorg. Allg. Chem.* **1981**, *478*, 13−19.
(95) Chen, X. A.; Li, M.; Chang, X. A.; Zang, H. G.; Xiao, W. Q. Synthesis and Crystal Structure of a Novel Pentaborate, $Na_3ZnB_5O_{10}$. *J. Solid State Chem.* **2007**, *180*, 1658−1663.
(96) Yan, X.; Luo, S. Y.; Lin, Z. S.; Yao, J. Y.; He, R.; Yue, Y. C.; Chen, C. T. $ReBe_2B_5O_{11}$ (Re = Y, Gd): Rare-Earth Beryllium Borates as Deep-Ultraviolet Nonlinear-Optical Materials. *Inorg. Chem.* **2014**, *53*, 1952−1954.
(97) Krogh-Moe, J. The Crystal Structure of the High-temperature Modification of Potassium Pentaborate. *Acta Crystallogr., Sect. B: Struct. Crystallogr. Cryst. Chem.* **1972**, *B28*, 168−172.
(98) Krogh-Moe, J. Least-squares Refinement of the Crystal Structure of Potassium Pentaborate. *Acta Crystallogr.* **1965**, *18*, 1088−1089.
(99) Wu, Y.; Yao, J. Y.; Zhang, J. X.; Fu, P. Z.; Wu, Y. C. Potassium Zinc Borate, $KZnB_3O_6$. *Acta Crystallogr., Sect. E: Struct. Rep. Online* **2010**, *E66*, No. i45.
(100) Jin, S. F.; Cai, G. M.; Wang, W. Y.; He, M.; Wang, S. C.; Chen, X. L. Stable Oxoborate with Edge-Sharing BO_4 Tetrahedra Synthesized under Ambient Pressure. *Angew. Chem., Int. Ed.* **2010**, *49*, 4967−4970.
(101) Zhang, J. H.; Kong, F.; Mao, J. G. $Ba_3[Ge_2B_7O_{16}(OH)_2]$-$(OH)(H_2O)$ and $Ba_3Ge_2B_6O_{16}$: Novel Alkaline-earth Borogermanates Based on Two Types of Polymeric Borate Units and GeO_4 Tetrahedra. *Inorg. Chem.* **2011**, *50*, 3037−3043.
(102) Yang, Y.; Pan, S. L.; Li, H. Y.; Han, J.; Chen, Z. H.; Zhao, W. W.; Zhou, Z. X. $Li_4Cs_3B_7O_{14}$: Synthesis, Crystal Structure, and Optical Properties. *Inorg. Chem.* **2011**, *50*, 2415−2419.
(103) Penin, N.; Touboul, M.; Nowogrocki, G. Crystal Structure of Two New Sodium Borates $Na_3B_7O_{12}$ and $Na_2Tl_2B_{10}O_{17}$. *J. Alloys Compd.* **2004**, *363*, 107−114.
(104) Sueno, S.; Clark, J. R.; Papike, J. J.; Konnert, J. A. Crystal-structure Refinement of Cubic Boracite. *Am. Mineral.* **1973**, *58*, 691−697.
(105) Mutailipu, M.; Zhang, M.; Su, X.; Yang, Z. H.; Chen, Y. N.; Pan, S. L. Structural Insights into Borates with an Anion-Templated Open-Framework Configuration: Asymmetric $K_2BaB_{16}O_{26}$ versus Centrosymmetric $K_3CsB_{20}O_{32}$ and $Na_2M_2NB_{18}O_{30}$ (M = Rb, Cs; N = Ba, Pb). *Chem. - Eur. J.* **2017**, *23*, 13910−13918.
(106) Krogh-Moe, J. The Crystal Structure of Sodium Diborate, $Na_2O.2B_2O_3$. *Acta Crystallogr., Sect. B: Struct. Crystallogr. Cryst. Chem.* **1974**, *B30*, 578−582.
(107) Krogh-Moe, J. The Crystal Structure of Potassium Siborate, $K_2O.2B_2O_3$. *Acta Crystallogr., Sect. B: Struct. Crystallogr. Cryst. Chem.* **1972**, *28B*, 3089−3093.
(108) Krzhizhanovskaya, M. G.; Bubnova, R. S.; Bannova, I. I.; Filatov, S. K. Crystal structure of $Rb_2Ba_4O_7$. *Crystallogr. Rep.* **1997**, *42*, 226−231.
(109) Ono, Y.; Nakaya, M.; Kajitani, T.; Sugawara, T.; Watanabe, N.; Shiraishi, H.; Komatsu, R. Lithium Potassium Borate and Lithium Rubidium Borate: New Non-linear Optical Crystals. *Acta Crystallogr., Sect. C: Cryst. Struct. Commun.* **2000**, *56*, 1413−1415.
(110) Zhao, W. W.; Pan, S. L.; Han, J.; Zhou, Z. X.; Tian, X. L.; Li, J. J. Synthesis, Crystal Structure and Optical Properties of a New Lead Fluoride Borate with Isolated $[B_9O_{21}]^{15-}$ Unit. *Inorg. Chem. Commun.* **2011**, *14*, 566−568.
(111) Krogh-Moe, J. The Crystal Structure of a Sodium Triborate Modification, β-$Na_2O(B_2O_3)_3$. *Acta Crystallogr., Sect. B: Struct. Crystallogr. Cryst. Chem.* **1972**, *B28*, 1571−1576.
(112) Penin, N.; Seguin, L.; Touboul, M.; Nowogrocki, G. Synthesis and Crystal Structure of Three $MM'B_9O_{15}$ Borates (M = Ba, Sr and M′ = Li; M = Ba and M′ = Na). *Int. J. Inorg. Mater.* **2001**, *3*, 1015−1023.
(113) Krogh-Moe, J. The Crystal Structure of α-Sodium Triborate, α-$Na_2O{\cdot}3B_2O_3$. *Acta Crystallogr., Sect. B: Struct. Crystallogr. Cryst. Chem.* **1974**, *30B*, 747−752.

https://dx.doi.org/10.1021/acs.chemrev.0c00796
Chem. Rev. 2021, 121, 1130−1202

(114) Krogh-Moe, J.; Wold-Hansen, P. S. The Crystal Structure of Hexalead Pentaborate, $6PbO.5B_2O_3$. *Acta Crystallogr., Sect. B: Struct. Crystallogr. Cryst. Chem.* **1973**, *B29*, 2242−2246.
(115) Yu, H. W.; Wu, H. P.; Pan, S. L.; Zhang, B. B.; Dong, L. Y.; Han, S. J.; Yang, Z. H. $Pb_4Zn_2B_{10}O_{21}$: a Congruently Melting Lead Zinc Borate with a Novel $[B_{10}O_{24}]$ Anionic Group and an Interesting $[Pb_4O_{12}]_\infty$ Chain. *New J. Chem.* **2014**, *38*, 285−291.
(116) Tu, J. M.; Keszler, D. A. New Layered Polyborates $Cs_2M_2B_{10}O_{17}$ (M = Na, K). *Inorg. Chem.* **1996**, *35*, 463−466.
(117) Jiao, A. Q.; Yu, H. W.; Wu, H. P.; Pan, S. L.; Zhang, X. W. A New Cesium Pentaborate with New $B_{10}O_{19}$ Building Blocks. *Inorg. Chem.* **2014**, *53*, 2358−2360.
(118) Yang, Y.; Pan, S. L.; Han, J.; Hou, X. L.; Zhou, Z. X.; Zhao, W. W.; Chen, Z. H.; Zhang, M. A New Lithium Rubidium Borate $Li_6Rb_5B_{11}O_{22}$ with Isolated $B_{11}O_{22}$ Building Blocks. *Cryst. Growth Des.* **2011**, *11*, 3912−3916.
(119) Chen, S. J.; Pan, S. L.; Zhao, W. W.; Yang, Z. H.; Wu, H. P.; Yang, Y. Synthesis, Crystal Structure and Characterization of a New Compound, $Li_3NaBaB_6O_{12}$. *Solid State Sci.* **2012**, *14*, 1186−1190.
(120) Chen, X. A.; Wu, L.; Chang, X. A.; Xiao, W. Q. Synthesis, Crystal Structure, and Spectrum Properties of a New Quaternary Borate $NaSr_7AlB_{18}O_{36}$ with the Cyclic $B_{18}O_{36}^{18-}$ Group, Notation of 6 × (3[2Δ + 1T]). *J. Chem. Crystallogr.* **2014**, *44*, 572−579.
(121) Yao, W. J.; Jiang, X. X.; Huang, H. W.; Xu, T.; Wang, X. S.; Lin, Z. S.; Chen, C. T. $Sr_8MgB_{18}O_{36}$. A New Alkaline-earth Borate with a Novel Zero-dimensional $(B_{18}O_{36})^{18-}$ Anion Ring. *Inorg. Chem.* **2013**, *52*, 8291−8293.
(122) Penin, N.; Seguin, L.; Gérand, B.; Touboul, M.; Nowogrocki, G. β-$Tl_2B_4O_7$: Compound Containing a New Three-Dimensional Borate Anion. *J. Solid State Chem.* **2001**, *160*, 139−146.
(123) Bubnova, R. S.; Krivovichev, S. V.; Shakhverdova, I. P.; Filatov, S. K.; Burns, P. C.; Krzhizhanovskaya, M. G.; Polyakova, I. G. Synthesis, Crystal Structure and Thermal Behavior of $Rb_3B_7O_{12}$, a New Compound. *Solid State Sci.* **2002**, *4*, 985−992.
(124) Tang, Z. H.; Chen, X. A.; Li, M. Synthesis and Crystal Structure of a New Strontium Borate, $Sr_2B_{16}O_{26}$. *Solid State Sci.* **2008**, *10*, 894−900.
(125) Krogh-Moe, J. The Crystal Structure of Pentapotassium Enneakaidekaborate, $5K_2O.19B_2O_3$. *Acta Crystallogr., Sect. B: Struct. Crystallogr. Cryst. Chem.* **1974**, *B30*, 1827−1832.
(126) Mutailipu, M.; Zhang, M.; Su, X.; Yang, Z. H.; Pan, S. L. $Na_8MB_{21}O_{36}$ (M = Rb and Cs): Noncentrosymmetric Borates with Unprecedented $[B_{21}O_{36}]^{9-}$ Fundamental Building Blocks. *Inorg. Chem.* **2017**, *56*, 5506−5509.
(127) Penin, N.; Seguin, L.; Touboul, M.; Nowogrocki, G. A New Cesium Borate $Cs_3B_{13}O_{21}$. *Solid State Sci.* **2002**, *4*, 67−76.
(128) Nowogrocki, G.; Penin, N.; Touboul, M. Crystal Structure of $Cs_3B_7O_{12}$ Containing a New Large Polyanion with 63 Boron Atoms. *Solid State Sci.* **2003**, *5*, 795−803.
(129) Becker, P.; Fröhlich, R. Crystal Structure of Trisodium Gallium Borate, $Na_3GaB_4O_9$, a New Anhydrous Borate Structure Type. *Z. Kristallogr. - New Cryst. Struct.* **2001**, *216*, 31−32.
(130) Huang, Y. Z.; Wu, L. M.; Wu, X. T.; Li, L. H.; Chen, L.; Zhang, Y. F. $Pb_2B_5O_9I$: An Iodide Borate with Strong Second Harmonic Generation. *J. Am. Chem. Soc.* **2010**, *132*, 12788−12789.
(131) Huppertz, H.; von der Eltz, B. Multianvil High-Pressure Synthesis of $Dy_4B_6O_{12}$: The First Oxoborate with Edge-Sharing BO_4 Tetrahedra. *J. Am. Chem. Soc.* **2002**, *124*, 9376−9377.
(132) Kindermann, B. Crystal Structure of CaB_4O_7. *Z. Kristallogr.* **1977**, *146*, 61−66.
(133) Block, S.; Perloff, A. The Crystal Structure of Barium Tetraborate, $BaO.2B_2O_3$. *Acta Crystallogr.* **1965**, *19*, 297−300.
(134) Krogh-Moe, J. The Crystal Structure of a Sodium Triborate Modification, β-$Na_2O.3B_2O_3$. 1972. *Acta Crystallogr., Sect. B: Struct. Crystallogr. Cryst. Chem.* **1972**, *B28*, 1571−1576.
(135) Becker, P. A. A Contribution to Borate Crystal Chemistry: Rules for the Occurrence of Polyborate Anion Types. *Z. Kristallogr.* **2001**, *216*, 523−533.
(136) Hawthorne, F. C.; Burns, P. C.; Grice, J. D. The Crystal Chemistry of Boron. In *Boron. Mineralogy, Petrology and Geochemistry*; Reviews in Mineralogy; Mineralogical Society of America, Washington, DC, 1996.
(137) Hao, Y.-C.; Hu, C.-L.; Xu, X.; Kong, F.; Mao, J.-G. $SrGe_2B_2O_8$ and $Sr_3Ge_2B_6O_{16}$: Novel Strontium Borogermanates with Three-Dimensional and Layered Anionic Architectures. *Inorg. Chem.* **2013**, *52*, 13644−13650.
(138) Li, R. K.; Chen, P. $KBa_7Mg_2B_{14}O_{28}F_5$, A New Borate with an Unusual Heptaborate Group and Double Perovskite Unit. *Acta Crystallogr., Sect. C: Cryst. Struct. Commun.* **2010**, *66*, No. i7-i8.
(139) Mutailipu, M.; Zhang, M.; Chen, Y. N.; Lu, X. Q.; Pan, S. L. The Structural Diversity of Halogen-centered Secondary Building Units: Two New Mixed-metal Borate Halides with Deep-ultraviolet Cut-off Edges. *Dalton Trans.* **2017**, *46*, 4923−4928.
(140) Zhang, X. W.; Yu, H. W.; Wu, H. P.; Pan, S. L.; Liu, L. L.; Jiao, A. Q.; Bai, C. Y. $Sr_8MB_{18}O_{36}$ (M = Zn or Cd): Design and Synthesis of Two New Borates with a Special Ratio of 8:1. *Chem. Lett.* **2014**, *43*, 1216−1218.
(141) Hering, S. A.; Haberer, A.; Kaindl, R.; Huppertz, H. High-pressure Synthesis and Crystal Structure of the New Holmium Oxoborate $Ho_{31}O_{27}(BO_3)_3(BO_4)_6$. *Solid State Sci.* **2010**, *12*, 1993−2002.
(142) Gasperin, M. Synthesis and Structure of Nickel Tetrabor-ouranate, $Ni_7B_4UO_{16}$. *Acta Crystallogr., Sect. C: Cryst. Struct. Commun.* **1989**, *45*, 981−983.
(143) Thompson, P. D.; Huang, J. F.; Smith, R. W.; Keszler, D. A. The Mixed Orthoborate Pyroborates $Sr_2Sc_2B_4O_{11}$ and $Ba_2Sc_2B_4O_{11}$: Pyroborate Geometry. *J. Solid State Chem.* **1991**, *95*, 126−135.
(144) Huang, H. W.; Liu, L. J.; Jin, S. F.; Yao, W. J.; Zhang, Y. H.; Chen, C. T. Deep-Ultraviolet Nonlinear Optical Materials: $Na_2Be_4B_4O_{11}$ and $LiNa_5Be_{12}B_{12}O_{33}$. *J. Am. Chem. Soc.* **2013**, *135*, 18319−18322.
(145) Meng, X. H.; Xia, M. J.; Li, R. K. $Li_3Ba_4Sc_3(BO_3)_4(B_2O_5)_2$: Featuring the Coexistence of Isolated BO_3 and B_2O_5 Units. *New J. Chem.* **2019**, *43*, 11469−11472.
(146) Luo, S. Y.; Yao, W. J.; Gong, P. F.; Yao, J. Y.; Lin, Z. S.; Chen, C. T. $Ca_3Na_4LiBe_4B_{10}O_{24}F$: A New Beryllium Borate with a Unique Beryl Borate in $^2[Be_8B_{16}O_{40}F_2]$ Layer Intrabridged by $[B_{12}O_{24}]$ Groups. *Inorg. Chem.* **2014**, *53*, 8197−8199.
(147) Wang, X. S.; Liu, L. J.; Xia, M. J.; Wang, X. Y.; Chen, C. T. Two Isostructural Multi-metal Borates: Syntheses, Crystal Structures and Characterizations of $M_3LiNa_4Be_4B_{10}O_{24}F$ (M = Sr, Cd). *Chin. J. Struct. Chem.* **2015**, *10*, 1617−1625.
(148) Chen, X. A.; Chen, Y. J.; Sun, C.; Chang, X. A.; Xiao, W. Q. Synthesis, Crystal Structure, Spectrum Properties, and Electronic Structure of a New Three-borate $Ba_4Na_2Zn_4(B_3O_6)_2(B_{12}O_{24})$ with Two Isolated Types of Blocks: 3[3Δ] and 3[2Δ + 1T]. *J. Alloys Compd.* **2013**, *568*, 60−67.
(149) Wang, Z.; Zhang, M.; Su, X.; Pan, S. L.; Yang, Z. H.; Zhang, H.; Liu, L. $Q_{18}Mg_6(B_5O_{10})_3(B_7O_{14})_2F$ (Q = Rb and Cs): New Borates Containing Two Large Isolated Polyborate Anions with Similar Topological Structures. *Chem. - Eur. J.* **2015**, *21*, 1414−1419.
(150) Chen, X. A.; Yue, J. Y.; Chang, X. A.; Xiao, Q. Q. Synthesis and Characterization of a New Borate $Ba_6Al_4B_{14}O_{33}$ with Building Blocks of AlO_4, Al_4O_{14}, BO_3, B_6O_{14}, and B_6O_{13}. *J. Solid State Chem.* **2017**, *245*, 174−183.
(151) Zachariasen, W. H. The Crystal Structure of Lithium Metaborate. *Acta Crystallogr.* **1964**, *17*, 749−751.
(152) Kim, J. B.; Lee, K. S.; Suh, I. H.; Lee, J. H.; Park, J. R.; Shin, Y. H. Strontium Metaborate, SrB_2O_4. *Acta Crystallogr., Sect. C: Cryst. Struct. Commun.* **1996**, *52*, 498−500.
(153) Zhao, D.; Cheng, W. D.; Zhang, H.; Hang, S. P.; Fang, M. Structure Determination and Characterization of Two Rare-earth Molybdenum Borate Compounds: $LnMoBO_6$ (Ln = La, Ce). *Dalton Trans.* **2008**, *28*, 3709−3714.
(154) Holcombe, C. E.; Johnson, D. H. Characterization of Uranium Borate (UB_2O_6) Crystals. *J. Cryst. Growth* **1980**, *49*, 207−210.

https://dx.doi.org/10.1021/acs.chemrev.0c00796
Chem. Rev. 2021, 121, 1130−1202

(155) Hinteregger, E.; Wurst, K.; Tribus, M.; Huppertz, H. High-pressure Synthesis and Characterization of the First Cerium Fluoride Borate CeB_2O_4F. *J. Solid State Chem.* **2013**, *204*, 47−52.
(156) Zhang, J. H.; Li, P. X.; Mao, J. G. $Ln_2GeB_2O_8$ (Ln = Nd, Sm−Tb): A Series of Luminescent Lanthanide (iii) Borogermanates with a Layered Structure. *Dalton Trans.* **2010**, *39*, 5301−5305.
(157) Belokoneva, E. L.; David, W. I. F.; Forsyth, J. B.; Knight, K. S. Structures and Phase Transitions of $PrBGeO_5$ in the Temperature Range 20-800 °C. *J. Phys.: Condens. Matter* **1998**, *10*, 9975−9989.
(158) Schaffers, K. I.; Keszler, D. A. Alkaline-earth Beryllium Borate $CaBeB_2O_5$. *Acta Crystallogr., Sect. C: Cryst. Struct. Commun.* **1993**, *49*, 647−650.
(159) Yao, W. J.; Wang, X. S.; Huang, H. W.; Xu, T.; Jiang, X. X.; Wang, X. Y.; Lin, Z. S.; Chen, C. T. $SrBeB_2O_5$: Growth, Crystal Structure and Optical Properties. *J. Alloys Compd.* **2014**, *593*, 256−260.
(160) Becker, P.; Fröhlich, R. Polymorphy of Monoclinic Terbium Triborate, TbB_3O_6. *Cryst. Res. Technol.* **2008**, *43*, 1240−1246.
(161) Zhang, F. F.; Zhang, F. Y.; Lei, B. H.; Yang, Z. H.; Pan, S. L. Synthesis, Characterization, and Theoretical Studies of (Pb_4O)-$Pb_2B_6O_{14}$: A New Lead(II) Borate with Isolated Oxygen-Centered Pb_4O Tetrahedra and Large Second Harmonic Generation Response. *J. Phys. Chem. C* **2016**, *120*, 12757−12764.
(162) Schönegger, S.; Wurst, K.; Heymann, G.; Huppertz, H. Hydrothermal Synthesis of a New lead(II) borate $(Pb_4O)Pb_2B_6O_{14}$-II. *Z. Naturforsch., B: J. Chem. Sci.* **2016**, *71*, 1233−1243.
(163) Pilz, T.; Nuss, H.; Jansen, M. $Li_2B_3O_4F_3$, A New Lithium-rich Fluorooxoborate. *J. Solid State Chem.* **2012**, *186*, 104−108.
(164) Li, L. Y.; Li, G. B.; Wang, Y. X.; Liao, F. H.; Lin, J. H. Bismuth Borates: One-Dimensional Borate Chains and Nonlinear Optical Properties. *Chem. Mater.* **2005**, *17*, 4174−4180.
(165) Yang, Y.; Pan, S. L.; Hou, X. L.; Dong, X. Y.; Su, X.; Yang, Z. H.; Zhang, M.; Zhao, W. W.; Chen, Z. H. $Li_5Rb_2B_7O_{14}$: a New Congruently Melting Compound with Two Kinds of B-O One-dimensional Chains and Short UV Absorption Edge. *CrystEngComm* **2012**, *14*, 6720−6725.
(166) Li, L.; Han, S. J.; Lei, B. H.; Dong, X. Y.; Wu, H. P.; Zhou, Z. X.; Yang, Z. H.; Pan, S. L. Two New Crystals in $Li_mCs_nB_{m+n}O_{2(m+n)}$(m + n = 5, 7; m > n) Series: Noncentrosymmetric $Li_5Cs_2B_7O_{14}$ and Centrosymmetric $Li_4CsB_5O_{10}$. *Inorg. Chem.* **2015**, *54*, 7381−7387.
(167) Emme, H.; Valldor, M.; Pöttgen, R.; Huppertz, H. Associating Borate and Silicate Chemistry by Extreme Conditions: High-Pressure Synthesis, Crystal Structure, and Properties of the New Borates $RE_3B_5O_{12}$ (RE = Er-Lu). *Chem. Mater.* **2005**, *17*, 2707−2715.
(168) Cakmak, G.; Nuss, J.; Jansen, M. LiB_6O_9F, the First Lithium Fluorooxoborate-Crystal Structure and Ionic Conductivity. *Z. Anorg. Allg. Chem.* **2009**, *635*, 631−636.
(169) Fayos, J.; Howie, R. A.; Glasser, F. P. Structure of Calcium Sodium Pentaborate. *Acta Crystallogr., Sect. C: Cryst. Struct. Commun.* **1985**, *41*, 1394−1396.
(170) Wu, L.; Zhang, Y.; Chen, X. L.; Kong, Y. F.; Sun, T. Q.; Xua, J. J.; Xu, Y. P. The Na_2O-SrO-B_2O_3 Diagram in the B-rich Part and the Crystal Structure of $NaSrB_5O_9$. *J. Solid State Chem.* **2007**, *180*, 1470−1475.
(171) Mutailipu, M.; Zhang, M.; Dong, X. Y.; Chen, Y. N.; Pan, S. L. Effects of the Orientation of $[B_5O_{11}]^{7-}$ Fundamental Building Blocks on Layered Structures Based on the Pentaborates. *Inorg. Chem.* **2016**, *55*, 10608−10616.
(172) Tu, J. M.; Keszler, D. A. $SrKB_5O_9$. *Acta Crystallogr., Sect. C: Cryst. Struct. Commun.* **1995**, *C51*, 341−343.
(173) Wiesch, A.; Bluhm, K. The First Cadmium Rare Earth Borates $CdLn(B_5O_{10})$ with Ln = La, Sm, Eu. *Acta Crystallogr., Sect. C: Cryst. Struct. Commun.* **1997**, *C53*, 1730−1733.
(174) Saubat, B.; Vlasse, M.; Fouassier, C. Synthesis and Structural Study of the New Rare Earth Magnesium Borates $LnMgB_5O_{10}$ (Ln = La, ..., Er). *J. Solid State Chem.* **1980**, *34*, 271−277.
(175) Schmitt, M. K.; Janka, O.; Poettgen, R.; Benndorf, C.; de Oliveira, M.; Eckert, H.; Pielnhofer, F.; Tragl, A.; Weihrich, R.; Joachim, B.; et al. $Mo_2B_4O_9$—Connecting Borate and Metal-Cluster Chemistry. *Angew. Chem., Int. Ed.* **2017**, *56*, 6449−6453.
(176) Emme, H.; Nikelski, T.; Schleid, T.; Pottgen, R.; Moller, M. H.; Huppertz, H. High-Pressure Synthesis, Crystal Structure, and Properties of the New Orthorhombic Rare-Earth meta-Oxoborates $RE(BO_2)_3$ (RE = Dy − Lu). *Z. Naturforsch., B: J. Chem. Sci.* **2014**, *59*, 202−215.
(177) Shi, G. Q.; Wang, Y.; Zhang, F. F.; Zhang, B. B.; Yang, Z. H.; Hou, X. L.; Pan, S. L.; Poeppelmeier, K. R. Finding the Next Deep-Ultraviolet Nonlinear Optical Material: $NH_4B_4O_6F$. *J. Am. Chem. Soc.* **2017**, *139*, 10645−10648.
(178) Wang, Y.; Zhang, B. B.; Yang, Z. H.; Pan, S. L. Cation-Tuned Synthesis of Fluorooxoborates: Towards Optimal Deep-Ultraviolet Nonlinear Optical Materials. *Angew. Chem., Int. Ed.* **2018**, *57*, 2150−2154.
(179) Wang, X. F.; Wang, Y.; Zhang, B. B.; Zhang, F. F.; Yang, Z. H.; Pan, S. L. CsB_4O_6F: A Congruent-melting Deep-ultraviolet Nonlinear Optical Material by Combining Superior Functional Units. *Angew. Chem., Int. Ed.* **2017**, *56*, 14119−14123.
(180) Zhang, Z. Z.; Wang, Y.; Zhang, B. B.; Yang, Z. H.; Pan, S. L. Polar Fluorooxoborate NaB_4O_6F: A Promising Material for Ionic Conduction and Nonlinear Optics. *Angew. Chem., Int. Ed.* **2018**, *57*, 6577−6581.
(181) Jantz, S. G.; Pielnhofer, F.; van Wüllen, L.; Weihrich, R.; Schäfer, M. J.; Höppe, H. The First Alkaline-Earth Fluorooxoborate $Ba[B_4O_6F_2]$-Characterisation and Doping with Eu^{2+}. *Chem. - Eur. J.* **2018**, *24*, 443−450.
(182) Zhang, Z. Z.; Wang, Y.; Zhang, B. B.; Yang, Z. H.; Pan, S. L. Designing Deep-UV Birefringent Crystals by Cation Regulation. *Chem. - Eur. J.* **2018**, *24*, 11267−11272.
(183) Zhang, Z. Z.; Wang, Y.; Zhang, B. B.; Yang, Z. H.; Pan, S. L. $CaB_5O_7F_3$: A Beryllium-Free Alkaline-Earth Fluorooxoborate Exhibits Excellent Nonlinear Optical Performances. *Inorg. Chem.* **2018**, *57*, 4820−4823.
(184) Luo, M.; Liang, F.; Song, Y. X.; Zhao, D.; Xu, F.; Ye, N.; Lin, Z. S. $M_2B_{10}O_{14}F_6$ (M = Ca, Sr): Two Noncentrosymmetric Alkaline Earth Fluorooxoborates as Promising Next-Generation Deep Ultraviolet Nonlinear Optical Materials. *J. Am. Chem. Soc.* **2018**, *140*, 3884−3887.
(185) Han, S. J.; Mutailipu, M.; Tudi, A.; Yang, Z. H.; Pan, S. L. $PbB_5O_7F_3$: A High-Performing Short-Wavelength Nonlinear Optical Material. *Chem. Mater.* **2020**, *32*, 2172−2179.
(186) Cheng, S.; Mutailipu, M.; Yang, Z.; Pan, S. A Promising Fluorooxoborate Framework with Flexibile Capability for Diverse Cations to Enhance the Second Harmonic Generation. *Chem. - Eur. J.* **2020**, *26*, 3723−3728.
(187) Shi, G. Q.; Zhang, F. F.; Zhang, B. B.; Hou, D. W.; Chen, X. L.; Yang, Z. H.; Pan, S. L. $Na_2B_6O_9F_2$: A Fluoroborate with Short Cutoff Edge and Deep-Ultraviolet Birefringent Property Prepared by an Open High-Temperature Solution Method. *Inorg. Chem.* **2017**, *56*, 344−350.
(188) Han, G. P.; Shi, G. Q.; Wang, Y.; Zhang, B. B.; Han, S. J.; Zhang, F. F.; Yang, Z. H.; Pan, S. L. $K_3B_6O_9F_3$: A New Fluorooxoborate with Four Different Anionic Units. *Chem. - Eur. J.* **2018**, *24*, 4497−4502.
(189) Zhang, Z. Z.; Wang, Y.; Li, H.; Yang, Z. H.; Pan, S. L. $BaB_8O_{12}F_2$: A Promising Deep-UV Birefringent Material. *Inorg. Chem. Front.* **2019**, *6*, 546−549.
(190) Tao, C.; Li, R. K. $KNiB_4O_6F_3$: A Layered Fluorooxoborate with Charge-oriented Ordering. *Chem. - Eur. J.* **2020**, *26*, 3709−3712.
(191) Dong, X. Y.; Shi, Y. J.; Zhou, Z. X.; Pan, S. L.; Yang, Z. H.; Zhang, B. B.; Yang, Y.; Chen, Z. H.; Huang, J. B. $M_2Cd_3B_{16}O_{28}$ (M = Rb, Cs): Two Isostructural Alkali Cadmium Borates with a New Type of Borate Layer. *Eur. J. Inorg. Chem.* **2013**, *2013*, 203−207.
(192) Zhang, X. Y.; Li, D. N.; Wu, H. P.; Yang, Z. H.; Pan, S. L. $M_2Ca_3B_{16}O_{28}$ (M = Rb, Cs): Structures Analogous to SBBO with Three-dimensional Open-framework Layers. *RSC Adv.* **2016**, *6*, 14205−14210.

https://dx.doi.org/10.1021/acs.chemrev.0c00796
Chem. Rev. 2021, 121, 1130−1202

(193) Dong, X. Y.; Wu, H. P.; Shi, Y. J.; Yu, H. W.; Yang, Z. H.; Zhang, B. B.; Chen, Z. H.; Yang, Y.; Huang, Z. J.; Pan, S. L.; et al. $Na_{11}B_{21}O_{36}X_2$ (X = Cl, Br): Halogen Sodium Borates with a New Graphene-Like Borate Double Layer. *Chem. - Eur. J.* **2013**, *19*, 7338−7341.
(194) Li, Y. H.; Yu, H. W.; Han, G. P.; Li, H.; Yang, Z. H.; Pan, S. L. $Ba_3B_{10}O_{17}F_2$·0.1KF: The First Mixed Alkali/alkaline-earth Metal Fluorooxoborate with Unprecedented Double-layered B−O/F Anionic Arrangement. *Chem. Commun.* **2019**, *55*, 8923−8926.
(195) Jiang, D. Q.; Wang, Y.; Zhang, B. B.; Han, G. P.; Yang, Z. H.; Pan, S. L. $K_{11}RbB_{28}O_{48}$: a New Triple-layered Borate with an Unprecedented $[B_{28}O_{57}]$ Fundamental Building Block. *Dalton Trans.* **2018**, *47*, 10833−10836.
(196) Krogh-Moe, J. Some New Compounds in the System Cesium Oxideboron Oxide. *Ark. Kemi.* **1958**, *12*, 247−249.
(197) Han, S. J.; Huang, C. M.; Tudi, A.; Hu, S. S.; Yang, Z. H.; Pan, S. L. β-CsB_9O_{14}: A Triple-Layered Borate with Edge-Sharing BO_4 Tetrahedra Exhibiting a Short Cutoff Edge and a Large Birefringence. *Chem. - Eur. J.* **2019**, *25*, 11514−11619.
(198) Krivovichev, S. V. Which Inorganic Structures are the Most Complex? *Angew. Chem., Int. Ed.* **2014**, *53*, 654−661.
(199) Huppertz, H. β-CaB_4O_7: A New Polymorph Synthesized under High-Pressure/High- Temperature Conditions. *Z. Naturforsch., B: J. Chem. Sci.* **2003**, *58*, 257−265.
(200) Krogh-Moe, J.; Magneli, A.; Seip, R.; Seip, H. M. The Crystal Structure of Strontium Diborate, SrO·$2B_2O_3$. *Acta Chem. Scand.* **1964**, *18*, 2055−2060.
(201) Stein, W. D.; Liebertz, J.; Becker, P.; Bohatý, L.; Braden, M. Structural Investigations of the Tetraborates MB_4O_7 (M = Pb, Sr, Ba). *Eur. Phys. J. B* **2012**, *85*, 236−241.
(202) Knyrim, J. S.; Schappacher, F. M.; Pöttgen, R.; Schmedt auf der Günne, J.; Johrendt, D.; Huppertz, H. Pressure-induced Crystallization and Characterization of the Tin Borate β-SnB_4O_7. *Chem. Mater.* **2007**, *19*, 254−262.
(203) Emme, H.; Weil, M.; Huppertz, H. High-Pressure Synthesis and Crystal Structure of the New Orthorhombic Polymorph β-HgB_4O_7. *Z. Naturforsch., B: J. Chem. Sci.* **2005**, *60*, 815−820.
(204) Crottaz, O.; Kubel, F.; Schmid, H. High Temperature Single Crystal X-ray Diffraction: Structure of Cubic Manganese Iodine and Manganese Bromine Boracites. *J. Solid State Chem.* **1995**, *120*, 60−63.
(205) Ross, N. L.; Angel, R. J. Crystal Structure of High Pressure SrB_2O_4(IV). *J. Solid State Chem.* **1991**, *90*, 27−30.
(206) Neumair, S. C.; Perfler, L.; Huppertz, H. Synthesis and Characterization of the Manganese Borate α-MnB_2O_4. *Z. Naturforsch., B: J. Chem. Sci.* **2011**, *66*, 882−888.
(207) Glätzle, M.; Hoerder, G. J.; Huppertz, H. $RE_2B_8O_{15}$ (RE = La, Pr, Nd). Syntheses of Three New Rare Earth Borates Isotypic to $Ce_2B_8O_{15}$. *Z. Naturforsch., B: J. Chem. Sci.* **2016**, *71*, 535−542.
(208) Li, L. Y.; Li, G. B.; Wang, Y. X.; Liao, F. H.; Lin, J. H. Bismuth Borates: Two New Polymorphs of BiB_3O_6. *Inorg. Chem.* **2005**, *44*, 8243−8248.
(209) Knyrim, J. S.; Becker, P.; Johrendt, D.; Huppertz, H. A New Non-Centrosymmetric Modification of BiB_3O_6. *Angew. Chem., Int. Ed.* **2006**, *45*, 8239−8241.
(210) Smith, P.; Garcia-Blanko, S.; Rivoir, L. The Crystal Structure of Anhydrous Zinc Metaborate $Zn_4O(BO_2)_6$. *Z. Kristallogr.* **1964**, *119*, 375−383.
(211) Belokoneva, E. L. Systematic, Properties, and Structure Predictions of New Borate Materials. *Cryst. Res. Technol.* **2008**, *43*, 1173−1182.
(212) Jiang, X. X.; Molokeev, M. S.; Gong, P. F.; Yang, Y.; Wang, W.; Wang, S. H.; Wu, S. F.; Wang, Y. X.; Huang, R. J.; Li, L. F.; et al. Near-Zero Thermal Expansion and High Ultraviolet Transparency in a Borate Crystal of $Zn_4B_6O_{13}$. *Adv. Mater.* **2016**, *28*, 7936−7940.
(213) Machida, K.; Ishino, T.; Adachi, G.; Shiokawa, J. Synthesis and Characterization of Europium(II)-Holoborates, $Eu_2B_5O_9Cl$ and $Eu_2B_5O_9Br$. *Mater. Res. Bull.* **1979**, *14*, 1529−1534.
(214) Egorova, B. V.; Olenev, A. V.; Berdonosov, P. S.; Kuznetsov, A. N.; Stefanovich, S. Y.; Dolgikh, V. A.; Mahenthirarajah, T.; Lightfoot, P. Lead−strontium Borate Halides with Hilgardite-type Structure and Their SHG Properties. *J. Solid State Chem.* **2008**, *181*, 1891−1898.
(215) Held, P.; Liebertz, J.; Bohaty, L. Crystal Structure of Dibarium Pentaborate Chloride, $Ba_2B_5O_9Cl$. *Z. Kristallogr. - New Cryst. Struct.* **2002**, *217*, 463−464.
(216) Machida, K.; Adachi, G.; Yasuoka, N.; Kasai, N.; Shiokawa, J. Crystal Structure of Europium(II) Bromoborate. *Inorg. Chem.* **1980**, *19*, 3807−3811.
(217) Belokoneva, E. L.; Kabalov, Y. K.; Dimitrova, O. V.; Stefanovich, S.Y. New Hilgardite-group Polyborate $Pb_2[B_5O_9]Br$ with High Optical Nonlinearity. *Crystallogr. Rep.* **2003**, *48*, 44−48.
(218) Ito, T.; Morimoto, N.; Sadanaga, R. The Crystal Structure of Boracite. *Acta Crystallogr.* **1951**, *4*, 310−316.
(219) Rowsell, J. L. C.; Taylor, N. J.; Nazar, L. F. Structure and Ion Exchange Properties of a New Cobalt Borate with a Tunnel Structure "Templated" by Na^+. *J. Am. Chem. Soc.* **2002**, *124*, 6522−6523.
(220) Li, L. Y.; Jin, X. L.; Li, G. B.; Wang, Y. X.; Liao, F. H.; Yao, G. Q.; Lin, J. H. Novel Rare Earth Polyborates. 2. Syntheses and Structures. *Chem. Mater.* **2003**, *15*, 2253−2260.
(221) Al-Ama, A. G.; Belokoneva, E. L.; Stefanovich, S. Yu.; Dimitrova, O. V.; Mochenova, N. N. Potassium Bromo-borate $K_3[B_6O_{10}]Br$ - a New Nonlinear Optical Material. *Crystallogr. Rep.* **2006**, *51*, 225−230.
(222) Wu, H. P.; Pan, S. L.; Poeppelmeier, K. R.; Li, H. Y.; Jia, D. Z.; Chen, Z. H.; Fan, X. Y.; Yang, Y.; Rondinelli, J. M.; Luo, H. S. $K_3B_6O_{10}Cl$: A New Structure Analogous to Perovskite with a Large Second Harmonic Generation Response and Deep UV Absorption Edge. *J. Am. Chem. Soc.* **2011**, *133*, 7786−7790.
(223) Zhang, M.; Su, X.; Pan, S. L.; Wang, Z.; Zhang, H.; Yang, Z. H.; Zhang, B. B.; Dong, L. Y.; Wang, Y.; Zhang, F. F.; Yang, Y. Linear and Nonlinear Optical Properties of $K_3B_6O_{10}Br$ Single Crystal: Experiment and Calculation. *J. Phys. Chem. C* **2014**, *118*, 11849−11856.
(224) Bai, C. Y.; Yu, H. W.; Han, S. J.; Pan, S. L.; Zhang, B. B.; Wang, Y.; Wu, H. P.; Yang, Z. H. Effect of Halogen (Cl, Br) on the Symmetry of Flexible Perovskite-related Framework. *Inorg. Chem.* **2014**, *53*, 11213−11220.
(225) Chen, Z. H.; Pan, S. L.; Dong, X. Y.; Yang, Z. H.; Zhang, M.; Su, X. Exploration of a New Compound in the M-B-O-X (M: alkali metals; X: halogen) System: Preparation, Crystal and Electronic Structures, and Optical Properties of $Na_3B_6O_{10}Br$. *Inorg. Chim. Acta* **2013**, *406*, 205−210.
(226) Han, S. J.; Wang, Y.; Pan, S. L.; Dong, X. Y.; Wu, H. P.; Han, J.; Yang, Y.; Yu, H. W.; Bai, C. Y. Noncentrosymmetric versus Centrosymmetric: Influence of the Na^+ Substitution on Structural Transition and Second-Harmonic Generation Property. *Cryst. Growth Des.* **2014**, *14*, 1794−1801.
(227) Zhang, M.; Pan, S. L.; Han, J.; Yang, Z. H.; Su, X.; Zhao, W. W. $Li_2Sr_4B_{12}O_{23}$: a New Alkali and Alkaline-earth Metal Mixed Borate with $[B_{10}O_{18}]^{6-}$ Network and Isolated $[B_2O_5]^{4+}$ Unit. *J. Solid State Chem.* **2012**, *190*, 92−97.
(228) Mutailipu, M.; Zhang, M.; Zhang, B. B.; Yang, Z. H.; Pan, S. L. The First Lead Fluorooxoborate PbB_5O_8F: Achieving the Coexistence of Large Birefringence and Deep-ultraviolet Cut-off Edge. *Chem. Commun.* **2018**, *54*, 6308−6311.
(229) Pilz, T.; Jansen, M. $Li_2B_6O_9F_2$, A New Acentric Fluorooxoborate. *Z. Anorg. Allg. Chem.* **2011**, *637*, 2148−2152.
(230) Penin, N.; Seguin, L.; Touboul, M.; Nowogrocki, G. Crystal Structures of Three MB_5O_8 (M = Cs, Rb) Borates (α-CsB_5O_8, γ-CsB_5O_8, and β-RbB_5O_8). *J. Solid State Chem.* **2001**, *161*, 205−213.
(231) Hyman, A.; Perloff, A.; Mauer, F.; Block, S. The Crystal Structure of Sodium Tetraborate. *Acta Crystallogr.* **1967**, *22*, 815−821.
(232) Penin, N.; Touboul, M.; Nowogrocki, G. Crystal Structure of a New Form of Sodium Octoborate β-$Na_2B_8O_{13}$. *J. Solid State Chem.* **2002**, *168*, 316−321.
(233) Krogh-Moe, J. The Crystal Structure of Lithium Diborate, $Li_2O·2B_2O_3$. *Acta Crystallogr.* **1962**, *15*, 190−193.

https://dx.doi.org/10.1021/acs.chemrev.0c00796
Chem. Rev. 2021, 121, 1130−1202

(234) Penin, N.; Touboul, M.; Nowogrocki, G. Refinement of α-CsB_9O_{14} Crystal Structure. *J. Solid State Chem.* **2003**, *175*, 348−352.
(235) Pauling, L. The Principles Determining the Structure of Complex Ionic Crystals. *J. Am. Chem. Soc.* **1929**, *51*, 1010−1026.
(236) Burdett, J. K.; McLarnan, T. J. An Orbital Interpretation of Pauling's Rules. *Inorg. Chem.* **1984**, *69*, 1119−1128.
(237) Huppertz, H. High-Pressure Preparation, Crystal Structure, and Properties of $RE_4B_6O_{15}$ (RE = Dy, Ho) with an Extension of the "Fundamental Building Block"-Descriptors. *Z. Naturforsch., B: J. Chem. Sci.* **2003**, *58*, 278−290.
(238) Chem, H.; Huppertz, H. High-Pressure Preparation, Crystal Structure, and Properties of α-$(RE)_2B_4O_9$ (RE = Eu, Gd, Tb, Dy): Oxoborates Displaying a New Type of Structure with Edge-Sharing BO_4 Tetrahedra. *Chem.—Eur. J.* **2003**, *9*, 3623−3633.
(239) Knyrim, J. S.; Roessner, F.; Jakob, S.; Johrendt, D.; Kinski, I.; Glaum, R.; Huppertz, H. Formation of Edge-Sharing BO_4 Tetrahedra in the High-Pressure Borate HP-NiB_2O_4. *Angew. Chem., Int. Ed.* **2007**, *46*, 9097−9100.
(240) Neumair, S. C.; Glaum, R.; Huppertz, H. Synthesis and Crystal Structure of the High-pressure Iron Borate β-FeB_2O_4. *Z. Naturforsch., B: J. Chem. Sci.* **2009**, *64*, 883−890.
(241) Neumair, S. C.; Kaindl, R.; Huppertz, H. Synthesis and Crystal Structure of the High-pressure Cobalt Borate HP-CoB_2O_4. *Z. Naturforsch., B: J. Chem. Sci.* **2010**, *65*, 1311−1317.
(242) Neumair, S. C.; Vanicek, S.; Kaindl, R.; Többens, D. M.; Martineau, C.; Taulelle, F.; Senker, J.; Huppertz, H. HP-KB_3O_5 Highlights the Structural Diversity of Borates: Corner-Sharing BO_3/BO_4 Groups in Combination with Edge-Sharing BO_4 Tetrahedra. *Eur. J. Inorg. Chem.* **2011**, *2011*, 4147−4152.
(243) Sohr, G.; Többens, D. M.; Schmedt auf der Günne, J.; Huppertz, H. HP-CsB_5O_8: Synthesis and Characterization of an Outstanding Borate Exhibiting the Simultaneous Linkage of All Structural Units of Borates. *Chem. - Eur. J.* **2014**, *20*, 17059−17067.
(244) Neumair, S. C.; Knyrim, J. S.; Oeckler, O.; Glaum, R.; Kaindl, R.; Stalder, R.; Huppertz, H. Intermediate States on the Way to Edge-Sharing BO_4 Tetrahedra in $M_6B_{22}O_{39}{\cdot}H_2O$ (M = Fe, Co). *Chem. - Eur. J.* **2010**, *16*, 13659−13670.
(245) Neumair, S. C.; Kaindl, R.; Huppertz, H. The New High-pressure Borate $Co_7B_{24}O_{42}(OH)_2{\cdot}2H_2O$-Formation of Edge-sharing BO_4 Tetrahedra in a Hydrated Borate. *J. Solid State Chem.* **2012**, *185*, 1−9.
(246) Fuchs, B.; Heymann, G.; Wang, X. F.; Tudi, A.; Bayarjargal, L.; Siegel, R.; Schmutzler, A.; Senker, J.; Joachim-Mrosko, B.; Saxer, A.; et al. $La_3B_6O_{13}(OH)$: The First Acentric High-Pressure Borate Displaying Edge-Sharing BO_4 Tetrahedra. *Chem. - Eur. J.* **2020**, *26*, 6851−6861.
(247) Jen, I. H.; Lee, Y. C.; Tsai, C. E.; Lii, K. H. Edge-Sharing BO_4 Tetrahedra in the Structure of Hydrothermally Synthesized Barium Borate: α-$Ba_3[B_{10}O_{17}(OH)_2]$. *Inorg. Chem.* **2019**, *58*, 4085−4088.
(248) Yang, L.; Fan, W. L.; Li, Ya. L.; Sun, H. G.; Wei, L.; Cheng, X. F.; Zhao, X. Theoretical Insight into the Structural Stability of $KZnB_3O_6$ Polymorphs with Different BO_x Polyhedral Networks. *Inorg. Chem.* **2012**, *51*, 6762−6770.
(249) Lou, Y. F.; Li, D. D.; Li, Z. L.; Jin, S. F.; Chen, X. L. Unidirectional Thermal Expansion in Edge-sharing BO_4 Tetrahedra Contained $KZnB_3O_6$. *Sci. Rep.* **2015**, *5*, 10996.
(250) Lou, Y. F.; Li, D. D.; Li, Z. L.; Zhang, H.; Jin, S. F.; Chen, X. L. Unidirectional Thermal Expansion in $KZnB_3O_6$: Role of Alkali Metals. *Dalton Trans.* **2015**, *44*, 19763−19767.
(251) Mutailipu, M.; Zhang, M.; Li, H.; Fan, X.; Yang, Z. H.; Jin, S. F.; Wang, G.; Pan, S. L. $Li_4Na_2CsB_7O_{14}$: A New Edge-sharing $[BO_4]^{5-}$ Tetrahedra Containing Borate with High Anisotropic Thermal Expansion. *Chem. Commun.* **2019**, *55*, 1295−1298.
(252) Guo, F. J.; Han, J.; Cheng, S. C.; Yu, S. J.; Yang, Z. H.; Pan, S. L. Transformation of the B−O Units from Corner-Sharing to Edge-Sharing Linkages in $BaMBO_4$ (M = Ga, Al). *Inorg. Chem.* **2019**, *58*, 8237−8244.
(253) Taylor, N. *Laser: The Inventor, the Nobel Laureate, and the Thirty-Year Patent War*; Simon Schuster: New York. 2007.
(254) Franken, P. A.; Hill, A. E.; Peters, C. W.; Weinreich, G. Generation of Optical Harmonics. *Phys. Rev. Lett.* **1961**, *7*, 118−119.
(255) Bordui, P. F.; Fejer, M. M. Inorganic Crystals for Nonlinear Optical Frequency Conversion. *Annu. Rev. Mater. Sci.* **1993**, *23*, 321−379.
(256) Halasyamani, P. S.; Poeppelmeier, K. R. Noncentrosymmetric Oxides. *Chem. Mater.* **1998**, *10*, 2753−2769.
(257) Zhang, W. G.; Yu, H. W.; Wu, H. P.; Halasyamani, P. S. Phase matching in Nonlinear Optical Compounds: A Materials Perspective. *Chem. Mater.* **2017**, *29*, 2655−2668.
(258) Kurtz, S. K.; Perry, T. T. A Powder Technique for the Evaluation of Nonlinear Optical Materials. *J. Appl. Phys.* **1968**, *39*, 3798−3813.
(259) Konig, H.; Hoppe, R. On Borates of the Alkaline Metals. II. On the Knowledge of LiB_3O_5. *Z. Anorg. Allg. Chem.* **1978**, *439*, 71−79.
(260) Lin, S. J.; Sun, Z. Y.; Wu, B. C.; Chen, C. T. The Nonlinear Optical Characteristics of a LiB_3O_5 Crystal. *J. Appl. Phys.* **1990**, *67*, 634−638.
(261) Wu, Y. C.; Jiang, A. D.; Lu, S. F.; Chen, C. T.; Shen, Y. S. Crystal Growth and Structure of $Li_2O_3B_2O_3$. *J. Synth. Cryst.* **1990**, *19*, 33−38.
(262) Bruck, E.; Raymakers, R. J.; Route, R. K.; Feigeison, R. S. Surface Stability of Lithium Triborate Crystals Grown from Excess B_2O_3 Solutions. *J. Cryst. Growth* **1993**, *128*, 933−937.
(263) Markgraf, S. A.; Furukawa, Y.; Sato, M. Top-seeded Solution Growth of LiB_3O_5. *J. Cryst. Growth* **1994**, *140*, 343−348.
(264) Pylneva, N.; Kosyakov, V.; Yurkin, A.; Bazarova, G.; Atuchin, V.; Kolesnikov, A.; Trukhanov, E.; Zilling, C. Real Structure of LiB_3O_5 (LBO) Crystals Grown in Li_2O-B_2O_3-MoO_3 System. *Cryst. Res. Technol.* **2001**, *36*, 1377−1384.
(265) Kosyakov, V. I.; Pylneva, N. A.; Bazarova, G. G.; Yurkin, A. M. Topology of Liquidus Surface in B_2O_3-$Li_2O{\cdot}B_2O_3$-$Li_2O{\cdot}MoO_3$-MoO_3 System: Implications to the Growth of Lithium Triborate Single Crystals. *Mater. Res. Bull.* **2001**, *36*, 573−584.
(266) Kokh, A. E.; Kononova, N. G.; Mennerat, G.; Villeval, P.; Durst, S.; Lupinski, D.; Vlezko, V.; Kokh, K. Growth of High Quality Large Size LBO Crystals for High Energy Second Harmonic Generation. *J. Cryst. Growth* **2010**, *312*, 1774−1778.
(267) Hu, Z. G.; Zhao, Y.; Yue, Y. C.; Yu, X. S. Large LBO Crystal Growth at 2 kg-level. *J. Cryst. Growth* **2011**, *335*, 133−137.
(268) Yu, L. H.; Liang, X. Y.; Xu, L.; Li, W. Q.; Peng, C.; Hu, Z. G.; Wang, C.; Lu, X. M.; Chu, Y. X.; Gan, Z. B.; et al. Optimization for High-energy and High-efficiency Broadband Optical Parametric Chirped-pulse Amplification in LBO near 800 nm. *Opt. Lett.* **2015**, *40*, 3412−3415.
(269) Zeng, X. M.; Zhou, K. N.; Zuo, Y. L.; Zhu, Q. H.; Su, J. Q.; Wang, X.; Wang, X. D.; Huang, X. J.; Jiang, X. J.; Jiang, D. B.; Guo, Y.; Xie, N.; Zhou, S.; Wu, Z. H.; Mu, J.; Peng, H.; Jing, F. Multi-petawatt Laser Facility Fully Based on Optical Parametric Chirped-pulse Amplification. *Opt. Lett.* **2017**, *42*, 2014−2017.
(270) Andreev, Y. M.; Naftaly, M.; Molloy, J. F.; Kokh, A. E.; Lanskii, G.V; Svetlichnyi, V. A.; Losev, V. F.; Kononova, N. G.; Kokh, K. A. LBO: Optical Properties and Potential for THz Application. *Laser Phys. Lett.* **2015**, *12*, 115402−115404.
(271) Krogh-Moe, J. Refinement of the Crystal Structure of Cesium Triborate. *Acta Crystallogr., Sect. B: Struct. Crystallogr. Cryst. Chem.* **1974**, *B30*, 1178−1180.
(272) Fu, P. Z.; Wang, J. X.; Hu, Z. G.; Wu, Y. C.; Yin, S. T.; Xu, Z. Y. Growth and Properties of Ultraviolet Nonlinear Optical Cesium Triborate. *J. Synth. Cryst.* **1999**, *28*, 215−218.
(273) Kagebayashi, Y.; Mori, Y.; Sasaki, T. Crystal Growth of Cesium Triborate CsB_3O_5 by Kryopoulos Technique. *Bull. Mater. Sci.* **1999**, *22*, 971−973.
(274) Kitano, H.; Matsui, T.; Sato, K.; Ushiyama, N.; Yoshimura, M.; Mori, Y.; Sasaki, T. Efficient 355-nm Generation in CsB_3O_5 Crystal. *Opt. Lett.* **2003**, *28*, 263−265.
(275) Xie, S. Y.; Lu, Y. Fu.; Zhang, X. F.; Le, X. Y.; Yang, C. L.; Wang, B. S.; Xu, Z. Y. 28.3 W 355 nm Laser Generated by Efficient

https://dx.doi.org/10.1021/acs.chemrev.0c00796
Chem. Rev. 2021, 121, 1130−1202

Third-harmonic in CsB_3O_5 Crystal. *Acta Phys. Sin.* **2016**, *65*, 184203−184209.
(276) Krzhizhanovskaya, M. G.; Kabalov, Yu. K.; Bubnova, R. S.; Sokolova, E. V.; Filatov, S. K. Crystal Structure of the Low-temperature Modification of α-RbB_3O_5. *Crystallogr. Rep.* **2000**, *45*, 572−577.
(277) Touboul, M.; Betourne, E.; Nowogrocki, G. Crystal Structure of Thallium Triborate, TlB_3O_5. *J. Solid State Chem.* **1997**, *131*, 370−373.
(278) Shoji, I.; Nakamura, H.; Ito, R.; Kondo, T.; Yoshimura, M.; Mori, Y.; Sasaki, T. Absolute Measurement of Second-Harmonic Nonlinear Optical Coefficients of $CsLiB_6O_{10}$ for Visible-to-Ultraviolet Second-Harmonic Wavelengths. *J. Opt. Soc. Am. B* **2001**, *18*, 302−307.
(279) Yap, Y. K.; Inagaki, M.; Nakajima, S.; Mori, Y.; Sasaki, T. High-power Fourth- and Fifth-harmonic Generation of a Nd:YAG Laser by Means of a $CsLiB_6O_{10}$. *Opt. Lett.* **1996**, *21*, 1348−1350.
(280) Sakuma, J.; Deki, K.; Finch, A.; Ohsako, Y.; Yokota, T. All-solid-state, High-power, Deep-UV Laser System Based on Cascaded Sum-frequency Mixing in $CsLiB_6O_{10}$ Crystals. *Appl. Opt.* **2000**, *39*, 5505−5511.
(281) Novák, O.; Turčičová, H.; Smrž, M.; Miura, T.; Endo, A.; Mocek, T. Picosecond Green and Deep Ultraviolet Pulses Generated by a High-power 100 kHz Thin-disk Laser. *Opt. Lett.* **2016**, *41*, 5210−5213.
(282) Sakuma, J.; Kaneda, Y.; Oka, N.; Ishida, T.; Moriizumi, K.; Kusunose, H.; Furukawa, Y. Continuous-wave 193.4 nm Laser with 120 mW Output Power. *Opt. Lett.* **2015**, *40*, 5590−5593.
(283) Nishioka, M.; Fukumoto, S.; Kawamura, F.; Yoshimura, M.; Mori, Y.; Sasaki, T. Improvement of Laser-induced Damage Tolerance in $CsLiB_6O_{10}$ for High-power UV Laser Source. In *Proceedings of the Lasers and Electro-Optics/Quantum Electronics and Laser Science Conference, Baltimore, MD, 1−6 June 2003*, 2003.
(284) Ueda, K.; Orii, Y.; Takahashi, Y.; Okada, G.; Mori, Y.; Yoshimura, M. Picosecond High-power 355-nm UV Generation in $CsLiB_6O_{10}$ Crystal. *Opt. Express* **2016**, *24*, 30465−30473.
(285) Sennova, N. A.; Cordier, G.; Albert, B.; Filatov, S. K.; Bubnova, R. S.; Isaenko, L. I.; Prosenc, M. H. Temperature- and Moisture-dependency of $CsLiB_6O_{10}$. A New Phase, β-$CsLiB_6O_{10}$. *Z. Kristallogr.* **2010**, *229*, 741−751.
(286) McMillen, C. D.; Giesber, H. G.; Kolis, J. W. The Hydrothermal Synthesis, Growth, and Optical Properties of γ-$LiBO_2$. *J. Cryst. Growth* **2008**, *310*, 299−305.
(287) Komatsu, R.; Sugawara, T.; Sassa, K.; Sarukura, N.; Liu, Z.; Izumida, S.; Segawa, Y.; Uda, S.; Fukuda, T.; Yamanouchi, K. Growth and Ultraviolet Application of $Li_2B_4O_7$ Crystals: Genration of the Fouth and Fifth Harmonics of Nd:$Y_3Al_5O_{12}$ Lasers. *Appl. Phys. Lett.* **1997**, *70*, 3492−3494.
(288) Sugawara, T.; Komatsu, R.; Uda, S. Linear and Nonlinear Optical Properties of Lithium Tetraborate. *Solid State Commun.* **1998**, *107*, 233−237.
(289) Komatsu, R.; Ono, Y.; Kajitani, T.; Rotermund, F.; Petrov, V. Optical Properties of a New Nonlinear Borate Crystal $LiRbB_4O_7$. *J. Cryst. Growth* **2003**, *257*, 165−168.
(290) Adamiv, V. T.; Burak, Y. V.; Romanyuk, M. M.; Romanyuk, G. M.; Teslyuk, M. New Nonlinear Optical $LiKB_4O_7$ Single Crystals: Dispersion of Refractive Indices. *Opt. Mater.* **2007**, *29*, 1501−1504.
(291) Mączka, M.; Waśkowska, A.; Majchrowski, A.; Żmija, J.; Hanuza, J.; Peterson, G. A.; Keszler, D. A. Crystal Structure and Phonon Properties of Noncentrosymmetric $LiNaB_4O_7$. *J. Solid State Chem.* **2007**, *180*, 410−419.
(292) Neumair, S. C.; Sohr, G.; Vanicek, S.; Wurst, K.; Kaindl, R.; Huppertz, H. The New High-pressure Sodium Tetraborate HP-$Na_2B_4O_7$. *Z. Anorg. Allg. Chem.* **2012**, *638*, 81−87.
(293) Zhang, B. B.; Yang, Z. H.; Yang, Y.; Lee, M. X.; Pan, S. L.; Jing, Q.; Su, X. p−(p,π^*) Interaction Mechanism Revealing and Accordingly Designed New Member in Deep-ultraviolet NLO Borates $Li_nM_{n-1}B_{2n-1}O_{4n-2}$ (M = Cs/Rb, n = 3, 4, 6). *J. Mater. Chem. C* **2014**, *2*, 4133−4141.
(294) Yang, Y.; Pan, S.; Hou, X.; Wang, C.; Poeppelmeier, K. R.; Chen, Z.; Wu, H.; Zhou, Z. A Congruently Melting and Deep UV Nonlinear Optical Material: $Li_3Cs_2B_5O_{10}$. *J. Mater. Chem.* **2011**, *21*, 2890−2894.
(295) Miessen, M.; Hoppe, R. New Borates of the Alkali Metals: $KLi_2[BO_3]$. *Z. Anorg. Allg. Chem.* **1985**, *521*, 7−14.
(296) Li, R. K. On the Anionic Group Approximation to the Borate Nonlinear Optical Materials. *Crystals* **2017**, *7*, 50−56.
(297) Liebertz, J.; Stahr, S. Zur Tieftemperaturphae Von BaB_2O_4. *Z. Kristallogr.* **1983**, *165*, 91−94.
(298) Itoh, K.; Marumo, F.; Kuwano, Y. β-Barium Borate Single Crystal Growth by a Direct Czochralski Method. *J. Cryst. Growth* **1990**, *106*, 728−731.
(299) Tang, D. Y.; Lin, S. T.; Dai, G. Q.; Lin, Q.; Zeng, W. R.; Zhao, Q. L.; Huang, Y. S. Growth of β-BaB_2O_4 Crystals from Molten Salts by the Top-seeded Pulling Technique. *J. Synth. Cryst.* **1990**, *19*, 21−27.
(300) Bosenberg, W. R.; Lane, R. J.; Tang, C. L. Growth of Large, High-Quality Beta-Barium Metaborate Crystals. *J. Cryst. Growth* **1991**, *108*, 394−398.
(301) Kouta, H.; Kuwano, Y. β-BaB_2O_4 Phase Matching-Direction Growth by the Czochralski Method. *J. Cryst. Growth* **1996**, *166*, 497−501.
(302) Tsvetkov, E. G.; Khranenko, G. G.; Solntsev, V. P. General Approaches to Design of a Reproducible Technique for the Growth of Large Crystals of Barium Meteborate (BBO) for Industrial Application. *J. Cryst. Growth* **2005**, *275*, e2123−e2128.
(303) Simonova, E. A.; Kuznetsov, A. B.; Shevchenko, V. S.; Kononova, N. G.; Kokh, A. E. Growth of Bulk β-BaB_2O_4 Crystals from Solution in LiF-Li_2O Melt and Study of Phase Equilibria. *J. Cryst. Growth* **2019**, *525*, 125186−125190.
(304) Chen, W.; Jiang, A. D.; Wang, G. F. J. Growth of High-quality and Large-sized β-BaB_2O_4 Crystal. *J. Cryst. Growth* **2003**, *256*, 383−386.
(305) Pan, S. L.; Smit, J. P.; Lanier, C. H.; Marvel, M. R.; Marks, L. D.; Poeppelmeier, K. R. Optical Floating Zone Growth of β-BaB_2O_4 from a $LiBa_2B_5O_{10}$-Based Solvent. *Cryst. Growth Des.* **2007**, *7*, 1561−1564.
(306) Cheng, L. K.; Bosenberg, W. R.; Tang, C. L. Ultraviolet Optical Parametric Oscillation in β-BaB_2O_4. *Appl. Phys. Lett.* **1988**, *53*, 175−177.
(307) Bosenberg, W. R.; Pelouch, W. S.; Tang, C. L. High-efficiency and Narrow-linewidth Operation of a Two-crystal β-BaB_2O_4 Optical Parametric Oscillator. *Appl. Phys. Lett.* **1989**, *55*, 1952.
(308) Imai, S.; Yamada, T.; Fujimori, Y.; Ishikawa, K. Third-harmonic Generation of an Alexandrite Laser in β-BaB_2O_4. *Appl. Phys. Lett.* **1989**, *54*, 1206−1208.
(309) Kondo, K.; Oka, M.; Wada, H.; Fukui, T.; Umezu, N.; Tatsuki, K.; Kubota, S. Demonstration of Long-term Reliability of a 266-nm, Continuous-wave, Frequency-quadrupled Solid-state Laser Using β-BaB_2O_4. *Opt. Lett.* **1998**, *23*, 195−197.
(310) Liu, Q.; Yan, X. P.; Fu, X.; Gong, M.; Wang, D. S. High Power All-solid-state Fourth Harmonic Generation of 266 nm at the Pulse Repetition Rate of 100 kHz. *Laser Phys. Lett.* **2009**, *6*, 203−206.
(311) Masuda, H.; Umezu, N.; Kimura, K.; Kubota, S. High-repetition-rate, 192−197 nm Pulse Generation in β-BaB_2O_4 by Intracavity Sum-frequency-mixing of a Ti:Sapphire Laser with a Frequency-quadrupled Nd:YAG laser. *Advanced Solid State Lasers.*; OSA Trends in Optics and Photonics; Optical Society of America, 1999; paper MF4.
(312) Masuda, H.; Kimura, K.; Eguchi, N.; Kubota, S.; Nogami, A. All-solid-state, Continuous-wave, 195 nm Light Generation in β-BaB_2O_4. *Adv. Solid State Lasers* **2001**, WA6.
(313) Nikolaev, N. A.; Andreev, Y. M.; Antsygin, V. D.; Bekker, T. B.; Ezhov, D. M.; Kokh, A. E.; Kokh, K. A.; Lanskii, G. V.; Mamrashev, A. A.; Svetlichnyi, V. A. Optical Properties of β-BBO and Potential for THz Applications. *J. Phys.: Conf. Ser.* **2018**, *951*, 012003.

https://dx.doi.org/10.1021/acs.chemrev.0c00796
Chem. Rev. 2021, 121, 1130−1202

(314) Jiang, T.; Dai, S. T.; Lin, W. X. Single-frequency Laser Pumped Optical Parametric Oscillator at 226 nm. *Laser Phys.* **2020**, *30*, 015801.
(315) Oseledchik, Y. S.; Prosvrnin, A. L.; Pisarevskiy, A. I.; Starshenko, V. V.; Osadchuk, V. V.; Belokrys, S. P.; Svitanko, N. V.; Korol, A. S.; Krikunov, S. A.; Selevich, A. F. New Nonlinear Optical Crystals: Strontium and Lead Tetraborates. *Opt. Mater.* **1995**, *4*, 669−674.
(316) Pan, F.; Shen, G. Q.; Wang, R. J.; Wang, X. Q.; Shen, D. Z. Growth, Characterization and Nonlinear Optical Properties of SrB_4O_7 Crystals. *J. Cryst. Growth* **2002**, *241*, 108−114.
(317) Petrov, V.; Noack, F.; Shen, D. Z.; Pan, F.; Shen, G. Q.; Wang, X. Q.; Komatsu, R.; Alex, V. Application of the Nonlinear crystal SrB_4O_7 for Ultrafast Diagnostics Converting to Wavelengths as Short as 125 nm. *Opt. Lett.* **2004**, *29*, 373−375.
(318) Trabs, P.; Noack, F.; Aleksandrovsky, A. S.; Zaitsev, A. I.; Petrov, V. Generation of Coherent Radiation in the Vacuum Ultraviolet Using Randomly Quasi-phase-matched Strontium Tetraborate. *Opt. Lett.* **2016**, *41*, 618−621.
(319) Vasiliev, A. D.; Cherepakhin, A. V.; Zaitsev, A. I. The Trigonal Polymorph of Strontium Tetraborate, β-SrB_4O_7. *Acta Crystallogr., Sect. E: Struct. Rep. Online* **2010**, *E66*, No. i48.
(320) Zaitsev, A. I.; Molokeev, M. S.; Cherepakhin, A. V.; Radionov, N. V.; Zamkov, A. V. Optical Birefringence of β-SrB_4O_7 Crystals with Strontium Substitutions. *17th International Conference on Crystal Growth and Epitaxy-ICCGE-17*, 2013.
(321) Marezio, M.; Remeika, J. P.; Dernier, P. D. The Crystal Structure of the High Pressure Phase CaB_2O_4(III). *Acta Crystallogr., Sect. B: Struct. Crystallogr. Cryst. Chem.* **1969**, *B25*, 955−964.
(322) Kusachi, I.; Kobayashi, S.; Takechi, Y.; Nakamuta, Y.; Nagase, T.; Yokoyama, K.; Momma, K.; Miyawaki, R.; Shigeoka, M.; Matsubara, S. Shimazakiite-4M and Shimazakiite-4O, $Ca_2B_2O_5$, Two Polytypes of a New Mineral from Fuka, Okayama Prefecture, Japan. *Mineral. Mag.* **2013**, *77*, 93−105.
(323) Yakubovich, O. V.; Simonov, M. A.; Belokoneva, E. L.; Egorov, Yu. K.; Belov, N. V. Crystalline Structure of Ca, Mg-diorthotriborate (pyroborate) kurchatovite $CaMg(B_2O_5)$. *Dokl. Akad. Nauk SSSR* **1976**, *230*, 837.
(324) Furmanova, N. G.; Maksimov, B. A.; Molchanov, V. N.; Kokh, A. E.; Kononova, N. G.; Fedorov, P. P. Crystal Structure of the New Barium Borate $Ba_5(BO_3)_2(B_2O_5)$. *Crystallogr. Rep.* **2006**, *51*, 219−224.
(325) Kudrjavtcev, D. P.; Oseledchik, Y. S.; Prosvirnin, A. L.; Svitanko, N. V. Growth of a New Strontium Borate Crystal $Sr_4B_{14}O_{25}$. *J. Cryst. Growth* **2003**, *254*, 456−460.
(326) Meng, X. Y.; Wen, X. H.; Liu, G. L. Structure and Stacking Faults in $Sr_2Be_2B_2O_7$ Crystal. *J. Korean Phys. Soc.* **2008**, *52*, 1277−1280.
(327) Wu, L.; Sun, J. C.; Zhang, Y.; Jin, S. F.; Kong, Y. F.; Xu, J. J. Structure Determination and Relative Properties of Novel Chiral Orthoborate $KMgBO_3$. *Inorg. Chem.* **2010**, *49*, 2715−2720.
(328) Kurbatov, R. V.; Solovyov, L. A.; Bazarov, B. G.; Subanakov, A. K.; Bazarova, J. G. Synthesis, Structure and Properties of $RbMgBO_3$. *Solid State Commun.* **2013**, *172*, 33−36.
(329) Wen, M.; Wu, H. P.; Su, X.; Lu, J. J.; Yang, Z. H.; Wu, X. H.; Pan, S. L. $ACaBO_3$ (A = Cs, Rb): Two New Cubic Borates with Isolated BO_3 Groups. *Dalton Trans.* **2017**, *46*, 4968−4974.
(330) Wu, L.; Chen, X. L.; Xu, Y. P.; Sun, Y. P. Structure Determination and Relative Properties of Novel Non-centrosymmetric Borates $MM'_4(BO_3)_3$ (M = Na, M' = Ca and M = K, M' = Ca, Sr). *Inorg. Chem.* **2006**, *45*, 3042−3047.
(331) Wang, S. C.; Ye, N. $Na_2CsBe_6B_5O_{15}$: An Alkaline Beryllium Borate as a Deep-UV Nonlinear Optical Crystal. *J. Am. Chem. Soc.* **2011**, *133*, 11458−11461.
(332) Xu, K.; Loiseau, P.; Aka, G. Growth and Characterization of a Nonlinear Borate Optical Crystal: $BaNaB_9O_{15}$. *J. Cryst. Growth* **2009**, *311*, 389−393.
(333) Chen, G. J.; Wu, Y. C.; Fu, P. Z. Synthesis and Crystal Structure of a New Cesium Barium Borate, $CsBaB_3O_6$. *J. Solid State Chem.* **2007**, *180*, 2194−2201.
(334) Zhao, S. G.; Gong, P. F.; Bai, L.; Xu, X.; Zhang, S. Q.; Sun, Z. H.; Lin, Z. S.; Hong, M. C.; Chen, C. T.; Luo, J. H. Beryllium-free $Li_4Sr(BO_3)_2$ for Deep-ultraviolet Nonlinear Optical Applications. *Nat. Commun.* **2014**, *5*, 4019.
(335) Khamaganova, T. N.; Trunov, V. K.; Dzhurinskii, B. F. The Crystal Structure of Calcium Samarium Oxide Borate $Ca_8Sm_2O_2(BO_3)_6$. *Russ. J. Inorg. Chem.* **1991**, *36*, 484−485.
(336) Aka, G.; Kahn-Harari, A.; Mougel, F.; Vivien, D.; Salin, F.; Coquelin, P.; Colin, P.; Pelenc, D.; Damelet, J. P. Linear- and Nonlinear-optical Properties of a New Gadolinium Calcium Oxoborate Crystal, $Ca_4GdO(BO_3)_3$. *J. Opt. Soc. Am. B* **1997**, *14*, 2238−2247.
(337) Aka, G.; Kahn-Harari, A.; Vivien, D.; Benitez, J. M.; Salin, F.; Godard, J. A New Non-linear and Neodymium Laser Self-frequency Doubling Crystal with Congruent Melting: $Ca_4GdO(BO_3)_3$ (GdCOB). *Eur. J. Solid State Inorg. Chem.* **1996**, *33*, 727−736.
(338) Zou, G. H.; Ma, Z. J.; Wu, K. C.; Ye, N. Cadmium-rare Earth Oxyborates $Cd_4ReO(BO_3)_3$ (Re = Y, Gd, Lu): Congruently Melting Compounds with Large SHG Responses. *J. Mater. Chem.* **2012**, *22*, 19911−19918.
(339) Pack, M. V.; Armstrong, D. J.; Smith, A. V.; Aka, G.; Ferrand, B.; Pelenc, D. Measurement of the chi(2) Tensor of $GdCa_4O(BO_3)_3$ and $YCa_4O(BO_3)_3$ Crystals. *J. Opt. Soc. Am. B* **2005**, *22*, 417−425.
(340) Wang, Z. P.; Liu, J. H.; Song, R. B.; Jiang, H. D.; Zhang, S. J.; Fu, K.; Wang, C. Q.; Wang, J. Y.; Liu, Y. G.; Wei, J. Q.; et al. Anisotropy of Nonlinear-Optical Property of RCOB (R = Y, Gd) Crystal. *Chin. Phys. Lett.* **2001**, *18*, 385−387.
(341) Liu, J. H.; Wang, C. Q.; Zhang, S. J.; Du, C. L.; Lu, J. H.; Wang, J. Y.; Chen, H. C.; Shao, Z. S.; Jiang, M. H. Investigation on Intracavity Second-harmonic Generation at 1.06 μm in $YCa_4O(BO_3)_3$ by Using an End-pumped Nd:YVO_4 Laser. *Opt. Commun.* **2000**, *182*, 187−191.
(342) Liu, J.; Xu, X.; Wang, C. Q.; Zhang, S.; Wang, J.; Chen, H.; Shao, Z.; Jiang, M. Intracavity Second-harmonic Generation of 1.06 μm in $GdCa_4O(BO_3)_3$ Crystals. *Appl. Phys. B: Lasers Opt.* **2001**, *72*, 163−166.
(343) Hammons, D.A.; Richardson, M.; Chai, B.H.T.; Chin, A.K.; Jollay, R. Scaling of Longitudinally Diode-pumped Self-frequency-doubling Nd:YCOB Lasers. *IEEE J. Quantum Electron.* **2000**, *36*, 991−999.
(344) Tu, X. N.; Wang, S.; Xiong, K. N.; Zheng, Y. Q.; Shi, E. W. Growth and Properties of Large Aperture YCOB Crystal for NLO Application. *J. Cryst. Growth* **2020**, *535*, 125527.
(345) Ballman, A. A. A New Series of Synthetic Borates Isostructural with the Carbonate Mineral Huntite. *Am. Miner.* **1962**, *47*, 1380−1383.
(346) Mills, A. D. Crystallographic Data for New Rare Earth Borate Compounds, $RX_3(BO_3)_4$. *Inorg. Chem.* **1962**, *1*, 960−961.
(347) Joubert, J. C.; White, W.; Roy, R. Synthesis and Crystallographic Data of Some Rare Earth-iron Borates. *J. Appl. Crystallogr.* **1968**, *1*, 318−319.
(348) Belokoneva, E. L.; Simonov, M. A.; Pashkova, A. V.; Timchenko, T. I.; Belov, N. V. Crystal-structure of High-temperature Monoclinal Modification of Nd, Al-borate, $NdAl_3(BO_3)_4$. *Sov. Phys. Dokl.* **1980**, *25*, 948−950.
(349) Leonyuk, N. I.; Leonyuk, L. I. Growth and Characterization of $RM_3(BO_3)_4$ Crystals. *Prog. Cryst. Growth Charact. Mater.* **1995**, *31*, 179−278.
(350) Filimonov, A. A.; Leonyuk, N. I.; Meissner, L. B.; Timchenko, T. I.; Rez, I. S. Nonlinear Optical Properties of an Isomorphic Family of Crystals with a Yttrium-Aluminum Borate (YAB) Structure. *Krist. Tech.* **1974**, *9*, 63−66.
(351) Rytz, D.; Gross, A.; Vernay, S.; Wesemann, V. $YAl_3(BO_3)_4$: a Novel NLO Crystal for Frequency Conversion to UV Wavelengths. *Proc. SPIE* **2008**, *6998*, 699814.

https://dx.doi.org/10.1021/acs.chemrev.0c00796
Chem. Rev. 2021, 121, 1130−1202

(352) Yu, X. S.; Yue, Y. C.; Yao, J. Y.; Hu, Z. G. $YAl_3(BO_3)_4$: Crystal Growth and Characterization. *J. Cryst. Growth* **2010**, *312*, 3029−3033.
(353) Yu, J. Q.; Liu, L. J.; Zhai, N. X.; Zhang, X.; Wang, G. L.; Wang, X. Y.; Chen, C. T. Crystal Growth and Optical Properties of $YAl_3(BO_3)_4$ for UV Applications. *J. Cryst. Growth* **2012**, *341*, 61−65.
(354) Liu, Q.; Yan, X. P.; Gong, M.; Liu, H.; Zhang, G.; Ye, N. High-power 266 nm Ultraviolet Generation in Yttrium Aluminum Borate. *Opt. Lett.* **2011**, *36*, 2653−2656.
(355) Ilas, S.; Loiseau, P.; Aka, G.; Taira, T. 240 kW Peak Power at 266 nm in Nonlinear $YAl_3(BO_3)_4$ Single Crystal. *Opt. Express* **2014**, *22*, 30325−30332.
(356) Wang, G. L.; Lu, J. H.; Cui, D. F.; Xu, X. Y.; Wu, Y. C.; Fu, P. Z.; Guan, X. G.; Chen, C. T. Efficient Second Harmonic Generation in a New Nonlinear $La_2CaB_{10}O_{19}$ Crystal. *Opt. Commun.* **2002**, *209*, 481−484.
(357) Wu, Y. C.; Fu, P. Z.; Zheng, F.; Wan, S. M.; Guan, X. G. Growth of a Nonlinear Optical Crystal $La_2CaB_{10}O_{19}$ (LCB). *Opt. Mater.* **2003**, *23*, 373−375.
(358) Zhang, J. X.; Wang, L. R.; Wu, Y.; Wang, G. L.; Fu, P. Z.; Wu, Y. C. High-efficiency Third Harmonic Generation at 355 nm Based on $La_2CaB_{10}O_{19}$. *Opt. Express* **2011**, *19*, 16722−16729.
(359) Li, K.; Zhang, L.; Xu, D. G.; Zhang, G. C.; Yu, H. J.; Wang, Y. Y.; Shan, F. X.; Wang, L. R.; Yan, C.; Wu, Y. C.; et al. High-power Picosecond 355 nm Laser Based on $La_2CaB_{10}O_{19}$ Crystal. *Opt. Lett.* **2014**, *39*, 3305−3307.
(360) Mascetti, J.; Fouassier, C.; Hagenmuller, P. Concentration Quenching of the Nd^{3+} Emission in Alkali Rare Earth Borates. *J. Solid State Chem.* **1983**, *50*, 204−212.
(361) Zhang, G. C.; Wu, Y. C.; Fu, P. Z.; Wang, G. F.; Pan, S. L.; Chen, C. T. A New Nonlinear Optical Borate Crystal $Na_3La_2(BO_3)_3$. *Chem. Lett.* **2001**, *30*, 456−457.
(362) Li, K.; Zhang, G. C.; Guo, S.; Zhang, X.; He, R.; Zhang, J. X.; Lin, Z. S.; Wu, Y. C. Linear and Nonlinear Optical Properties of $Na_3La_2(BO_3)_3$ Crystal. *Opt. Laser Technol.* **2013**, *54*, 407−412.
(363) Gravereau, P.; Chaminade, J. P.; Pechev, S.; Nikolov, V.; Ivanova, D.; Peshev, P. $Na_3La_9O_3(BO_3)_8$, a New Oxyborate in the Ternary System $Na_2O-La_2O_3-B_2O_3$: Preparation and Crystal Structure. *Solid State Sci.* **2002**, *4*, 993−998.
(364) Zhang, G. C.; Wu, Y. C.; Li, Y. G.; Chang, F.; Pan, S. L.; Fu, P. Z.; Chen, C. T. Flux Growth and Characterization of a New Oxyborate Crystal $Na_3La_9O_3(BO_3)_8$. *J. Cryst. Growth* **2005**, *275*, e1997−e2001.
(365) Li, Y. G.; Wu, Y. C.; Zhang, G. C.; Fu, P. Z.; Bai, X. Y. Flux Growth and Optical Properties of $Na_3La_9O_3(BO_3)_8$ Crystals. *J. Cryst. Growth* **2006**, *292*, 468−471.
(366) Zhang, J. X.; Wang, G. L.; Liu, Z. L.; Wang, L. R.; Zhang, G. C.; Zhang, X.; Wu, Y.; Fu, P. Z.; Wu, Y. C. Growth and Optical Properties of a New Nonlinear $Na_3La_9O_3(BO_3)_8$ Crystal. *Opt. Express* **2010**, *18*, 237−243.
(367) Zhang, J. X.; Wang, L. R.; Li, Y.; Wang, G. L.; Zhang, G. C.; Wu, Y. C. 355 nm Laser Generation Based on $Na_3La_9O_3(BO_3)_8$ Crystal. *Opt. Express* **2012**, *20*, 16490−16493.
(368) Mutailipu, M.; Xie, Z. Q.; Su, X.; Zhang, M.; Wang, Y.; Yang, Z. H.; Janjua, M.; Pan, S. L. Chemical Cosubstitution-Oriented Design of Rare-Earth Borates as Potential Ultraviolet Nonlinear Optical Materials. *J. Am. Chem. Soc.* **2017**, *139*, 18397−18405.
(369) Li, Y. F.; Liang, F.; Song, H. M.; Liu, W.; Lin, Z. S.; Zhang, G. C.; Wu, Y. C. $Rb_7SrY_2(B_5O_{10})_3$: A Rare-Earth Pentaborate with Moderate Second-Harmonic Response and Interesting Phase Matching Behavior. *Inorg. Chem.* **2019**, *58*, 8943−8947.
(370) Feng, J. H.; Xu, X.; Hu, C. L.; Mao, J. G. $K_6ACaSc_2(B_5O_{10})_3$ (A = Li, Na, $Li_{0.7}Na_{0.3}$): Nonlinear-Optical Materials with Short UV Cutoff Edges. *Inorg. Chem.* **2019**, *58*, 2833−2839.
(371) Xie, Z. Q.; Mutailipu, M.; He, G. J.; Han, G. P.; Wang, Y.; Yang, Z. H.; Zhang, M.; Pan, S. L. A Series of Rare-Earth Borates $K_7MRE_2B_{15}O_{30}$ (M = Zn, Cd, Pb; RE = Sc, Y, Gd, Lu) with Large Second Harmonic Generation Responses. *Chem. Mater.* **2018**, *30*, 2414−2423.
(372) Kuznetsov, A. B.; Ezhov, D. M.; Kokh, K. A.; Kononova, N. G.; Shevchenko, V. S.; Uralbekov, B.; Bolatov, A.; Svetlichnyi, V. A.; Lapin, I. N.; Simonova, E. A.; et al. Nonlinear Optical Crystals $K_7CaR_2(B_5O_{10})_3$ (R = Nd, Yb), Growth and Properties. *J. Cryst. Growth* **2019**, *519*, 54−59.
(373) Kuznetsov, A. B.; Ezhov, D. M.; Kokh, K. A.; Kononova, N. G.; Shevchenko, V. S.; Rashchenko, S. V.; Pestryakov, E. V.; Svetlichnyi, V. A.; Lapin, I. N.; Kokh, A. E. Flux Growth and Optical Properties of $K_7CaY_2(B_5O_{10})_3$ Nonlinear Crystal. *Mater. Res. Bull.* **2018**, *107*, 333−338.
(374) Yu, H. W.; Pan, S. L.; Wu, H. P.; Zhao, W. W.; Zhang, F. F.; Li, H. Y.; Yang, Z. H. A new Congruent-melting Oxyborate, $Pb_4O(BO_3)_2$ with Optimally Aligned BO_3 Triangles Adopting Layered-type Arrangement. *J. Mater. Chem.* **2012**, *22*, 2105−2110.
(375) Levin, E. M.; Mcdaniel, C. L. The System Bi_2O_3-B_2O_3. *J. Am. Ceram. Soc.* **1962**, *45*, 355−360.
(376) Liebertz, J. Metrik und Raumgruppe von BiB_3O_6. *Z. Kristallogr. - Cryst. Mater.* **1982**, *158*, 319−319.
(377) Fröhlich, R.; Bohaty, L.; Liebertz, J. The Crystal Structure of Bismuth Borate, BiB_3O_6. *Acta Crystallogr., Sect. C: Cryst. Struct. Commun.* **1984**, *C40*, 343−344.
(378) Becker, P.; Liebertz, J.; Bohatý, L. Top-seeded Growth of Bismuth Triborate, BiB_3O_6. *J. Cryst. Growth* **1999**, *203*, 149−155.
(379) Hellwig, H.; Liebertz, J.; Bohatý, L. Linear Optical Properties of the Monoclinic Bismuth Borate BiB_3O_6. *J. Appl. Phys.* **2000**, *88*, 240−244.
(380) Du, C.; Wang, Z.; Liu, J.; Xu, X.; Teng, B.; Fu, K.; Wang, J.; Liu, Y.; Shao, Z. Efficient Intracavity Second-harmonic Generation at 1.06 μm in a BiB_3O_6 (BIBO) Crystal. *Appl. Phys. B: Lasers Opt.* **2001**, *73*, 215−217.
(381) Ishii, N.; Kitano, K.; Kanai, T.; Watanabe, S.; Itatani, J. Carrier-Envelope-Phase-Preserving, Octave-Spanning Optical Parametric Amplification in the Infrared Based on BiB_3O_6 Pumped by 800 nm Femtosecond Laser Pulses. *Appl. Phys. Express* **2011**, *4*, 022701.
(382) Jia, Y. C.; Vázquez de Aldana, J. R.; Romero, C.; Ren, Y. Y.; Lu, Q. M.; Chen, F. Femtosecond-Laser-Inscribed BiB_3O_6 Nonlinear Cladding Waveguide for Second-Harmonic Generation. *Appl. Phys. Express* **2012**, *5*, 072701.
(383) Li, Y.; Huang, J. G.; Huang, Z. M.; Nikolaev, N.; Lanskii, G.; Mamrashev, A.; Andreev, Y. Optical Properties of BiB_3O_6 in the Terahertz Range. *Results Phys.* **2020**, *16*, 102815.
(384) Dinnebier, R. E.; Hinrichsen, B.; Lennie, A.; Jansen, M. High-pressure Crystal Structure of the Non-linear Optical Compound BiB_3O_6 from Two-dimensional Powder Diffraction Data. *Acta Crystallogr., Sect. B: Struct. Sci.* **2009**, *B65*, 1−10.
(385) Cherepakhin, A. V.; Zaitsev, A. I.; Aleksandrovsky, A. S.; Zamkov, A. V. Optical and Nonlinear Optical Properties of Orthorhombic BiB_3O_6. *Opt. Mater.* **2012**, *34*, 790−792.
(386) Barbier, J.; Cranswick, L. M. D. The Non-centrosymmetric Borate Oxides, $MBi_2B_2O_7$ (M = Ca, Sr). *J. Solid State Chem.* **2006**, *179*, 3958−3964.
(387) Becker, P.; Herd, P. Crystal Growth and Basic Characterisation of the Bismuth Borate $Bi_2B_8O_{15}$. *Cryst. Res. Technol.* **2001**, *36*, 1353−1356.
(388) Hu, C.; Mutailipu, M.; Wang, Y.; Guo, F. J.; Yang, Z. H.; Pan, S. L. The Activity of Lone Pair Contributing to SHG Response in Bismuth Borates: a Combination Investigation from Experiment and DFT Calculation. *Phys. Chem. Chem. Phys.* **2017**, *19*, 25270−25276.
(389) Petrakovskii, G. A.; Sablina, K. A.; Pankrats, A. I.; Velikanov, D. A.; Balaev, A. D.; Bayukov, O. A.; Tugarinov, V. I.; Vorotynov, A. M.; Vasil'ev, A. D.; Romanenko, G. V.; et al. Synthesis of the New Oxocuprate $Cu_5Bi_2B_4O_{14}$ and Investigation of Its Structural, Magnetic, and Resonant Properties. *Phys. Solid State* **2002**, *44*, 1339−1344.
(390) Pan, S. L.; Smit, J. P.; Marvel, M. R.; Stampler, E. S.; Haag, J. M.; Baek, J.; Halasyamani, P. S.; Poeppelmeier, K. R. Synthesis, Crystal Structure, and Nonlinear Optical Properties of $Bi_2Cu_5B_4O_{14}$. *J. Solid State Chem.* **2008**, *181*, 2087−2091.

https://dx.doi.org/10.1021/acs.chemrev.0c00796
Chem. Rev. 2021, 121, 1130−1202

(391) Xia, M. J.; Jiang, X. X.; Lin, Z. S.; Li, R. K. All-Three-in-One": A New Bismuth-Tellurium-Borate Bi_3TeBO_9 Exhibiting Strong Second Harmonic Generation Response. *J. Am. Chem. Soc.* **2016**, *138*, 14190−14193.
(392) Baucher, A.; Gasperin, M. Sur une nouvelle Famille d'oxydes Multiples a base de bore: $MIM'^{V}B_2O_6$ (M=Tl, Rb; M′ = Nb, Ta). *Mater. Res. Bull.* **1975**, *10*, 469−472.
(393) Becker, P.; Bohatý, L.; Fröhlich, R. $CsNbOB_2O_5$: the Basic Structure Type of the Borates $AMOB_2O_5$ (A = K, Rb, Cs, Tl; M = Nb, Ta). *Acta Crystallogr. Sect. C, Cryst.l Struct. Communi.* **1995**, *C51*, 1721−1723.
(394) Nicholls, J. F. H.; Chai, B. H. T.; Corker, D. L.; Calabrese, J. C.; Henderson, B. KNB (KNb_2BO_6) & its Isomorphs - A New Family of Non-Linear Optical Materials. *Proc. SPIE* **1993**, *1863*, 54−59.
(395) Nicholls, J. F. H.; Henderson, B.; Chai, B. H. T. The Nonlinear Optical Properties of the XYB_2O_6 Family of Compounds. *Opt. Mater.* **2001**, *16*, 453−462.
(396) Huang, C.; Zhang, J.-H.; Hu, C.-L.; Xu, X.; Kong, F.; Mao, J.-G. $KSbB_2O_6$ and $BaSb_2B_4O_{12}$: Novel Boroantimonates with 3D Anionic Architectures Composed of 1D Chains of SbO_6 Octahedra and B_2O_5 Groups. *Inorg. Chem.* **2014**, *53*, 3847−3853.
(397) Choisnet, J.; Groult, D.; Raveau, B.; Gasperin, M. Nouvelles Structures a Tunnels de Section Pentagonale $K_3Nb_3B_2O_{12}$ et $K_3Ta_3B_2O_{12}$. *Acta Crystallogr., Sect. B: Struct. Crystallogr. Cryst. Chem.* **1977**, *B33*, 1841−1845.
(398) Moran, K. L.; Gier, T. E.; Harrison, W. T. A.; Stucky, G. D.; Eckert, H.; Eichele, K.; Wasylishen, R. E. Synthesis and Characterization of Mixed ZnSe/GaP Semiconductor Species Included in the Sodalite Structure. *J. Am. Chem. Soc.* **1993**, *115*, 10553−10558.
(399) Bluhm, K.; Park, C. H. $Pb(BAsO_5)/Pb_6(AsO_4)[B(AsO_4)_4]$ - a New Crystal Structure Type in the System $PbO/B_2O_3/As_2O_5$ with Remarks about $Pb(BAsO_5)$. *Z. Naturforsch., B: J. Chem. Sci.* **1996**, *51*, 313−318.
(400) Smith, R. W.; Koliha, L. J. A New Noncentrosymmetric Orthoborate $[Ba_2Zn(BO_3)_2]$. *Mater. Res. Bull.* **1994**, *29*, 1203−1210.
(401) Smith, R. W.; Keszler, D. A. The Noncentrosymmetric Orthoborate $BaZn_2(BO_3)_2$. *J. Solid State Chem.* **1992**, *100*, 325−330.
(402) Zhang, W. G.; Yu, H. W.; Wu, H. P.; Halasyamani, P. S. Crystal Growth and Associated Properties of a Nonlinear Optical Crystal-$Ba_2Zn(BO_3)_2$. *Crystals* **2016**, *6*, 68−74.
(403) Duan, M. H.; Xia, M. J.; Li, R. K. $Ba_5Zn_4(BO_3)_6$: A Nonlinear-Optical Material with Reinforced Interlayer Connections and Large Second-Harmonic-Generation Response. *Inorg. Chem.* **2017**, *56*, 11458−11461.
(404) Zhao, S. G.; Zhang, J.; Zhang, S. Q.; Sun, Z. H.; Lin, Z. S.; Wu, Y. C.; Hong, M. H.; Luo, J. H. A New UV Nonlinear Optical Material $CsZn_2B_3O_7$: ZnO_4 Tetrahedra Double the Efficiency of Second-Harmonic Generation. *Inorg. Chem.* **2014**, *53*, 2521−2527.
(405) Yu, H. W.; Wu, H. P.; Pan, S. L.; Yang, Z. H.; Hou, X. L.; Su, X.; Jing, Q.; Poeppelmeier, K. R.; Rondinelli, J. M. $Cs_3Zn_6B_9O_{21}$: A Chemically Benign Member of the KBBF Family Exhibiting the Largest Second Harmonic Generation Response. *J. Am. Chem. Soc.* **2014**, *136*, 1264−1267.
(406) Harrison, D. E.; Hummel, F. A. The System $ZnO{\cdot}CdO{\cdot}B_2O_3$, Phase Relationships and Fluorescence. *J. Electrochem. Soc.* **1959**, *106*, 24−26.
(407) Whitaker, A.; Channell, A. D. Phase Equilibria in the System $CdO-ZnO-B_2O_3$ at 850°C. *J. Mater. Sci.* **1993**, *28*, 2489−2493.
(408) Zhang, F.; Shen, D. Z.; Shen, G. Q.; Wang, X. Q. Properties of a New Nonlinear Optical Crystal $CdZn_2B_2O_6$. *Chin. Phys. Lett.* **2008**, *25*, 1301−1304.
(409) Zhang, F.; Shen, D. Z.; Shen, G. Q.; Wang, X. Q. Growth and Characterization of Non-linear Optical Crystal $Cd_3Zn_3B_4O_{12}$. *Mater. Res. Bull.* **2008**, *43*, 3188−3194.
(410) Kazanskaya, E. V.; Sandomirsky, P. A.; Simonov, M. A. Below The Crystal Structure of $LiCdBO_3$. *Dokl. Akad. Nauk SSSR* **1978**, *238*, 1340−1343.
(411) Yin, X. D.; Huang, Q. Z.; Ye, S. S.; Lei, S. R.; Chen, C. T. Search for the Borate Nonlinear Optical Material−Synthesis of Lithium Cadmium Borate α-$LiCdBO_3$. *Acta Chim. Sin.* **1985**, *43*, 822 in Chinese.
(412) Yu, H. W.; Wu, H. P.; Pan, S. L.; Zhang, B. B.; Wen, M.; Yang, Z. H.; Li, H. Y.; Jiang, X. Z. Noncentrosymmetric Cubic $CsCdBO_3$ with Bichromophore. *Eur. J. Inorg. Chem.* **2013**, *2013*, 5528−5533.
(413) Chen, Y. Q.; Liang, J. K.; Gu, Y. X.; Luo, J.; Li, J. B.; Rao, G. H. Synthesis and Crystal Structure of a Novel Hexaborate, $Na_2ZnB_6O_{11}$. *Powder Diffr.* **2010**, *25*, 9−14.
(414) Xu, X.; Hu, C. L.; Kong, F.; Zhang, J. H.; Mao, J. G. $Ca_{10}Ge_{16}B_6O_{51}$ and $Cd_{12}Ge_{17}B_8O_{58}$: Two Types of New 3D Frameworks Based on BO_4 Tetrahedra and 1D $[Ge_4O_{12}]_n$ Chains. *Inorg. Chem.* **2011**, *50*, 8861−8868.
(415) Schmitt, M. K.; Janka, O.; Niehaus, O.; Dresselhaus, T.; Poettgen, R.; Pielnhofer, F.; Weihrich, R.; Krzhizhanovskaya, M.; Filatov, S.; Bubnova, R.; et al. Synthesis and Characterization of the High-Pressure Nickel Borate γ-NiB_4O_7. *Inorg. Chem.* **2017**, *56*, 4217−4228.
(416) Knyrim, J. S.; Emme, H.; Doeblinger, M.; Oeckler, O.; Weil, M.; Huppertz, H. Synthesis and Crystal Structure of the New High-Pressure Phase CdB_2O_4. *Chem. - Eur. J.* **2008**, *14*, 6149−6154.
(417) Sohr, G.; Falkowski, V.; Huppertz, H. The New Silver Borate $Ag_3B_5O_9$. *J. Solid State Chem.* **2015**, *225*, 114−119.
(418) Jansen, M.; Scheld, W. Silber(I)-orthoborat. *Z. Anorg. Allg. Chem.* **1981**, *477*, 85−87.
(419) Sohr, G.; Falkowski, V.; Schauperl, M.; Liedl, K. R.; Huppertz, H. Structure, Thermal Behavior, and Vibrational Spectroscopy of the Silver Borate AgB_3O_5. *Eur. J. Inorg. Chem.* **2015**, *2015*, 527−533.
(420) Wiesch, A.; Bluhm, K. $Ag_2Cs[B_{15}O_{24}]$: An Anhydrous Quaternary Silver(I)-Borate with a New Helical Borate Anion. *Z. Naturforsch., B: J. Chem. Sci.* **1998**, *53*, 157−160.
(421) Zhang, W. L.; Cheng, W. D.; Zhang, H.; Geng, L.; Lin, C. S.; He, Z. Z. A Strong Second-harmonic Generation Material $Cd_4BiO(BO_3)_3$ Originating from 3-Chromophore Asymmetric Structures. *J. Am. Chem. Soc.* **2010**, *132*, 1508−1509.
(422) Liebertz, J.; Wostrack, A.; Wirth, V.; Hellwig, H.; Held, P.; Bohatý, L. Das azentrische Wismutzinkborat $Bi_2Zn_2B_2O_7$: Kristallstruktur und Züchtung Sowie Lineare und Nichtlineare Optische Eigenschaften. *Z. Kristallogr. Suppl.* **1997**, *12*, 185.
(423) Barbier, J.; Penin, N.; Cranswick, L. M. D. Melilite-type Borates $Bi_2ZnB_2O_7$ and $CaBiGaB_2O_7$. *Chem. Mater.* **2005**, *17*, 3130−3136.
(424) Li, F.; Hou, X. L.; Pan, S. L.; Wang, X. Growth, Structure, and Optical Properties of a Congruent Melting Oxyborate, $Bi_2ZnOB_2O_6$. *Chem. Mater.* **2009**, *21*, 2846−2850.
(425) Li, F.; Hou, X. L.; Pan, S. L.; Yao, J. A Novel Nonlinear Optical Crystal $Bi_2ZnOB_2O_6$. *Cryst. Growth Des.* **2009**, *9*, 4091−4095.
(426) Su, X.; Wang, Y.; Yang, Z. H.; Huang, X. C.; Pan, S. L.; Li, F.; Lee, M. X. Experimental and Theoretical Studies on the Linear and Nonlinear Optical Properties of $Bi_2ZnOB_2O_6$. *J. Phys. Chem. C* **2013**, *117*, 14149−14157.
(427) Yu, H. W.; Wu, H. P.; Jing, Q.; Yang, Z. H.; Halasyamani, P. S.; Pan, S. L. Polar Polymorphism: α-, β-, and γ-$Pb_2Ba_4Zn_4B_{14}O_{31}$-Synthesis, Characterization, and Nonlinear Optical Properties. *Chem. Mater.* **2015**, *27*, 4779−4788.
(428) Ye, N.; Zeng, W. R.; Wu, B. C.; Huang, X. Y.; Chen, C. T. Crystal Structure of Barium Aluminium Borate, $BaAl_2B_2O_7$. *Z. Kristallogr. NCS* **1998**, *213*, 452−452.
(429) Ye, N.; Zeng, W. R.; Wu, B. C.; Chen, C. T. Two New Nonlinear Optical Crystals: $BaAl_2B_2O_7$ and $K_2Al_2B_2O_7$. *Proc. SPIE* **1998**, *3556*, 21−23.
(430) Hu, Z. G.; Higashiyama, T.; Yoshimura, M.; Yap, Y. K.; Mori, Y.; Sasaki, T. A New Nonlinear Optical Borate Crystal $K_2Al_2B_2O_7$ (KAB). *Jpn. J. Appl. Phys.* **1998**, *37*, L1093−L1094.
(431) Ye, N.; Zeng, W. R.; Jiang, J.; Wu, B. C.; Chen, C. T.; Feng, B.; Zhang, X. New Nonlinear Optical Crystal $K_2Al_2B_2O_7$. *J. Opt. Soc. Am. B* **2000**, *17*, 764−768.
(432) Lu, J. H.; Wang, G. L.; Xu, Z. Y.; Chen, C. T.; Wang, J. Y.; Zhang, C. Q.; Liu, Y. G. Efficient 266 nm Ultraviolet Beam Generation in $K_2Al_2B_2O_7$ Crystal. *Chin. Phys. Lett.* **2002**, *19*, 680.

https://dx.doi.org/10.1021/acs.chemrev.0c00796
Chem. Rev. 2021, 121, 1130−1202

(433) Liu, C. L.; Liu, L. J.; Zhang, X.; Wang, L. R.; Wang, G. L.; Chen, C. T. Crystal Growth and Optical Properties of Non-UV Absorption $K_2Al_2B_2O_7$ Crystals. *J. Cryst. Growth* **2011**, *318*, 618−620.
(434) Tran, T. T.; Koocher, N. Z.; Rondinelli, J. M.; Halasyamani, P. S. Beryllium-free β-$Rb_2Al_2B_2O_7$ as a Possible Deep-ultraviolet Nonlinear Optical Material Replacement for $KBe_2BO_3F_2$. *Angew. Chem.* **2017**, *129*, 3015−3019.
(435) Wang, Y. G.; Li, R. K. $K_2Fe_2B_2O_7$: A Transparent Nonlinear Optical Crystal with Frustrated Magnetism. *J. Solid State Chem.* **2010**, *183*, 1221−1225.
(436) Smith, R. W.; Kennard, M. A.; Dudik, M. J. Structure and Properties of the Noncentrosymmetric Oxide Borate $K_2Ga_2O(BO_3)_2$. *Mater. Res. Bull.* **1997**, *32*, 649−656.
(437) Yang, Z.; Liang, J. K.; Chen, X. L.; Chen, J. R. Ab Initio Determination of a New Compound. β-$SrGaBO_4$, from Powder X-ray Diffraction Data. *J. Solid State Chem.* **2002**, *165*, 119−124.
(438) Maczka, M.; Szymborska-Malek, K.; Gagor, A.; Majchrowski, A. Growth and Characterization of Acentric $BaHf(BO_3)_2$ and $BaZr(BO_3)_2$. *J. Solid State Chem.* **2015**, *225*, 330−334.
(439) Shin, Y.; Lee, D. W.; Hong, J.; Kwak, K.; Ok, K. M. Second-harmonic Generating Properties of Polar Noncentrosymmetric Aluminoborate Solid Solutions, $Al_{5-x}Ga_xBO_9$ ($0.0 \leq x \leq 0.5$). *Dalton Trans.* **2012**, *41*, 3233−3238.
(440) Park, H. S.; Bakhtiiarov, A.; Zhang, W.; Vargas-Baca, I.; Barbier, J. Non-centrosymmetric $Ba_3Ti_3O_6(BO_3)_2$. *J. Solid State Chem.* **2004**, *177*, 159−164.
(441) Kong, F.; Jiang, H. L.; Hu, T.; Mao, J. G. CsB_3GeO_7 and $K_2B_2Ge_3O_{10}$: Explorations of New Second-order Nonlinear Optical Materials in the Borogermanate Systems. *Inorg. Chem.* **2008**, *47*, 10611−10617.
(442) Xu, X.; Hu, C. L.; Kong, F.; Zhang, J. H.; Mao, J. G.; Sun, J. L. $Cs_2GeB_4O_9$: a New Second-Order Nonlinear-Optical Crystal. *Inorg. Chem.* **2013**, *52*, 5831−5837.
(443) Lin, Z. E.; Zhang, J.; Yang, G. Y. Synthesis and Structure of $KBGe_2O_6$: The First Chiral Zeotype with 7-ring Channels. *Inorg. Chem.* **2003**, *42*, 1797−1799.
(444) Braeuchle, S.; Wurst, K.; Huppertz, H. Synthesis and Structural Characterization of $Ca_{12}Ge_{17}B_8O_{58}$. *Z. Naturforsch., B: J. Chem. Sci.* **2016**, *71*, 1141−1146.
(445) Parise, J. B.; Gier, T. E. Hydrothermal Syntheses and Stuctural Refinements of Single Crystal $LiBGeO_4$ and $LiBSiO_4$. *Chem. Mater.* **1992**, *4*, 1065−1067.
(446) Pan, S.; Smit, J. P.; Watkins, B.; Marvel, M. R.; Stern, C. L.; Poeppelmeier, K. R. Synthesis, Crystal Structure and Nonlinear Optical Properties of $Li_6CuB_4O_{10}$: A Congruently Melting Compound with Isolated $[CuB_4O_{10}]^{6-}$ units. *J. Am. Chem. Soc.* **2006**, *128*, 11631−11634.
(447) Solov'eva, L. P.; Bakakin, V. V. Crystal Structure of Potassium Boratofluoroberyllate $KBe_2BO_3F_2$. *Sov. Phys. Crystallogr.* **1970**, *15*, 802−805.
(448) Baidina, I. A.; Bakakin, V. V.; Batsanova, L. R.; Pal'chik, N. A.; Podberezskaya, N. V.; Solov'eva, L. P. X-ray Structural Study of Borato-Fluoroberyllates with the Composition $MBe_2BO_3F_2$ (M = Na, K, Rb, Cs). *J. Struct. Chem.* **1976**, *16*, 963−965.
(449) Guo, S.; Kang, L.; Liu, L. J.; Xia, M. J.; Lin, Z. S.; Huang, Q.; Hou, Z. Y.; Tang, C. C.; Wang, X. Y.; Chen, C. T. Deep-ultraviolet Nonlinear Optical Crystal $NaBe_2BO_3F_2$—Structure, Growth and Optical Properties. *J. Cryst. Growth* **2019**, *518*, 45−50.
(450) Chen, C. T.; Luo, S. Y.; Wang, X. Y.; Wang, G. L.; Wen, X. L.; Wu, H. X.; Zhang, X.; Xu, Z. Y. Deep UV Nonlinear Optical Crystal: $RbBe_2(BO_3)F_2$. *J. Opt. Soc. Am. B* **2009**, *26*, 1519−1525.
(451) Huang, H. W.; Chen, C. T.; Wang, X. Y.; Zhu, Y.; Wang, G. L.; Zhang, X.; Wang, L. R.; Yao, J. Y. Ultraviolet Nonlinear Optical Crystal: $CsBe_2BO_3F_2$. *J. Opt. Soc. Am. B* **2011**, *28*, 2186−2190.
(452) Peng, G.; Ye, N.; Lin, Z. S.; Kang, L.; Pan, S. L.; Zhang, M.; Lin, C. S.; Long, X. F.; Luo, M.; Chen, Y.; et al. $NH_4Be_2BO_3F_2$ and γ-Be_2BO_3F: Overcoming the Layering Habit in $KBe_2BO_3F_2$ for the Next-Generation Deep-Ultraviolet Nonlinear Optical Materials. *Angew. Chem., Int. Ed.* **2018**, *57*, 8968−8972.
(453) Wang, X. Y.; Yan, X.; Luo, S. Y.; Chen, C. T. Flux Growth of Large KBBF Crystals by Localized Spontaneous Nucleation. *J. Cryst. Growth* **2011**, *318*, 610−612.
(454) Togashi, T.; Kanai, T.; Sekikawa, T.; Watanabe, S.; Chen, C. T.; Zhang, C. Q.; Xu, Z. Y.; Wang, J. Y. Generation of Vacuum-ultraviolet Light by an Optically Contacted, Prism-coupled $KBe_2BO_3F_2$ Crystal. *Opt. Lett.* **2003**, *28*, 254−256.
(455) Wang, G. L.; Wang, X. Y.; Zhou, Y.; Chen, Y. H.; Li, C. M.; Zhu, Y.; Xu, Z. Y.; Chen, C. T. 12.95 mW Sixth Harmonic Generation with $KBe_2BO_3F_2$ Crystal. *Appl. Phys. B: Lasers Opt.* **2008**, *91*, 95−97.
(456) Kanai, T.; Wang, X. Y.; Adachi, S.; Watanabe, S.; Chen, C. T. Watt-level Tunable Deep Ultraviolet Light Source by a KBBF Prism-coupled Device. *Opt. Express* **2009**, *17*, 8696−8703.
(457) Xu, B.; Liu, L. J.; Wang, X. Y.; Chen, C. T.; Zhang, X.; Lin, S. J. Generation of High Power 200 mW Laser Radiation at 177.3 nm in $KBe_2BO_3F_2$ Crystal. *Appl. Phys. B: Lasers Opt.* **2015**, *121*, 489−494.
(458) Dai, S. B.; Chen, M.; Zhang, S. J.; Wang, Z. M.; Zhang, F. F.; Yang, F.; Wang, Z. C.; Zong, N.; Liu, L. J.; Wang, X. Y.; et al. 2.14 mW Deep-ultraviolet Laser at 165 nm by Eighth-harmonic Generation of a 1319 nm Nd: YAG Laser in KBBF. *Laser Phys. Lett.* **2016**, *13*, 035401.
(459) Xu, Z. Y.; Zhang, S. J.; Zhou, X. J.; Zhang, F. F.; Yang, F.; Wang, Z. M.; Zong, N.; Liu, G. D.; Zhao, L.; Yu, L.; Chen, C. T.; Wang, X. Y.; Peng, Q. J. Advances in Deep Ultraviolet Laser Based High-resolution Photoemission Spectroscopy. *Front. Inform. Technol. Electron. Eng.* **2019**, *20*, 885−913.
(460) Huang, H. W.; Yao, J. Y.; Lin, Z. S.; Wang, X. Y.; He, R.; Yao, W. X.; Zhai, N.; Chen, C. T. Molecular Engineering Design to Resolve the Layering Habit and Polymorphism Problems in Deep UV NLO Crystals: New Structures in $MM'Be_2B_2O_6F$ (M = Na, M' = Ca; M=K, M' = Ca, Sr). *Chem. Mater.* **2011**, *23*, 5457−5463.
(461) Huang, H. W.; Yao, J. Y.; Lin, Z. S.; Wang, X. Y.; He, R.; Yao, W. J.; Zhai, N. X.; Chen, C. T. $NaSr_3Be_3B_3O_9F_4$: A Promising Deep-Ultraviolet Nonlinear Optical Material Resulting from Cooperative Alignment of the $[Be_3B_3O_{12}F]^{10-}$ Anionic Group. *Angew. Chem., Int. Ed.* **2011**, *50*, 9141−9144.
(462) Guo, S.; Liang, F.; Liu, L. J.; Xia, M. J.; Fang, Z.; Wu, R. F.; Wang, X. Y.; Lin, Z. S.; Chen, C. T. $LiSr_3Be_3B_3O_9F_4$: A New Ultraviolet Nonlinear Optical Crystal for Fourth-harmonic Generation of Nd:YAG Lasers. *New J. Chem.* **2017**, *41*, 4269−4272.
(463) Guo, S.; Jiang, X. X.; Liu, L. J.; Xia, M. J.; Fang, Z.; Wang, X. Y.; Lin, Z. S.; Chen, C. T. $BaBe_2BO_3F_3$: A KBBF-Type Deep-Ultraviolet Nonlinear Optical Material with Reinforced $[Be_2BO_3F_2]_\infty$ Layers and Short Phase Matching Wavelength. *Chem. Mater.* **2016**, *28*, 8871−8875.
(464) Xia, W. B.; Lin, Z. S.; Wu, Y. C.; Chen, C. T. A New Type of Potential Nonlinear Optical Material-Beryllium Fluoride Borate. *J. Synth. Cryst.* **2005**, *34*, 597 in Chinese.
(465) Wang, X. S.; Liu, L. J.; Wang, X. Y.; Bai, L.; Chen, C. T. Growth and Optical Properties of the Novel Nonlinear Optical Crystal $NaSr_3Be_3B_3O_9F_4$. *CrystEngComm* **2015**, *17*, 925−929.
(466) Fang, Z.; Hou, Z. Y.; Yang, F.; Liu, L. J.; Wang, X. Y.; Xu, Z. Y.; Chen, C. T. High-efficiency UV Generation at 266 nm in a New Nonlinear Optical Crystal $NaSr_3Be_3B_3O_9F_4$. *Opt. Express* **2017**, *25*, 26500−26507.
(467) Hou, Z. Y.; Liu, L. J.; Fang, Z.; Yang, L.; Yan, D. X.; Wang, X. Y.; Xu, D. G.; Chen, C. T. High-power 266 nm Laser Generation with a $NaSr_3Be_3B_3O_9F_4$ Crystal. *Opt. Lett.* **2018**, *43*, 5599−5602.
(468) Lei, S. R.; Huang, Q. Z.; Zheng, Y. F.; Jiang, A. D.; Chen, C. T. Structure of Calcium Fluoroborate, $Ca_5(BO_3)_3F$. *Acta Crystallogr., Sect. C: Cryst. Struct. Commun.* **1989**, *C45*, 1861−1863.
(469) Chen, G. J.; Wu, Y. C.; Fu, P. Z. Growth and Characterization of a New Nonlinear Optical Crystal $Ca_5(BO_3)_3F$. *J. Cryst. Growth* **2006**, *292*, 449−453.
(470) Xu, K.; Loiseau, P.; Aka, G.; Maillard, R.; Maillard, A.; Taira, T. Nonlinear Optical Properties of $Ca_5(BO_3)_3F$ Crystal. *Opt. Express* **2008**, *16*, 17735−17744.
(471) Bai, C. Y.; Han, S. J.; Pan, S. L.; Bian, Q.; Yang, Z. H.; Zhang, X. W.; Lin, X. X.; Jing, Q. Z. Reinvestigation and Characterization of

https://dx.doi.org/10.1021/acs.chemrev.0c00796
Chem. Rev. 2021, 121, 1130−1202

the Magnesium Borate Fluoride $Mg_5(BO_3)F$. *Z. Anorg. Allg. Chem.* **2014**, *640*, 2013−2018.
(472) Reckeweg, O.; Schulz, A.; DiSalvo, F. J. Orthoborate Halides with the Formula $(M^{+II})_5(BO_3)_3X$: Syntheses, Crystal Structures and Raman Spectra of $Eu_5(BO_3)_3Cl$ and $Ba_5(BO_3)_3X$ (X = Cl, Br). *Z. Naturforsch., B: J. Chem. Sci.* **2011**, *66*, 359−365.
(473) Machida, K.; Ishino, T.; Adachi, G.; Shiokawa, J. Synthesis and Characterization of Europium (II) Holoborates, $Eu_2B_5O_9Cl$ and $Eu_2B_5O_9Br$. *Mater. Res. Bull.* **1979**, *14*, 1529−1534.
(474) Dong, X. Y.; Jing, Q.; Shi, Y. J.; Yang, Z. H.; Pan, S. L.; Poeppelmeier, K. R.; Young, J.; Rondinelli, J. M. $Pb_2Ba_3(BO_3)_3Cl$: A Material with Large SHG Enhancement Activated by Pb-chelated BO_3 Groups. *J. Am. Chem. Soc.* **2015**, *137*, 9417−9422.
(475) Jing, Q.; Dong, X. Y.; Yang, Z. H.; Pan, S. L. Synthesis and Optical Properties of the First Lead Borate Bromide with Isolated BO_3 Groups: $Pb_2Ba_3(BO_3)_3Br$. *Dalton Trans.* **2015**, *44*, 16818−16823.
(476) Zou, G. H.; Zhang, L. Y.; Ye, N. Synthesis, Structure, and Characterization of a New Promising Nonlinear Optical Crystal: $Cd_5(BO_3)_3F$. *CrystEngComm* **2013**, *15*, 2422−2427.
(477) McMillen, C. D.; Stritzinger, J. T.; Kolis, J. W. Two Novel Acentric Borate Fluorides: $M_3B_6O_{11}F_2$ (M = Sr, Ba). *Inorg. Chem.* **2012**, *51*, 3953−3955.
(478) Yu, H. W.; Wu, H. P.; Pan, S. L.; Yang, Z. H.; Su, X.; Zhang, F. F. A Novel Deep UV Nonlinear Optical Crystal $Ba_3B_6O_{11}F_2$, with a New Fundamental Building Block, B_6O_{14} Group. *J. Mater. Chem.* **2012**, *22*, 9665−9670.
(479) Li, H. Y.; Wu, H. P.; Su, X.; Yu, H. W.; Pan, S. L.; Yang, Z. H.; Lu, Y.; Han, J.; Poeppelmeier, K. R. $Pb_3B_6O_{11}F_2$: The First Non-centrosymmetric Lead Borate Fluoride with a Large Second Harmonic Generation Response. *J. Mater. Chem. C* **2014**, *2*, 1704−1710.
(480) Huang, Z. J.; Su, X.; Pan, S. L.; Dong, X. Y.; Han, S. J.; Yu, H. W.; Zhang, M.; Yang, Y.; Cui, S. F.; Yang, Z. H. $Sr_3B_6O_{11}F_2$: A Promising Polar Fluoroborate with Short UV Absorption Edge and Moderate Second Harmonic Generation Response. *Scr. Mater.* **2013**, *69*, 449−452.
(481) Wu, H. P.; Yu, H. W.; Yang, Z. H.; Hou, X. L.; Su, X.; Pan, S. L.; Poeppelmeier, K. R.; Rondinelli, J. M. Designing a Deep-Ultraviolet Nonlinear Optical Material with a Large Second Harmonic Generation Response. *J. Am. Chem. Soc.* **2013**, *135*, 4215−4218.
(482) Wu, H. P.; Yu, H. W.; Zhang, W. G.; Cantwell, J.; Poeppelmeier, K. R.; Pan, S. L.; Halasyamani, P. S. Top-Seeded Solution Crystal Growth and Linear and Nonlinear Optical Properties of $Ba_4B_{11}O_{20}F$. *Cryst. Growth Des.* **2017**, *17*, 1404−1410.
(483) Zou, G. H.; Lin, C.; Jo, H.; Nam, G.; You, T. S.; Ok, K. M. Pb_2BO_3Cl: A Tailor-Made Polar Lead Borate Chloride with Very Strong Second Harmonic Generation. *Angew. Chem., Int. Ed.* **2016**, *55*, 12078−12082.
(484) Luo, M.; Song, Y. X.; Liang, F.; Ye, N.; Lin, Z. S. Pb_2BO_3Br: A Novel Nonlinear Optical Lead Borate Bromine with a KBBF-type Structure Exhibiting Strong Nonlinear Optical Response. *Inorg. Chem. Front.* **2018**, *5*, 916−921.
(485) Yu, H. W.; Koocher, N. Z.; Rondinelli, J. M.; Halasyamani, P. S. Pb_2BO_3I: A Borate Iodide with the Largest Second-Harmonic Generation (SHG) Response in the $KBe_2BO_3F_2$ (KBBF) Family of Nonlinear Optical (NLO) Materials. *Angew. Chem., Int. Ed.* **2018**, *57*, 6100−6103.
(486) Wang, Z. J.; He, J. G.; Hu, B.; Shan, P.; Xiong, Z. Y.; Su, R. B.; He, C.; Yang, X. M.; Long, X. F. $Ca_2B_5O_9Cl$ and $Sr_2B_5O_9Cl$: Nonlinear Optical Crystals with Deep-Ultraviolet Transparency Windows. *ACS Appl. Mater. Interfaces* **2020**, *12*, 4632−4637.
(487) Pekov, I. V.; Zubkova, N. V.; Pautov, L. A.; Yapaskurt, V. O.; Chukanov, N. V.; Lykova, I. S.; Britvin, S. N.; Sidorov, E. G.; Pushcharovsky, D. Y. Chubarovite, $KZn_2(BO_3)Cl_2$, A New Mineral Species from the Tolbachik Volcano, Kamchatka. *Can. Mineral.* **2015**, *53*, 273−284.
(488) Huang, Q.; Liu, L. J.; Wang, X. Y.; Li, R. K.; Chen, C. T. Beryllium-Free KBBF Family of Nonlinear-Optical Crystals: $AZn_2BO_3X_2$ (A = Na, K, Rb; X = Cl, Br). *Inorg. Chem.* **2016**, *55*, 12496−12499.
(489) Yang, G. S.; Gong, P. F.; Lin, Z. S.; Ye, N. $AZn_2BO_3X_2$(A = K, Rb, NH_4; X = Cl, Br): New Members of KBBF Family Exhibiting Large SHG Response and the Enhancement of Layer Interaction by Modified Structures. *Chem. Mater.* **2016**, *28*, 9122−9131.
(490) Bekker, T. B.; Rashchenko, S. V.; Solntsev, V. P.; Yelisseyev, A. P.; Kragzhda, A. A.; Bakakin, V. V.; Seryotkin, Y. V.; Kokh, A. E.; Kokh, K. A.; Kuznetsov, A. B. Growth and Optical Properties of $Li_xNa_{1-x}Ba_{12}(BO_3)_7F_4$ Fluoride Borates with "Antizeolite" Structure. *Inorg. Chem.* **2017**, *56*, 5411−5419.
(491) Keszler, D. A.; Akella, A.; Schaffers, K. I.; Alekel, T. New Borate Structures for NLO Applications. *MRS Proc.* **1993**, *329*, 15.
(492) Li, R. K.; Zeng, Q. D. Crystal Growth, Structure and Phase Transition of the Nonlinear Optical Crystal $BaCaBO_3F$. *J. Cryst. Growth* **2013**, *382*, 47−51.
(493) Zhang, G. C.; Liu, H. J.; Wang, X.; Fan, F. D.; Fu, P. Z. Growth and Characterization of Nonlinear Optical Crystal $BaCaBO_3F$. *J. Cryst. Growth* **2006**, *289*, 188−191.
(494) Xu, K.; Loiseau, P.; Aka, G. $BaCaBO_3F$: A Nonlinear Optical Crystal Investigated for UV Light Generation. *J. Cryst. Growth* **2009**, *311*, 2508−2512.
(495) Li, R. K.; Chen, P. Cation Coordination Control of Anionic Group Alignment to Maximize SHG Effects in the $BaMBO_3F$ (M = Zn, Mg) Series. *Inorg. Chem.* **2010**, *49*, 1561−1565.
(496) Xia, M. J.; Li, R. K. Growth, Structure and Optical Properties of Nonlinear Optical Crystal $BaZnBO_3F$. *J. Solid State Chem.* **2016**, *233*, 58−61.
(497) Mutailipu, M.; Zhang, M.; Wu, H. P.; Yang, Z. H.; Shen, Y. H.; Sun, J. L.; Pan, S. L. $Ba_3Mg_3(BO_3)_3F_3$ Polymorphs with Reversible Phase Transition and High Performances as Ultraviolet Nonlinear Optical Materials. *Nat. Commun.* **2018**, *9*, 3089.
(498) Park, H.; Barbier, J. Crystal Structures of the New Borate Fluorides $BaMBO_3F_2$ (M = Ga, Al). *J. Solid State Chem.* **2000**, *155*, 354−358.
(499) Hu, Z. G.; Yue, Y. C.; Chen, X. A.; Yao, J. Y.; Wang, J. N.; Lin, Z. S. Growth and Structure Redetermination of a Nonlinear $BaAlBO_3F_2$ Crystal. *Solid State Sci.* **2011**, *13*, 875−878.
(500) Yue, Y.; Hu, Z.; Zhou, Y.; Wang, J.; Zhang, X.; Chen, C.; Xu, Z. Growth and Nonlinear Optical Properties of $BaAlBO_3F_2$ Crystal. *J. Opt. Soc. Am. B* **2011**, *28*, 861−866.
(501) Yang, L.; Yue, Y. C.; Yang, F.; Hu, Z. G.; Xu, X. Y. 266 nm Ultraviolet Light Generation in Ga-doped $BaAlBO_3F_2$ Crystals. *Opt. Lett.* **2016**, *41*, 1598−1600.
(502) Zhao, S. G.; Gong, P. F.; Luo, S. Y.; Liu, S. J.; Li, L.; Asghar, M. A.; Khan, T.; Hong, M. C.; Lin, Z. S.; Luo, J. H. Beryllium-Free $Rb_3Al_3B_3O_{10}F$ with Reinforced Interlayer Bonding as a Deep-Ultraviolet Nonlinear Optical Crystal. *J. Am. Chem. Soc.* **2015**, *137*, 2207−2210.
(503) Yu, H. W.; Wu, H. P.; Pan, S. L.; Wang, Y.; Yang, Z. H.; Su, X. New Salt-Inclusion Borate, $Li_3Ca_9(BO_3)_7{\cdot}2[LiF]$: A Promising UV NLO Material with the Coplanar and High Density BO_3 Triangles. *Inorg. Chem.* **2013**, *52*, 5359−5365.
(504) Zhao, S. G.; Kang, L.; Shen, Y. G.; Wang, X. D.; Asghar, M. A.; Lin, Z. S.; Xu, Y. Y.; Zeng, S. Y.; Hong, M. C.; Luo, J. H. Designing a Beryllium-free Deep-ultraviolet Nonlinear Optical Material Without a Structural Instability Problem. *J. Am. Chem. Soc.* **2016**, *138*, 2961−2964.
(505) Zhao, B. Q.; Bai, L.; Li, B. X.; Zhao, S. G.; Shen, Y. G.; Li, X. F.; Ding, Q. R.; Ji, C. M.; Lin, Z. S.; Luo, J. H. Crystal Growth and Optical Properties of Beryllium-Free Nonlinear Optical Crystal $K_3Ba_3Li_2Al_4B_6O_{20}F$. *Cryst. Growth Des.* **2018**, *18*, 1168−1172.
(506) Wu, H. W.; Yu, H. P.; Pan, S. L.; Halasyamani, P. S. Deep-Ultraviolet Nonlinear-Optical Material $K_3Sr_3Li_2Al_4B_6O_{20}F$: Addressing the Structural Instability Problem in $KBe_2BO_3F_2$. *Inorg. Chem.* **2017**, *56*, 8755−8758.
(507) Yu, H. W.; Young, J.; Wu, H. P.; Zhang, W. G.; Rondinelli, J. M.; Halasyamani, P. S. The Next-generation of Nonlinear Optical

https://dx.doi.org/10.1021/acs.chemrev.0c00796
Chem. Rev. 2021, 121, 1130−1202

Materials: $Rb_3Ba_3Li_2Al_4B_6O_{20}F$-Synthesis, Characterization, and Crystal Growth. *Adv. Opt. Mater.* **2017**, *5*, 1700840.
(508) Shen, Y. G.; Zhao, S. G.; Yang, Y.; Cao, L. L.; Wang, Z. J.; Zhao, B. Q.; Sun, Z. H.; Lin, Z. S.; Luo, J. H. A New KBBF-family Nonlinear Optical Material with Strong Interlayer Bonding. *Cryst. Growth Des.* **2017**, *17*, 4422−4427.
(509) Shen, Y. G.; Jia, J. R.; Liu, Z. Q.; Wang, J. B.; Zhao, S. G.; Luo, J. H. Structurally Stable Borate as a UV Nonlinear Optical Material. *Inorg. Chem. Commun.* **2017**, *84*, 127−130.
(510) Meng, X. H.; Liang, F.; Xia, M. J.; Lin, Z. S. Beryllium-Free Nonlinear-Optical Crystals $A_3Ba_3Li_2Ga_4B_6O_{20}F$ (A = K and Rb): Members of the $Sr_2Be_2(BO_3)_2O$ Family with a Strong Covalent Connection between the $^2[Li_2Ga_4B_6O_{20}F]^{9-}$ Double Layers. *Inorg. Chem.* **2018**, *57*, 5669−5676.
(511) Barbier, J. The Non-centrosymmetric Borate Chlorides $Ba_2TB_4O_9Cl$ (T= Al, Ga). *Solid State Sci.* **2007**, *9*, 344−350.
(512) Zhang, J. X.; Zhang, S. F.; Wu, Y. C.; Wang, J. Y. New Nonlinear Optical Crystal: $NaBa_4Al_2B_8O_{18}Cl_3$. *Inorg. Chem.* **2012**, *51*, 6682−6686.
(513) Fang, J. Z.; Wang, K. P.; Ren, X. C.; Zhang, J. X.; Zhang, G. C.; Wang, J. Y.; Wu, Y. C. Growth, Optical and Electrical Properties of a Nonlinear Optical Crystal $NaBa_4Al_2B_8O_{18}Cl_3$. *CrystEngComm* **2013**, *15*, 2972−2977.
(514) Yu, H. W.; Pan, S. L.; Wu, H. P.; Yang, Z. H.; Dong, L. Y.; Su, X.; Zhang, B. B.; Li, H. Y. Effect of Rigid Units on the Symmetry of the Framework: Design and Synthesis of Centrosymmetric $NaBa_4(B_5O_9)_2F_2Cl$ and Noncentrosymmetric $NaBa_4(AlB_4O_9)_2Br_3$. *Cryst. Growth Des.* **2013**, *13*, 3514−3521.
(515) Wen, M.; Su, X.; Wu, H. P.; Lu, J. J.; Yang, Z. H.; Pan, S. L. $NaBa_4(GaB_4O_9)_2X_3$ (X = Cl, Br) with NLO-active GaO_4 Tetrahedral Unit: Experimental and ab Initio Studies. *J. Phys. Chem. C* **2016**, *120*, 6190−6197.
(516) Wu, H. P.; Pan, S. L.; Yu, H. W.; Jia, D. Z.; Chang, A. M.; Li, H. Y.; Zhang, F. F.; Huang, X. Growth, Thermal and Optical Properties of a Novel Nonlinear Optical Material $K_3B_6O_{10}Cl$. *CrystEngComm* **2012**, *14*, 799−803.
(517) Xia, M. J.; Xu, B.; Li, R. K. Growth and Nonlinear Optical Properties of $K_3B_6O_{10}Br$ Crystal. *J. Cryst. Growth* **2014**, *404*, 65−68.
(518) Xu, B.; Hou, Z. Y.; Xia, M. J.; Liu, L. J.; Wang, X. Y.; Li, R. K.; Chen, C. T. High Average Power Third Harmonic Generation at 355 nm with $K_3B_6O_{10}Br$ Crystal. *Opt. Express* **2016**, *24*, 10345−10351.
(519) Wu, Y.; Wu, H. P.; Wang, Y.; Zhang, L.; Zhang, Q. L.; Meng, L. P.; Wang, L. R.; He, C. J.; Zhang, D. X.; Guo, H. Y.; et al. 1.21-W 532-nm Picosecond Green Laser Generated by Second-harmonic Generation Using $K_3B_6O_{10}Cl$ as a Nonlinear Optical Crystal. *Opt. Eng.* **2018**, *57*, 066112.
(520) Wang, Z. J.; Qiao, H. M.; Su, R. B.; Hu, B.; Yang, X. M.; He, C.; Long, X. F. $Mg_3B_7O_{13}Cl$: A New Quasi-Phase Matching Crystal in the Deep-Ultraviolet Region. *Adv. Funct. Mater.* **2018**, *28*, 1804089.
(521) Zhang, B. B.; Shi, G. Q.; Yang, Z. H.; Zhang, F. F.; Pan, S. L. Fluorooxoborates: Beryllium-Free Deep-Ultraviolet Nonlinear Optical Materials without Layered Growth. *Angew. Chem., Int. Ed.* **2017**, *56*, 3916−3919.
(522) Cong, R. H.; Wang, Y.; Kang, L.; Zhou, Z. Y.; Lin, Z. S.; Yang, T. An Outstanding Second-harmonic Generation Material BiB_2O_4F: Exploiting the Electron-withdrawing Ability of Fluorine. *Inorg. Chem. Front.* **2015**, *2*, 170−176.
(523) Brenier, A. The Self-doubling and Summing Lasers: Overview and Modeling. *J. Lumin.* **2000**, *91*, 121−132.
(524) Yu, H. H.; Pan, Z. B.; Zhang, H. J.; Wang, J. Y. Recent Advances in Self-frequency-doubling Crystals. *J. Materiomics.* **2016**, *2*, 55−65.
(525) Johnson, L. F.; Ballman, A. A. Coherent Emission from Rare Earth Ions in Electro-optic Crystals. *J. Appl. Phys.* **1969**, *40*, 297.
(526) Dorozhki, L. M.; Kuratev, I. I.; Leonyuk, N. I.; Timchenko, T. I.; Shestakov, A. V. Nonlinear Optical Properties of Neodymium Yttrium Aluminum Borate Crystals. *Sov. Technol. Phys. Lett.* **1981**, *7*, 555−556.
(527) Lu, B. S.; Wang, J.; Pan, H. F.; Jiang, M.; Liu, E.; Hou, X. Excited Emission and Self-frequency-doubling Effect of NYAB Crystal. *Chin. Phys. Lett.* **1986**, *3*, 413−416.
(528) Schütz, I.; Freitag, I.; Wallenstein, R. Miniature Self-frequency-doubling CW Nd:YAB Laser Pumped by a Diode-laser. *Opt. Commun.* **1990**, *77*, 221−225.
(529) Hemmati, H. Diode-pumped Self-frequency-doubled Neodymium Yttrium Aluminum Borate (NYAB) Laser. *IEEE J. Quantum Electron.* **1992**, *28*, 1169−1171.
(530) Bartschke, J.; Knappe, R.; Boller, K. J.; Wallenstein, R. Investigation of Efficient Self-frequency-doubling Nd:YAB Lasers. *IEEE J. Quantum Electron.* **1997**, *33*, 2295−2300.
(531) Dawes, J. M.; Dekker, P.; Burns, P.; Piper, J. A. Self-Frequency-Doubling Ytterbium Lasers. *Opt. Rev.* **2005**, *12*, 101−104.
(532) Wang, P.; Dekker, P.; Dawes, J. M.; Piper, J. A.; Liu, Y. G.; Wang, J. Y. Efficient Continuous-wave Self-frequency-doubling Green Diode-pumped $Yb:YAl_3(BO_3)_4$ Lasers. *Opt. Lett.* **2000**, *25*, 731−733.
(533) Dekker, P.; Dawes, J. M.; Piper, J. A.; Liu, Y. G.; Wang, J. Y. 1.1 W CW Self-frequency-doubled Diode-pumped $Yb:YAl(BO_3)_4$ Laser. *Opt. Commun.* **2001**, *195*, 431−436.
(534) Brenier, A.; Tu, C. Y.; Qiu, M. W.; Jiang, A. D.; Li, J. F.; Wu, B. C. Spectroscopic Properties, Self-frequency Doubling, and Self-sum Frequency Mixing in $GdAl_3(BO_3)_4:Nd^{3+}$. *J. Opt. Soc. Am. B* **2001**, *18*, 1104−1110.
(535) Brenier, A.; Tu, C. Y.; Li, J. F.; Zhu, Z. J.; Wu, B. C. Spectroscopy, Laser Operation at 1.3 μm and Self-frequency Doubling in $GdAl_3(BO_3)_4$: Nd^{3+}. *Opt. Commun.* **2001**, *200*, 355−358.
(536) Mougel, F.; Aka, G.; Kahn-Harari, A.; Hubert, H.; Benitez, J. M.; Vivien, D. Infrared Laser Performance and Self-frequency Doubling of $Nd^{3+}:Ca_4GdO(BO_3)_3$ (Nd:GdCOB). *Opt. Mater.* **1997**, *8*, 161−173.
(537) Mougel, F.; Augé, F.; Aka, G.; Kahn-Harari, A.; Vivien, D.; Balembois, F.; Georges, P.; Brun, A. New Green Self-frequency-doubling Diode-pumped $Nd:Ca_4GdO(BO_3)_3$ Laser. *Appl. Phys. B: Lasers Opt.* **1998**, *67*, 533−535.
(538) Lucas-Leclin, G.; Augé, F.; Auzanneau, S. C.; Balembois, F.; Georges, P.; Brun, A.; Mougel, F.; Aka, G.; Vivien, D. Diode-pumped Self-frequency-doubling $Nd:GdCa_4O(BO_3)_3$ Lasers: toward Green Microchip Lasers. *J. Opt. Soc. Am. B* **2000**, *17*, 1526−1530.
(539) Wang, J. Y.; Zhang, H. J.; Wang, Z. P.; Yu, H. H.; Zong, N.; Ma, C. Q.; Xu, X. Y.; Jiang, M. H. Watt-level Self-frequency-doubling Nd:GdCOB Lasers. *Opt. Express* **2010**, *18*, 11058−11062.
(540) Yu, H. H.; Zong, N.; Pan, Z. B.; Zhang, H. J.; Wang, J. Y.; Wang, Z. P.; Xu, X. Y. Efficient High-power Self-frequency-doubling Nd:GdCOB Laser at 545 and 530 nm. *Opt. Lett.* **2011**, *36*, 3852−3854.
(541) Du, J. H.; Wang, J. Y.; Yu, H. H.; Zhang, H. J. 17.9 W Continuous-wave Self-frequency-doubled Nd:GdCOB Laser. *Opt. Lett.* **2020**, *45*, 327−330.
(542) Bajor, A.; Kisielewski, J.; Kłos, A.; Kopczyński, K.; Łukasiewicz, T.; Mierczyk, J.; Młyńczak, J. Assessment of Gadolinium Calcium Oxoborate (GdCOB) for Laser Applications. *Opto-Electron. Rev.* **2011**, *19*, 439−448.
(543) Brenier, A.; Wu, Y.; Zhang, J.; Wu, Y.; Fu, P. Laser Properties of the Diode-pumped Nd^{3+}-doped $La_2CaB_{10}O_{19}$ Crystal. *J. Appl. Phys.* **2010**, *108*, 093101.
(544) Brenier, A.; Wu, Y.; Fu, P.; Guo, R.; Jing, F.; Zu, Y. Spectroscopy and Self-frequency Doubling of the $^4F_{3/2} \rightarrow {}^4I_{13/2}$ Laser Channel in the $La_2CaB_{10}O_{19}:Nd^{3+}$ Bi-functional Crystal. *Appl. Phys. B: Lasers Opt.* **2007**, *86*, 673−676.
(545) Fang, Q. N.; Yu, H. H.; Zhang, H. J.; Zhang, G. C.; Wang, J. Y.; Wu, Y. C. Output Power Enhancement of a Self-frequency-doubled Laser by Selective Excitation of Inequivalent Active Centers in $La_2CaB_{10}O_{19}$ (Nd:LCB) Crystal. *Opt. Lett.* **2017**, *42*, 4861−4864.
(546) Rulmont, A.; Tarte, P. Lanthanide Borogermanates $LnBGeO_5$: Synthesis and Structural Study by X-ray Diffractometry and Vibrational Spectroscopy. *J. Solid State Chem.* **1988**, *75*, 244−250.
(547) Kaminskii, A. A.; Butashin, A. V.; Maslyanizin, I. A.; Mill, B. V.; Mironov, V. S.; Rozov, S. P.; Sarkisov, S. E.; Shigorin, V. D. Pure

https://dx.doi.org/10.1021/acs.chemrev.0c00796
Chem. Rev. 2021, 121, 1130−1202

and Nd^{3+}-, Pr^{3+}-Ion Doped Trigonal Acentric $LaBGeO_5$ Single Crystals Nonlinear Optical Properties, Raman Scattering, Spectroscopy, Crystal Field Analysis, and Simulated Emission of Their Activators. *Phys. Status Solidi.* **1991**, *125*, 671−696.
(548) Hirohashi, J.; Taniuchi, T.; Hatori, M.; Imai, K.; Sakairi, M.; Matsukura, M.; Takekawa, S.; Motegi, H.; Makio, S.; Miyazawa, S. et al. 300 mW 355 nm Generation by PP-$LaBGeO_5$. Advanced Solid State Lasers. *OSA Technical Digest*; Optical Society of America, 2014, paper ATu4A.4.
(549) Capmany, J.; Jaque, D.; Garcıía Solé, S. J.; Kaminskii, A. A. Continuous Wave Laser Radiation at 524 nm from a Self-frequency-doubled Laser of $LaBGeO_5:Nd^{3+}$. *Appl. Phys. Lett.* **1998**, *72*, 531−533.
(550) Capmany, J.; Jaque, D.; García Solé, S. J. Continuous Wave Laser Radiation at 1314 and 1386 nm and Infrared to Red Self-frequency Doubling in Nonlinear $LaBGeO_5:Nd^{3+}$ Crystal. *Appl. Phys. Lett.* **1999**, *75*, 2722−2724.
(551) Xia, M. J.; Li, R. K. Crystal Growth and Spectral Properties of $Nd:Ca_5(BO_3)_3F$. *Cryst. Res. Technol.* **2012**, *47*, 1243−1248.
(552) Schaffers, K. I.; Deloach, L. D.; Payne, S. A. Crystal Growth, Frequency Doubling, and Infrared Laser Performance of $Yb^{3+}:BaCaBO_3F$. *IEEE J. Quantum Electron.* **1996**, *32*, 741−748.
(553) Zhao, W.; Zhou, W. W.; Song, M. J.; Wang, G. F.; Du, J. M.; Yu, H. J.; Chen, J. X. Polarization Spectroscopic Properties of a Potential Self-frequency Doubling Crystal, $Nd^{3+}:BaCaBO_3F$. *Opt. Mater.* **2011**, *33*, 647−654.
(554) Goldstein, D. H. *Polarized Light*; CRC: Boca Raton, FL, 2011.
(555) Niu, S. Y.; Joe, G.; Zhao, H.; Zhou, Y. C.; Orvis, T.; Huyan, H. X.; Salman, J.; Mahalingam, K.; Urwin, B.; Wu, J. B.; et al. Giant Optical Anisotropy in a Quasi-one-dimensional Crystal. *Nat. Photonics* **2018**, *12*, 392−396.
(556) Vegas, A.; Cano, F. H.; García-Blanco, S. The Crystal Structure of Calcium Orthoborate: a Redetermination. *Acta Crystallogr., Sect. B: Struct. Crystallogr. Cryst. Chem.* **1975**, *B31*, 1416−1419.
(557) Lu, X. A.; You, Z. Y.; Li, J. F.; Zhu, Z. J.; Jia, G. H.; Wang, Y.; Wu, B. C.; Tu, C. Y. Growth and Properties of Pure and Rare earth-doped $Ca_3(BO_3)_2$ Single Crystal. *J. Cryst. Growth* **2005**, *281*, 416−425.
(558) Akella, A.; Keszler, D. A. Structure and Eu^{2+} Luminescence of Dibarium Magnesium Orthoborate. *Mater. Res. Bull.* **1995**, *30*, 105−111.
(559) Lv, X. S.; Wang, P.; Yu, H. J.; Hu, Y. Y.; Zhang, H. D.; Qiu, C. C.; Li, J.; Wang, X. P.; Liu, B.; Zhang, Y. Y. Growth and Optical Properties of a Promising Deep-ultraviolet Birefringent Crystal $Ba_2Mg(BO_3)_2$. *Opt. Mater. Express* **2019**, *9*, 3835−3842.
(560) Zhang, M.; An, D. H.; Hu, C.; Chen, X. L.; Yang, Z. H.; Pan, S. L. Rational Design via Synergistic Combination Leads to an Outstanding Deep-ultraviolet Birefringent $Li_2Na_2B_2O_5$ Material with an Unvalued B_2O_5 Functional Gene. *J. Am. Chem. Soc.* **2019**, *141*, 3258−3264.
(561) Kokh, A. E.; Kononova, N. G.; Bekker, T. B.; Fedorov, P. P.; Nigmatulina, E. A.; Ivanova, A. G. An Investigation of the Growth of β-BaB_2O_4 Crystals in the BaB_2O_4-NaF System and New Fluoroborate $Ba_2Na_3[B_3O_6]_2F$. *Crystallogr. Rep.* **2009**, *54*, 146−151.
(562) Bekker, T. B.; Kokh, A. E.; Kononova, N. G.; Fedorov, P. P.; Kuznetsov, S. V. Crystal Growth and Phase Equilibria in the BaB_2O_4-NaF System. *Cryst. Growth Des.* **2009**, *9*, 4060−4063.
(563) Wang, X.; Xia, M. J.; Li, R. K. A Promising Birefringent Crystal $Ba_2Na_3(B_3O_6)_2F$. *Opt. Mater.* **2014**, *38*, 6−9.
(564) Zhang, H.; Zhang, M.; Pan, S. L.; Yang, Z. H.; Wang, Z.; Bian, Q.; Hou, X. L.; Yu, H. W.; Zhang, F. F.; Wu, K.; et al. $Na_3Ba_2(B_3O_6)_2F$: Next Generation of Deep-ultraviolet Birefringent Materials. *Cryst. Growth Des.* **2015**, *15*, 523−529.
(565) Liebertz, J.; Fröhlich, R. Struktur und Kristallchemie von $Ba_2M(B_3O_6)_2$ mit M = Ca, Cd, Mg, Co und Ni. *Z. Kristallogr.* **1984**, *168*, 293−297.
(566) Zhao, J.; Ma, Y. Y.; Li, R. K. Characterization of Polarizer Made of the Deep-UV Birefringent Crystal $Ba_2Mg(B_3O_6)_2$. *Appl. Opt.* **2015**, *54*, 9949−9953.
(567) Bugaris, D. E.; zur Loye, H.-C. Materials Discovery by Flux Crystal Growth: Quaternary and Higher Order Oxides. *Angew. Chem., Int. Ed.* **2012**, *51*, 3780−3811.
(568) Wan, S.; Zheng, G.; Yao, Y.; Zhang, B.; Qian, X.; Zhao, Y.; Hu, Z.; You, J. Investigation on the Structure of a LiB_3O_5−$Li_2Mo_3O_{10}$ High-Temperature Solution for Understanding the $Li_2Mo_3O_{10}$ Flux Behavior. *Inorg. Chem.* **2017**, *56*, 3623−3630.
(569) Lin, Z. S.; Jiang, X. X.; Kang, L.; Gong, P. F.; Luo, S. Y.; Lee, M. X. First-principles Materials Applications and Design of Nonlinear Optical Crystals. *J. Phys. D: Appl. Phys.* **2014**, *47*, 253001.
(570) Lin, J.; Lee, M. H.; Liu, Z. P.; Chen, C. T.; Pickard, C. J. Mechanism for Linear and Nonlinear Optical Effects in β-BaB_2O_4 Crystals. *Phys. Rev. B: Condens. Matter Mater. Phys.* **1999**, *60*, 13380−13389.
(571) Jing, Q.; Yang, G.; Hou, J.; Sun, M. Z.; Cao, H. B. Positive and Negative Contribution to Birefringence in a Family of Carbonates: A Born Effective Charges Analysis. *J. Solid State Chem.* **2016**, *244*, 69−74.
(572) Jing, Q.; Yang, G.; Chen, Z. H.; Dong, X. Y.; Shi, Y. J. A Joint Strategy to Evaluate the Microscopic Origin of the Second-Harmonic-Generation Response in Nonpolar $ABCO_3F$ Compounds. *Inorg. Chem.* **2018**, *57*, 1251−1258.
(573) Lin, C. S.; Zhou, A. Y.; Cheng, W. D.; Ye, N.; Chai, G. L. Atom-Resolved Analysis of Birefringence of Nonlinear Optical Crystals by Bader Charge Integration. *J. Phys. Chem. C* **2019**, *123*, 31183−31189.
(574) Cheng, X. Y.; Li, Z. H.; Wu, X. T.; Hong, M. C.; Whangbo, M.; Deng, S. Q. Key Factors Controlling the Large Second Harmonic Generation in Nonlinear Optical Materials. *ACS Appl. Mater. Interfaces* **2020**, *12*, 9434−9439.
(575) Qi, L.; Chen, Z.; Shi, X.; Zhang, X.; Jing, Q.; Li, N.; Jiang, Z.; Zhang, B.; Lee, M.-H. $A_3BBi(P_2O_7)_2$ (A = Rb, Cs; B = Pb, Ba): Isovalent Cation Substitution to Sustain Large Second-Harmonic Generation Responses. *Chem. Mater.* **2020**, *32*, 8713−8723.
(576) Xiong, L.; Chen, J.; Lu, J.; Pan, C. Y.; Wu, L. M. Monofluorophosphate: A New Source of Deep-ultraviolent Nonlinear Optical Materials. *Chem. Mater.* **2018**, *30*, 7823−7830.
(577) Zhang, B. B.; Han, G. P.; Wang, Y.; Chen, X. L.; Yang, Z. H.; Pan, S. L. Expanding Frontiers of Ultraviolet Nonlinear Optical Materials with Fluorophosphates. *Chem. Mater.* **2018**, *30*, 5397−5403.
(578) Lu, X. F.; Chen, Z. H.; Shi, X. R.; Jing, Q.; Lee, M. H. Two Pyrophosphates with Large Birefringences and Second-Harmonic Responses as Ultraviolet Nonlinear Optical Materials. *Angew. Chem., Int. Ed.* **2020**, *59*, 17648−17656.
(579) Kang, L.; Lin, Z. S.; Liu, F.; Huang, B. Removal of A-Site Alkali and Alkaline Earth Metal Cations in $KBe_2BO_3F_2$-Type Layered Structures to Enhance the Deep-Ultraviolet Nonlinear Optical Capability. *Inorg. Chem.* **2018**, *57*, 11146−11156.
(580) Kang, L.; Luo, S. Y.; Peng, G.; Ye, N.; Wu, Y. C.; Chen, C. T.; Lin, Z. S. First-Principles Design of a Deep-Ultraviolet Nonlinear-Optical Crystal from $KBe_2BO_3F_2$ to $NH_4Be_2BO_3F_2$. *Inorg. Chem.* **2015**, *54*, 10533−10535.
(581) Bian, Q.; Yang, Z. H.; Wang, Y.; Cao, C.; Pan, S. L. Predicting Global Minimum in Complex Beryllium Borate System for Deep-ultraviolet Functional Optical Applications. *Sci. Rep.* **2016**, *6*, 34839.
(582) Bian, Q.; Yang, Z. H.; Wang, Y.; Mutailipu, M.; Ma, Y. M.; Pan, S. L. Computer-Assisted Design of a Superior Be_2BO_3F Deep-Ultraviolet Nonlinear-Optical Material. *Inorg. Chem.* **2018**, *57*, 5716−5719.
(583) Oganov, A. R.; Pickard, C. J.; Zhu, Q.; Needs, R. J. Structure Prediction Drives Materials Discovery. *Nat. Rev. Mater.* **2019**, *4*, 331−348.
(584) Ryan, K.; Lengyel, J.; Shatruk, M. Crystal Structure Prediction via Deep Learning. *J. Am. Chem. Soc.* **2018**, *140*, 10158−10168.
(585) Cong, R. H.; Yang, T.; Sun, J. L.; Wang, Y. X.; Lin, J. H. Observation of the Sixth Polymorph of BiB_3O_6: In Situ High-Pressure Raman Spectroscopy and Synchrotron X-ray Diffraction Studies on the β-Polymorph. *Inorg. Chem.* **2013**, *52*, 7460−7466.

https://dx.doi.org/10.1021/acs.chemrev.0c00796
Chem. Rev. 2021, 121, 1130−1202

(586) Liu, Y.; Liu, X.; Liu, S.; Ding, Q.; Li, Y.; Li, L.; Zhao, S.; Lin, Z.; Luo, J.; Hong, M. An Unprecedented Antimony (III) Borate with Strong Linear and Nonlinear Optical Responses. *Angew. Chem., Int. Ed.* **2020**, *59*, 7793−7796.
(587) Huang, C. M.; Mutailipu, M.; Zhang, F. F.; Griffith, K. J.; Hu, C.; Yang, Z. H.; Poeppelmeier, K. R.; Pan, S. L. Expanding the Chemistry of Borates with Functionalized $[BO_2]^-$ Anions. Under revision for publication.

https://dx.doi.org/10.1021/acs.chemrev.0c00796
Chem. Rev. 2021, 121, 1130−1202